

UNIVERSITÀ DEGLI STUDI DI CASSINO E DEL LAZIO
MERIDIONALE

CORSO DI DOTTORATO IN METODI, MODELLI E TECNOLOGIE PER
L'INGEGNERIA

DIPARTIMENTO DI INGEGNERIA CIVILE E MECCANICA



**Numerical methods for a sustainable future:
indoor environmental quality and innovative energy
systems analysis**

by

Giorgio Grossi

Dissertation for the purpose of obtaining the degree of Doctor of Philosophy,
to be defended publicly on Tuesday 16 January 2024

SUPERVISORS

Prof. Fausto Arpino

Prof. Gino Cortellessa

COORDINATOR

Prof. Fabrizio Marignetti

UNIVERSITÀ DEGLI STUDI DI CASSINO E DEL LAZIO
MERIDIONALE
CORSO DI DOTTORATO IN METODI, MODELLI E TECNOLOGIE PER
L'INGEGNERIA
XXXVI CICLO

January 11, 2024


Author: **Giorgio Grossi**

Title: **Numerical methods for a sustainable future: indoor
environmental quality and innovative energy systems analysis**

Department: **Dipartimento di Ingegneria Civile e Meccanica**

Degree: **Doctor of Philosophy**

Permission is herewith granted to university to circulate and to have copied for non-commercial purposes, at its discretion, the above title upon the request of individuals or institutions.



Signature of Author

THE AUTHOR RESERVES OTHER PUBLICATION RIGHTS, AND NEITHER THE THESIS NOR EXTENSIVE EXTRACTS FROM IT MAY BE PRINTED OR OTHERWISE REPRODUCED WITHOUT THE AUTHOR'S WRITTEN PERMISSION.

THE AUTHOR ATTESTS THAT PERMISSION HAS BEEN OBTAINED FOR THE USE OF ANY COPYRIGHTED MATERIAL APPEARING IN THIS THESIS (OTHER THAN BRIEF EXCERPTS REQUIRING ONLY PROPER ACKNOWLEDGEMENT IN SCHOLARLY WRITING) AND THAT ALL SUCH USE IS CLEARLY ACKNOWLEDGED.

CONTENTS

Summary	v
List of symbols	vii
Prologue	1
1 Introduction	3
1.1 Research background, motivation and scope.....	4
1.2 Dissertation outline	5
I Indoor environmental quality: applications	7
2 Aerosol dispersion in indoor environments	9
2.1 Introduction	10
2.2 Case studies and research objectives.....	10
2.3 Methodology.....	11
2.3.1 Eulerian-Lagrangian based model to simulate airborne particles dispersion	12
2.3.2 Droplet emission model	13
3 Aerosol dispersion and SARS-CoV-2 risk assessment in a car cabin	17
3.1 Introduction	18
3.2 Materials and methods	19
3.2.1 Eulerian-Lagrangian based model to simulate the airborne particle spread within the car cabin	20
3.2.2 Computational domain, boundary conditions and investigated scenarios	21
3.2.3 Estimation of the dose received by susceptible subjects and infectious risk assessment	25
CFD analyses	26
Well-mixed approach	27
Probability of secondary transmission	28
3.3 Numerical model validation by PIV data	28
3.4 Results and discussion.....	35
3.4.1 Influence of the position of the infected subject in the car cabin	35
3.4.2 Influence of the HVAC system flow rate.....	39
3.4.3 Influence of the HVAC ventilation mode	40
3.4.4 Influence of the expiratory activity: breathing vs. speaking	43
3.4.5 Distribution of secondary cases.....	44
3.4.6 Strengths and weaknesses.....	46
3.5 Conclusions	47

4	Aerosol dispersion in a university lecture room	49
4.1	Introduction	50
4.2	Materials and methods	51
4.2.1	Mathematical model.....	52
4.2.2	Scenario analysed	52
4.2.3	Experimental campaign	53
	Measurements for the definition of boundary conditions	53
	Measurements for the validation of the numerical model	54
4.3	Numerical model validation.....	55
4.4	Results and discussions	59
4.4.1	Analysis of droplet behaviour, age and distribution	61
4.4.2	Assessment of the mean droplet concentration in the seats area	65
4.5	Conclusions	68
5	Effectiveness of a portable personal air cleaner in reducing the airborne transmission of respiratory pathogens	69
5.1	Introduction	70
5.1.1	Routes of transmission and role of the ventilation.....	70
5.1.2	Air cleaners and personalized ventilation.....	71
5.1.3	Aims of the work.....	71
5.2	Materials and methods	72
5.2.1	Numerical model	74
	Eulerian approach in close proximity scenario	74
	Eulerian approach in shared indoor environments	75
5.2.2	Personal air cleaner in a close proximity scenario	75
5.2.3	Personal air cleaner in a shared indoor environment	80
5.3	Results.....	83
5.3.1	Effectiveness of the air cleaner in a close proximity scenario	83
5.3.2	Effectiveness of the air cleaner in shared indoor environments	85
5.4	Conclusions	88
II	Indoor environmental quality: benchmark for CFD validation	91
6	Experimental characterisation of ventilation flow in a real car cabin: a benchmark case	93
6.1	Introduction	94
6.2	Methodology	95
6.2.1	Airflow measurements at the vents outlet.....	96
6.2.2	PIV experimental setup	98
	PIV data uncertainty quantification	101
6.3	Results and discussions	102
6.3.1	Airflow measurements at the vents outlet, 5-hole pressure probe	102
6.3.2	PIV measurements	103
	Time-averaged velocity fields and measurement uncertainty	103
	Flow fluctuations and their uncertainties.....	111
6.4	Conclusions	119

7	On the effectiveness of Reynolds-averaged and subgrid scale models in predicting flows inside car cabins	121
7.1	Introduction	122
7.2	Methodology.....	124
7.2.1	PIV experimental setup.....	124
7.2.2	Geometry modelling.....	125
7.2.3	Definition of the inlet mean velocity boundary condition	126
7.2.4	Case study.....	127
7.2.5	Methodology for thermal comfort assessment.....	127
7.3	Numerical setup.....	129
7.3.1	Setup for URANS simulations	129
7.3.2	Setup for LES simulations.....	131
7.4	Numerical model validation against PIV measurements.....	132
7.5	Discussion of velocity and temperature fields, and thermal comfort analysis.....	141
7.5.1	Numerical mean velocity and temperature fields	142
7.5.2	Thermal comfort assessment.....	146
7.6	Conclusions	148
III	Energy conversion systems and decarbonization	149
8	Green hydrogen for energy storage and natural gas system decarbonization	151
8.1	Introduction	152
8.2	Description of the PtH ₂ integrated energy system.....	155
8.3	PtH ₂ integrated energy system model	157
8.3.1	Photovoltaic system.....	157
8.3.2	Electrolysis unit.....	158
8.3.3	Storage unit	159
8.3.4	Natural gas network consumption	160
8.3.5	Avoided carbon dioxide emissions calculation	160
8.4	Economic assessment methodology	161
8.5	Case study.....	163
8.6	Results and discussions	164
8.6.1	Economic evaluations	166
8.6.2	Sensitivity analysis to the χ coefficient.....	167
8.7	Conclusions	169
Epilogue		171
9	Conclusions and outlook	173
9.1	Concluding remarks and future perspectives.....	174
9.1.1	Part I.....	174
9.1.2	Part II.....	176
9.1.3	Part III	177
A	Appendix A	179
A.1	Governing equations of fluid dynamics	180

A.1.1	Simplified mathematical models.....	180
A.2	Physics of turbulent flows.....	182
A.2.1	Reynolds-Averaged Navier-Stokes (RANS) simulations.....	183
A.2.2	Large Eddy Simulations (LES)	186
A.3	The Finite Volume Method (FVM)	187
A.3.1	FVM for diffusion problems	188
A.3.2	FVM for convection-diffusion problems	190
A.4	Pressure-velocity coupling: SIMPLE, PISO and PIMPLE algorithms	195
A.4.1	SIMPLE algorithm.....	196
A.4.2	PISO algorithm	197
A.4.3	PIMPLE algorithm.....	198
B	Appendix B	199
B.1	Fan strength: level 1	200
B.2	Fan strength: level 2	205
B.3	Fan strength: level 4	210
	References	215
	Acknowledgements	239
	List of publications	241

SUMMARY

In the face of the profound challenges posed by the 21st century, sustainable development stands as an imperative, reflecting our shared responsibility to address environmental, social, and economic concerns, ensuring a better quality of life for present and future generations.

This doctoral dissertation offers a pathway to a safer and more sustainable future, seeking novel solutions that address both the immediate need for healthier indoor spaces and the long-term goal of achieving a carbon-neutral landscape. It is divided into three main parts, each consisting of self-contained chapters. Part I and II use experimental and Computational Fluid Dynamics (CFD) approaches to study indoor air quality and thermal comfort (the first two pillars of indoor environmental quality) in both large and micro indoor environments.

Specifically, in Part I, the focus is initially on a car cabin micro-environment: the risk of infection from SARS-CoV-2 Delta variant of passengers sharing a car cabin with an infected subject for a 30-min journey is estimated through an integrated approach combining a predictive emission-to-risk approach and a validated CFD numerical model. The findings demonstrate that CFD approaches are essential for properly assessing individual risk in such confined spaces, and that simple zero-dimensional models produce misleading results. One limitation of this study is the simplified geometry adopted for the numerical analyses, which is addressed in Part II of this thesis. Later, the attention shifts to a large indoor environment: a university lecture room. A CFD tool is developed and validated to study the dynamics of droplets emitted by an infected subject speaking in front of the class for 2 h, replicating a 2-h lesson. The influence of three different air supply rates (3.75 ACH, 7.5 ACH and 15 ACH) on particles age, distribution throughout the room and concentration within selected control volumes surrounding the rows of benches is analysed. The main finding is that better control of local airflow patterns is needed in indoor environments, as increasing the airflow rate provided by Heating, Ventilation and Air Conditioning (HVAC) systems might have adverse local effects. Consequently, the last chapter of this section introduces the design of a portable personal air cleaner intended to control local airflow patterns in large indoor spaces and reduce the airborne transmission of respiratory pathogens. CFD analyses revealed that the effectiveness of the device is 96% in close proximity scenarios and 99.5% in large indoor environments.

Part II, relying on the results presented in the preceding section, presents a comprehensive benchmark with Particle Image Velocimetry measurements and CFD simulations of a real car cabin. A comparison is made between unsteady Reynolds-averaged Navier-Stokes (URANS) and large eddy simulation approaches, evidencing that the URANS produces satisfactory results and is suitable for studying the thermal-fluid dynamics fields inside real car cabins. The URANS model is then applied to characterize the mean thermal-fluid dynamics fields in winter and summer conditions, and to perform a thermal comfort analysis. This analysis leads to the conclusion that passengers sharing the same car may

have contrasting comfort perceptions. This point must be considered in the design and operation of the HVAC systems, since the environment must meet the minimum comfort requirements for all the occupants. In this regard, validated CFD tools become essential as they allow to faithfully predict the airflow patterns in this and other indoor environments.

Part III differs from the first two sections and addresses sustainability from an environmental and energy perspective, investigating solutions to promote the diffusion of renewable energy sources and the replacement of fossil fuels. This is achieved by evaluating the feasibility of small-scale Power-to-Hydrogen (PtH₂) systems distributed across the national natural gas transmission network (NGTN), in correspondence of the several regulating and measuring stations present there. The idea is to use the surplus electricity produced by photovoltaic power systems to produce green hydrogen, which is then injected into the natural gas pipelines. This solution, known as line-pack storage, could provide the storage capacity needed to manage the future large energy production from renewables. A mathematical model has been developed to study the hourly operation of the proposed PtH₂ system and to determine the optimal sizing for each subsystem comprising the plant. Findings reveal the need for a hydrogen buffer to balance its production (dependent on the intermittent electricity production from renewables) with its injection in the NGTN (dependent on the natural gas consumption by end-users). The results also show that in the best-case scenario, the cost of hydrogen production is 5.10 EUR kg⁻¹ and the PtH₂ plant allows to save about 32 tonnes of CO₂ emissions per year.

LIST OF SYMBOLS

The notation used is given here in the following order: upper-case Roman, lower-case Roman, upper-case Greek, lower-case Greek, constants, acronyms and abbreviations, superscripts, and subscripts.

Upper-case Roman

AER	Air exchange rate via ventilation	h^{-1}
C	Number of secondary cases	-
$C_{ann,tot}$	Total annualised cost	EUR
C_D	Drag coefficient	-
Co	Courant number	-
C_p	Specific heat at constant pressure	$\text{J kg}^{-1} \text{K}^{-1}$
C_{rep}	Replacement cost of the component	EUR
C_v	Specific heat at constant volume	$\text{J kg}^{-1} \text{K}^{-1}$
$C_{vl,avg}$	Average well-mixed viral load concentration	RNA copies m^{-3}
$D(c_v)$	Dose of RNA copies inhaled by the exposed subject	RNA copies
$E(\kappa)$	Spectral energy	$\text{m}^3 \text{s}^{-2}$
E^{coarse}	Average error in a coarse grid solution	-
E^{fine}	Average error in a fine grid solution	-
E_{vl}	Viral load emission rate	RNA copies h^{-1}
EF_f	Emission factor of the fuel	$\text{kg CO}_2/\text{Sm}^3$
ER _N	Droplet number emission rate	droplet s^{-1}
ER _V	Droplet volume emission rate	$\mu\text{l s}^{-1}$
F_{Basset}	Basset force	N

F_{BM}	Brownian motion force	N
F_{body}	Body force	N
F_D	Drag force	N
F_G	Gravity force	N
$F_{interaction}$	Interaction force	N
F_{Magnus}	Magnus force	N
F_{pp}	Particle-particle interaction force	N
$F_{pressure}$	Pressure force	N
F_{pw}	Particle-wall interaction force	N
$F_{Saffman}$	Saffman force	N
$F_{surface}$	Surface force	N
F_{VM}	Virtual mass force	N
G	LES filter function (Equation (A.27))	
G	Actual solar radiation per unit surface	$W m^{-2}$
G_{NOCT}	Solar radiation at nominal operating conditions	$W m^{-2}$
G_{STC}	Solar radiation per unit surface at <i>STC</i>	$W m^{-2}$
HHV	Higher Heating Value	$MJ Sm^{-3}$
HID_{63}	Human infectious dose for 63% of susceptible subjects	RNA copies
I	Turbulence intensity	-
I_{cl}	Clothing insulation	$m^2 K W^{-1}$
ICC	Initial Capital Cost	EUR
IR	Inhalation rate	$m^3 h^{-1}$
$IVRR$	Infectious virus removal rate	h^{-1}
L	Turbulent characteristic length	m
LCC	Life-cycle Cost	EUR

LCOH	Levelized Cost Of Hydrogen	EUR kg ⁻¹
LES _{IQ}	LES index of quality	-
M	Metabolic rate	W m ⁻²
$M_{hydrogen}$	Total mass of hydrogen produced during the useful life of the system	kg
MM_{CO_2}	Molar mass of carbon dioxide	kg mol ⁻¹
N	Droplet number concentration	part. cm ⁻³
\mathcal{N}	Number of statistically uncorrelated samples	-
NOCT	Nominal Operating Cell Temperature	°C
OM	Operation and Maintenance cost	EUR
P	Formal order of accuracy of the algorithm	-
P_{EL}	Input power to the electrolyser	kW
P_{grid}	Power taken from the electric grid	kW
$P_I(C_V)$	Probability of infection of the exposed subject	-
P_{PV}	Power produced by the PV system	W
P_{RPV}	Power produced by the single PV panel at <i>STC</i>	W
Pe	Peclet number	-
Pr	Prandtl number	-
Q	Volumetric flow rate	m ³ h ⁻¹
$\mathcal{R}_{xx}, \mathcal{R}_{yy}$	Reynolds normal stresses	m ² s ⁻²
\mathcal{R}_{xy}	Reynolds shear stress	m ² s ⁻²
R	Individual risk of infection	-
R_{comp}	Component lifetime	yr
R_{event}	Event reproduction number	-
R_{proj}	Project lifetime	yr
R_{rem}	Remaining life of the component at the end of the project lifetime	yr

R_{rep}	Replacement cost duration	yr
RC	Replacement cost	EUR
Re	Reynolds number	-
Re_t	Turbulence Reynolds number	-
S	Number of susceptible occupants	-
S_x	Source term of the quantity x	
SOC_{HST}	State of charge of the HST	-
Stk	Stokes number	-
T	Temperature	K, °C
T_0	Reference temperature (Equation (A.11))	K
T_{PV}	Actual temperature of the PV panel	°C
T_a	Ambient temperature (Equation (8.2))	°C
$T_{a,NOCT}$	Ambient temperature at nominal operating conditions	°C
T_{FT}	Flow-through time	s
T_{H_2}	Hydrogen supply temperature	K
T_{in}	Inside temperature	°C
T_{out}	Outside temperature	°C
$T_{PV,STC}$	PV panel temperature at STC	°C
T_{tot}	Total exposure time	s
U_x	Expanded uncertainty of the quantity x	
V	Droplet volume concentration	$\mu\text{l cm}^{-3}$
V_{cabin}	Volume of the car cabin	m^3
$V_{H_2,EL}$	Volume of hydrogen produced by the electrolyser	m^3
$V_{H_2,inj}$	Volume of hydrogen injected into the NG network	m^3
$V_{H_2,st}$	Volume of hydrogen stored	m^3

V_{p-post}	Particle volume after evaporation	ml
V_{p-pre}	Particle volume before evaporation	ml
W	Effective mechanical power	$W m^{-2}$
X_c	Carbon mole fraction	mol carbon/mol fuel
Z	Hydrogen compressibility factor	-

Lower-case Roman

a	Amplitude of the sinusoidal velocity profile applied to the receiver mouth	$m s^{-1}$
b_i	Body force per unit volume along the i -direction (Equations (A.2) –(A.4))	$N m^{-3}$
c_v	Viral load carried by the airborne respiratory droplets	RNA copies ml^{-1}
d_d	Droplet diameter	m
d_{eq}	Weighted mean diameter of droplets	m
d_f	Fuel density	$mol Sm^{-3}$
e_i	Internal energy per unit mass	$J kg^{-1}$
f	Frequency of the sinusoidal velocity profile applied to the receiver mouth	s^{-1}
f_{cl}	Clothing surface area factor	-
f_d	Discount rate	-
f_i	Numerical solutions obtained with grid spacing equal to h_i	-
f_{PV}	Attenuation coefficient	-
$f\#$	f-number of a lens	-
h_c	Convective heat transfer coefficient	$W m^{-2} K^{-1}$
i	Real discount rate	-
i'	Nominal discount rate	-
ir	Expected inflation rate	-

k_c	Coverage factor	-
k	Turbulent kinetic energy	$m^2 s^{-2}$
$k_{resolved}$	Resolved turbulent kinetic energy	$m^2 s^{-2}$
k_{total}	Total turbulent kinetic energy	$m^2 s^{-2}$
l	Characteristic size of the largest eddies	m
ℓ	Turbulent mixing length	m
m	Mass	kg
m_f	Fuel quantity	Sm^3
$m_{H_2,EL}$	Mass of hydrogen produced	kg
\mathbf{n}	Unit surface normal vector	-
n_p	Number of data points	-
n_{PV}	Number of photovoltaic panels	-
ny	Year number	-
p	Pressure	Pa
p_a	Water vapor partial pressure	Pa
r	Eddy size	m
r_f	Refinement factor adopted for the generation of the different grids	-
s_u	Sample standard deviation of the velocity component u	$m s^{-1}$
t	Time	s
t_a	Air temperature (Equations (7.2)–(7.4))	$^{\circ}C$
t_{cl}	Clothing surface temperature (Equations (7.2)–(7.4))	$^{\circ}C$
t_i	Instant of time	-
\bar{t}_r	Mean radiant temperature (Equations (7.2) and (7.3))	$^{\circ}C$
tCO_2	Amount of carbon dioxide emissions	tonne

\mathbf{u}	Velocity vector	m s^{-1}
u	Velocity component in the x direction	m s^{-1}
u_A	Random standard uncertainty (Equation (6.1))	
u_B	Systematic (bias) uncertainty (Equation (6.1))	
u_l	Large-scale velocity	m s^{-1}
u_r	Combined standard uncertainty	
v	Velocity component in the y direction	m s^{-1}
\mathcal{V}	Average air speed of the environment (Equation (7.5))	m s^{-1}
\mathcal{V}_{ag}	Relative air speed resulting from the body movement (Equations (7.5) and (7.6))	m s^{-1}
\mathcal{V}_{ar}	Relative air velocity (Equations (7.4) and (7.5))	m s^{-1}
w	Velocity component in the z direction	m s^{-1}
w_{EL}	Specific energy consumption of the electrolyser	kWh kg^{-1}
\mathbf{x}_d	Droplet trajectory	m
x, y, z	Cartesian directions	m
y^+	Dimensionless wall distance	-

Upper-case Greek

Γ	Diffusion coefficient (Equation (A.38))	
Δ	Cutoff width	m
Δh	Characteristic size of the mesh cell	m
Δt	Pulse separation	ms
$\Delta \theta$	Time resolution, set to 1 h (Equation (8.3))	
$\Delta \vartheta$	Time step	s
Φ	Dissipation function	$\text{kg m}^{-1} \text{s}^{-3}$
Ω	Vorticity	s^{-1}

Lower-case Greek

α_p	Power temperature coefficient	$^{\circ}\text{C}^{-1}$
α_x	Under-relaxation factor for the variable x (Section A.4)	-
β	Coefficient of volumetric expansion	K^{-1}
δ	Hydrogen fraction in the blend	-
δ_{ij}	Kronecker delta	
ε	Turbulent kinetic energy dissipation rate	$\text{m}^2 \text{s}^{-3}$
η	Kolmogorov length scale	m
κ	Thermal conductivity	$\text{W m}^{-1} \text{K}^{-1}$
κ	Wave number (Section A.2)	m^{-1}
λ	Second viscosity ($\lambda = -2/3\mu$)	Pa s
μ	Dynamic viscosity	Pa s
μ_T	Eddy (turbulent) viscosity	Pa s
ν	Molecular viscosity	$\text{m}^2 \text{s}^{-1}$
ν_{SGS}	SGS viscosity	$\text{m}^2 \text{s}^{-1}$
ρ	Air density	kg m^{-3}
ρ_0	Reference density (Equation (A.11))	kg m^{-3}
ρ_d	Droplet density	kg m^{-3}
ρ_{H_2}	Hydrogen density	kg m^{-3}
ρ_{xy}	Cross-correlation coefficient between u and v components	-
τ_d	Droplet response time	s
τ_f	Flow characteristic time scale	s
τ_{SGS}	Subgrid-scale Reynolds stresses	$\text{kg m}^{-1} \text{s}^{-2}$
φ	General property per unit mass	

χ	Minimum allowed number of days with injection of H ₂ in the NG network, expressed as a fraction of a year	-
ψ	Velocity profiles data point	m s ⁻¹
ω	Specific dissipation rate	s ⁻¹

Constants

R_g	Universal gas constant (8.314 J mol ⁻¹ K ⁻¹)
$R_{specific}$	Specific gas constant (=287 J kg ⁻¹ K ⁻¹ for dry air)
π	pi (3.14159)

Acronyms and abbreviations

1D	One-dimensional
2D	Two-dimensional
3D	Three-dimensional
ACH	Air changes per hour
AEL	Alkaline Electrolysis Cell
ASHRAE	American Society of Heating, Refrigerating and Air-Conditioning Engineers
BC	Boundary conditions
CCS	Carbon Capture and Storage
CDC	Centres for Disease Control and Prevention
CFD	Computational Fluid Dynamics
CPU	Central Processing Unit
CV	Control volume
DFSEM	Divergence Free Synthetic Eddy Method
DNS	Direct numerical simulation

DSO	Distribution System Operator
EPA	Environmental Protection Agency
FOV	Field of view
FVM	Finite Volume Method
HEPA	High Efficiency Particulate Air filter
HST	Hydrogen storage tank
HVAC	Heating, Ventilation and Air Conditioning
IAQ	Indoor air quality
IEQ	Indoor environmental quality
IRP	Infectious respiratory particle
ISO	International Organization for Standardization
KE	Kinetic energy
LES	Large eddy simulation
LPT	Lagrangian Particle Tracking
MP#	Measuring plane #
Nd:YAG	Neodymium-doped Yttrium Aluminum Garnet
NG	Natural gas
NGTN	NG Transmission Network
NRMSE	Normalized RMSE
OpenFOAM	Open Source Field Operation and Manipulation
PEMEL	Proton Exchange Membrane Electrolysis Cell
PISO	Pressure Implicit with Splitting of Operator
PIV	Particle Image Velocimetry
PMV	Predicted Mean Vote
PPD	Predicted Percentage Dissatisfied

ProCap	Probe Capture
PtG	Power to Gas
PtH ₂	Power to Hydrogen
PV	Photovoltaic
PVGIS	Photovoltaic Geographical Information System
RANS	Reynolds-averaged Navier-Stokes
RES	Renewable Energy Source
RMS	Regulating and Measuring Station
RMSE	Root Mean Squared Error
RNG	Re-Normalisation Group
SDG	Sustainable Development Goal
SGS	Subgrid scale
SIMPLE	Semi-Implicit Method for Pressure-Linked Equations
SOEL	Solid Oxide Electrolysis Cell
SST	Shear Stress Transport
STC	Standard Test Conditions
TKE	Turbulent kinetic energy
TMA	Turbulent Mixing Airflow
TSO	Transmission System Operator
URANS	Unsteady RANS
WALE	Wall Adapting Local Eddy-viscosity
WHO	World Health Organization

Superscripts

$\bar{\varphi}$	Time-averaged quantity
-----------------	------------------------

φ'	Fluctuating component ($\varphi' = \varphi - \bar{\varphi}$)
$\tilde{\varphi}$	Filtered quantity

Subscripts

d	Droplet
exp, i	Experimental data
EL	Electrolyser
inj	Injected
max	Maximum
min	Minimum
$model, i$	Modelling data

PROLOGUE

1

INTRODUCTION

1.1 RESEARCH BACKGROUND, MOTIVATION AND SCOPE

One of the most important matters of our century is *sustainable development*¹ [1]. This concept reflects our collective responsibility to address environmental, social, and economic concerns, ensuring a better quality of life for both present and future generations. With the global population expected to rise from the current 8 billion to over 10 billion by the end of the century [2], and the corresponding increase in energy demand, we face unprecedented challenges. These challenges demand a multidisciplinary approach, converging science, engineering, and innovation. To drive this transformative change and provide a roadmap to a more sustainable and equitable future, in 2015 the United Nations have defined the Sustainable Development Goals (SDGs). These goals consist of seventeen interlinked objectives, each comprising several targets, some to be achieved by 2030 and others with no end date [3].

The present dissertation aims to contribute in tackling some of these goals: SDG 3 (*good health and well-being*: ensure healthy lives and promote well-being for all at all ages), SDG 7 (*affordable and clean energy*: ensure access to affordable, reliable, sustainable and modern energy for all), SDG 11 (*sustainable cities and communities*: make cities and human settlements inclusive, safe, resilient, and sustainable), SDG 13 (*climate action*: take urgent action to combat climate change and its impacts), SDG 15 (*life on land*: protect, restore and promote sustainable use of terrestrial ecosystems, sustainably manage forests, combat desertification, and halt and reverse land degradation and halt biodiversity loss). SDGs 3 and 11 place a paramount emphasis on the well-being and security of individuals in our global society, underscoring the importance of ensuring clean and safe environments. Considering that we, as a society, spend most of our time indoors [4,5], the assessment of indoor environmental quality (IEQ) assumes a central role. This involves the evaluation of indoor air quality (IAQ), thermal comfort, lighting comfort, and acoustic comfort as the four primary factors impacting the quality of life of individuals [5–7]. Part I and II of this booklet give a contribution in this field, focusing on the first two IEQ pillars (i.e., IAQ and thermal comfort), both in micro and large indoor environments.

SDGs 7, 13, 15 are instead devoted to environmental sustainability, conservation, and climate action. In this sense, green hydrogen is a game changer, enabling the diffusion of renewable energy sources (RESs) and the replacement of fossil fuels to achieve a carbon-neutral energy landscape [8,9]. The adoption of green hydrogen also contributes to achieving SDGs 3 and 11, since replacing fossil fuels means reducing the emissions of pollutants improving the air quality. These aspects are addressed in Part III of the dissertation, where the feasibility of green hydrogen production (via photovoltaic-powered electrolyzers) and its blending with natural gas is assessed. This solution is particularly promising since it allows to store the excess renewable electricity produced, and to decarbonize the industrial processes (SDG 9 - *industry, innovation and infrastructure*) and the building sector (SDG 11), among others.

All parts are introduced in more detail and with literature background later in this booklet. In the next section, the outline of the dissertation is provided.

¹ The concept of *sustainable development*, as eloquently expressed in the Brundtland Report in 1987, emphasizes the duty to satisfy the needs of the present without compromising the ability of future generations to meet their own needs.

1.2 DISSERTATION OUTLINE

This doctoral thesis consists of three parts, each addressing a specific topic and composed of self-contained chapters. Below, a description of each part is given, linking it to the general context provided in the preceding section and guiding readers through the document. Concluding remarks and future perspective are provided in Chapter 9.

I. INDOOR ENVIRONMENTAL QUALITY: APPLICATIONS

This section presents case studies in the field of indoor air quality, which is the first pillar of the indoor environmental quality. The focus is on the analysis, conducted through both experiments and Computational Fluid Dynamics (CFD) simulations, of the spread and distribution of virus-laden droplets emitted by a subject sharing an indoor space with other individuals.

Chapter 2 introduces the topic and explains the common methodology used in the analyses carried out in Chapters 3, 4 and 5. This methodology is based on resolving the flow field within a Eulerian framework and tracking the exhaled airborne droplets using a Lagrangian approach.

Chapter 3 investigates particles dispersion and inhalation inside a car cabin, assessing the risk of SARS-CoV-2 infection for passengers sharing the car with an infected individual during a 30-min journey. The effects of various geometrical, emission and thermo-fluid dynamics influence parameters have been evaluated. Findings evidence the need for CFD approaches to assess the risk for the occupants and the potential of numerical analyses in designing the Heating, Ventilation and Air Conditioning (HVAC) systems and airflow patterns, especially for environments characterized by fixed seating arrangements.

Chapter 4 shifts the attention to a large indoor environment: a university lecture room. The study explores the effects of changing the airflow rate provided by the ventilation system on the distribution of airborne droplets emitted by a teacher speaking in front of the class during a 2-h lesson. Results show that increasing the air flow rate from the HVAC system is not always an effective solution to improve indoor air quality and reduce occupant exposure.

This prompted the design a portable personal air cleaner, allowing a better control over local airflow patterns and providing effective protection for susceptible subjects. Chapter 5 presents this concept and describes the tests carried out to assess the effectiveness of the device in both close proximity (typical face-to-face configuration at a conversational distance between two subjects) and shared indoor environments (the university classroom discussed in Chapter 4).

II. INDOOR ENVIRONMENTAL QUALITY: BENCHMARK FOR CFD VALIDATION

The second part of this dissertation (Chapters 6 and 7) leverages the findings of Chapter 3, which emphasizes the value of CFD in studying and designing the airflow patterns within indoor microenvironments like car cabins. However, the reliability and credibility of numerical results strongly depend on the simplifications made (both in terms of geometry and mathematical modelling). The absence of such studies in the existing scientific literature, as far as the author's knowledge at the time of writing, prompted the development of an extended and comprehensive benchmark study to provide insights into the ventilation flow in real car cabins, and produce an experimental database for the validation of numerical simulations.

Chapter 6 describes the experimental campaign, carried out on a commercial car in the Aerodynamics Laboratories at Delft University of Technology. Firstly, the flow velocity at the exit of the vents was characterised by means of 5-hole pressure probe measurements. Then, the flow velocity fields were measured by Particle Image Velocimetry (PIV) at three longitudinal sections inside the car cabin. The time-averaged air velocity fields are presented and discussed, as well as the velocity fluctuations in terms of quadrant analysis, Reynolds stresses and turbulent kinetic energy. Moreover, a detailed uncertainty analysis of the experimental results is presented.

Experimental measurements are employed in Chapter 7 to develop and validate a CFD tool, capable of modelling the fluid dynamics in real car cabins. Here, the performance of both unsteady Reynolds-averaged Navier-Stokes (URANS) and large eddy simulation (LES) approaches is assessed considering both the accuracy and the computational resources required. The validated URANS model, owing to the very good agreement with experimental data and the lower CPU times, is then applied to characterize the airflow patterns in winter and summer conditions and perform a thermal comfort analysis.

III. ENERGY CONVERSION SYSTEMS AND DECARBONIZATION

The last part of this booklet has a different tenor with respect to the previous ones. It delves into the complex current energy landscape in search of a solution to contribute to the diffusion of renewable energy sources and the replacement of fossil fuels. Green hydrogen has been identified as one of the key energy carriers in the transition to RESs due to its versatility and integrability with other clean technologies for energy production and consumption. It has the potential to flexibly transfer energy across sectors, both in terms of time and space. In particular, green hydrogen can be used to address the storage requirements necessary to efficiently handle the future large energy production from RES through the Power to Hydrogen (PtH₂) technology. Essentially, surplus electrical energy from renewables can be used to produce green hydrogen, which can then be injected in the natural gas transmission network NGTN that offers huge line-pack storage capabilities. This solution is examined by Chapter 8, where a mathematical model has been developed to assess the dynamic operation of an integrated PtH₂ system for green hydrogen production using photovoltaic-powered electrolyzers and its injection into the NGTN, upstream of a Regulating and Measuring Station (RMS) located in central Italy. The underlying idea is to produce green hydrogen in small plants connected to the RMSs distributed across the country.

I

INDOOR ENVIRONMENTAL QUALITY: APPLICATIONS

2

AEROSOL DISPERSION IN INDOOR ENVIRONMENTS

This chapter serves as an introduction to the subjects addressed in Part I of this dissertation. First, Section 2.1 underscores the significance of investigating the impact of mechanical ventilation on indoor air quality and aerosol transport. Section 2.2 defines the indoor environments investigated and outlines the research objectives. Lastly, Section 2.3 illustrates the adopted methodology, with a particular focus on the Eulerian-Lagrangian based CFD model here developed, and the droplet emission model implemented in the code.

2.1 INTRODUCTION

The transmission of respiratory viruses may occur through three basic routes [10,11]. *Spray* transmission, traditionally known as *large-droplet* transmission, involves virus-laden *drops* (i.e., particles larger than 100 μm in diameter) emitted by an infected person and deposited on the mucosal surfaces of a susceptible subject. *Inhalation* transmission refers to respiratory droplets suspended in the air (particles below 100 μm in diameter, also known as *aerosol* or *airborne droplets*) that are exhaled by an infected person and inhaled by a susceptible subject. Finally, *touch* transmission refers to animate or inanimate surfaces contaminated by virus-laden drops and/or droplets, being touched by a person then touching their mucosa. The airborne droplet route has been recognized as the primary pathway of infection transmission in indoor environments [10,12,13]. Ballistic drops owe their movement to the momentum gained when they are released [14] and rapidly settle in a range lower than 0.6 m from the source [11], therefore they are a source of contagion only for the subject in close proximity to the source (or by touch transmission in the long range). Conversely, particles with a diameter lower than 100 μm can remain suspended in the air for a prolonged time and travel from a long distance in an indoor environment [14–16], likely infecting multiple individuals sharing the same space of the infected. For these reasons, the commonly recommended safe distance of 1-2 m, widely adopted in most countries to reduce the spread of SARS-CoV-2, can be useful outdoors but is insufficient in indoor environments [14,17]; rather, it is crucial to study the effects of ventilation and air flow patterns, as they strongly influence particles transport and distribution [18]. Natural ventilation effectively reduces air contaminants and improves indoor air quality [19]. However, during the coldest and hottest months of the year, it is avoided due to the disparity between outdoor climatic conditions and the desired thermo-hygrometric comfort [20,21]. Therefore, it is essential to investigate the effect of Heating, Ventilation and Air Conditioning systems on indoor air quality and aerosol transport.

2.2 CASE STUDIES AND RESEARCH OBJECTIVES

In the upcoming chapters, our attention will be directed towards exploring three distinct indoor environments, to provide insights into the diverse situations that individuals may experience every day. Both micro and large environments are investigated, as the dynamics of particles can vary significantly, affecting the exposure and risks for susceptible subjects.

Chapter 3 investigates particles dispersion and inhalation inside a car cabin, assessing the risk of SARS-CoV-2 infection for passengers sharing the car with an infected individual during a 30-min journey. Car cabins are indeed environments of concerns in terms of the diffusion of respiratory pathogens due to their extensive worldwide usage and the potential for non-household individuals to share this space, as is likely to occur with car-sharing and carpooling solutions in large cities. The effects of various geometrical, emission and thermo-fluid dynamics influence parameters have been evaluated, evidencing the need for CFD approaches to design HVAC systems. Findings also revealed that in indoor environments characterized by fixed seating arrangements, the risk of infection can, in principle, be controlled by properly designing the flow patterns of the environment, i.e., moving towards personalized ventilation solutions.

A large shared indoor environment is, instead, explored in Chapter 4. Here, the focus is on the distribution of airborne droplets emitted by a teacher positioned inside a university

lecture room during a two-hour speaking activity (so replicating a two-hour lesson), as a function of different air supply rates from the HVAC system. Lecture rooms are worth of investigation as they are one of the most susceptible indoor environments for infection transmission, with high occupant concentration, long occupation time and the presence of at least 1 person always speaking. Findings revealed that increasing the air flow rate from the HVAC system is not always an effective solution to improve the indoor air quality and reduce occupant exposure. Even for these environments, an interesting solution for better control over local airflow patterns and providing effective protection could be the adoption of personalized ventilation, acting on several sub-volumes within a wider indoor environment. This aspect is addressed in Chapter 5, where the effectiveness of a newly designed portable personal air cleaner in reducing the airborne transmission of respiratory pathogens is assessed, in both close proximity (typical face-to-face configuration at a conversational distance between two subjects) and shared indoor environments (the university classroom discussed in Chapter 4).

The scenarios mentioned above have been analysed by means of CFD simulations and experimental measurements following a consistent approach, as detailed in the following section.

2.3 METHODOLOGY

The methodology adopted in this part (Part II) of the present dissertation relies on an integrated approach summarized by the following main steps:

- development of a three-dimensional, non-isothermal Eulerian-Lagrangian numerical model to describe the dispersion and distribution of airborne droplets in indoor environments. These droplets are emitted by a person speaking or simply breathing over a specific time interval. The numerical model is based on a Eulerian-Lagrangian approach, wherein the continuum equations are solved for the air flow (continuous phase) and Newton's equation of motion is solved for each droplet (discrete phase).
- experimental measurements are conducted to define the boundary conditions and validate the numerical results.
- adoption of a droplet emission model based on experimental data, as a function of the expiratory activity (i.e., speaking and breathing). Thermo-fluid dynamics fields predicted in close proximity to the emitter subject were validated by Cortellessa et al., against Particle Image Velocimetry measurements carried out in the laboratories of the Delft University of Technology [11].
- assessment of aerosol distribution within the indoor environments under investigation.

Numerical investigations have been performed using the open-source OpenFOAM code, which is based on the finite volume method (FVM). An introductory description of the FVM is provided in Appendix A.

2.3.1 EULERIAN-LAGRANGIAN BASED MODEL TO SIMULATE AIRBORNE PARTICLES DISPERSION

The droplet-laden flow evolving in the investigated indoor environments can be regarded as a dispersed dilute two-phase flow, since the spacing between droplets is sufficiently large and the particle volume fraction sufficiently low ($<10^{-3}$) [22,11]. Fluid-particle interaction is here solved by using a Eulerian-Lagrangian approach, modelling the air (i.e., the continuous phase) with a Eulerian approach and tracking the particles (i.e., the discrete phase) individually by solving a force balance equation (Lagrangian Particle Tracking, LPT).

Particles are assumed to be spherical. The trajectory of a single particle in a shear flow can be expressed by the Newton Second Law [23–25]:

$$m_d \frac{d\mathbf{u}_d}{dt} = \mathbf{F}_{body} + \mathbf{F}_{surface} + \mathbf{F}_{interaction} \quad (2.1)$$

where \mathbf{F}_{body} is the body force, $\mathbf{F}_{surface}$ is the surface force and $\mathbf{F}_{interaction}$ is the interaction force. Body force is given by the sum of gravity and virtual mass forces:

$$\mathbf{F}_{body} = \mathbf{F}_G + \mathbf{F}_{VM} \quad (2.2)$$

The virtual mass force \mathbf{F}_{VM} in equation (2.2) arises due to the acceleration of the fluid surrounding the accelerating particle. This force can be neglected when the relative acceleration is small.

Surface force is the sum of drag, pressure, Basset, Saffman and Magnus forces, as described by the following equation:

$$\mathbf{F}_{surface} = \mathbf{F}_D + \mathbf{F}_{pressure} + \mathbf{F}_{Basset} + \mathbf{F}_{Saffman} + \mathbf{F}_{Magnus} \quad (2.3)$$

For particles with a small diameter, pressure, Saffman and Magnus forces can be safely neglected compared to drag forces. In addition, when the fluid density is much smaller than the particle density, the Basset force can also be considered negligible [25].

Finally, interaction force is the sum of Brownian motion force (\mathbf{F}_{BM}), particle-particle interaction force (\mathbf{F}_{pp}), and particle-wall interaction force (\mathbf{F}_{pw}):

$$\mathbf{F}_{interaction} = \mathbf{F}_{BM} + \mathbf{F}_{pp} + \mathbf{F}_{pw} \quad (2.4)$$

Brownian motion force can be neglected, since the particles considered are of the order of microns in size. Particle-particle interaction forces must be considered for dense particle suspensions [25]; particle-wall interaction forces are important in dense flows, as well as in wall-dominated dilute flows [22]. These forces are assumed to be negligible in the proposed investigations.

According to the above discussion, the droplet motion inside the airflow is described by solving the LPT equations below:

$$m_d \frac{d\mathbf{u}_d}{dt} = \mathbf{F}_D + \mathbf{F}_G \quad (2.5)$$

$$\frac{d\mathbf{x}_d}{dt} = \mathbf{u}_d \quad (2.6)$$

The drag force is given by Crowe et al. [22]:

$$\mathbf{F}_D = m_d \frac{18}{\rho_d \cdot d_d^2} C_D \frac{Re_d(\mathbf{u} - \mathbf{u}_d)}{24} \quad (2.7)$$

The droplet density has been considered constant and equal to 1200 kg m^{-3} as representative of the density of non-volatile components carried by respiratory droplets [26–28]. The Re_d is calculated as:

$$Re_d = \frac{\rho(\mathbf{u} - \mathbf{u}_d)d_d}{\mu} \quad (2.8)$$

whereas the drag coefficient, C_D , in equation (2.7) is evaluated as a function of the droplet Reynolds number:

$$C_D = \begin{cases} \frac{24}{Re_d} & \text{if } Re_d < 1 \\ \frac{24}{Re_d} (1 + 0.15 \cdot Re_d^{0.687}) & \text{if } 1 \leq Re_d \leq 1000 \\ 0.44 & \text{if } Re_d > 1000 \end{cases} \quad (2.9)$$

Droplet collisions are considered to be elastic and the equations of motion for the droplets are solved assuming a one-way coupling: the flow field affects the droplet motion whereas the effect of the particles on the airflow is negligible.

2.3.2 DROPLET EMISSION MODEL

Particle emission from the infected subject was modelled as a function of the expiratory activity, i.e., speaking and breathing. In particular, the particle number emission rate (ER_N , particle s^{-1}), i.e., the size dependent number of particles exhaled by the infected subject per unit time, was estimated for speaking and breathing on the basis of the experimental analyses carried out by Johnson et al. [29] and Morawska et al. [30]. They measured the number distribution of particles from $0.5 \mu\text{m}$ to about $1000 \mu\text{m}$ in close proximity of the mouth of an adult person while breathing and speaking, in order to consider the droplet evaporation phenomenon negligible. This measurement was extremely complex due to the quick evaporation phenomenon typical of the respiratory particles as soon as they are emitted. The experimental analysis was performed in a purpose-built wind tunnel (named the Expired Droplet Investigation System, EDIS) applying two separate measurement techniques to cover the whole size range: an aerodynamic particle sizer (up to $20 \mu\text{m}$) and a droplet deposition analysis ($20\text{--}1000 \mu\text{m}$). For further details on the experimental apparatus and the methodology adopted, the readers are kindly suggested referring to the above-mentioned papers [29,30].

Here, for the sake of brevity, just the simplified particle number distributions considered to make the simulations affordable are shown. Indeed, the original distributions [29,30] have been fitted through simplified distributions made up of five size ranges. Due to the negligible contribution to the infection risk of *spray* borne respiratory particles [11,31,32], the five size ranges here considered are limited to the airborne respiratory particle range ($<90 \mu\text{m}$). Volume distributions and emission rates ($\text{ER}_v, \mu\text{l s}^{-1}$) were calculated considering the particles as spheres. Since the evaporation phenomenon occurs quickly as soon as the particles are emitted [33,34], in the CFD model the post-evaporation number and volume distributions were considered. To this end, the volume particle distribution before evaporation (i.e., as emitted) was reduced to that resulting from the quick evaporation considering a volume fraction of non-volatiles in the initial particle of 1% [33]. This particle evaporation phenomenon reduces the particle diameter to about 20% of the initial emitted size. The particle number and volume distributions pre- and post-evaporation (fitted by five size ranges) adopted in the simulations and the corresponding number and volume emission rates are summarized in Table 2.1 for both the expiratory activities investigated.

As concerns the thermo-fluid dynamics fields in close proximity of the emitter subject, numerical values were validated by Cortellessa et al. [11] against the fields measured with the PIV technique.

Table 2.1. Particle number (dN/dlog(d_d)) and volume (dV/dlog(d_d)) distributions pre- and post-evaporation fitted by five size ranges as adopted in the simulations for breathing and speaking expiratory activities. Particle number (ER_N) and volume (ER_V) emission rates are also reported.

Expiratory activity	Pre-evaporation					Post-evaporation				
	Particle diameter (size range), d _d (µm)	dN/dlog(d _d) (part. cm ⁻³)	dV/dlog(d _d) (µl cm ⁻³)	ER _N (part. s ⁻¹)	ER _V (µl s ⁻¹)	Particle diameter (size range), d _d (µm)	dN/dlog(d _d) (part. cm ⁻³)	dV/dlog(d _d) (µl cm ⁻³)	ER _N (part. s ⁻¹)	ER _V (µl s ⁻¹)
breathing	2.4 µm (<1.9 to 3.2 µm)	0.312	2.33×10 ⁻⁹	32.6	2.43×10 ⁻⁷	0.5 µm (<0.7 µm)	0.312	2.33×10 ⁻¹¹		
	4.1 µm (3.2 to 5.4 µm)	0.016	5.80×10 ⁻¹⁰	1.6	6.11×10 ⁻⁸	0.9 µm (0.7 to 1.2 µm)	0.016	5.80×10 ⁻¹²		
	7.1 µm (5.4 to 9.3 µm)	0.005	1.03×10 ⁻⁹	0.6	1.09×10 ⁻⁷	1.5 µm (1.2 to 2.0 µm)	0.005	1.03×10 ⁻¹¹		
	16.0 µm (9.3 to 27.3 µm)	0.001	2.15×10 ⁻⁹	0.2	4.52×10 ⁻⁷	3.4 µm (2.0 to 5.9 µm)	0.001	2.15×10 ⁻¹¹		
	35.8 µm (27.3 to 46.9 µm)	<0.001	3.44×10 ⁻¹³	<0.1	3.63×10 ⁻¹¹	7.7 µm (5.9 to 10.1 µm)	<0.001	3.44×10 ⁻¹⁵		
	Total	N=0.078	V=1.92×10 ⁻⁹	33.4	8.65×10 ⁻⁷	Total	N=0.078	V=1.92×10 ⁻¹¹		
speaking	4.6 µm (<0.5 to 4.6 µm)	0.266	1.39×10 ⁻⁸	217.6	1.14×10 ⁻⁵	1 µm (<1 µm)	0.266	1.39×10 ⁻¹⁰		
	9.0 µm (4.6 to 17.7 µm)	0.035	1.33×10 ⁻⁸	20.3	7.81×10 ⁻⁶	1.9 µm (1.0 to 3.8 µm)	0.035	1.33×10 ⁻¹⁰		
	23.2 µm (17.7 to 30.4 µm)	0.013	8.75×10 ⁻⁸	3.1	2.05×10 ⁻⁵	5 µm (3.8 to 6.6 µm)	0.013	8.75×10 ⁻¹⁰		
	45.5 µm (30.4 to 68.2 µm)	0.016	8.08×10 ⁻⁷	5.7	2.83×10 ⁻⁴	9.8 µm (6.6 to 14.7 µm)	0.016	8.08×10 ⁻⁹		
	78 µm (68 to 90 µm)	0.015	3.83×10 ⁻⁶	1.8	4.48×10 ⁻⁴	16.8 µm (14.7 to 19.2 µm)	0.015	3.83×10 ⁻⁸		
	Total	N=0.249	V=7.71×10 ⁻⁷	248.6	7.71×10 ⁻⁴	Total	N=0.249	V=7.71×10 ⁻⁹		

3

AEROSOL DISPERSION AND SARS-CoV-2 RISK ASSESSMENT IN A CAR CABIN

In this chapter, the risk of infection from SARS-CoV-2 Delta variant of passengers sharing a car cabin with an infected subject for a 30-min journey is estimated through an integrated approach combining a recently developed predictive emission-to-risk approach and a validated CFD numerical model. Different scenarios are investigated to evaluate the effect of the infected subject position within the car cabin, the airflow rate of the HVAC system, the HVAC ventilation mode, and the expiratory activity (breathing vs. speaking). The numerical simulations here performed reveal that the risk of infection is strongly influenced by several key parameters; as an example, under the same ventilation mode and emitting scenario, the risk of infection ranges from zero to roughly 50% as a function of the HVAC flow rate. The results obtained also demonstrate that (i) simplified zero-dimensional approaches limit proper evaluation of the risk in such confined spaces, conversely, (ii) CFD approaches are needed to investigate the complex fluid dynamics in similar indoor environments, and, thus, (iii) the risk of infection in indoor environments characterized by fixed seats can be in principle controlled by properly designing the flow patterns of the environment.

This chapter is based on the following published articles:

Arpino F., Cortellessa G., Grossi G. and Nagano H. (2022). A Eulerian-Lagrangian approach for the non-isothermal and transient CFD analysis of the aerosol airborne dispersion in a car cabin. *Building and Environment*, 209, 108648.

Arpino F., Grossi G., Cortellessa G., Mikszewski A., Morawska L., Buonanno G. and Stabile L. (2022). Risk of SARS-CoV-2 in a car cabin assessed through 3D CFD simulations. *Indoor air*, 32(3), e13012.

Keywords: car cabin, CFD analysis, respiratory particles, risk of infection, SARS-CoV-2, virus transmission

3.1 INTRODUCTION

Transport microenvironments are confined spaces of concern in terms of SARS-CoV-2 risk of infection due to the high crowding indexes (number of people relative to the size of the confined space) and the possible inadequate clean (pathogen-free) air supply. Indeed, a number of outbreaks occurred worldwide in buses, airplanes, and ships [35–42]. These outbreaks are mainly due to the airborne transmission of inhalable virus-laden airborne respiratory particles (i.e., particles below 100 μm in diameter) which are capable of remaining suspended in the air then likely infecting simultaneously numerous susceptible subjects that share the same confined space of the infected subject. This route of transmission was accepted as the main pathway of infection transmission only in the spring 2021 when, faced with the accumulating scientific evidence [13,43–48], both US CDC and WHO released updated guidelines reporting the negligible role of the spray borne particles (larger particles $>100 \mu\text{m}$ quickly settling due to their inertia) and fomites (i.e., contaminated surfaces) with respect to the airborne respiratory particles (WHO, April 30th, 2021; US CDC, May 7th, 2021). Indeed, SARS-CoV-2 virus has been detected in airborne samples collected in indoor environments such as hospital microenvironments [45–47,49] (where certain presence of infected subjects allows simpler particle samplings) but also in transport microenvironments [50,51], including passenger cars [52]. Thus, despite the implementation of spray borne and surface touch mitigation strategies (i.e., wearing cloth or surgical masks, and washing hands), whose effectiveness on airborne respiratory particles is questionable, reducing the airborne SARS-CoV-2 concentration in such environments is essential in view of reducing the risk of infection of susceptible people exposed. To this end, providing appropriate pathogen-free air supply rates (i.e., air exchange rates) represents a key approach in view of reducing the airborne SARS-CoV-2 concentration in those environments [43,53–55]. Beyond increased dilution, improved ventilation strategies (e.g., personal and displacement) are also needed that can more effectively remove airborne contaminants from the breathing zone, instead of simply dispersing particles across the room. Although public transport microenvironments (trains, airplanes, and buses) could provide, at least in principle, air exchange rates defined by technical standards (e.g., as a function of the occupancy), the ventilation rates in private cars are set by the passengers according to their air quality/thermal comfort perception rather than contaminant removal concerns. Indeed, an epidemiological study, carried out in Singapore in 2020 to explore the transmission risk factors for COVID-19, recognized a significant risk of transmission among non-household contacts sharing a vehicle with an infected subject [56].

A priori estimates of the risk of infection in cars can be carried out adopting prospective assessments based on a known/estimated emission of virus-laden particles and then diluting them in the indoor environment through either simplified zero-dimensional approaches or complex 3D transient approaches [11,54,55,57–60]. Zero-dimensional approaches are based on the simplified hypothesis of complete and instantaneous mixing of the emission to achieve a uniform spatial concentration within the environment; they represent a practical solution to easily obtain rough estimates of concentrations and risks when site-specific information regarding the ventilation, geometry, position of the source, etc. are not available [59,61]. Nonetheless, perfectly mixed conditions (hereinafter referred

to as “well-mixed”) are unlikely in spaces with high ventilation rates [62,63], thus, such hypothesis is even less accurate for large indoor environments characterized by reduced mixing [64] or small confined spaces, as car cabins, where the position of inlet air vents of the HVAC system, the air flow rate entering the car cabin, the air recirculation and its filtration can significantly affect the airflow in the cabin, and then the exposure and risk of passengers [65]. Indeed, even if the average air exchange rate in car cabins can be quite high (e.g., $>100 \text{ h}^{-1}$ when high fan speeds are set or windows are kept open [65,66]), stagnation regions can occur as a result of the specific airflow patterns across the cabin itself. Therefore, for these environments the average risk evaluated through well-mixed models could overestimate or underestimate the actual risk of some of the passengers in the car.

For these reasons, Computational Fluid Dynamics represents an essential approach to investigate the risk of infection in car cabins as it provides detailed information about spatial and temporal virus-laden particle distribution, as a function of specific boundary conditions and ventilation scenarios, by solving the well-known mass, momentum, and energy conservation equations alongside with a proper turbulence model [67–73].

In this study, an integrated approach is developed and applied with the aim of estimating the risk of infection from SARS-CoV-2 Delta variant of susceptible individuals sharing the car cabin with an infected person under the outside air intake conditions (i.e., HVAC system in operation, no recirculation, windows closed). The approach here presented integrates a predictive emission-to-risk approach, able to determine the risk of infection from the viral load emitted by the infected subject [53,74], with a Eulerian-Lagrangian model numerically solved using the open-source OpenFOAM software. The CFD model was experimentally validated against Particle Image Velocimetry measurements available in the scientific literature [75,76] then providing a validated and suitable approach which can be applied to numerically investigate particle dispersion problems in similar environments.

The integrated approach was then applied to different scenarios to evaluate the effect of the following influence parameters: (i) position of the infected subject within the car cabin, (ii) air flow rate of the HVAC system, (iii) HVAC ventilation mode and (iv) expiratory activity (i.e., breathing vs. speaking). A further aim of this study is demonstrating that the risk of infection in indoor environments characterized by fixed seats can be in principle controlled by properly designing the flow patterns of the environment.

PRACTICAL IMPLICATIONS

The study investigated the risk of infection in car cabins combining a predictive emission-to-risk approach and a validated CFD approach. The findings illustrate a methodology for designing proper ventilation systems for car cabin in view of reducing and controlling the risk of infection of passengers.

3.2 MATERIALS AND METHODS

The integrated approach proposed is based on the following steps:

- application of a transient non-isothermal 3D Eulerian-Lagrangian numerical model, validated against PIV measurements, to describe particle spread once emitted by an infected speaking/breathing passenger located in a car cabin compartment (Section 2.3.1).

- description of the emission scenario, i.e., definition of the airborne respiratory particle emission rate of an adult while breathing/speaking [11,60] (Section 2.3.2).
- calculation of the dose inhaled by the susceptible car occupants for a 30-min journey through the CFD simulations and estimate of the corresponding SARS-CoV-2 infection risk and number of secondary cases on the basis of a predictive emission-to-risk approach [53,74] based on the viral load emitted by the infected subject, the dose of viral load received by the exposed subject, and a dose-response model (Section 3.2.3).

Among the possible scenarios that could be considered, the present study investigates the effects of (i) position of the infected subject within the car cabin, (ii) air flow rate of the HVAC system, (iii) HVAC ventilation mode and (iv) expiratory activity. On the other hand, parameters such as journey duration, car occupancy, and side car windows temperature and opening were considered fixed in the simulations. In particular, as hereinafter detailed, the simulations were performed considering a journey duration of 30 min (as representative of the average duration of business trips by car in Europe [77]), an occupation of four passengers (i.e., representative of four workers adopting car-sharing/carpooling solutions), and windows completely closed during the whole journey (as likely occurring when driving on trafficked and polluted roads).

3.2.1 EULERIAN-LAGRANGIAN BASED MODEL TO SIMULATE THE AIRBORNE PARTICLE SPREAD WITHIN THE CAR CABIN

The mathematical-numerical model was developed using the open-source finite volume based OpenFOAM software, to have a fully open and flexible tool with complete control of the variables employed for particle dispersion assessment. It is based on a Eulerian-Lagrangian approach, in which the continuum equations are solved for the air flow (continuous phase) and Newton's equation of motion is solved for each particle (discrete phase). Velocity, pressure and temperature fields in the car cabin were numerically predicted by solving the mass, momentum and energy conservation equations under the assumption of three-dimensional, unsteady, turbulent and compressible flow with ideal gas behaviour. Turbulence was modelled using the URANS approach, and specifically the Shear Stress Transport (SST) $k-\omega$ model [78] since it turned out to be the most suitable one to predict airflow patterns within the car cabin under investigation (see Section 3.3). Transient computations were performed employing the PIMPLE algorithm, which is a combination of PISO (Pressure-Implicit with Splitting of Operators) and SIMPLE (Semi-Implicit Method for Pressure-Linked Equations) algorithms. Details about the governing partial differential equations and the adopted algorithms are provided in Appendix A. The overall transient phenomenon is simulated as consecutive steady-state time steps; when the number of iterations (for a specific time step) reaches the convergence, the algorithm moves on to the next time step until the solution of the investigated phenomenon is complete. A time step of 0.1 s was adopted and as criterion for time step convergence was considered the absolute tolerance of the solver $<10^{-5}$.

The computed numerical fields were averaged over a selected time interval to reach a quasi-steady state condition: once the quasi-steady state condition is achieved, the flow field is frozen and is used to transport the particles injected by the emitter (i.e., the infected subject) over time during speaking and breathing activities. The particle number and

volume distributions adopted in the simulations, and the corresponding number and volume emission rates, have already been discussed in Section 2.3.2.

3.2.2 COMPUTATIONAL DOMAIN, BOUNDARY CONDITIONS AND INVESTIGATED SCENARIOS

The Eulerian-Lagrangian based model is applied to the analysis of particle dispersion and inhalation in a car cabin evaluating the effects of different geometrical, emission and thermo-fluid dynamics influence parameters.

The car cabin sizes are 2.47 m × 1.53 m × 1.19 m, corresponding to a total internal volume of 3.46 m³, which is representative of a “large car” according to the United States Environmental Protection Agency (EPA) Fuel Economy Regulations for 1977 and Later Model Year. Four occupants were considered in the car cabin: the driver sitting in the left front seat and three passengers sitting in the right front seat, right rear seat, and left rear seat, respectively, whereas there was no occupant in the rear middle seat. Three HVAC system ventilation modes were investigated: front ventilation mode (air entering the cabin through four front vents; the sizes of each vent are 10.2 cm × 8.5 cm), windshield defrosting mode (air entering through one vent located under the windshield; the sizes of the vent are 133 cm × 1.5 cm) and mixed ventilation (all the five vents enabled). All the ventilation modes were tested considering outside air intake provided by a HVAC system, which is with no air recirculation; the windows were considered closed for the entire duration of the journey. Different HVAC flow rates (from 10% to 100% of the maximum flow rate), Q (m³ h⁻¹), were investigated: in particular, the intermediate air flow rate (flow rate at the 50% of the maximum fan capacity, hereinafter referred to as $Q_{50\%}$) is set at 216 m³ h⁻¹ on the basis of the value adopted by Pirouz et al. in their study [79]; this value is consistent with the intermediate fan capacity reported by Ullrich et al. [80] for a real car whose internal volume is comparable to that of the cabin model employed for the scenarios under study.

It is noted that the flow rate also affects the velocity at the inlet sections and then the velocity field in the car cabin; moreover, in the simulations here performed a single angle of inlet airflow rate was adopted. The position of the outlet sections also has an effect on the velocity field in the car cabin. In this case, two outlet sections (each measuring 17.0 cm × 8.5 cm) are placed behind the rear seats in the lower-left and lower-right corners, as reported in the experimental case-study adopted to validate the CFD approach here proposed [75,76] (Section 3.3). The computational domains employed for numerical simulations are available in Figure 3.1.

In the case of front and mixed ventilation mode, the computational domain is the one in the lower right corner of Figure 3.1: a rectangular duct is connected to each of the front supply openings, allowing the development of the flow velocity profile before entering the cabin through the air vents; when only front ventilation is enabled, the same computational domain is employed but the patch defining the windshield defrosting inlet is modelled as an adiabatic wall (i.e., the vent is closed). On the other hand, for simulation of scenarios where only windshield defrosting vent is enabled, the computational domain is the one in the lower left corner in Figure 3.1. Boundaries not specified in Figure 3.1 have been modelled as adiabatic walls.

In Table 3.1 the boundary conditions imposed for numerical simulations are detailed for the different ventilation modes considered in the present study.

Assuming winter climatic conditions, a temperature of 283.15 K was applied to the car windows and inlet air temperature was set to 293.15 K. Passenger face temperatures were

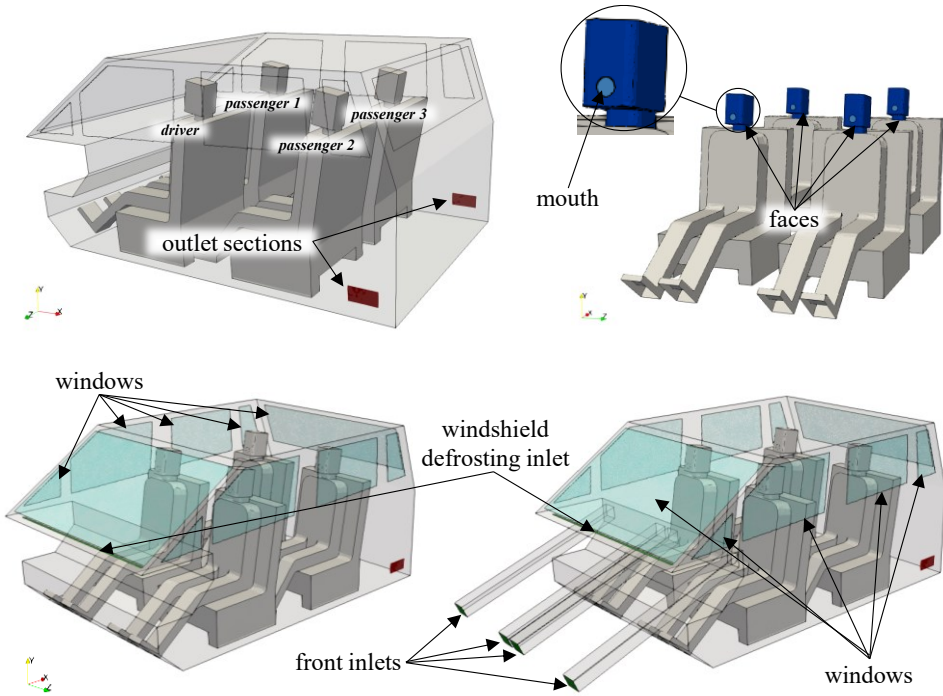


Figure 3.1. Computational domains with boundary patches.

set to 306.15 K [81]. Since a relatively high-velocity fluid flow was numerically simulated and people in the car cabin were supposed to wear winter clothes with a superficial temperature roughly equal to surrounding air, body temperature plume was neglected. When both front and windshield defrosting inlets are enabled, the air flow rate is split as follows: each front vent introduces the 12.5% of the prescribed flow rate and the windshield vent the 50% remaining. For turbulent quantities, the turbulence intensity I (%) and the turbulent mixing length ℓ (m) were specified. The latter was calculated as 7% of the characteristic length L (m), assumed to be equal to the jet width. The emitter (infected subject) and receiver (susceptible subject) mouths were modelled as circular surfaces with a radius of 2 cm. A temperature of 308.15 K was imposed at the mouths of both the emitter and the receiver. As boundary condition for air velocity at the mouths of the emitter and the receiver, fixed velocities equal to 1.11 m s^{-1} and 0.32 m s^{-1} in magnitude were imposed for speaking and breathing activities, respectively; these values were taken as the mean values of the sinusoids during exhalation and inhalation reported by Abkarian et al. [82] and Cortellessa et al. [11]. In particular, in Cortellessa et al. [11] face-to-face interactions between two subjects in close contact were simulated, thus the air flow and particle dynamics were only affected by the breathing/speaking dynamics of the emitter and the receiver. In the present study, the air flow and particle dynamics are mostly affected by the air flow rates entering (and exiting) the car cabin through the vents; moreover, the position, orientation and distance among the passengers allow to neglect the mutual influence of their breathing/speaking dynamics. Thus, adopting constant (mean) expiration and inhalation rates, instead of the sinusoidal dynamics, can be considered an appropriate simplification. All subjects were assumed to be mouth-

breathers, thus airborne particles were expired and inhaled through the mouth. For particle injection, a random velocity direction from the emitter's mouth was evaluated as Abkarian et al. [82], considering a conical jet flow with an angle of 22 deg. As concerns the velocity vector direction from the emitter's mouth, a conical jet flow was considered, adopting a cone angle of 22 deg with random velocity directions at intervals of 0.1 s. This adopted angle was calculated by Abkarian et al. [82] to enclose 90% of the particles in a cone passing through the mouth exit and was verified to remain stable over time after the initial cycles.

Finally, regarding the boundary conditions of the particles, the LPT was solved applying an *escape* boundary condition to all the surfaces of the computational domain, except for the entry sections (where a *rebound* boundary condition was adopted). In other words, the particles touching the external surfaces (of the domain and of the subjects) disappear and cannot re-enter the computational domain, thus avoiding accumulation of viral load in the environment.

Simulations were performed employing hexahedral-based unstructured computational grids, realized with the open-source *snappyHexMesh* algorithm. The adopted grids are composed by 7,899,968 cells (mixed and front ventilation scenarios) and 7,737,311 cells (windshield defrosting ventilation scenario) and are properly refined in correspondence of solid walls and in the jet region, where significant velocity gradients are expected. Grid sensitivity analysis was conducted for the validation configuration, whereby predicted velocity values were compared to PIV measurements carried out on a scaled-down cabin model (see Section 3.3). For the case study, in order to reproduce reality-based scenarios, the computational domain was scaled up by a factor equal to 1.7, according to the dimensions of the model used by Chang et al. in their study [83], and the seats tilt was slightly reduced. The computational grids were constructed preserving the mesh topology, maximum and minimum size.

By way of illustration, the grid employed for mixed ventilation and front ventilation scenarios is depicted in Figure 3.2.

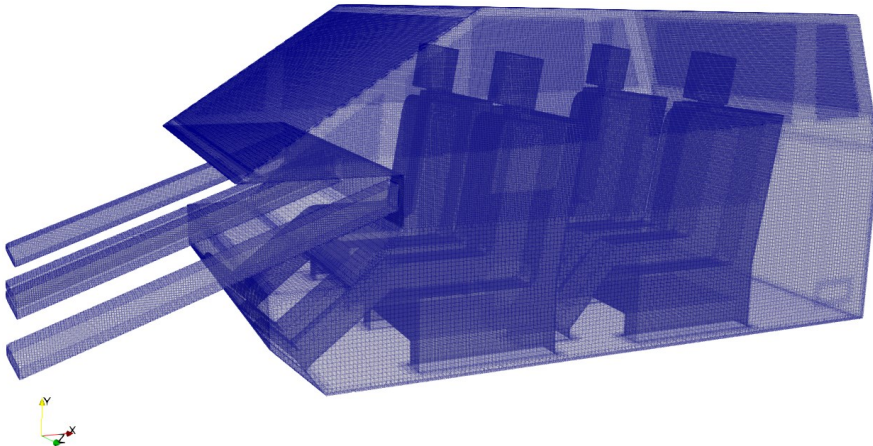


Figure 3.2. Computational grid employed for mixed ventilation and front ventilation scenarios.

Table 3.1. Boundary conditions set for the different ventilation modes.

Surface	BC for velocity	BC for pressure	BC for temperature	BC for k	BC for ω	Lagrangian
front inlets	(10%) $Q_{10\%} = 43.2 \text{ m}^3 \text{ h}^{-1}$					
	(25%) $Q_{25\%} = 108 \text{ m}^3 \text{ h}^{-1}$					
	(50%) $Q_{50\%} = 216 \text{ m}^3 \text{ h}^{-1}$					
	(75%) $Q_{75\%} = 324 \text{ m}^3 \text{ h}^{-1}$					
	(100%) $Q_{100\%} = 432 \text{ m}^3 \text{ h}^{-1}$					
	(50%) $Q_{50\%} = 216 \text{ m}^3 \text{ h}^{-1}$					
front ventilation windshield ventilation	-	$\partial p / \partial \mathbf{n} = 0$	$T = 293.15 \text{ K}$	$I = 5\%$	$\ell = 0.07L$	<i>rebound</i>
	(10%) $Q_{10\%} = 43.2 \text{ m}^3 \text{ h}^{-1}$					
windshield defrosting inlet	(25%) $Q_{25\%} = 108 \text{ m}^3 \text{ h}^{-1}$					
	(50%) $Q_{50\%} = 216 \text{ m}^3 \text{ h}^{-1}$					
	(75%) $Q_{75\%} = 324 \text{ m}^3 \text{ h}^{-1}$					
	(100%) $Q_{100\%} = 432 \text{ m}^3 \text{ h}^{-1}$					
front ventilation windshield ventilation	-					
	(50%) $Q_{50\%} = 216 \text{ m}^3 \text{ h}^{-1}$	$p = 101325 \text{ Pa}$	$T = 293.15 \text{ K}$	$k = 0.1 \text{ m}^2 \text{ s}^{-2}$	$\partial \omega / \partial \mathbf{n} = 0$	<i>escape</i>
outlet sections adiabatic walls windows faces	$\partial \mathbf{u} / \partial \mathbf{n} = 0$		$\partial T / \partial \mathbf{n} = 0$	standard wall functions		
	$\mathbf{u} = 0$		$T = 283.15 \text{ K}$			
		$\partial p / \partial \mathbf{n} = 0$	$T = 306.15 \text{ K}$			
emitter mouth	speaking $ \mathbf{u} = 1.11 \text{ m s}^{-1}$					<i>rebound</i>
	breathing $ \mathbf{u} = 0.32 \text{ m s}^{-1}$					
receiver mouth	$ \mathbf{u} = 0.32 \text{ m s}^{-1}$			$k = 0.1 \text{ m}^2 \text{ s}^{-2}$	$\partial \omega / \partial \mathbf{n} = 0$	<i>escape</i>

The risk of infection was evaluated for different exposure scenarios aimed at evaluating the effect of the influence parameters under investigation. In particular, the following influence parameters were analysed: (i) influence of the position of the infected subject in the car cabin (i.e., driver vs. passenger sitting in the right rear seat); (ii) influence of the HVAC system flow rate (i.e., from 10% to 100% of the maximum flow rate, hereinafter also referred to as airflow ratio); (iii) influence of the HVAC ventilation mode (i.e., mixed, front, and windshield defrosting); (iv) influence of the expiratory activity (i.e., breathing vs. speaking). The scenarios and the corresponding parameters adopted in the simulations are summarized in Table 3.2. Please note that the exposed susceptible subjects were considered breathing through the mouth while sitting.

Table 3.2. Scenarios investigated through CFD analyses: definition of the parameters adopted to evaluate the effect of the influence parameters.

Scenarios investigated	Position of the infected subject	HVAC system flow rate	HVAC ventilation mode	Expiratory activity of the infected subject
influence of the position of the infected subject	driver, passenger sitting in the right rear seat (passenger 3 of Figure 3.1)	$Q_{50\%}$	mixed	speaking
influence of the HVAC system flow rate	driver	$Q_{10\%}, Q_{25\%}, Q_{50\%}, Q_{75\%}, Q_{100\%}$	mixed	speaking
influence of the HVAC ventilation mode	driver	$Q_{50\%}$	mixed, front, windshield defrosting	speaking
influence of the expiratory activity	driver	$Q_{50\%}$	windshield defrosting	speaking, breathing

3.2.3 ESTIMATION OF THE DOSE RECEIVED BY SUSCEPTIBLE SUBJECTS AND INFECTIOUS RISK ASSESSMENT

The risk of infection of the exposed subjects can be calculated based on the dose of viral load (RNA copies considering the viable/infectious fraction) received by susceptible subjects as they inhale virus-laden respiratory particles emitted by the infected subject. Then, a dose-response model is adopted to convert the dose of viral load into a risk of infection.

The dose of viral load is the product of the respiratory particle dose received by the susceptible subjects during the exposure event and the viral load carried by the airborne respiratory droplets emitted by the infected subject. The viral load (c_v) carried by the particles was retrieved from data available in the scientific literature. Here the viral load of the Delta variant (B.1.617.2 SARS-CoV-2) was adopted, which was dominant across much of the world when the present study was carried out. In particular, the c_v distribution data provided by Teyssou et al. [84] (median value of 7.83 \log_{10} RNA copies ml^{-1}) were fitted with a quartile simulation approach. In other words, a Monte Carlo simulation was performed by proportionally selecting random values within each quartile (1st quartile

range 4.3-6.3 \log_{10} RNA copies ml^{-1} , 2nd quartile range 6.3-7.8 \log_{10} RNA copies ml^{-1} , 3rd quartile range 7.8-8.8 \log_{10} RNA copies ml^{-1} , 4th quartile range 8.8-9.4 \log_{10} RNA copies ml^{-1}) to obtain 20,000 c_v values. The respiratory particle dose received by each susceptible subject in the car cabin is evaluated through both CFD analyses and well-mixed approach.

CFD ANALYSES

The dose of RNA copies carried by respiratory airborne particles and then inhaled by the susceptible subject for each c_v value ($D(c_v)$) was calculated as

$$D(c_v) = c_v \int_0^{T_{tot}} V_{p-pre}(t) dt \quad (\text{RNA copies}) \quad (3.1)$$

where $V_{p-pre}(t)$ is the dose of airborne particles inhaled as a function of the exposure time (t), and T_{tot} is the total exposure time (30 min). The viral load carried by the respiratory particle is related to the initial particle volume (i.e., before evaporation) since the evaporation leads to a reduction in the particle volume (the RNA copies do not evaporate); thus, the V_{p-pre} term has been adopted as the dose of airborne particles calculated with the initial (pre-evaporation) volume. On the contrary, the actual dose in terms of volume of respiratory particles inhaled by the susceptible occupants is referred to the actual volume at the time of inhalation (i.e., post-evaporation; hereinafter referred to as V_{p-post}). Indeed, the respiratory particles dynamics is driven by the post-evaporation particle size, whereas the viral load they carry is a function of the pre-evaporation particle size.

From the dose of viral load (i.e., the dose of RNA copies), the probability of infection of the exposed subject for each c_v ($P_I(c_v)$) was calculated adopting a well-known exponential dose-response model [61,85]:

$$P_I(c_v) = 1 - e^{-\frac{D(c_v)}{HID_{63}}} \quad (\%) \quad (3.2)$$

where HID_{63} represents the human infectious dose for 63% of susceptible subjects (i.e., the number of RNA copies needed to initiate the infection with a probability of 63%). For SARS-CoV-2, a HID_{63} value of 7×10^2 RNA copies was applied as recently estimated by Gale [86]. It is observed that in subsequent work, Gale [87] increased the RNA copy-to-plaque-forming unit (pfu) ratio used in the thermodynamic dose-response model from 3.6×10^2 (based on Vicenzi et al. [88]) to 10^4 RNA copies:pfu, which improves agreement with the dose-response estimates of Zhang and Wang [89]. This adjustment increases the HID_{63} value approximately thirtyfold to 2×10^4 RNA copies [87]. However, using the golden Syrian hamster model, Hawks et al. [90] found RNA levels in air samples to be ~200 times higher than pfu levels one and two days post inoculation, with infectious virus non-detect afterwards despite the persistence of RNA detections. This indicates a kinetic aspect to the RNA:pfu ratio likely associated with the immune response that affects the infectious virus fraction [91]. As the focus here is on modelling the early time period of infection for an infected host previously naïve to SARS-CoV-2, use of the HID_{63} value of 7×10^2 RNA copies is maintained. This is also generally consistent with the predictions of a novel dose-response approach developed by Henriques et al. [91]. Furthermore, variants of concern such as Delta and Omicron may have greater infectiousness with a lower HID_{63} , providing another reason to continue with the original model of Gale [86] given the great uncertainty in the dose-response model for humans.

In order to consider the range of possible viral load values, the individual risk of infection (R) of each exposed passenger was calculated through a Monte Carlo simulation with

20,000 realizations, in which the viral load (c_v) was sampled randomly from the previously defined distribution and then assigned as the RNA concentration of the exhaled particle volume to calculate the inhaled dose of RNA copies (D) and the resulting probability of infection (P_I) for each realization. The mean of the 20,000 P_I values is calculated as the individual risk (R) for each passenger based on their respective inhaled doses.

WELL-MIXED APPROACH

To compare the risks of infection obtained through the detailed CFD analyses proposed here with those that would have been calculated adopting the well-mixed hypothesis, the risk of infection of the susceptible subjects was also assessed adopting the simplified zero-dimensional model assuming complete and instantaneous mixing of the viral emissions. In this case, the dose of RNA copies received by the susceptible individuals was estimated on the basis of the average well-mixed viral load concentration in the car cabin $C_{vl,avg}$ (RNA copies m^{-3}) over the course of the 30-min journey, based on the analytical solution of Miller et al. [58]:

$$C_{vl,avg}(c_v, t) = \frac{E_{vl}(c_v)}{V_{cabin} \cdot IVRR} \left[1 - \frac{1}{IVRR \cdot t} (1 - e^{-IVRR \cdot t}) \right] \quad (\text{RNA copies } m^{-3}) \quad (3.3)$$

where V_{cabin} (m^3) is the volume of the car cabin under investigation, $IVRR$ (h^{-1}) represents the infectious virus removal rate in the space investigated, and E_{vl} is the viral load emission rate (RNA copies h^{-1}). $IVRR$ is the sum of three contributions [92]: the particle deposition on surfaces (here assumed equal to $0.24 h^{-1}$ [93]), the viral inactivation (here assumed equal to $0.63 h^{-1}$ [48]), and the average air exchange rate via ventilation (AER, h^{-1}). The latter was calculated as the ratio between the airflow rate provided by the HVAC systems and the cabin volume: AERs were equal to 12.5, 31.2, 62.4, 93.6, and $124.9 h^{-1}$ at $Q_{10\%}$, $Q_{25\%}$, $Q_{50\%}$, $Q_{75\%}$, and $Q_{100\%}$ flow rates, respectively. E_{vl} was calculated as the product of the viral load (c_v , obtained from simulation as described previously) and the cumulative, pre-evaporation airborne volume emission rate (ER_v) obtained from Table 2.1 (i.e., 7.71×10^{-4} and $8.65 \times 10^{-7} \mu l s^{-1}$ for speaking and breathing, respectively).

The dose of RNA copies inhaled by the exposed subject was then estimated as:

$$D(c_v, t) = IR \cdot C_{vl,avg}(c_v, t) \cdot t \quad (\text{RNA copies}) \quad (3.4)$$

with IR being the inhalation rate and equal to $0.54 m^3 h^{-1}$ for an adult just breathing while sitting [94,95].

As with the analysis based on the CFD results, a Monte Carlo simulation was performed to estimate the individual risk (R) of each susceptible passenger based on the viral load of the emitting host. For speaking, a simulation to calculate R using Equation (3.2) was performed for each of the three ER_v values presented earlier. The distribution of secondary cases and R_{event} were calculated using the Bernoulli trial approach (Equation (3.5)) for the most representative well-mixed scenarios as further described in Section 3.4.

In terms of the emission rate in units of infectious doses of Delta SARS-CoV-2, or “quanta” when considering the HID_{63} , the equivalent values modelled herein for the 25th, 50th, and 75th percentile viral loads for speaking are 8.0, 252, and 2524 quanta h^{-1} for the pre-evaporation volume up to $90 \mu m$ in diameter. There are no literature values for comparison for the Delta or Omicron variants, but a recent Omicron outbreak at a party in a restaurant in Norway [96] suggests high emission rates are likely. For example, using Equations (3.2)–(3.4) for a ca. $145 m^2$ room with 3 m ceilings and a 74% probability of

infection for a 4.5-hour exposure leads to emission rate estimates of 470 and 1650 quanta h^{-1} for $IVRR$ values of 1.5 and 6.0 h^{-1} , respectively, using an IR of $\sim 0.5 \text{ m}^3 \text{ h}^{-1}$. Thus, the emission rates evaluated herein appear plausible also considering the rapid spread of both Delta and Omicron variants.

PROBABILITY OF SECONDARY TRANSMISSION

Beyond the individual risk, which is the mean of an overdispersed distribution and thus masks substantial variability in outcomes, it is of interest to calculate the probability of secondary transmission from the car journey, which is a function of the number of susceptible occupants of the car (S). Specifically, the probability of discrete numbers of secondary cases (C) arising can be estimated using a Bernoulli trial approach, which is an improvement over past works [54,60] using the percentile values of a continuous distribution of C obtained from the simple product of R and S for each realization. Similarly to the methodology of Goyal et al. [97], successful transmission for each passenger (assuming all passengers are fully susceptible) is modelled by drawing a random uniform variable $U(0,1)$ and comparing it with the P_I value for that passenger, with successful transmission occurring when $U(0,1) < P_I$. This was performed for each of the three susceptible passengers for each realization, and the number of secondary cases (C) for an individual realization was calculated by summing up the successful trials as follows:

$$C = \sum_{S=1}^{S=3} \text{Ber}(P_I)_S \quad (\text{secondary cases}) \quad (3.5)$$

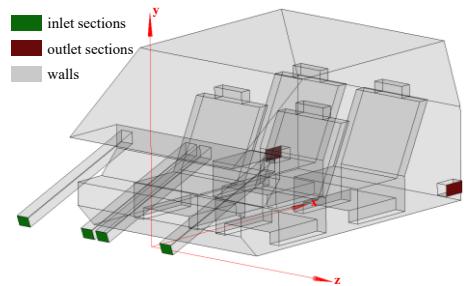
The end result of the simulation is a discrete probability distribution of secondary cases (C), with the mean value representing the event reproduction number (R_{event}) of the 30-min car journey in accordance with the definition of Tupper et al. [98].

3.3 NUMERICAL MODEL VALIDATION BY PIV DATA

The car cabin micro-environment considered for the validation of the numerical model is the one described by Y. Ozeki et al. in [76]. They presented an experimental campaign on the glass-made scaled-down car cabin model available in Figure 3.3a, by employing the PIV technique [99].



(a) scale car model for PIV measurements [76]



(b) computational domain

Figure 3.3. Scale car model and computational domain.

The car cabin model is a scale model 1450 mm long, 700 mm high and 900 mm wide. The air is fed inside the cabin through four openings located on the dashboard, with a total flow rate equal to $100 \text{ m}^3 \text{ h}^{-1}$.

PIV measurements were taken along the longitudinal plane (measurement plane) of the model passing through the centre of the air vent in front of the driver seat; with reference to the coordinates system in Figure 3.3b, the measurement plane corresponds to the x-y plane at $z=0.3945 \text{ m}$. In order to validate the proposed numerical model, experiments conducted by Y. Ozeki et al. [76] were faithfully reproduced numerically. The computational domain employed for numerical model validation is available in Figure 3.3b, where inlet and outlet sections are highlighted in green and red colour, respectively; surfaces with a *no slip* boundary condition are coloured grey. Boundary conditions imposed for numerical simulations are detailed in Table 3.3.

Table 3.3. Boundary conditions set for numerical model validation (SST $k-\omega$ model).

Surface	BC for velocity	BC for pressure	BC for temperature	BC for k	BC for ω
inlet sections	$Q = 100 \text{ m}^3 \text{ h}^{-1}$	$\frac{\partial p}{\partial n} = 0$	$T = 300 \text{ K}$	$I = 5\%$	$\ell = 0.07L$
outlet sections	$\frac{\partial \mathbf{u}}{\partial \mathbf{n}} = 0$	$p = 101325 \text{ Pa}$	$T = 300 \text{ K}$	$k = 0.1 \text{ m}^2 \text{ s}^{-2}$	$\frac{\partial \omega}{\partial \mathbf{n}} = 0$
walls	$\mathbf{u} = 0$	$\frac{\partial p}{\partial n} = 0$	$\frac{\partial T}{\partial \mathbf{n}} = 0$	standard wall functions	

The adopted computational grid, of which an x-y clipping at $z=0.3945 \text{ m}$ is available in Figure 3.4, is composed of 2,905,807 cells.

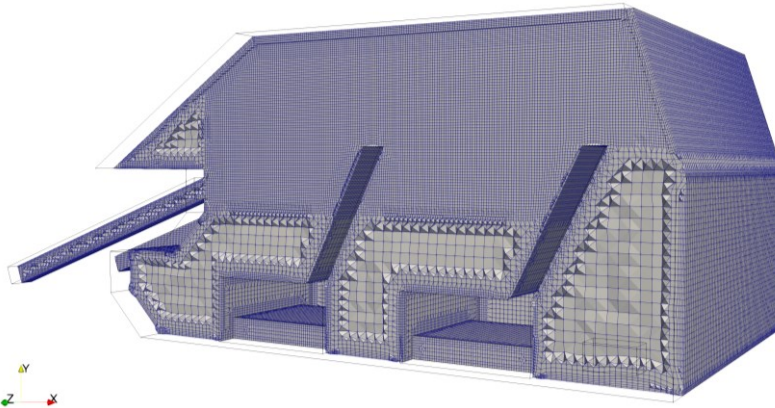


Figure 3.4. Computational grid employed (Mesh 3, 2905807 cells) for velocity field validation.

It was determined with a proper sensitivity analysis, carried out considering three grids whose main parameters are reported in Table 3.4. From coarse (Mesh 1) to fine (Mesh 3) grid, meshes are uniformly refined, equally reducing the cell size in the whole domain and roughly doubling the number of cells at each refinement step. Moreover, all grids are

properly refined in correspondence of solid walls and in the jet region, where significant velocity gradients are expected.

Comparisons were made in terms of velocity profiles on a selected x-y plane at $z=0.3945$ m (measuring plane), in four different sections ($x=0.45$ m, $x=0.65$ m, $x=0.85$ m and $x=1.05$ m), calculating the deviation with respect to the finest mesh (Mesh 3).

Table 3.4. Details of the computational meshes.

Mesh #	Number of Cells	Skewness max	Non orthogonality max
1	747,321	3.45	50
2	1,559,007	2.19	50
3	2,905,807	3.79	50

Results from mesh sensitivity analysis are shown in Figure 3.5a evidencing, as expected, a progressive reduction of the velocity average percentage deviation with respect to Mesh 3 as the number of cells increases. It may also be noticed that the average percent deviation between Mesh 2 and Mesh 3 is less than 5%: 1,559,007 cells would be thus sufficient to guarantee a solution independent of the grid size, but Mesh 3 has been selected to ensure greater accuracy. The minimum, maximum and average y^+ values obtained using Mesh 3 are equal to 0.083, 87.921 and 4.207, respectively.

For the selected mesh with 2,905,807 cells, time step sensitivity analysis was performed in terms of the maximum Courant number [100], which for simplicity is here reported for a mono-dimensional case:

$$Co = \frac{u \cdot \Delta t}{\Delta h} \quad (3.6)$$

where u ($m s^{-1}$) is the flow velocity, Δt (s) is the time step and Δh (m) is the characteristic size of the mesh cell. Once the spatial grid is selected (and hence Δh is fixed), varying the Courant number means varying the time step. Three values of maximum Courant number were investigated ($Co=1, 2, 5$) and the deviation among the velocity profiles was calculated with respect to the $Co=1$ (smallest time step) case. In Figure 3.5b, results of time step independence analysis are shown in terms of average percentage velocity deviation with respect to the $Co=1$ case as a function of the maximum Courant number. Based on such results, a maximum $Co=2$ was selected since the average deviation with respect to the $Co=1$ case is lower than 1% in almost all sections.

Since the flow field periodically oscillates over time in the jet region, mesh sensitivity analysis and numerical model validation were conducted in terms of time-averaged velocity fields, consistent with the PIV measurements. Further analyses were then conducted to establish the proper averaging time interval. Four numerical probes were placed on the measurement plane at the locations indicated in Figure 3.6, monitoring the time-evolution of quantities of interest. In Figure 3.7, Figure 3.8 and Figure 3.9 the progressive time-average of air velocity is shown for Mesh 1, 2 and 3 respectively, together with the percentage deviation of the progressive average up to a given time level with respect to the average calculated up to the previous time level. Analysis of the charts in Figure 3.9 reveals that, for Mesh 3, a minimum averaging time interval of 180 seconds is necessary to ensure that the deviation among calculated progressive averages remains below 1% for all probes. The averaged velocity field numerically obtained in correspondence of the measurement plane, employing the SST $k-\omega$ turbulence model, is

available in Figure 3.10. A jet region is clearly visible in correspondence of the air vent, with a maximum air velocity of about 3 m s^{-1} , while the bottom zone of the domain is characterized by a much lower air velocity, of about 0.5 m s^{-1} , confirming that the adopted mesh refinement strategy is optimal. Comparisons between PIV measurements and numerical results are illustrated in Figure 3.11 in terms of velocity profiles on the measuring plane, in four different sections: $x=0.45 \text{ m}$, $x=0.65 \text{ m}$, $x=0.85 \text{ m}$ and $x=1.05 \text{ m}$. The performances of the following turbulence models were analysed: Standard $k-\omega$ [101,102], SST $k-\omega$ [78], Standard $k-\epsilon$ [103], Realizable $k-\epsilon$ [104] and Re-Normalisation Group (RNG) $k-\epsilon$ [105]. As no proper convergence was obtained when using the Standard $k-\omega$ model, results for such model are not presented.

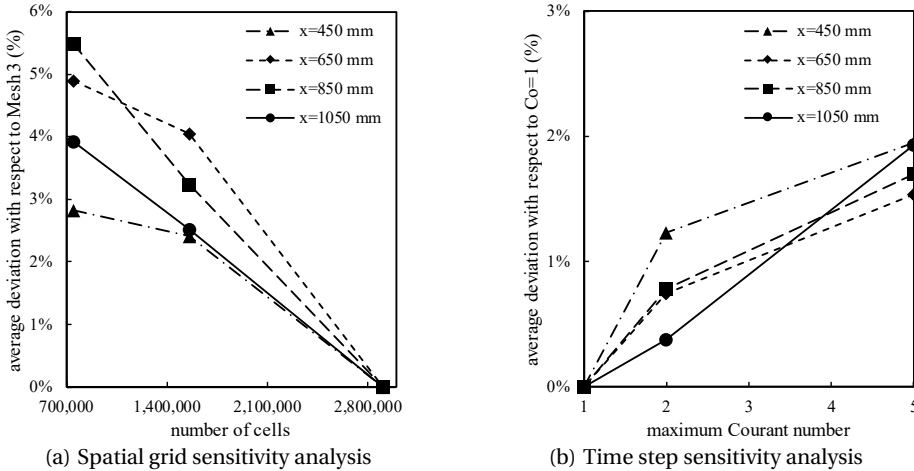


Figure 3.5. Spatial and temporal sensitivity analyses.

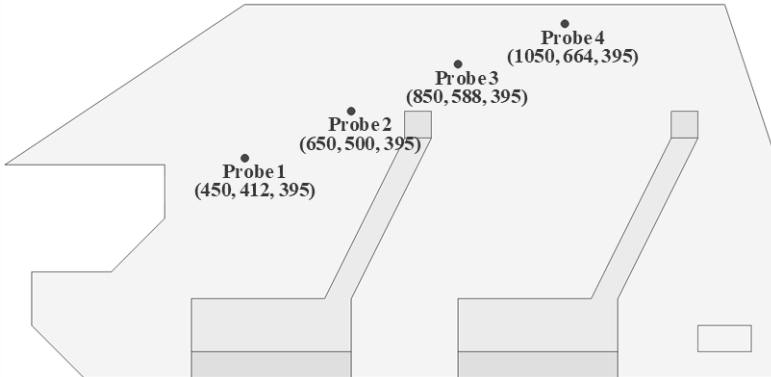


Figure 3.6. Location of the probes inside the computational domain, with coordinates specified in mm.

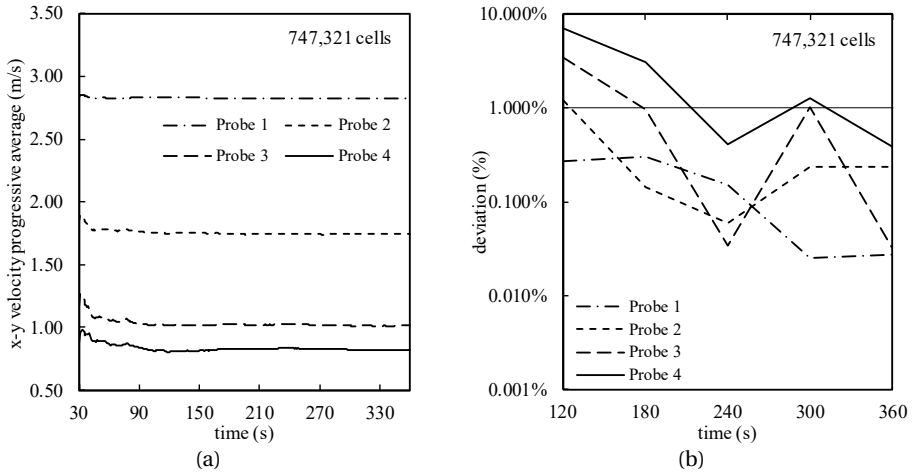


Figure 3.7. (a) progressive time-average and (b) percentage deviation of progressive average up to a given time level with respect to the average calculated up to previous time level evaluated employing Mesh 1.

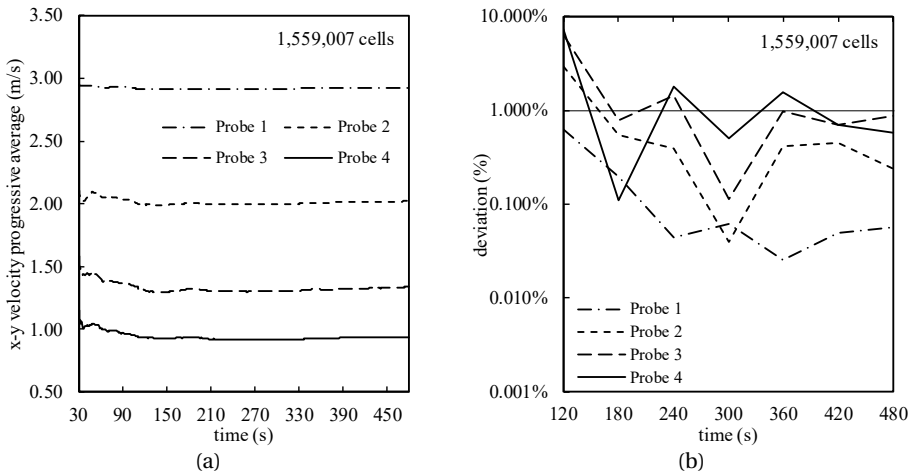


Figure 3.8. (a) progressive time-average and (b) percentage deviation of progressive average up to a given time level with respect to the average calculated up to previous time level evaluated employing Mesh 2.

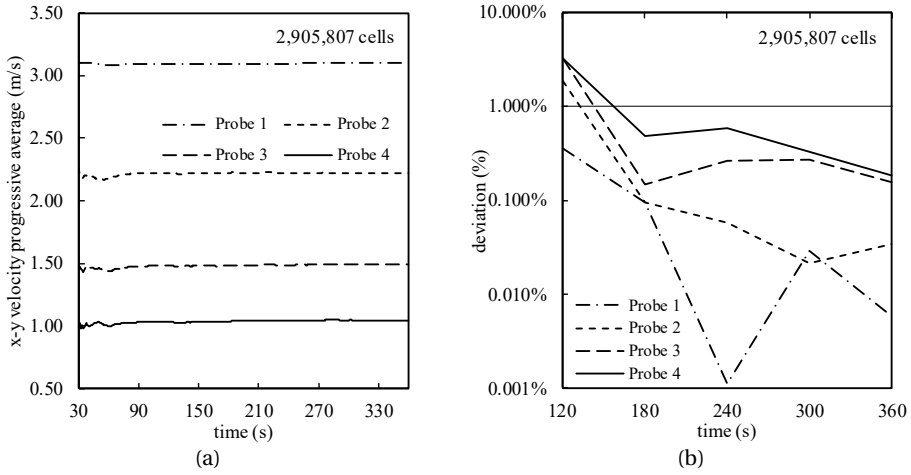


Figure 3.9. (a) progressive time-average and (b) percentage deviation of progressive average up to a given time level with respect to the average calculated up to previous time level evaluated employing Mesh 3.

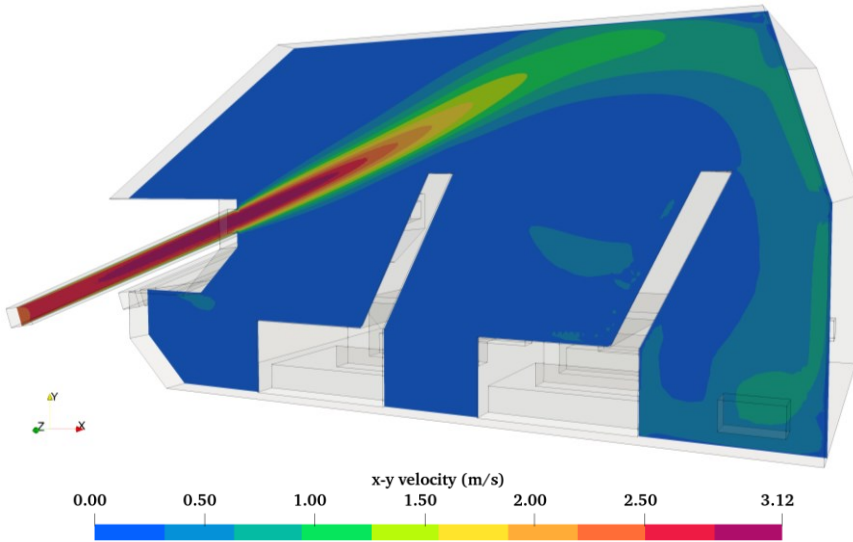


Figure 3.10. x-y velocity contours on the slice at z=0.3945 m (measuring plane) with SST $k-\omega$ turbulence model.

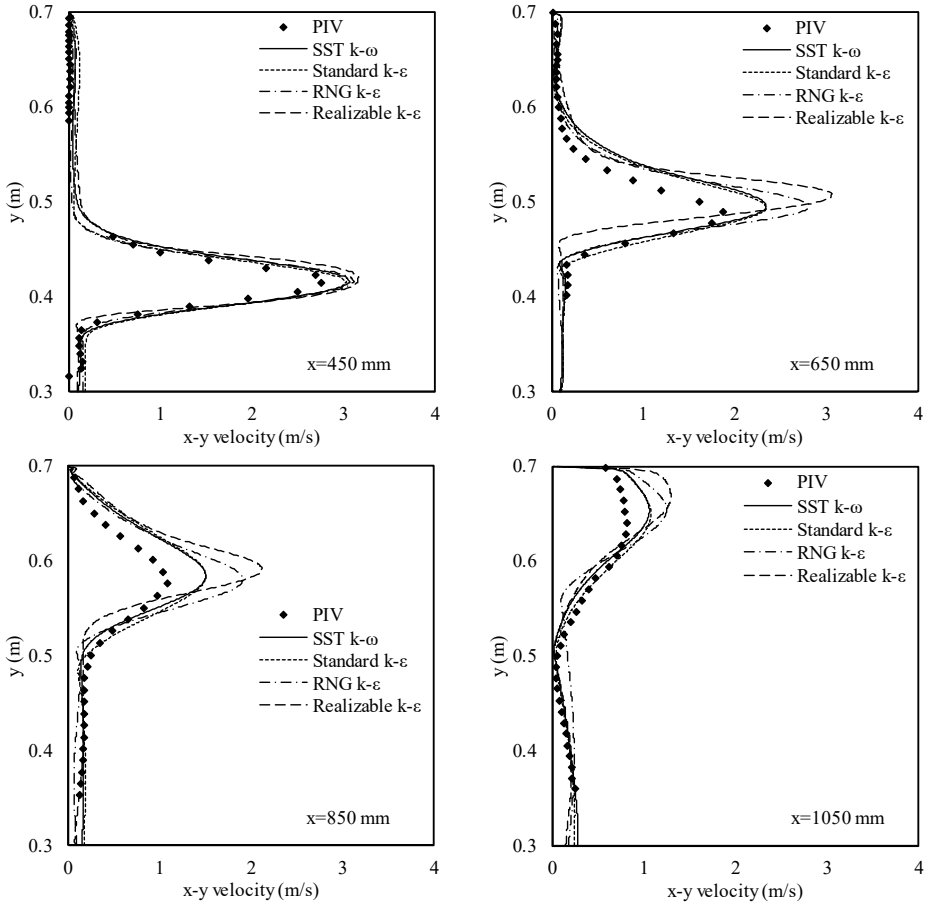


Figure 3.11. Experimental and numerical velocity profiles comparison within a selected x-y plane at $z=0.3945$ m obtained in four different sections: $x=0.45$ m, $x=0.65$ m, $x=0.85$ m and $x=1.05$ m.

To quantitatively compare the ability of different turbulence models to reproduce experiments, the Root Mean Square Error (RMSE) between the predicted and measured data was calculated according to the following equation:

$$\text{RMSE} = \sqrt{\frac{\sum_{i=1}^{n_p} (\psi_{exp,i} - \psi_{model,i})^2}{n_p}} \quad (3.7)$$

where $\psi_{exp,i}$ is a data point from the experimental data, $\psi_{model,i}$ is the corresponding data point from the modelling results and n_p is the number of points.

The calculated RMSEs between the predicted and measured velocity profiles for all considered sections are listed in Table 3.5. An analysis of this table reveals that the RMSEs for the SST $k-\omega$ and Standard $k-\epsilon$ models are significantly lower than those obtained with the other turbulence models, and they are very close to each other. The Realizable $k-\epsilon$

model produced the largest RMSEs, while the RMSE associated with the RNG $k-\epsilon$ model is comparable to that of Standard $k-\epsilon$ and SST $k-\omega$ models only for $x=0.45$ m and $x=1.05$ m. It follows that Standard $k-\epsilon$ and SST $k-\omega$ models returned the best results with comparable RMSEs values. Between these two models, SST $k-\omega$ has been selected for the present numerical investigations due to its lower required CPU time compared to the Standard $k-\epsilon$ model.

Table 3.5. RMSE between the numerically predicted air velocity and the data measured by PIV.

Section	RMSE (m s ⁻¹)			
	SST $k-\omega$ model	Standard $k-\epsilon$ model	Realizable $k-\epsilon$ model	RNG $k-\epsilon$ model
x=0.45 m	0.178	0.166	0.257	0.178
x=0.65 m	0.300	0.274	0.562	0.373
x=0.85 m	0.208	0.228	0.388	0.324
x=1.05 m	0.120	0.119	0.205	0.199
Global values	0.210	0.203	0.373	0.276

3.4 RESULTS AND DISCUSSION

3.4.1 INFLUENCE OF THE POSITION OF THE INFECTED SUBJECT IN THE CAR CABIN

Table 3.6 presents the results of doses in terms of volume of airborne respiratory particles inhaled (V_{p-post}) by the susceptible occupants of the car cabin and their individual infection risk for different position of the infected subject (driver vs. passenger #3) in case of mixed ventilation at 50% of the maximum HVAC flow rate ($Q_{50\%}$), speaking activity and 30-min exposure scenario. Individual risks evaluated through the analytical, zero-dimensional well-mixed approach are also reported.

Table 3.6. Doses in terms of volume of airborne respiratory particles (V_{p-post}) inhaled by the susceptible occupants of the car cabin and their individual infection risk for different position of the infected subject (driver vs. passenger #3) in case of mixed ventilation at $Q_{50\%}$, speaking activity, and 30-min exposure scenario. Infection risks evaluated through the well-mixed approach are also reported.

Driver infected				Passenger #3 infected			
Susceptible subject	Inhaled volume (ml)	Individual infection risk (%)		Susceptible subject	Inhaled volume (ml)	Individual infection risk (%)	
		CFD	Well-mixed			CFD	Well-mixed
Driver		emitter		Driver	5.17×10^{-11}	0.30%	
Passenger #1	1.89×10^{-9}	9.2%		Passenger #1	1.42×10^{-9}	7.2% 42%	
Passenger #2	8.68×10^{-9}	26%	42%	Passenger #2	1.59×10^{-11}	0.09%	
Passenger #3	4.49×10^{-9}	18%		Passenger #3		emitter	

Results show that, in the case of the driver infected, the highest dose (8.68×10^{-9} ml) and individual risk (26%) are received by the passenger #2 (left rear seat, i.e., just behind the driver), whereas the passenger #1 (front right seat, i.e., just on the right side of the driver) receives the lowest dose (1.89×10^{-9} ml) and risk (9.2%). Lower doses and risks are received

when the infected individual is passenger #3: the highest dose (1.42×10^{-9} ml) and individual risk (7.2%) are received by the passenger #1, whereas risks lower than 1% are received by the driver and the passenger #2.

The reason for such different exposure and risk conditions of the susceptible occupants, occurring as a function of the position of the infected subject, is strictly related to the specific airflow patterns in the car cabin. This is graphically reported in Figure 3.12, Figure 3.13 and Figure 3.14 where streamlines (both from the HVAC vents and the infected driver while speaking) and mean velocity contours as well as the spatial distributions of the airborne respiratory particles after 30 min are reported for the driver infected scenario. Figure 3.12 clearly shows that the streamlines of the airflows entering the domain from the HVAC system move from the vents, likely carrying the respiratory particles emitted by the driver (slightly moving upwards due to the warm buoyant air exhaled) and conveying them towards the passenger just sitting behind him (passenger #2). In fact, Figure 3.13 demonstrates that the airflow emitted by the driver is conveyed to the back seats by the airflow coming from the front and windshield vents; as a consequence, higher exposure to respiratory particles of the passenger #2 occurs, as also shown by the spatial distributions of the airborne respiratory particles (Figure 3.14).

A completely different airborne particle distribution can be observed in Figure 3.15 when the passenger #3 is the infected. This is clearly shown in Figure 3.16 where the airflows exiting the mouth of the infected passenger #3 are graphed. In fact, the airflow emitted by the passenger #3 almost reaches the passenger #1 and then is immediately redirected towards the outlet sections by the HVAC system airflow. In such condition, the airborne particles are mainly confined in the rear seats. Anyway, due to the large inertia typical of super-micrometric particles, the respiratory particles emitted by the passenger #3 are likely not able to follow the airflow then leading to a larger exposure (and consequently dose and risk) of the passenger #1, that is, the passenger sitting just ahead of the infected subject, with respect to the other occupants as represented in Figure 3.15.

For the well-mixed analytical solution, the individual risk is 42% for all passengers regardless of position. This value overestimates the risks received by susceptible subjects in the case of driver infected estimated through the CFD (maximum values 26%) and, even more, the one they receive for the case of passenger #3 being infected (maximum risk 7.2%). The overestimation resulting from the well-mixed approach demonstrates the effectiveness of the HVAC system in reducing the exposure of passengers to virus-laden particles through flow patterns allowing cleaner air in their breathing zones.

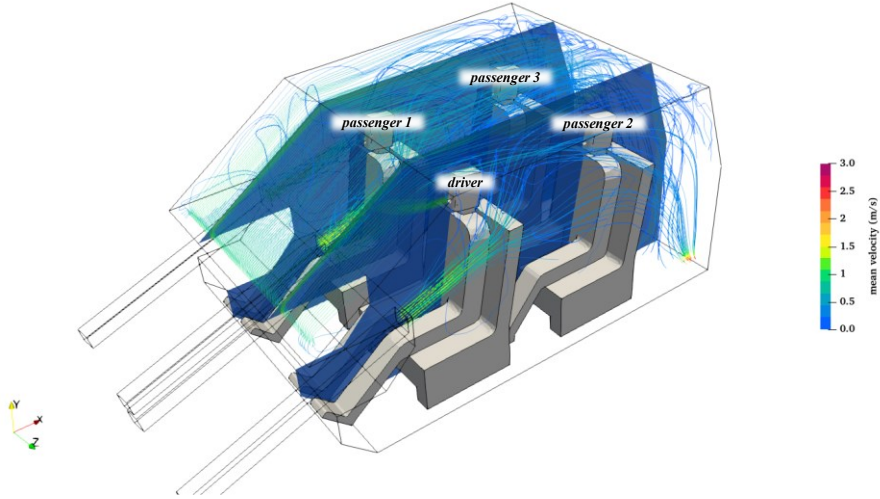


Figure 3.12. Streamlines of the airflows entering the domain from the inlet vents and mean velocity contours on x-y slices at $z=-0.38$ m and $z=0.38$ m in case of mixed ventilation mode at 50% ($Q_{50\%}$), speaking activity, driver infected.

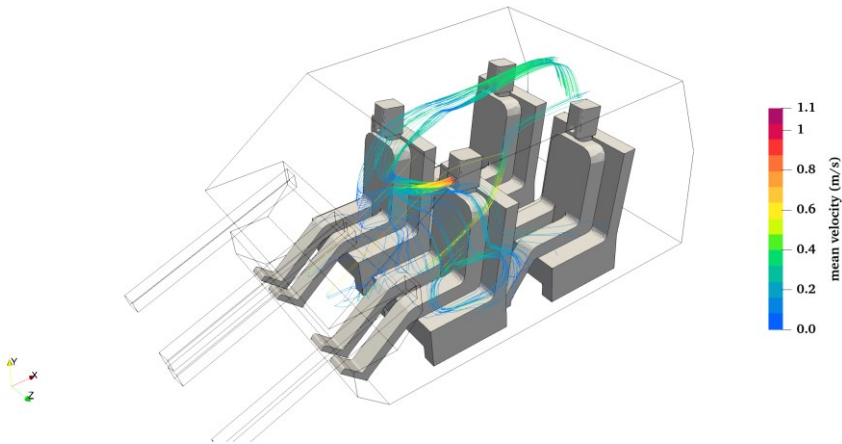


Figure 3.13. Streamlines of the airflows (coloured by velocity) exiting the mouth of the infected driver in case of mixed ventilation mode at 50% ($Q_{50\%}$) and speaking activity.

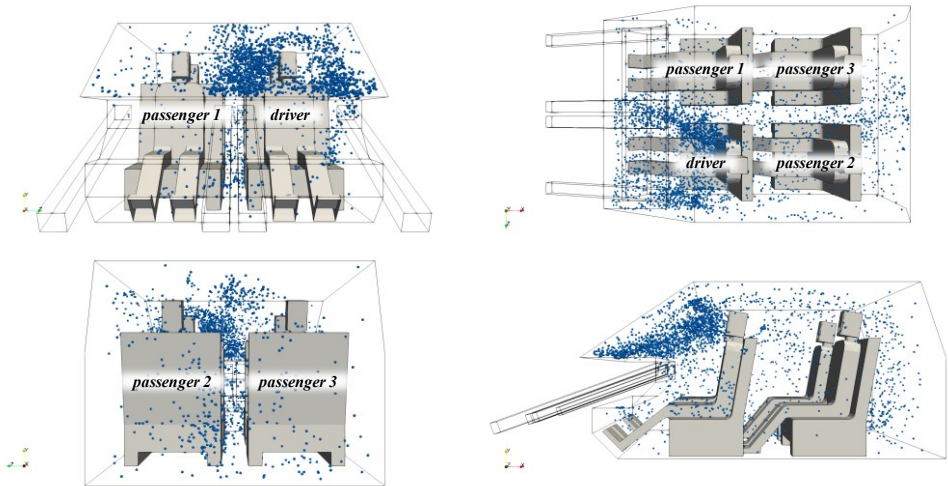


Figure 3.14. Spatial particle distribution after 30 min in case of mixed ventilation mode at 50%, speaking activity, driver infected.

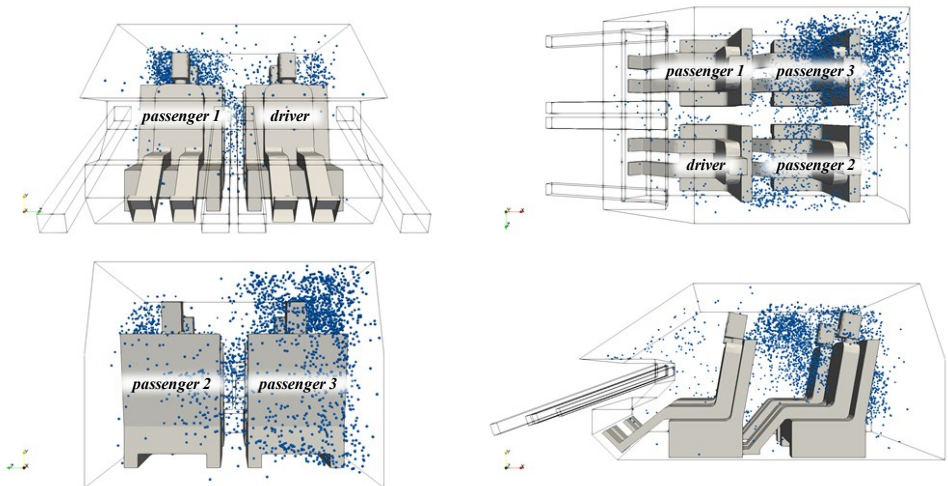


Figure 3.15. Spatial particle distribution after 30 min in case of mixed ventilation mode at 50%, speaking activity, passenger #3 infected.

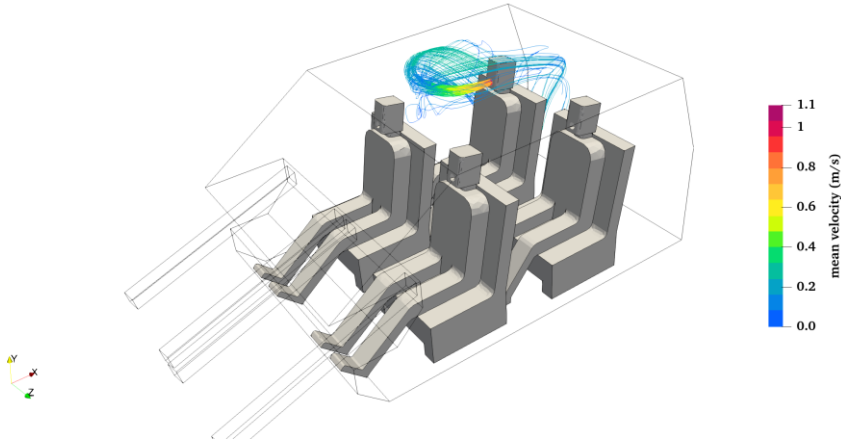


Figure 3.16. Streamlines of the airflows (coloured by velocity) exiting the mouth of the infected passenger #3 in case of mixed ventilation mode at 50% and speaking activity.

3.4.2 INFLUENCE OF THE HVAC SYSTEM FLOW RATE

In Table 3.7 results of doses in terms of volume of airborne respiratory particles (V_{p-post}) inhaled by the susceptible occupants of the car cabin and their individual infection risk for different HVAC flow rates (expressed as airflow ratio with respect to the maximum flow rate) in case of mixed ventilation, driver infected, speaking activity, and 30-min exposure scenario are reported.

When the driver is the infected subject, as already shown in the previous section, the highest doses and risks are (in most of the cases) received by the passenger just sitting behind them (passenger #2). As expected, the dose and risk values are strongly influenced by the flow rate provided. As an example, for passenger #2, the risk is <1% for very high flow rates (i.e., $\geq Q_{75\%}$) but it strongly increases with air flow ratios $\leq Q_{50\%}$ reaching an individual risk of $\sim 50\%$ for $Q_{10\%}$. Similar trends were found for the other passengers with maximum infection risks equal to 32% and 51%, at $Q_{10\%}$, for passengers #1 and #3, respectively. Nonetheless, despite a general decreasing trend of the risk as the HVAC flow rate increases, it is important to note that the risk for passengers seated in the back does not constantly reduce (for instance, the risks at $Q_{25\%}$ and $Q_{75\%}$ are lower than at $Q_{50\%}$ and $Q_{100\%}$, respectively). This is due to the specific air flow patterns occurring at those flow rates which likely undermine the effectiveness of the particle removal towards the exit sections. In case of low air exchange rate ($Q_{10\%}$) the lowest difference among the passengers in terms of risk of infection was detected. This is likely related to the lowest efficiency of the HVAC system in conveying the virus-laden respiratory particles towards the outlet sections, then letting them disperse within the car cabin: indeed, the ratio between the maximum and minimum risk values decreases with the HVAC flow rate then demonstrating a more homogenous concentration. In this respect, it is not surprising that the closest match of the well-mixed results to the average passenger risk calculated through the CFD approach occurs with $Q_{10\%}$ (~ 12.5 air changes per hour). In this case the CFD-based passenger risks for passengers #1 and #2 are $>50\%$ and in good agreement with the well-mixed approach (55%). Conversely, when the air flow ratio is $> Q_{50\%}$, as shown in the previous section, the risk is significantly overestimated using the well-mixed approach.

It should be noted that all the scenarios here presented consider the HVAC system in operation under outside air intake conditions. When the HVAC system is not in operation or is operated under recirculation ventilation conditions, the actual air exchange rate is clearly lower. Indeed, it is mainly due to the car cabin and ducts leakages, and for this reason, it is strongly affected by the vehicle velocity: previous papers have shown that the air exchange rate can be lower than 5 h^{-1} [66,106], which is well below that obtained under the outside air intake condition at the $Q_{10\%}$ flow rate here investigated. For such lower AER values, based on what shown above, the well-mixed approach can be considered a useful tool to roughly estimate the risk of the exposed subjects: as an example, for a ventilation condition with air recirculation characterized by an AER equal to 2 h^{-1} , the estimate of the risk of infection for the passengers provided by the well-mixed approach is $>60\%$.

Table 3.7. Doses in terms of volume of airborne respiratory particles ($V_{p\text{-post}}$) inhaled by the susceptible occupants of the car cabin and their individual infection risk for different HVAC flow rates ($Q_{10\%}$ to $Q_{100\%}$) in case of mixed ventilation, driver infected, speaking activity, and 30-min exposure scenario. Infection risks evaluated through the well-mixed approach are also reported.

HVAC air flow ratio	Inhaled volume (ml)			Individual infection risk (%)			
	Passenger #1	Passenger #2	Passenger #3	Passenger #1	Passenger #2	Passenger #3	All Passengers
				CFD	CFD	CFD	Well-mixed
$Q_{100\%}$	0	1.32×10^{-10}	5.22×10^{-10}	0	0.76%	2.9%	35%
$Q_{75\%}$	4.59×10^{-12}	7.97×10^{-11}	3.62×10^{-10}	0.03%	0.46%	2.0%	38%
$Q_{50\%}$	1.89×10^{-9}	8.68×10^{-9}	4.49×10^{-9}	9.2%	26%	18%	42%
$Q_{25\%}$	1.87×10^{-8}	1.67×10^{-9}	1.42×10^{-9}	36%	8.3%	7.2%	48%
$Q_{10\%}$	8.30×10^{-8}	1.02×10^{-7}	1.37×10^{-8}	51%	53%	32%	55%

3.4.3 INFLUENCE OF THE HVAC VENTILATION MODE

In Table 3.8 the doses in terms of volume of airborne respiratory particles ($V_{p\text{-post}}$) inhaled by the susceptible occupants of the car cabin and their individual infection risk for different HVAC ventilation modes in case of $Q_{50\%}$ flow rate, driver infected, speaking activity, and 30-min exposure scenario are reported.

Data clearly highlight that the ventilation mode strongly affects the risk of the passengers. For mixed ventilation mode (air entering the cabin through four front vents and one windshield vent), as shown in previous sections, the highest dose is received by the passenger #2 (individual risk of 26% at $Q_{50\%}$). Nonetheless, the worst exposure condition experienced by the passengers is in case of windshield defrosting mode (air entering through one vent located under the windshield), since their risk ranges from 22% (passenger #3) to 59% (passenger #2). When the front ventilation mode is adopted, the risks for passengers sitting in the rear seats are almost negligible, whereas the risk for passenger #1 is extremely high (53%). These data can be better explained by referring to the streamlines, main velocity contours and spatial particle distributions. Flow patterns for mixed ventilation mode have been already discussed in Section 3.4.1, where, for the driver infected scenario, the accumulation of respiratory particles in the breathing zone of the passenger #2 has been demonstrated. In case of front ventilation mode, the airflow entering the cabin impacts the front seats and passengers, changes its direction, and forms a recirculation area (Figure 3.17). As a result, higher concentrations of respiratory particles

occur in the front compartment, preventing their spread towards the rear seats (Figure 3.18) throughout the entire journey.

On the contrary, in the case of windshield defrosting mode, the respiratory particles emitted by the driver and moving upwards due to the buoyancy forces are transported to the rear region of the car cabin by the airflow injected through the windshield vent, not encountering any obstacles. This is graphically represented by both the streamlines of the airflows from the inlet vents (Figure 3.19) and those exiting the mouth of the infected driver (Figure 3.20). As a direct consequence of both the airflow patterns and the infected subject position, the airborne particles are mainly confined in the left region of the car (Figure 3.21) then explaining the reason why the passenger #2 is the most exposed.

Having shown these differences in terms of risk of infection among the ventilation modes, the well-mixed solution provides a reasonable approximation of the results for the windshield defrosting mode, whereas the front ventilation mode is clearly the least well mixed within the car cabin, and therefore the zero-dimensional model significantly overestimates the risk for the back seat passengers by over two orders of magnitude.

Table 3.8. Doses in terms of volume of airborne respiratory particles (V_{p-post}) inhaled by the susceptible occupants of the car cabin and their individual infection risk for different HVAC ventilation modes in case of $Q_{50\%}$ flow rate, driver infected, speaking activity, and 30-min exposure scenario. Infection risks evaluated through the well-mixed approach are also reported.

HVAC ventilation mode	Inhaled volume (ml)			Individual infection risk (%)			
	Passenger #1	Passenger #2	Passenger #3	Passenger #1	Passenger #2	Passenger #3	All Passengers
				CFD	CFD	CFD	Well-mixed
front mode	1.13×10^{-7}	2.99×10^{-11}	9.74×10^{-12}	53%	0.17%	0.06%	
windshield defrosting mode	1.36×10^{-8}	2.29×10^{-7}	6.31×10^{-9}	32%	59%	22%	42%
mixed mode	1.89×10^{-9}	8.68×10^{-9}	4.49×10^{-9}	9.2%	26%	18%	

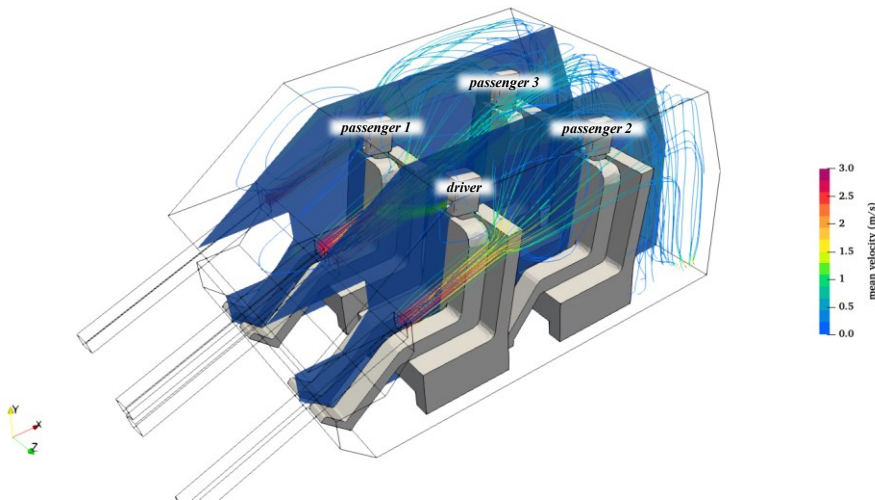


Figure 3.17. Streamlines and mean velocity contours on x-y slices at $z=-0.38$ m and $z=0.38$ m in case of front ventilation mode at 50% ($Q_{50\%}$), speaking activity, driver infected.

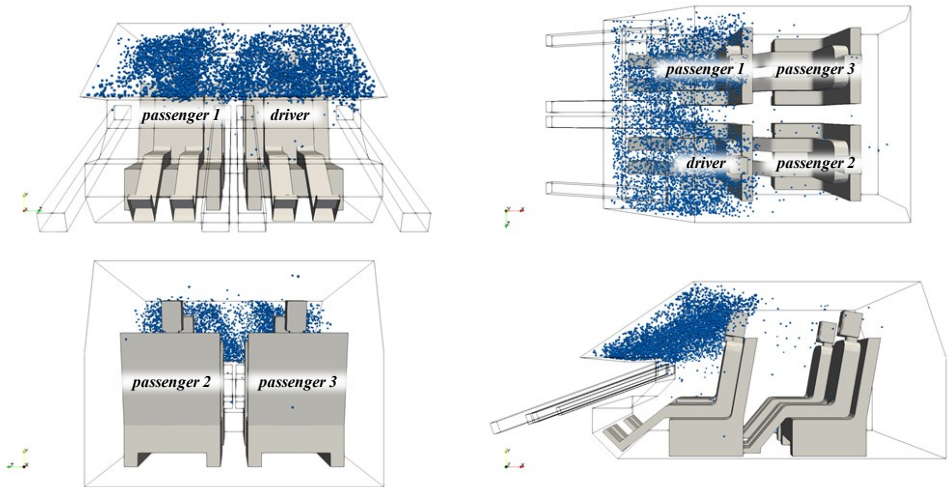


Figure 3.18. Spatial particle distribution after 30 min in case of front ventilation mode at 50% ($Q_{50\%}$), speaking activity, driver infected.

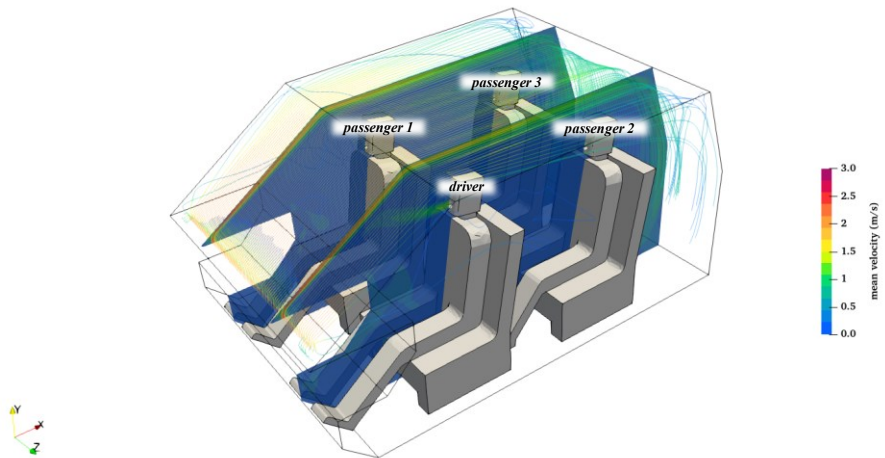


Figure 3.19. Streamlines of the airflows entering the domain from the inlet vents and mean velocity contours on x-y slices at $z=-0.38$ m and $z=0.38$ m in case of windshield defrosting ventilation mode at 50% ($Q_{50\%}$), speaking activity, driver infected.

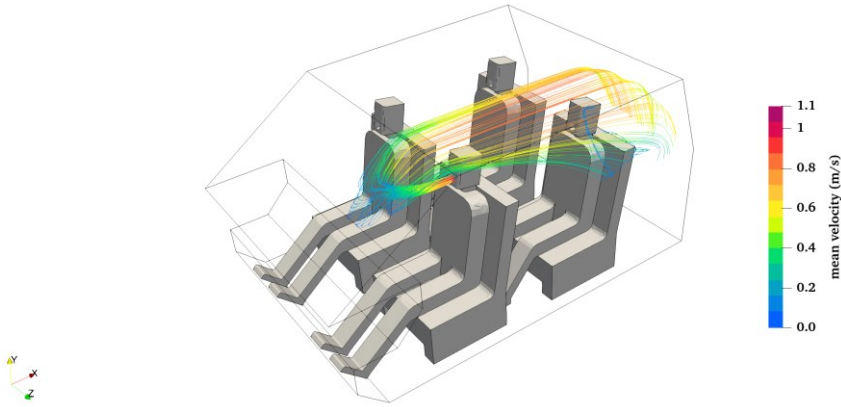


Figure 3.20. Streamlines of the airflows (coloured by velocity) exiting the mouth of the infected driver in case of windshield defrosting ventilation mode at 50% ($Q_{50\%}$), speaking activity.

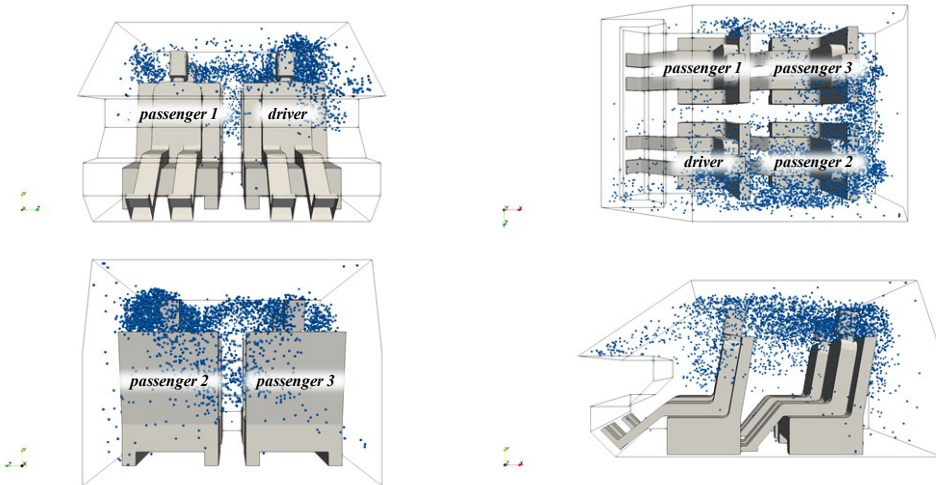


Figure 3.21. Spatial particle distribution after 30 min in case of windshield defrosting ventilation mode at 50% ($Q_{50\%}$), speaking activity, driver infected.

3.4.4 INFLUENCE OF THE EXPIRATORY ACTIVITY: BREATHING VS. SPEAKING

In Table 3.9 the doses in terms of volume of airborne respiratory particles (V_{p-post}) inhaled by the susceptible occupants of the car cabin and their individual infection risk are compared for two expiratory activities (breathing and speaking) in the case of $Q_{50\%}$ flow rate, windshield defrosting ventilation mode, driver infected, and 30-min exposure scenario (which represents the worst exposure condition among those reported in previous sections). In the case of breathing, very low airborne particle volumes are inhaled by all the passengers leading to negligible risks of infection (well below 1%): this is due to the low number of particles emitted and their reduced velocity at the exit of the infected

subject's mouth (please see the emission rate discussed in Section 2.3.2). In the case of breathing activity of the infected subject, the most exposed susceptible is passenger #3 (not passenger #2 as resulting from speaking activity), and their risk (although negligible) is tenfold the one received by the other two passengers. The difference between speaking and breathing activities can also be visually observed comparing the spatial particle distributions of Figure 3.21 (speaking activity) and Figure 3.22 (breathing activity), where the latter clearly shows a much lower particle concentration in the car cabin. For the case of breathing, as already reported for speaking, the well-mixed analytical solution provides a rough estimate of the average passenger risk ($\sim 0.2\%$ versus $\sim 0.07\%$).

Table 3.9. Doses in terms of volume of airborne respiratory particles (V_{p-post}) inhaled by the susceptible occupants of the car cabin and their individual infection risk for different expiratory activities (breathing and speaking) in case of $Q_{50\%}$ flow rate, windshield defrosting ventilation mode, driver infected, and 30-min exposure scenario. Infection risks evaluated through the well-mixed approach are also reported.

Expiratory activity	Inhaled volume (ml)			Individual infection risk (%)			
	Passenger #1	Passenger #2	Passenger #3	Passenger #1	Passenger #2	Passenger #3	All Passengers
				CFD	CFD	CFD	Well-mixed
breathing	2.53×10^{-12}	2.18×10^{-12}	3.06×10^{-11}	0.01%	0.01%	0.18%	0.21%
speaking	1.36×10^{-8}	2.29×10^{-7}	6.31×10^{-9}	32%	59%	22%	42%

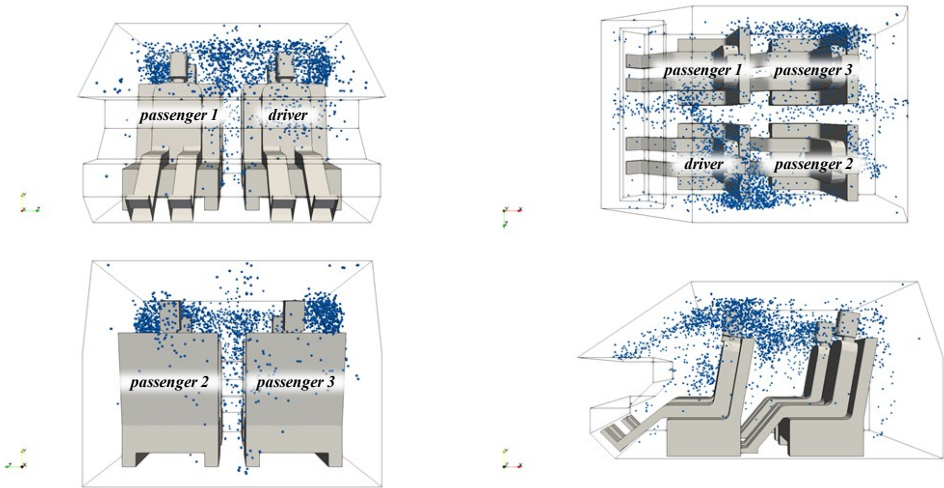


Figure 3.22. Spatial particle distribution after 30 min in case of windshield defrosting ventilation mode at 50% ($Q_{50\%}$), breathing activity, driver infected.

3.4.5 DISTRIBUTION OF SECONDARY CASES

Results of the Bernoulli trial calculations reporting the probability of discrete numbers of secondary cases and the Re_{vent} are summarized in Figure 3.23 for different scenarios. All the scenarios tested through the CFD approach are reported as well as the two scenarios presenting well-mixed results comparable to the CFD ones, that is, mixed mode

ventilation at $Q_{10\%}$ flow rate for speaking and mixed mode ventilation at $Q_{50\%}$ flow rate for breathing.

The Bernoulli trial data show that there are three model scenarios where the average number of secondary cases (R_{event}) exceeds 1 (the $Q_{10\%}$ flow rate condition for both well-mixed and CFD models, and the windshield defrosting mode at the $Q_{50\%}$ flow rate). Supporting the use of the well-mixed approach for $Q_{10\%}$ flow rate, the distribution of secondary cases (C) is also very similar to that obtained from CFD, with the probability of zero cases being ~40% and thus the probability of at least one transmission occurring being ~60%. There are three speaking scenarios for which there is over a 90% probability of nobody being infected ($C = 0$) (mixed mode with driver infected at $Q_{75\%}$ and $Q_{100\%}$, and mixed mode with passenger infected at $Q_{50\%}$). For the front mode scenario, there is a high risk for the front seat passenger, but the probability that none of the backseat passengers gets infected is over 99%. Thus, the front mode is a viable ventilation strategy when the driver is infected and no passenger sits in the front seat, as there is effective aerodynamic containment between the front and back of the car. For the breathing emission rates evaluated herein, there is a very low probability of a secondary transmission (~0.2%) for the 30-min journey.

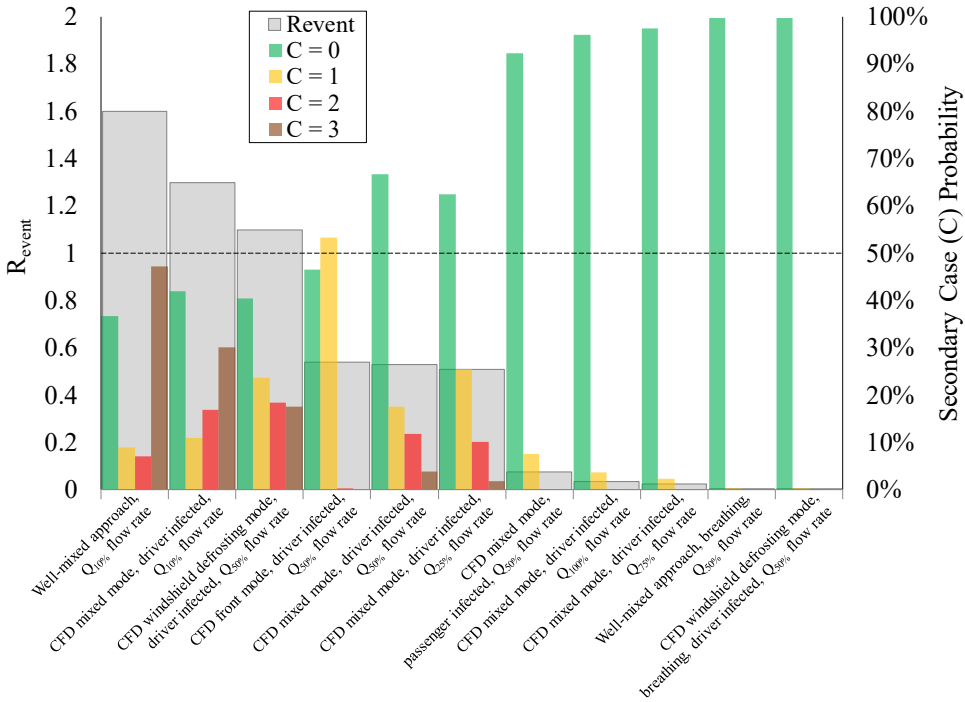


Figure 3.23. Results of Bernoulli trial calculations for R_{event} and the probability distribution of secondary cases (C) for the scenarios under investigation.

3.4.6 STRENGTHS AND WEAKNESSES

The results shown in the previous sections highlight the strengths of the CFD approach for a proper evaluation of the risk of infection in small, confined spaces affected by a particular fluid dynamic due to high flow rates entering the cabin, or ventilation systems not designed for mixing (e.g., front). Simplified analytical approaches, such as zero-dimensional models, may inaccurately estimate the risk of the exposed subjects by a large amount. However, for the 10% flow condition and mixed-mode ventilation, the zero-dimensional well-mixed approach produces quite similar results in terms of both the average risk (and thus R_{event}) and the probability distribution of secondary cases. The parameters under which well-mixed approaches are most defensible requires further evaluation, using CFD and possibly field investigations (e.g., tracer tests) to inform such generalizations; nonetheless, it is clear that well-mixed models can perform very well in scenarios characterized by low air exchange rates where the flow patterns are not able to provide a proper particle removal from the breathing zone of the exposed subjects: this is also typical of other larger indoor environments, such as naturally-ventilated buildings [64], where well-mixed models were shown to predict the attack rates of documented SARS-CoV-2 outbreaks [54,59].

It is noted that the solutions here reported are very specific of the car cabin under investigation and of the boundary conditions set. As an example, considerations have not been given to: (i) the effect of mitigation solutions, such as vaccination and face masks [59], that could reduce the individual risk of infection of passengers; (ii) the presence of a possible fifth passenger sitting in the middle of the rear row, typical of five-seater cars (please consider that their exposure could be different from the other passengers sitting in the rear seats due to limited shielding effect of the front seats); (iii) the influence of side window opening; (iv) the impact of journey duration. Nonetheless, some practical suggestions can be argued from the scenarios investigated; in particular, it was clearly shown that the common-sense norm suggesting that the occupants should sit as far apart as possible in the car (i.e., single passenger sitting in the back seats) can be misleading. Indeed, apart from the front ventilation mode, the passenger sitting in the front seat (close to the driver) presents risks of infection lower than those sitting in the back seats. Thus, since the use of the front window defrosting is mostly required (e.g., to avoid that the humidity in the air condensates on the glass), a mixed ventilation mode (i.e., simultaneous use of front and windshield inlet sections) should be adopted and the passenger should sit close to the driver to receive a lower risk. Besides, mixed ventilation mode is preferred when more than two occupants are sitting in the car, as the windscreen ventilation increases the exposure (and so the dose and the risk) of back seats occupants. Despite these general suggestions, it is important to highlight that generalizing the obtained CFD results to other passenger vehicles could lead to mistakes. Indeed, car cabins comparable in terms of volume and emission rates could present different infection risks for the susceptible occupants as a function of the position of the inlet vents (some cars also have ducts to the rear-seat area), the adjustable angle of inlet airflow rate, the air flow rate split amongst the different vents, and the position of the outlet sections (considering that in actual cars the particle exfiltration just relies upon leakages of the cabin): these aspects are here not considered and could be involved in future developments of the study. Regardless, the results show that CFD is necessary to evaluate the fate of these particles more accurately and that a proper design of the HVAC system (e.g., in terms of positioning of the inlet and outlet vents, etc.), in view of significantly reducing the risk of infection, is suitable. This is a key finding since it demonstrates that in indoor environments

characterized by fixed seats, the risk of infection can, in principle, be controlled by properly designing the flow patterns of the environment, i.e., moving towards an *ad-hoc* personalized ventilation [107,108].

3.5 CONCLUSIONS

This study proposed and applied an integrated approach combining a validated CFD transient model and a recently developed predictive emission-to-risk approach to estimate the SARS-CoV-2 Delta variant risk of infection in a car cabin under different conditions in terms of ventilation (ventilation mode and airflow rate of the HVAC system) and emission scenarios (expiratory activity, that is, breathing vs. speaking, and position of the infected subject within the car cabin).

The results of the study clearly showed that the risk of infection, and consequently the probability of secondary cases, is strongly influenced by the ventilation mode, the HVAC flow rate, the position of the infected subject, and the expiratory activity. As an example, in the case of the driver infected and speaking for the entire journey, a reduced ventilation (low flow rate) or a less effective ventilation (e.g., windshield defrosting mode) can cause a high risk of infection (>50% for at least one of the passengers) then leading to a high probability (~60%) of at least one secondary case in only 30-min of exposure. The risk of infection is clearly reduced when (i) higher flow rates are adopted, as they dilute the virus-laden respiratory droplets emitted by the infected subject, or (ii) the infected subject just breathes instead of speaking (for those scenarios, the probability that none of the passengers gets infected is >90%).

Furthermore, the front ventilation mode evaluated herein provides effective aerodynamic containment between the front and back of the vehicle, meaning passengers sitting in the back seats are better protected from an infected driver relative to mixing ventilation. On the contrary, the windshield defrosting leads to the highest average risk among the passengers; anyway, since the use of front window defrosting is sometimes needed, according to the findings of the CFD analyses, a practical suggestion could be adopting a mixed ventilation mode.

Findings of the study demonstrated that CFD approaches are needed to properly address the individual risk in such confined spaces as the fluid-dynamic conditions significantly affect the airflow patterns and, consequently, the spatial distribution of the virus-laden respiratory particles within the cabin. Thus, simplified zero-dimensional approaches assessing the average risk of the susceptible (not accounting for the specific flow patterns in the confined space) can lead to miscalculation of the risk of the exposed subjects, particularly for ventilation modes not designed for mixing. Indeed, the well-mixed solutions for a speaking infected subject shown here are roughly comparable with the CFD ones only in case of very low flow rates (10% of the maximum flow rate), that is, when the reduced airflow rates do not effectively clean the breathing zone of the exposed subjects and the virus-laden concentrations are likely homogenous within the car cabin.

Summarizing, CFD modelling is a valuable tool to produce such recommendations for specific applications, which are not possible with simple zero-dimensional models. Even if the CFD results here provided are not directly transferable to other cars (due to the case-specific geometry, vent positions, etc.), the finding here indicates that *ad-hoc* designing of the airflow of closed environments in view of reducing and controlling the risk of infection is achievable, especially when the spatial locations of the occupants are fixed.

4

AEROSOL DISPERSION IN A UNIVERSITY LECTURE ROOM

The airborne droplet route has been recognized as the main pathway of infection transmission in indoor environments, drawing the attention to a proper design of HVAC systems. This is particularly relevant for gathering spaces such as schools and universities, due to the high crowding levels and the long exposure times. Using 3D CFD numerical simulations based on a Eulerian-Lagrangian approach and validated against velocity measurements, the present chapter investigates the distribution over time of airborne droplets (aerosol) emitted in correspondence of the teacher position inside a lecture room, during a two-hour speaking activity (so reproducing a two-hour lesson), as a function of different air supply rates from the HVAC system.

Results show that increasing the air supply rate is not always an effective solution to reduce the aerosol concentration in correspondence of the positions occupied by the students attending the lesson. In fact, for the specific case under investigation, the aerosol concentration around the classroom seats does not always decrease when increasing the supply rate, even though the overall number of particles in the room decreases. This behaviour is mainly due to the asymmetric disposition of the seats with respect to the diffusers and the extraction grilles and underlines the importance of CFD approaches in investigating the fluid dynamics in indoor environments.

This chapter is based on the following published article:

Arpino F., Cortellesa G., D'Alicandro A. C., Grossi G., Massarotti N. and Mauro A. (2023). CFD analysis of the air supply rate influence on the aerosol dispersion in a university lecture room. *Building and Environment*, 235, 110257.

Keywords: airborne transmission, CFD analysis, Eulerian-Lagrangian model, classroom, ventilation, Air Changes per Hour (ACH)

4.1 INTRODUCTION

Lecture rooms, such as school or university classrooms, are one of the most susceptible indoor environments for infection transmission. The reasons are that there is a high occupant concentration, the occupation time is likely higher than 1 hour and there is at least 1 person always speaking. Even though assessing the contagion risk in lecture rooms is of critical importance, it is not an easy task because these environments are not standardized, differ for layout, number of occupants, HVAC layout (position of inlet and outlet sections), natural or mechanical ventilation, volumetric inflow rate and velocity, and many other factors. In this sense, CFD is a valid support for mass transport and airflow investigations because it allows to numerically simulate different scenarios in a relatively low time [109]. Looking at the scientific literature, there are several studies employing the CFD technique to better understand aerosol transport in indoor environments. Among others, Abuhegazy et al. [16] numerically investigated aerosol transport and surface deposition in a realistic classroom environment, analysing the effects of droplets size, position of the particle source, presence of barriers and opening windows. The authors found that the HVAC system layout and the droplet source position have a fundamental role in droplet distribution in the classroom. Mirzaie et al. [110] carried out 3D simulations to study the dispersion of virus-laden droplets emitted by a person coughing in front of a classroom with and without partitions around the seats, for different airflow velocities induced by the ventilation system; they found that when the classroom is equipped with partitions, seats are exposed to a lower average droplet concentration and that the number of droplet suspended in the air decreases as the ventilation system inlet velocity increases. Foster and Kinzel [111] compared the airborne transmission and probability of infection predicted with mathematical (Wells-Riley) and CFD methods, comparing the effects of the absence and presence of mechanical ventilation; they evidenced that the risk of exposure to airborne virus-laden droplets seems to be not strongly related to the distance between the source and the receiver, highlighting the importance of properly designing HVAC systems. He et al. [112] used a Eulerian drift-flux method to examine the transmission of exhaled droplets between two seated subjects breathing in a typical office room, under three different total volume ventilation strategies. Numerical simulations evidenced that different ventilation strategies lead to different zones of higher risk in the room and different values of particle concentration. Arjmandi et al. [113] evaluated the impact of five different HVAC systems on the dispersion of airborne particles in a classroom and on thermal comfort. The authors found that the position of the inlets and outlets influences the contagion risk and the thermal comfort. Rencken et al. [17] employed the species transport model to predict the aerosol concentration distribution in a typical classroom, comparing the results to those obtained under the well-mixed assumption, concluding that natural ventilation could carry droplets from an infected person near the window to other occupants. Despite the presence of these and other studies [19,114–120], the effect of different ventilation regimes on local airflow patterns and particle dispersion in indoor environments still requires more investigation [121]. In fact, very few of the above-mentioned works explores the effects of different flow rates on particles distributions and several limitations can be highlighted in the models employed. First, many models do not provide a Lagrangian description for particles motion; secondly, simplified number and

size distributions are adopted for droplets expelled by the infected subject, not relying on experimental data; lastly a proper validation of numerical models is not always available. To fill this gap, in the present study a three-dimensional, non-isothermal Eulerian-Lagrangian numerical model, properly validated in terms of velocity fields, is applied to investigate the motion and distribution of airborne droplets inside a real university lecture room, evaluating the effects of different air supply rates from the ventilation system. Droplets are emitted by a source reproducing an infected subject speaking in front of the class (e.g., a professor) during a two-hour lesson, as a function of different air supply rates from the HVAC system. The aim of the study is to assess the effectiveness of validated CFD tools in providing useful information: (i) for a proper design of HVAC systems; (ii) to optimize the system capability in evacuating pollutants and pathogens from the room efficiently; (iii) for the management of the HVAC system, by analysing the aerosol distribution in the room as a function of the ACH. In order to analyse the aerosol distribution as a function of HVAC system design and operation, the room has been assumed to be empty and the thermal plume of possible occupants has then been neglected. The numerical model relies on experimental measurements performed in the empty room to define the boundary conditions for CFD simulations and to validate the model itself. The effectiveness of the HVAC system at different ACH, while the droplets source is fixed, has been investigated considering both the age of particles suspended in the domain and their concentration in selected control volumes enclosing the possible breathing area of seated room occupants. By looking at the age of particles, it is possible to determine if they are evacuated in a short period of time or if they persist suspended in the air. On the other hand, the control volumes approach allows to calculate the mean exposure to aerosol droplets in different zones, while the HVAC system is operating, because, as reported in the cited literature, the contagion risk can vary in the room. The windows have been considered closed to analyse only the effect of the HVAC system and the ACH.

The chapter is organized as follows: Section 4.2 describes the methodology adopted, the case study and the experimental measurements; detailed validation of numerical results and performances of different turbulence models are available in Section 4.3; in Section 4.4 the aerosol distribution obtained numerically for the three investigated ACH is presented and discussed, while conclusions are drawn in Section 4.5.

4.2 MATERIALS AND METHODS

The numerical tool developed in the present study is based on an integrated approach, summarized by the following main steps:

- development of a three-dimensional, non-isothermal Eulerian-Lagrangian numerical model to describe airborne droplet dispersion and distribution inside a lecture room emitted by a person continuously speaking for two hours in transient conditions; this is based on a Eulerian-Lagrangian approach, in which the continuum equations are solved for the air flow (continuous phase) and Newton's equation of motion is solved for each droplet (discrete phase).
- experimental measurements to define the boundary conditions and to validate the numerical results.
- adoption of a droplet emission model based on the measured number distribution of particles emitted by an adult person while speaking (Section 2.3.2).

Thermo-fluid dynamics fields predicted in close proximity of the emitter subject were validated by Cortellessa et al. [11] against Particle Image Velocimetry measurements carried out in the laboratories of the Delft University of Technology.

- assessment of the aerosol distribution within the lecture room under investigation.

4.2.1 MATHEMATICAL MODEL

The droplet-laden flow evolving in the lecture room can be regarded as a dispersed dilute two-phase flow [11]. Fluid-particle interaction is solved by using the Eulerian-Lagrangian approach described in Section 2.3.1. Numerical investigations were performed employing the finite volume method based open-source OpenFOAM code, under the assumption of three-dimensional, unsteady, non-isothermal and turbulent flow. The Boussinesq approximation was adopted to describe buoyancy forces, assuming that the air density varies linearly with temperature [122]. Turbulence was modelled using the URANS approach, analysing the performances of SST $k-\omega$ [78] and RNG $k-\epsilon$ models [105]. SST $k-\omega$ showed better agreement with experimental results and required less CPU time with respect to RNG $k-\epsilon$ (see Section 4.3). The computed numerical fields were averaged over a selected time interval to reach a quasi-steady state condition. The quasi-steady state flow condition is then employed to transport the airborne particles injected by the emitter (i.e., the infected subject) over time during speaking activity. Details about the particle number and volume distributions adopted in the simulations, and the corresponding number and volume emission rates, are given in Section 2.3.2. Details about the governing partial differential equations are instead reported in Appendix A.

4.2.2 SCENARIO ANALYSED

Mass transport in the air is strongly influenced by the convective air flow; in indoor environments the convective flow depends on the natural ventilation, through windows and doors, and on the mechanical ventilation induced by HVAC systems. This work investigates the transport and distribution of droplets emitted by a source reproducing an infected subject continuously speaking for two hours (e.g., a professor in front of the class during a two-hour lesson), evaluating the effects of different air supply rates: 3.75 ACH, 7.5 ACH (i.e., the nominal operating conditions) and 15 ACH. Analyses were performed on a lecture room located in the Department of Engineering of the University of Naples “Parthenope”, whose picture is shown in Figure 4.1a.

The 3D reproduction of the room (i.e., the computational domain employed for numerical model validation) is depicted in Figure 4.1b; its overall dimensions are 8.78 m \times 7.23 m \times 2.88 m in the x, y, and z directions respectively; there are four rows of seats and one teacher’s desk. The air flow rate is supplied by a Turbulent Mixing Airflow (TMA) system, through 8 helical swirl diffusers arranged in two parallel rows at a distance of 2.40 m, 5.43 m from the south wall (i.e., the wall at $y=0$) and spaced 2.02 m in the x direction. Three exhaust grilles (with dimensions of 0.65 m \times 0.28 m) are located on the east wall at a height of 2.50 m, with a spacing of 1.60 m. The numerical model was validated comparing predicted and measured velocity fields under the nominal operating conditions of the HVAC (i.e., ACH=7.5), and was then applied to assess the droplet dispersion within the room under different ventilation regimes.

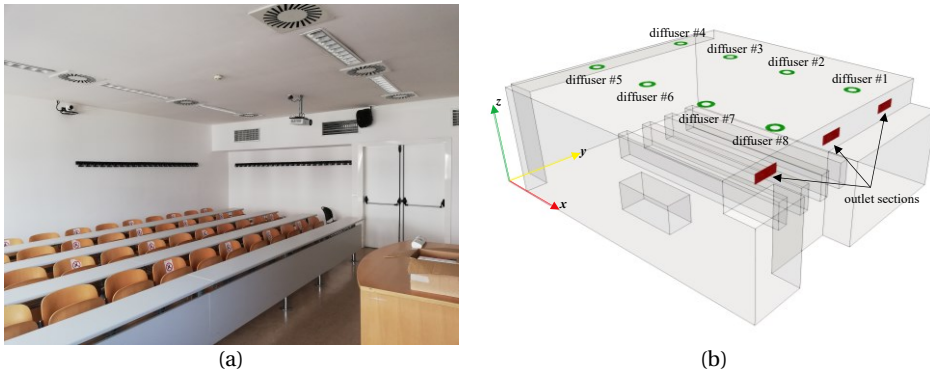


Figure 4.1. Picture (a) and 3D model (b) of the lecture room under study.

4.2.3 EXPERIMENTAL CAMPAIGN

Experiments were conducted to determine the inlet velocity boundary conditions employed for CFD simulations (i.e., velocity values at the diffusers) and the magnitude velocity in different points of the room to provide experimental data for the validation of the numerical model. While taking measurements, the door and the windows were kept closed to avoid disturbances and ensure the repeatability of the experimental conditions, and no occupants were present in the room; numerical simulations were carried under the same conditions, thus simulating the effect of the mechanical ventilation only. The total volumetric airflow from the centralized HVAC system was maintained constant and at the nominal operating conditions. Uncertainties associated with the measurements have been evaluated considering both *type A* and *type B* contributions [123]; the expanded uncertainty U , obtained multiplying the combined standard uncertainty by a coverage factor k_c , has been evaluated selecting $k_c=2$ for a confidence level of 95%. The metrological characteristics of the instruments employed in the experimental campaign are reported in Table 4.1.

Table 4.1. Metrological characteristics declared by the manufacturers of the adopted instruments.

Instrument	Measured quantity	Range	Accuracy	Resolution
volume flow hood	volumetric flow ($\text{m}^3 \text{h}^{-1}$)	40 to 4000 $\text{m}^3 \text{h}^{-1}$	$\pm (3\% \text{ read value} + 12 \text{ m}^3 \text{h}^{-1})$	$1 \text{ m}^3 \text{h}^{-1}$
	temperature ($^\circ\text{C}$)	-20 to +70 $^\circ\text{C}$	$\pm 0.5 \text{ }^\circ\text{C} (0 \text{ to } +70 \text{ }^\circ\text{C})$	$0.1 \text{ }^\circ\text{C}$
hot wire probe	velocity magnitude (m s^{-1})	0 to 30 m s^{-1}	$\pm (0.03 \text{ m s}^{-1} + 4\% \text{ read value})$	0.01 m s^{-1}
	temperature ($^\circ\text{C}$)	-20 to +70 $^\circ\text{C}$	$\pm 0.5 \text{ }^\circ\text{C} (0 \text{ to } +70 \text{ }^\circ\text{C})$	$0.1 \text{ }^\circ\text{C}$

MEASUREMENTS FOR THE DEFINITION OF BOUNDARY CONDITIONS

The HVAC system serves several rooms and the air supplied to a specific classroom may not be known a priori. For this reason, as well as to mediate the statistical oscillations, the volumetric air inflow was measured at each diffuser using a *volume flow hood*. The measured flow rates are listed in Table 4.2, together with the expanded uncertainties; the AER under nominal operating conditions has been calculated from the measured volumetric flow rates and is equal to 7.5 h^{-1} .

Table 4.2. Inlet flow measurements for boundary conditions definition.

Diffuser	Experimental results ($\text{m}^3 \text{s}^{-1}$)	
	Flow rate	Expanded uncertainty U
1	0.0481	0.0100
2	0.0388	0.0094
3	0.0439	0.0097
4	0.0448	0.0099
5	0.0451	0.0098
6	0.0436	0.0096
7	0.0347	0.0092
8	0.0444	0.0098
AER (h^{-1})		7.5

In addition to velocity, temperature values were also measured. Registered values differ by 1 K at most; therefore, temperature at the inlet can be assumed constant and was set to 295.15 K in the numerical simulations.

MEASUREMENTS FOR THE VALIDATION OF THE NUMERICAL MODEL

To validate the velocity field predicted with CFD simulations, velocity magnitudes were measured with a *hot-wire anemometer probe* at 8 points of the room (highlighted with red spheres in Figure 4.2). Such type of velocity probe is able to measure the module of the velocity with no information about the three velocity components. The employed measuring instrument was calibrated and so reliable information about measurement uncertainty was available. In fact, uncertainty quantification is crucial for any numerical tool validation. Points coordinates and measured velocity values with expanded uncertainties are listed in Table 4.3. The location of the probes was chosen with reference to the diffusers position within the classroom. In particular, the eight probes were placed within the diffusers air cone jet, arranged in a uniform x-y grid, with the aim to minimize the placement uncertainty, and at a height $z=1.70$ m, as this value represents the average height of a person standing in the room.

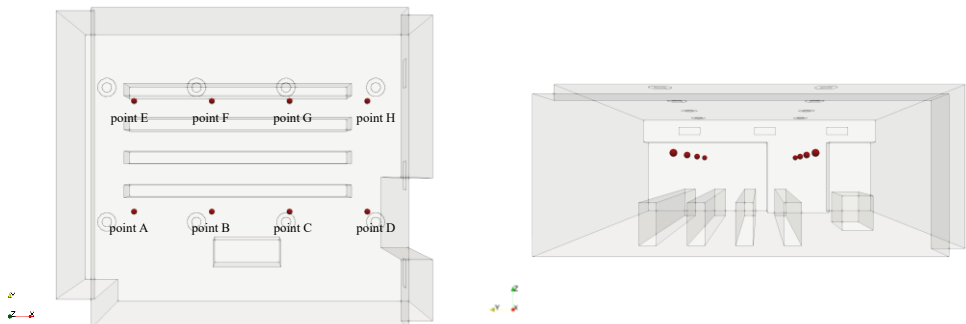


Figure 4.2. Velocity measurement point locations inside the lecture room.

Table 4.3. Velocity measurements at specific points for numerical model validation.

Point	Coordinates (m)			Experimental results (m s^{-1})	
	x	y	z	Mean velocity	Expanded uncertainty U
A	1.63	2.55	1.70	0.06	0.02
B	3.53	2.55	1.70	0.09	0.03
C	5.43	2.55	1.70	0.07	0.03
D	7.33	2.55	1.70	0.08	0.03
E	1.63	5.25	1.70	0.06	0.02
F	3.53	5.25	1.70	0.04	0.02
G	5.43	5.25	1.70	0.06	0.03
H	7.33	5.25	1.70	0.04	0.02

4.3 NUMERICAL MODEL VALIDATION

The numerical model was validated by comparing predicted and measured velocity values at the points shown in Figure 4.2, adopting SST $k-\omega$ and RNG $k-\epsilon$ turbulence models. The computational domain considered for validation is depicted in Figure 4.1b. The inlet sections are highlighted in green, while the outlet sections are coloured red; the unlabelled boundary patches are modelled as walls. A hexahedral-based unstructured grid was used, as shown in the clipped view in Figure 4.3, realized by employing the open source *snappyHexMesh* algorithm. The proper mesh size was determined by a sensitivity analysis considering three different grids, whose main characteristics are listed in Table 4.4. The average percent deviation amongst velocity profiles obtained with Mesh 2 and 3 is less than 1%, therefore 1,558,632 cells are sufficient to provide a solution independent from the mesh size. The minimum, maximum and average y^+ values obtained using Mesh 2 are equal to 0.058, 84.437 and 7.795 respectively. At the diffuser patches, the cell size is of 0.01m.

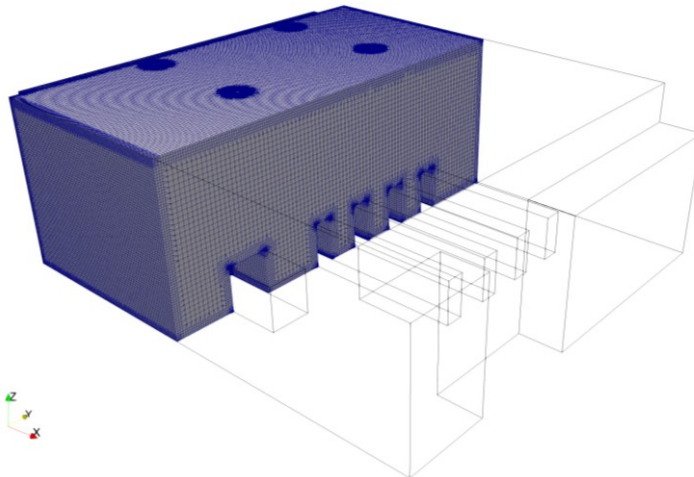


Figure 4.3. Computational grid employed in numerical simulations (Mesh 2, 1558632 cells).

Table 4.4. Details of the computational grids used for the sensitivity analysis.

Mesh #	Number of Cells	Skewness max	Non orthogonality max
1	781,194	2.66	50
2	1,558,632	3.14	50
3	3,149,724	2.63	50

Numerical simulations were conducted using the PISO algorithm (see Appendix A), setting to 2 the maximum value allowed for the Courant number. The boundary conditions employed for numerical model validation are detailed in Table 4.5.

Table 4.5. Boundary conditions set for numerical model validation.

Surface	BC for velocity	BC for pressure	BC for temperature	BC for k	BC for ω	BC for ε
inlet sections (diffusers)	see Table 4.2	$\frac{\partial p}{\partial \mathbf{n}} = 0$	$T = 295.15 \text{ K}$	$I = 10\%$	$\ell = 0.07L$	$\ell = 0.07L$
outlet sections	$\frac{\partial \mathbf{u}}{\partial \mathbf{n}} = 0$	$p = 101325 \text{ Pa}$	$\frac{\partial T}{\partial \mathbf{n}} = 0$	$\frac{\partial k}{\partial \mathbf{n}} = 0$	$\frac{\partial \omega}{\partial \mathbf{n}} = 0$	$\frac{\partial \varepsilon}{\partial \mathbf{n}} = 0$
walls	$\mathbf{u} = 0$	$\frac{\partial p}{\partial \mathbf{n}} = 0$	$\frac{\partial T}{\partial \mathbf{n}} = 0$	standard wall functions		

A swirling behaviour was prescribed for the velocity at the inlet sections, adopting experimentally measured flow rates (Table 4.2) and a constant rotation value of 128 rpm. As to the turbulent quantities, the turbulence intensity $I(\%)$ and the turbulent mixing length $\ell(m)$ were specified; the latter was calculated as the 7% of the characteristic length $L(m)$, set equal to the radial length of the diffusers. Mesh sensitivity analysis and numerical model validation were conducted in terms of time-averaged velocity fields. To establish the proper averaging time interval, eight numerical probes were placed in correspondence of the physical measurements points represented in Figure 4.2, monitoring the time-evolution of the quantities of interest and calculating the percentage deviation of the progressive average up to a given time level with respect to the average calculated up to the previous time level. Investigations have shown that an averaging time-interval size of 1800 s is sufficient to ensure a deviation among calculated progressive averages of less than 1% for all probes. The first 180 s are not included in the averaging interval since fluctuations of the probes are not stable. In Figure 4.4 the velocity progressive average obtained with Mesh 2 is presented for the virtual probes placed in the domain, for both the turbulence models adopted; a flattening in the curves can be noticed as the time-averaging interval increases, thus justifying the adopted approach.

Numerical versus experimental comparison is shown in Figure 4.5 for the measuring points at $y=2.55 \text{ m}$ and in Figure 4.6 for the measuring points at $y=5.25 \text{ m}$.

The experimental velocity measurements were carried out at $z=1.70 \text{ m}$. Since the flow field develops mainly in the z direction (normal to the ceiling) the experimental measurements were carried out by orienting the sensor in that direction while the velocity values in the other directions are negligible. The numerical simulations confirm what observed during the experimental campaign. The plots show a good agreement between predicted and

measured data, with the numerical values contained within the uncertainty bars for most of the experimental points.

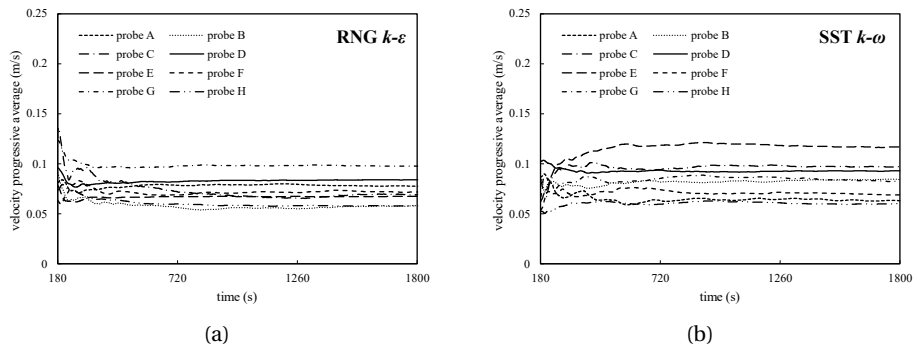


Figure 4.4. Velocity progressive averages obtained with Mesh 2 at points A–H, for (a) RNG $k-\epsilon$ model and (b) SST $k-\omega$ model.

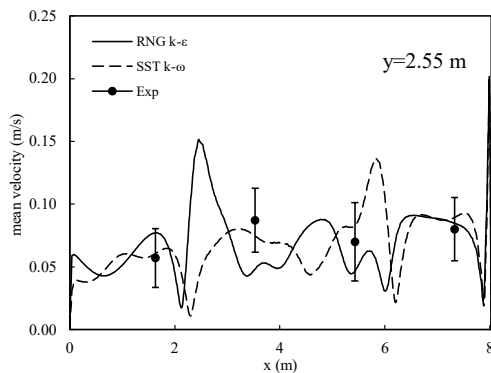


Figure 4.5. Comparison between numerical results and measurement data for probes placed at $y=2.55$ m.

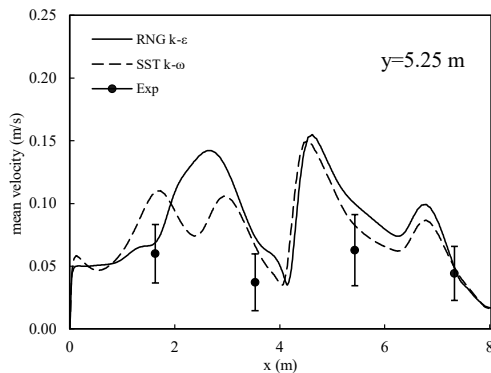


Figure 4.6. Comparison between numerical results and measurement data for probes placed at $y=5.25$ m.

The RMSE between the predicted and measured data was also calculated for both tested turbulence models, using the expression (3.7) presented in the preceding chapter. The calculated RMSEs are listed in Table 4.6, together with numerical results and the CPU times.

Table 4.6. Computed velocities, RMSEs and CPU times for the two investigated turbulence models.

Point	Mean velocity (m s ⁻¹)	
	SST $k-\omega$	RNG $k-\epsilon$
A	0.061	0.077
B	0.074	0.048
C	0.083	0.046
D	0.089	0.085
E	0.109	0.069
F	0.066	0.073
G	0.082	0.100
H	0.049	0.049
RMSE (m s⁻¹)	0.023	0.026
CPU time (s)	455770	513548

The SST $k-\omega$ model showed better agreement with experimental data and required a lower CPU time than the RNG $k-\epsilon$ model, being thus selected for further numerical simulations. Validation of the numerical model has been made for the eulerian velocity field. However, it can be proven that the proposed validation is also effective for the lagrangian field, by introducing the particle Stokes number [124]:

$$\text{Stk} = \frac{\tau_d}{\tau_f} \quad (4.1)$$

where the droplet response time, $\tau_d(s)$, is given by:

$$\tau_d = d_{eq}^2 \frac{\rho_d}{18\mu} \quad (4.2)$$

and the characteristic time scale in the flow, $\tau_f(s)$, is assumed equal to $1/\omega$ [125]; d_{eq} is the weighted mean diameter of droplets, where the weights are the post-evaporated $dN/d\log(d_d)$, as reported in Table 2.1 (Section 2.3.2).

The calculated Stokes number is not larger than 0.1 everywhere, therefore particles faithfully follow the fluid flow. As the largest values of the Stokes number are observed in correspondence of the emitter, in Figure 4.7 the calculated Stk on the y-z slice at $x=4.39$ m (vertical plane crossing the emitter's mouth in its middle) is depicted, showing that its value is well below 0.1 everywhere.

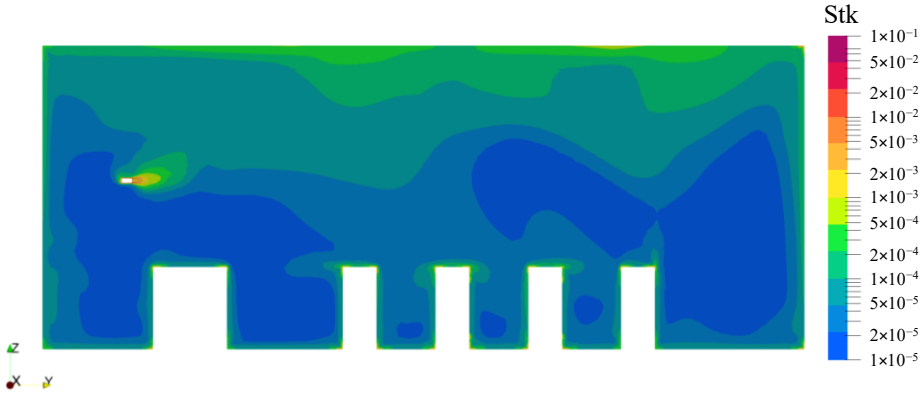


Figure 4.7. y - z slice at $x = 4.39$ m showing the Stokes number spatial distribution.

4.4 RESULTS AND DISCUSSIONS

To evaluate the spread and distribution of particles within the lecture room during the two-hour speaking activity of an infected subject, a single droplet source was modelled. A cylinder has been placed in the domain at a height of 1.60 m, with its basis having a radius of 0.021 m and representing the mouth of the speaking subject. The computational domain employed is shown in Figure 4.8, while boundary conditions adopted for droplet spread simulations are detailed in Figure 4.7 and Figure 4.8.

The mesh adopted is composed of 1,591,198 cells and has the same topology of the grid employed for numerical model validation; the increased number of cells with respect to Mesh 2 is due to the presence of the cylinder, where the grid size is equal to 0.0025m.

As already outlined in Section 4.2.1, three air flow rates were investigated: 3.75 ACH, 7.5 ACH and 15 ACH. The base case is represented by 7.5 ACH, that is the rated capacity of the HVAC system. When halving and doubling the ACH, flow rates and rpm of each diffuser have been halved and doubled respectively. Knowing the area of each diffuser, that is 0.1 m², mean velocities at the inlet patches can be calculated dividing the adopted flow rates by the area; the air speed at the diffusers ranges from a minimum of 0.174 m s⁻¹ (diffuser 7, 3.75 ACH) to a maximum of 0.962 m s⁻¹ (diffuser 1, 15 ACH).

The velocity set as boundary condition for the injector is the mean value of sinusoids during exhalation and inhalation reported by Abkarian et al. [82] and Cortellessa et al. [11] for the speaking activity. A constant average velocity was applied to the patch of the cylinder having its normal along the positive y direction (highlighted in green in Figure 4.8), representing the average velocity of air exhalation in a respiratory act during speaking. This BC was also validated in Ref. [11] by PIV experimental analysis.

For particle injection, random velocity directions at intervals of 0.1s are imposed from the emitter's mouth, considering a conical jet flow with an angle of 22 deg. In fact, as indicated by Abkarian et al. [82], the fluid flow coming out of the mouth during speaking activity diffuses with a conical direction with an opening angle of 22 deg; a "conical injection" lagrangian BC was thus applied to the patch, on the surface of the cylinder having its normal along the positive y direction, with the same angle, allowing the particles to be injected with the same directions of the fluid dynamics field. Buoyancy effects of the

injected particles have been taken into account by assuming a temperature of 308.15K for the exhaled air.

Finally, as concerns the boundary conditions for the particles, the Lagrangian Particle Tracking model was solved by applying an *escape* boundary condition over all the surfaces of the computational domain except for entry sections (for which a *rebound* boundary condition was adopted). With such conditions the adhesion of droplets to the walls is also modelled, since the particles touching the external surfaces of the domain are assumed to disappear and cannot re-enter the computational domain.

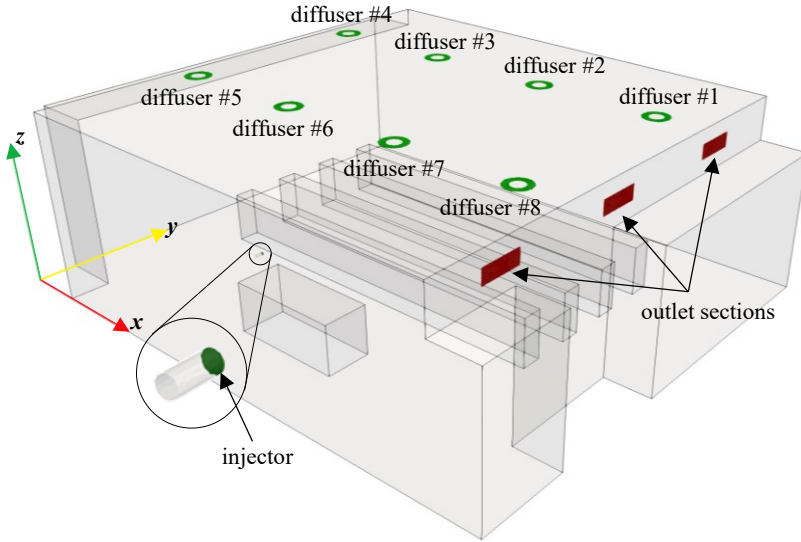


Figure 4.8. Inlet and outlet boundaries considered for the numerical description of droplets spread inside the room.

Table 4.7. Boundary conditions adopted for numerical predictions.

Surface	BC for velocity	BC for pressure	BC for temperature	BC for k	BC for ω	Lagrangian
diffusers	see Table 4.8	$\frac{\partial p}{\partial n} = 0$	$T = 295.15 \text{ K}$	$I = 10\%$	$\ell = 0.07L$	<i>rebound</i>
outlet sections	$\frac{\partial \mathbf{u}}{\partial n} = 0$	$p = 101325 \text{ Pa}$	$\frac{\partial T}{\partial n} = 0$	$\frac{\partial k}{\partial n} = 0$	$\frac{\partial \omega}{\partial n} = 0$	<i>escape</i>
walls	$\mathbf{u} = 0$	$\frac{\partial p}{\partial n} = 0$	$\frac{\partial T}{\partial n} = 0$	standard wall functions		<i>escape</i>
injector	$ \mathbf{u} = 1.38 \text{ m s}^{-1}$	$\frac{\partial p}{\partial n} = 0$	$T = 308.15 \text{ K}$	$k = 0.1 \text{ m}^2 \text{ s}^{-2}$	$\frac{\partial \omega}{\partial n} = 0$	<i>rebound</i>

Table 4.8. Detailed boundary conditions for the velocity at the inlet sections.

Diffuser	ACH=3.75		ACH=7.5		ACH=15	
	Flow rate (m ³ s ⁻¹)	rpm	Flow rate (m ³ s ⁻¹)	rpm	Flow rate (m ³ s ⁻¹)	rpm
1	0.0241		0.0481		0.0962	
2	0.0194		0.0388		0.0776	
3	0.0220		0.0439		0.0878	
4	0.0224	64	0.0448	128	0.0896	256
5	0.0226		0.0451		0.0902	
6	0.0218		0.0436		0.0872	
7	0.0174		0.0347		0.0694	
8	0.0222		0.0444		0.0888	

4.4.1 ANALYSIS OF DROPLET BEHAVIOUR, AGE AND DISTRIBUTION

The quantity and relative percentage of droplets suspended in the air, settled on surfaces and evacuated through the extraction grilles by the HVAC system after two hours are reported in Table 4.9 for the three ventilation regimes analysed.

Table 4.9. Number, percentage, and volume of droplets suspended in the air, settled, and evacuated after two hours, for the three analysed AERs.

AER (h ⁻¹)	Droplets suspended in the air, %, ml	Droplets settled, %, ml	Droplets evacuated, %, ml
3.75	222987, 12.59%, 8.38×10 ⁻⁵	1436850, 81.15%, 5.40×10 ⁻⁴	110700, 6.25%, 4.16×10 ⁻⁵
7.5	62169, 3.51%, 2.34×10 ⁻⁵	1092781, 61.72%, 4.11×10 ⁻⁴	615587, 34.77%, 2.31×10 ⁻⁴
15	42495, 2.40%, 1.60×10 ⁻⁵	1372273, 77.51%, 5.16×10 ⁻⁴	355769, 20.09%, 1.34×10 ⁻⁴

With the ventilation system at the minimum load (i.e., with 3.75 ACH), there is a higher number of droplets suspended in the air and settled, due to the lower velocity values. The air flow at a low speed cannot reach the bottom of the classroom and consequently is not able to effectively convey the droplets towards the extraction grilles resulting in a higher number of droplets still suspended in the air, while most of the droplets settle on surfaces. Droplets deposited on desks can pose a hazard to the susceptible subjects in the room, since they can be inhaled after contact between the desk and the skin. Doubling the ACH (from 3.75 to 7.5) reduces the droplets suspended in the air by 73%, further doubling the ACH (from 7.5 to 15) reduces the droplets only by 32%. The case with 15 ACH has a higher percentage of droplets settled than the 7.5 ACH case; a reason can be the higher inlet velocity that pushes down the droplets, enhancing their settling. As a result, the 7.5 ACH has the best performance in terms of droplets evacuated and requires a lower energy consumption than 15 ACH, while the 3.75 ACH is not recommended due to the poor performance. The above findings highlight the importance of considering the droplets that deposit on surfaces and not only those suspended in the air. CFD analyses can be a valuable tool to assess both the deposited and suspended droplets.

To assess the effectiveness of the ventilation system, it is also important to evaluate the age of droplets suspended in air (i.e., their residence time inside the classroom). Depicted in Figure 4.9 is the particles repartition as a function of the age after two hours, expressed

as a percentage of the total (i.e., *particles with an age within a specified range/total particles*) and grouped in ranges of 300 s.

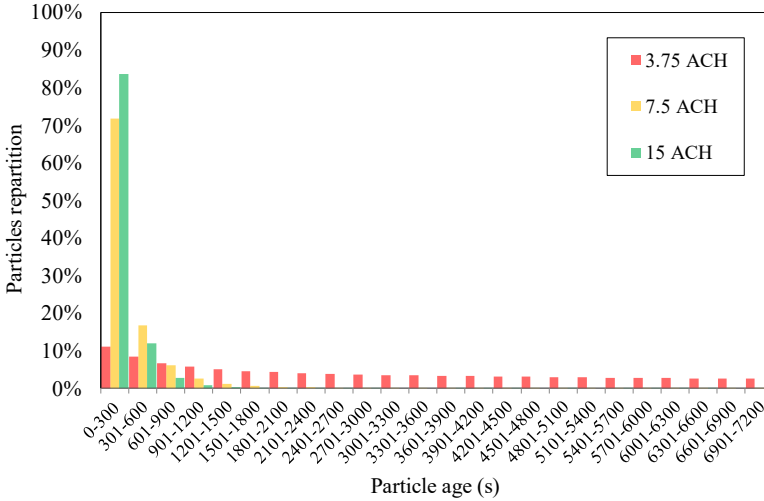
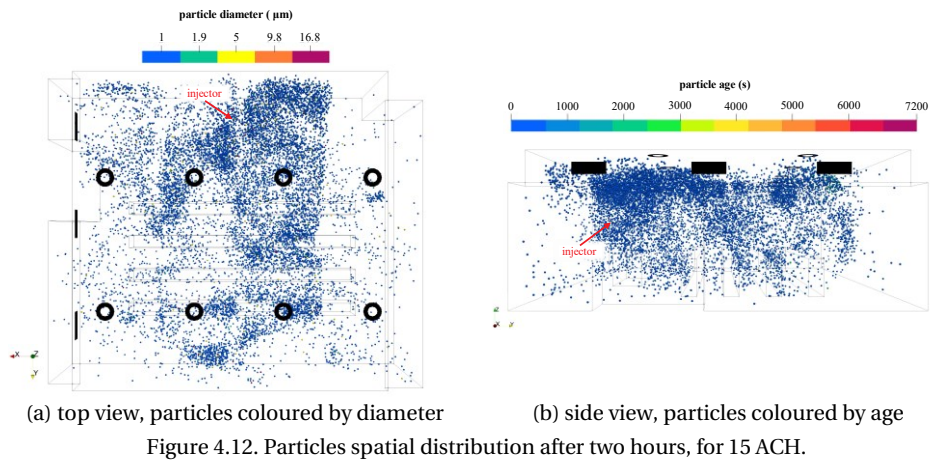
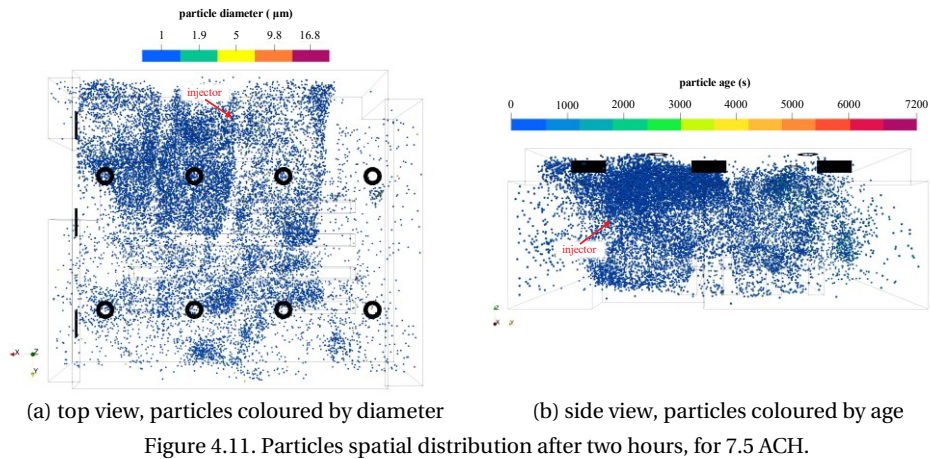
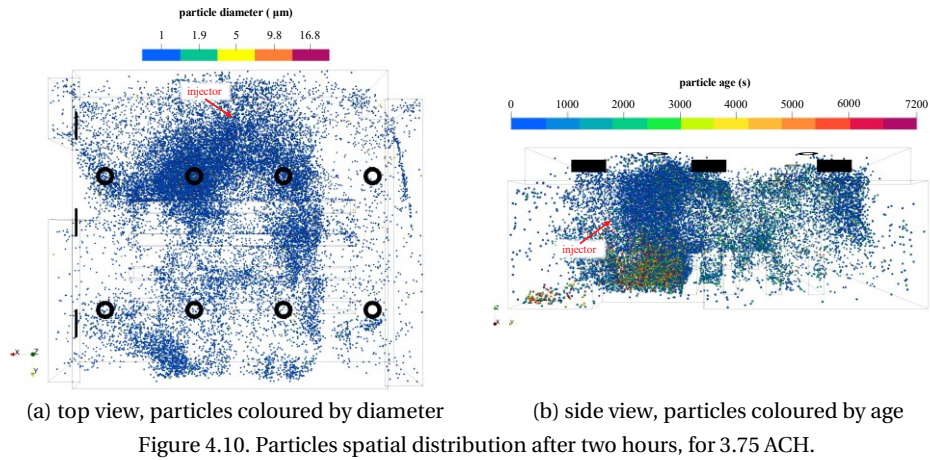


Figure 4.9. Particles repartition by age, after two hours.

For the case with 15 ACH the percentage of droplets with an age higher than 900 s is very low (~ 3%), while for the case with 7.5 ACH is ~8% and, in both cases, there are no droplets with an age higher than 2100 s. Even though there is an improvement when passing from 7.5 to 15 ACH, it is not significant, also considering the increase in energy consumption. For the case with 3.75 ACH there are droplets that are suspended in the air since the beginning (age of 7200 s), resulting in a very poor evacuation efficiency, evidencing that the air flow provided by the HVAC system is not enough to guarantee a good indoor air quality in terms of aerosol removal effectiveness. In Figure 4.10 the particle distribution in the room after two hours is shown for the case of 3.75 ACH, with droplets coloured by their diameter (Figure 4.10a, top view) and their residence time (Figure 4.10b, side view). The side view unveils the presence of several particles with an age exceeding 3000 s, mainly concentrated in the immediate surroundings of the emitter, confirming the poor efficiency of the HVAC system under this ventilation regime. When increasing the AER to 7.5 h⁻¹ and 15 h⁻¹, distributions shown in Figure 4.11 and Figure 4.12 are obtained, respectively. It is possible to observe that not only the number of droplets suspended in the air decreases, but also their age, when enhancing the ventilation (see Figure 4.11b and Figure 4.12b). Moreover, a similar aerosol distribution is observed for all investigated flow rates: particles are mainly concentrated in the area before the rows of seats (where the emitter is standing); this may be due also to the position of the extraction grilles, with one located before the first row of seats and two after. Therefore, one solution could be having the extraction grilles distributed on both the side walls (i.e., those with surface normal along the x direction) so as to enhance the removal of particles and have two grilles close to the emitter. As regards the particles diameter, by looking at Figure 4.10a, Figure 4.11a and Figure 4.12a it can be concluded that the air supply rate has no noticeable effect on the dimensions of the airborne droplets emitted; in fact, in all three cases the smallest particles (i.e., with a diameter of 1 µm) prevail.



The spatial distribution shown in Figure 4.10, Figure 4.11 and Figure 4.12 can be better explained looking at the streamlines exiting the mouth of the emitter and the velocity fields on the x-y plane at $z=1.60\text{m}$ and the x-z planes at $y=2.55\text{m}$ and $y=5.25\text{m}$, depicted in Figure 4.13, Figure 4.14 and Figure 4.15 for 3.75 h^{-1} , 7.5 h^{-1} and 15 h^{-1} respectively.

In the case of 3.75 h^{-1} (Figure 4.10 and Figure 4.13) velocities are quite low away from the diffusers. The air exhaled by the emitter rises because of buoyancy and then interacts with the air coming from the inlet vents, as emphasized by the streamlines. As a consequence, the expiratory particles are carried upwards and then spread in the room, explaining the reason why they are more concentrated in the upper part of the room and on the right side of the injector. When increasing the air supply rate to 7.5 h^{-1} (Figure 4.11 and Figure 4.14), particles are still more present in the upper area of the room, but evenly distributed; in fact, as well represented by the streamlines, the higher velocities cause more disturbance to the warm breath exhaled by the speaker, that, however, is still sufficient to lift the particles. When the air supply rate is increased further (15 h^{-1} , Figure 4.12 and Figure 4.15), the air speed increases and strongly affects the air coming out of the emitter mouth; in this case, streamlines are braided and directed towards the left of the speaker, where the particles are mostly located.

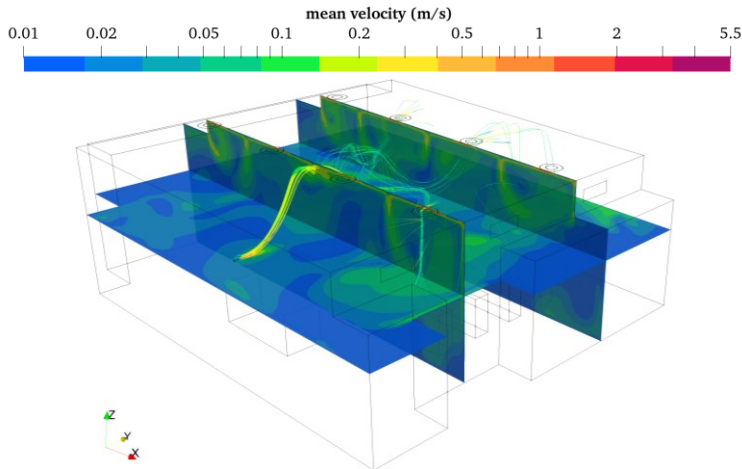


Figure 4.13. Mean velocity fields on the x-y plane at $z=1.60\text{m}$ and the x-z planes at $y=2.55\text{m}$ and $y=5.25\text{m}$, together with the streamlines exiting the mouth of the emitter (coloured by mean velocity), for 3.75 ACH .

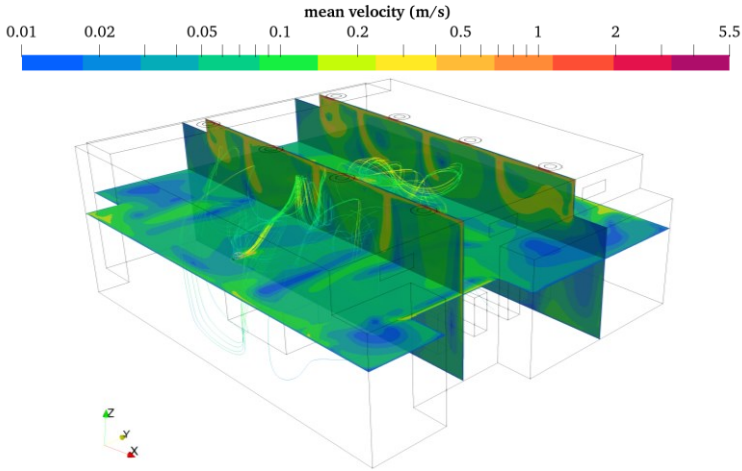


Figure 4.14. Mean velocity fields on the x-y plane at $z=1.60\text{m}$ and the x-z planes at $y=2.55\text{m}$ and $y=5.25\text{m}$, together with the streamlines exiting the mouth of the emitter (coloured by mean velocity), for 7.5 ACH.

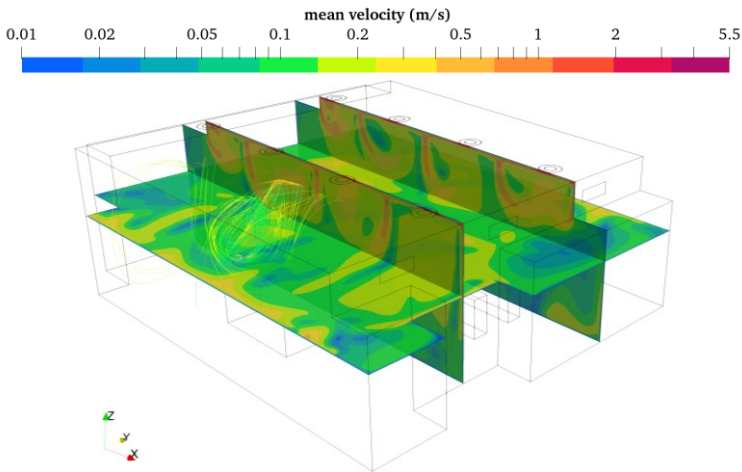


Figure 4.15. Mean velocity fields on the x-y plane at $z=1.60\text{m}$ and the x-z planes at $y=2.55\text{m}$ and $y=5.25\text{m}$, together with the streamlines exiting the mouth of the emitter (coloured by mean velocity), for 15 ACH.

4.4.2 ASSESSMENT OF THE MEAN DROPLET CONCENTRATION IN THE SEATS AREA

Another relevant aspect to consider is the evaluation of the average dose of particles to which possible occupants are exposed while following a two-hour lesson, when the teacher represents the infected subject. To this extent, twelve control volumes have been selected as depicted in Figure 4.16, where the position of injector, diffusers and exhaust grilles is also highlighted, and the average amount of airborne respiratory droplets

(expressed in ml) in each volume has been calculated, for the investigated AERs (i.e., 3.75 h^{-1} , 7.5 h^{-1} and 15 h^{-1}).

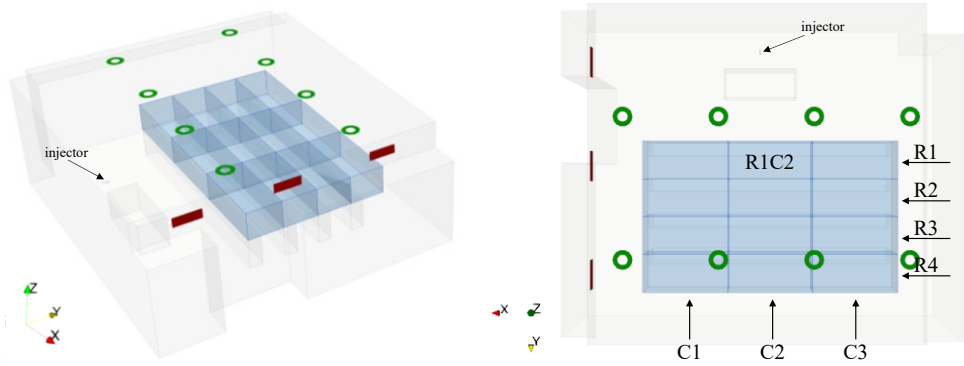


Figure 4.16. Control volumes selected for the analysis.

Each control volume is 1.97 m wide, 0.88 m deep and 0.72 m high; it extends from the benches up to a height of 1.5 m, enclosing the breathing zone of the occupants and allowing to estimate their exposure to the particles emitted by the infected subject while speaking in front of the class. Results are summarized in Table 4.10 and displayed in a graphical form in Figure 4.17.

Table 4.10. List of the airborne respiratory particles (expressed in ml) inside the selected control volumes, for the different air change rates.

Box	Volume of airborne respiratory particles (ml)		
	3.75 ACH	7.5 ACH	15 ACH
<i>R1C1</i>	2.58×10^{-5}	6.05×10^{-5}	1.66×10^{-5}
<i>R1C2</i>	2.19×10^{-5}	3.60×10^{-5}	3.09×10^{-5}
<i>R1C3</i>	2.71×10^{-5}	5.69×10^{-6}	4.07×10^{-6}
<i>R2C1</i>	3.19×10^{-5}	3.37×10^{-5}	1.53×10^{-5}
<i>R2C2</i>	1.09×10^{-5}	4.38×10^{-5}	4.57×10^{-5}
<i>R2C3</i>	4.63×10^{-5}	1.71×10^{-5}	2.68×10^{-5}
<i>R3C1</i>	1.65×10^{-5}	1.84×10^{-5}	9.91×10^{-6}
<i>R3C2</i>	4.90×10^{-5}	4.37×10^{-5}	1.68×10^{-5}
<i>R3C3</i>	1.59×10^{-5}	1.19×10^{-5}	5.59×10^{-6}
<i>R4C1</i>	2.10×10^{-5}	2.55×10^{-5}	7.26×10^{-6}
<i>R4C2</i>	4.52×10^{-6}	3.05×10^{-5}	3.63×10^{-5}
<i>R4C3</i>	7.36×10^{-6}	5.32×10^{-6}	8.71×10^{-6}

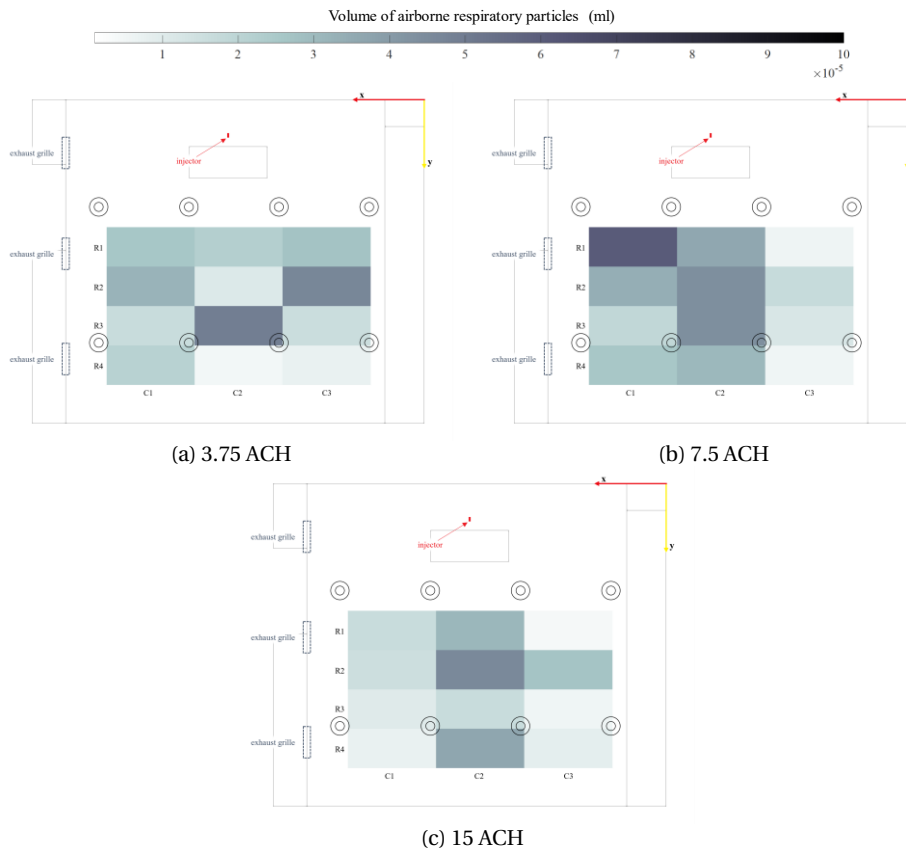


Figure 4.17. Colormaps of the airborne respiratory particles (expressed in ml) inside the selected control volumes, for the different AERs.

Based on the results obtained, two main considerations can be made:

- the most critical control volume (i.e., with the highest parcels concentration) changes with the air supply rate.
- even though the overall number of droplets suspended in the air decreases when increasing the ACH (look at Table 4.9 and Figure 4.10, Figure 4.11, Figure 4.12), at a local level there is not always an improvement; conversely, in multiple control volumes the particle concentration increases.

This behaviour may be attributed to the asymmetric disposition of the seats with respect to diffusers and to the extraction grilles, proving that increasing the AER is not always an effective solution to remove particles. Similar findings are highlighted by the study of Pantelic and Tham [114], and in Chapter 3 of the present dissertation where the risk of SARS-CoV-2 inside car cabins has been assessed; in fact, two of the messages conveyed are that local air flow patterns must be taken into account when considering the risk of exposure to airborne diseases in indoor environments and that the sole air change rate is not sufficient to assess the effectiveness of air distribution systems. An interesting solution to have a better control on local airflow patterns and provide effective protection could be the adoption of a personalized ventilation, acting on several sub-volumes within a wider

indoor environment. This aspect is addressed in Chapter 5, where the effectiveness of a newly designed portable personal air cleaner in reducing the airborne transmission of respiratory pathogens is assessed, in both close proximity and shared indoor environments scenarios.

4.5 CONCLUSIONS

In the present study, 3D CFD simulations have been performed to investigate the motion and distribution of droplets emitted by a particles source that reproduces an infected subject speaking (e.g., a professor) for 2 h inside a university lecture room. The aim of the study is to assess the effectiveness of validated CFD tools in providing useful information: (i) for a proper design of HVAC systems; (ii) to optimize the system capability in evacuating pollutants and pathogens from the room efficiently; (iii) for the management of the HVAC system, by analysing the aerosol distribution in the room as a function of the AER. In order to analyse the aerosol distribution as a function of HVAC system design and operation, the room has been assumed to be empty and the thermal plume of possible occupants has then been neglected. Numerical results have been validated against measurement data collected inside a lecture room located in the Department of Engineering of the University of Naples "Parthenope", in the absence of occupants.

As the objective of the present work is the analysis of droplet distribution as a function of HVAC design and operation, excluding any other influential parameter, the main limitation of the study is represented by the absence of occupants in the room. The presence of occupants in the room will be considered in future studies.

The employed numerical model is based on a Eulerian-Lagrangian approach, solving the mass, momentum and energy conservation equations for the air flow (continuous phase) and Newton's equation of motion for each droplet (discrete phase). It has been validated under the nominal operating conditions of the HVAC system (i.e., 7.5 ACH) against velocity measurements acquired at specific points of the room, testing the SST $k-\omega$ and RNG $k-\epsilon$ turbulence models. SST $k-\omega$ has shown better performance in terms of RMSE and has required less computational resources. For these reasons, it has been selected for the numerical simulations. The validated numerical tool has been employed to evaluate the influence of three different air supply rates (3.75 ACH, 7.5 ACH and 15 ACH) on particles age, distribution in the whole room and concentration inside selected control volumes surrounding the rows of benches.

Obtained results show that increasing the air supply rate is not always an effective solution to improve the indoor air quality (assuming that it is related to the droplet concentration). In fact, even though the overall number of droplets in the room decreases, at a local level the increased air flow produces negative effects, raising the risk of exposure in many of the selected control volumes. These phenomena suggest that: (i) local air flow patterns must be considered when designing ventilation systems and when assessing the risk of exposure to airborne diseases; (ii) CFD is essential to investigate the complex thermo-fluid dynamics of indoor environments and (iii) the AER is not enough to assess the effectiveness of HVAC systems.

5

EFFECTIVENESS OF A PORTABLE PERSONAL AIR CLEANER IN REDUCING THE AIRBORNE TRANSMISSION OF RESPIRATORY PATHOGENS

The airborne transmission in indoor environments represents the main pathway of respiratory pathogens, and most of the indoor environments do not have adequate ventilation to contain the risk of infection. This is particularly relevant for gathering spaces such as restaurants, schools, offices, etc. due to the long exposure times and high crowding levels. This chapter investigates the effectiveness of a novel patented personal air cleaner in reducing the airborne transmission of respiratory pathogens both in close proximity (considering a typical face-to-face configuration at a conversational distance) and in shared indoor environments despite maintaining distancing (lecture room). The effectiveness of the portable protection device was investigated using transient 3D CFD numerical simulations. The mathematical model employed, validated through experimental measurements, is based on a Eulerian-Lagrangian approach, describing the air flow as the continuous phase and infectious respiratory particles as the discrete phase. The CFD analyses revealed that the air cleaner could strongly reduce the inhalation of respiratory pathogens in both the investigated scenarios. The air cleaner effectiveness in the case of a close proximity scenario, expressed as relative reduction of volume of infectious respiratory particles inhaled by the exposed subject, resulted >92%. In the case of use in a shared indoor environment, instead, during a 2-h lesson, the relative reduction of volume concentration of infectious particles in the breathing zone of the exposed subject was >99%.

This chapter is based on the following published article:

Cortellessa G., Canale C., Stabile L., Grossi G., Buonanno G. and Arpino F. (2023). Effectiveness of a portable personal air cleaner in reducing the airborne transmission of respiratory pathogens. *Building and Environment*, 235, 110222.

Keywords: portable personal air cleaner; close proximity; SARS-CoV-2; virus transmission; CFD analyses; infectious respiratory particles

5.1 INTRODUCTION

5.1.1 ROUTES OF TRANSMISSION AND ROLE OF THE VENTILATION

COVID-19 pandemic unveiled the critical role of indoor environments in terms of respiratory virus spread [14,126]. This is due to the effect of the principal transmission route of many respiratory infectious diseases, i.e., the airborne transmission [10,12,13]. Indeed, virus-laden respiratory particles emitted by infected subjects remain suspended in the air likely reaching high concentrations causing secondary infections within susceptible subjects sharing the same confined space (even when non in close proximity to the infected subject) [12,14,127]. This route of transmission was recognized very late by public health authorities (i.e., WHO and CDC) despite researchers suddenly advised about the main role of such transmission route [12,43,44,128]. Consequently, public health authorities supported mitigation measures mostly facing routes of transmission not occurring via airborne, such as social distancing and disinfecting surfaces to limit the fomite transmission. However, studies on the effectiveness of non-pharmaceutical interventions against COVID-19 spread introduced by government worldwide clearly showed that environmental measures to disinfect and clean surfaces and objects in public and semi-public places did not produce significant reduction of the COVID-19 spread [129]. On the contrary, small gathering cancellations and closure of educational institutions, i.e., activity characterized by high crowding indexes in indoor environments with inadequate ventilation, significantly affected the COVID-19 spread [129]. Nonetheless, after the early stage of the pandemics, characterized by emergency response to the COVID, drastic solutions as closing indoor environments (like schools) could no longer represent feasible solutions [130].

A valuable support to reduce the SARS-CoV-2 airborne transmission in indoor environments, is represented by the building ventilation. In fact, Buonanno et al. [131] recently reported the very first proof of the effect of the ventilation against COVID-19 airborne transmission on a largescale experiment as they compared outbreaks occurring in classrooms with and without mechanical ventilation systems in Italian schools: a >70% lower risk of infection in classrooms with mechanical ventilation systems was detected with respect to natural ventilation ones.

Although the ventilation rates have been raised over the years by various standards worldwide for highly occupied indoor microenvironments [132,133], these standards mostly aimed at guaranteeing good indoor air quality and thermal comfort without a proper consideration to control airborne infection [134]. Therefore, zeroing the risk of infection in indoor environments is practically unfeasible for many respiratory viruses since particularly high ventilation rates (not usually achievable even by the most advanced ventilation standards) would have needed in case of highly emitting infected subjects, i.e., due to extremely contagious viruses and variants (e.g., Omicron) [135], intense expiratory [59,74] and/or high physical activities [136]. Thus, other non-pharmaceutical measures should be adopted simultaneously in view of a further reduction of the risk of infection.

5.1.2 AIR CLEANERS AND PERSONALIZED VENTILATION

A valuable support could be provided by adopting, along with general ventilation systems, (i) air cleaners, i.e., portable devices able to pull the indoor air through filters removing airborne particles and then making the particle-free air circulate back into the indoor environment, or (ii) personalized ventilation solutions providing pathogen-free air (either with local air extraction or injection) in the breathing zone of the susceptible subjects in order to reduce their risk of infection [107,108,137–144].

The air cleaners represent an easy-to-use, commercially available, solution. Their effectiveness in reducing the airborne transmission of respiratory pathogens is related to the filtration efficiency of the filter and to the flow rate of the device: higher filtration efficiencies and flow rates lead to higher clean (pathogen-free) air delivered to the room and then higher removal rates of the respiratory particles emitted by infected subjects in the environments [145,146]. Several studies demonstrated the support of the air cleaners in reducing the exposure to airborne respiratory pathogens in indoor environments (including hospitals) [147–150], nonetheless, such support can be limited in case of abovementioned superspreading events [59].

Personalized ventilation, differently from air cleaners, doesn't aim just at increasing the respiratory particle removal rate in the indoor environment but it aims, indeed, at reducing the exposure in the breathing zone of exposed subjects through ad-hoc designed air flow patterns. Such solution represents an energy efficient approach with respect to general ventilation alone since, in the latter case, the entire space is ventilated (including the unoccupied volume) supplying huge amount of conditioned air [138,151], whereas personalized ventilation requires lower (but properly designed) flow rates. Personalized ventilation is in principle a basic approach but, in order to perform efficiently in practice, its design has to be carefully considered since the airflow interaction in the vicinity of the human body is complex and also affects the thermal comfort of people [152,153]. Indeed, the type and geometry of the air supply terminal devices represent a topic needed for further studies [151,154–157].

Most of the experimental and numerical studies currently reported in the scientific literature deals with personalized ventilation systems relying upon fixed ducts injecting and extracting air at a fixed location (e.g., a fixed workplace, an office desk, a bus seat, a theatre seat, etc.) [137,143,151,158]. Thus, slightly different orientations, positioning, height of the person could affect the effectiveness of the personalized ventilation. Moreover, despite personalized ventilation systems could guarantee a more efficient energy use, supply and extraction air flows need to be channelled (and, in case, connected to the HVAC system), consequently, the installation of personalized ventilation systems is not cheap and, once installed, they are not significantly adaptable [107,159].

Summarizing, in order to reduce the airborne transmission of respiratory pathogens, technical solutions condensing the advantages of air cleaners (i.e., portability, cheapness, and ease of use) and personalized ventilation (i.e., fluid dynamic performances) could be successful.

5.1.3 AIMS OF THE WORK

The aim of the present study is to evaluate the effectiveness of a newly designed portable personal air cleaner (recently patented; patent n. 102022000010346) in reducing the airborne transmission of respiratory pathogens as well as airborne particles. The device was conceived as a ductless apparatus capable of reducing the concentration of infectious

respiratory particles (IRPs) in the breathing region of the exposed person. This is achieved by supplying filtered air through an ad-hoc flow pattern that is properly designed to avoid thermal discomfort and/or prevent respiratory particles from entering the particle-free area. CFD analyses are here performed to test the portable personal air cleaner both in close proximity and for people sharing the same indoor environment but not in close proximity when the infected subject is speaking. Close proximity simulations were performed considering a typical face-to-face configuration at a conversational distance between emitter and receiver, whereas indoor environment simulations were performed considering the university lecture room experimentally and numerically characterized in the preceding chapter of this dissertation.

5.2 MATERIALS AND METHODS

The patented portable personal air cleaner (patent n. 102022000010346) is able to provide clean air in the breathing zone of exposed subjects as it creates a protected volume in which users can breathe clean air with pollutant and respiratory pathogen concentrations considerably lower than those in the room environment. The device is based on the concept of personalized ventilation and presents small dimensions to guarantee its portability. In Figure 5.1 the schematic of the proposed device is available, and the main dimensions (affecting the functionality of the device) are highlighted.

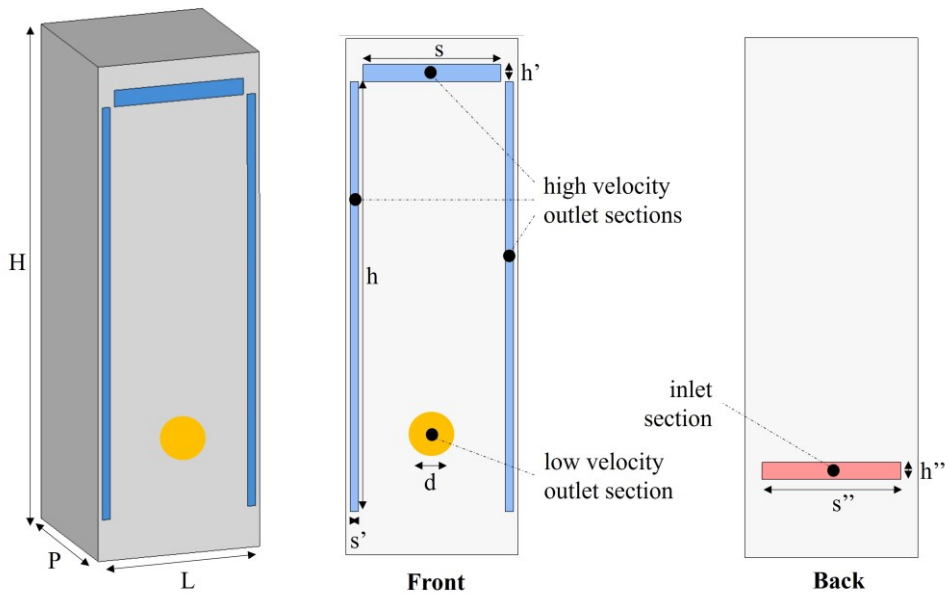


Figure 5.1. Schematic of the portable personal air cleaner.

The device, designed to be powered by a battery, receives air from the environment through an inlet section. Then, the sampled air passes through a filtration section designed to remove airborne and respiratory particles from the flow with a 100% filtration efficiency.

Such a high efficiency can be achieved, for the typical respiratory particle size ranges, by commercial filters (e.g., HEPA or electrostatic filters).

The cleaned air is reintroduced into the environment through four distinct sections: three high-velocity sections (positioned vertically on the sides and horizontally at the top of the device) and a low-velocity section characterized by high swirl motion (rotational motion of the air through the axis of the nozzle). The device was conceived as a rectangular parallelepiped with dimensions of 10 cm × 10 cm × 30 cm. The main geometrical and operational characteristics of the portable personal protection device are summarized in Table 5.1. The three high-velocity sections provide a total flow rate of 35.6 m³ h⁻¹, whereas the low-velocity section flow rate is equal to 2.0 m³ h⁻¹. Thus, the average air velocities are equal to 3.0 m s⁻¹ and 1.8 m s⁻¹, respectively.

Table 5.1. Main geometric characteristics of the portable personal air cleaner.

Geometrical parameter	Size (cm)
length of the air cleaner, L	10
depth of the air cleaner, P	10
height of the air cleaner, H	30
diameter of the low velocity outlet section, d	2
height of the high velocity side outlet sections, h	25
width of the high velocity side outlet sections, s'	0.5
length of the high velocity upper outlet section, s	8
width of the high velocity upper outlet section, h'	1
length of the inlet section, s''	8
width of the inlet section, h''	1

The air cleaner was designed to ensure the maximum protection effectiveness when placed on table, desk etc. at a recommended distance of about 40 cm from the susceptible individual. To this purpose, the functionality of the device is based on the sophisticated fluid-dynamic field generated by the specific outlet sections. In particular, the clean air jets exiting the high-velocity sections produce a fluid-dynamic shield which encloses a sheltered microenvironment capable of protecting a susceptible from airborne and respiratory particles. At the same time, through the low-velocity section, clean air is injected into this microenvironment, enhancing individual protection as it prevents particles from re-entering from the highly concentrated room environment. Such low-velocity air flow rate was specifically designed to prevent thermal discomfort for users. In fact, the lower velocity at the outlet section and the swirl motion result in a very low final velocity of the air flow that reaches the user. Analogously, the high-velocity air flow rates were designed with release angles not directly reaching the user. In Figure 5.2 a qualitative representation of the release angles and fluid flow directions is given, whereas in Table 5.2 the values of the release angles of the jets at the air cleaner outlet sections are summarized: here α represents the upper jet direction with respect to a horizontal plane while β_1 and β_2 represent the side jet directions with respect to a vertical plane.

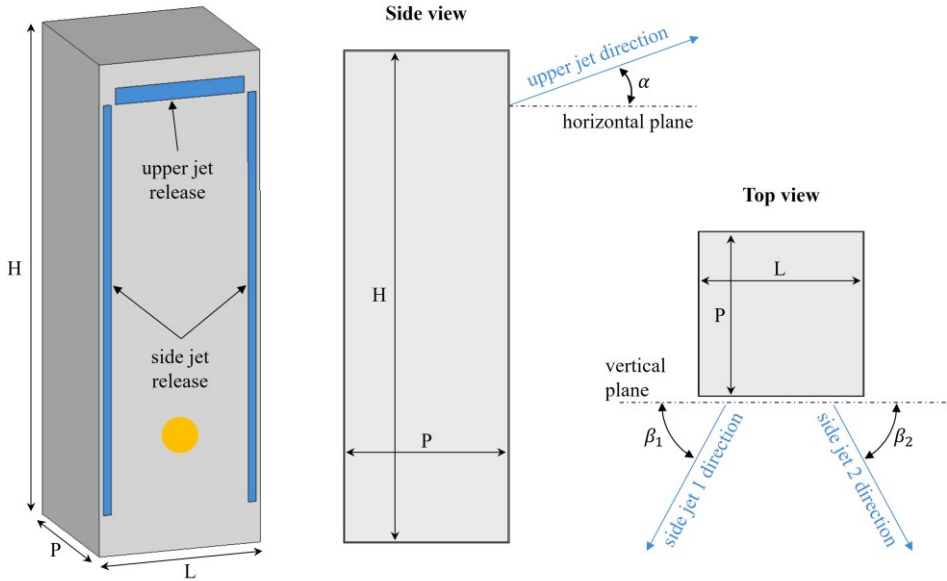


Figure 5.2. Release angles and directions of the air flows exiting the high-velocity sections.

Table 5.2. Release angles of the jets at the air cleaner outlet sections.

Outlet sections	α	β_1	β_2
upper jet release	50 deg	-	-
side jet 1 release	30 deg	45 deg	-
side jet 2 release	30 deg	-	45 deg

5.2.1 NUMERICAL MODEL

The particle-laden flow evolving in the scenarios here outlined can be regarded as a dispersed dilute two-phase flow [11] and fluid-particle interaction is solved with the Eulerian-Lagrangian approach, as already discussed in Section 2.3.1. The emission model considered for the IRPs exhaled by the infected subject, instead, is discussed in Section 2.3.2, where the particle number and volume distributions adopted in the simulations, and the corresponding number emission rates, are also reported. Numerical investigations were performed employing the open-source OpenFOAM code, based on the finite volume formulation.

EULERIAN APPROACH IN CLOSE PROXIMITY SCENARIO

The numerical model adopted for the resolution of velocity, pressure and temperature fields in close proximity scenario was recently developed by Cortellessa et al. [11] and it is employed here for the evaluation of the effectiveness of the personal air cleaner.

The CFD technique was adopted for the numerical description of velocity, pressure, and temperature fields, along with the motion and interaction of the particles with the fluid. The substantial complexity of the adopted approach has paid off by allowing a detailed description in space and time of the thermo-fluid dynamics coupled fields and the associated particles motion. Turbulence was modelled using the URANS approach, closing continuum equations with the Realizable k - ϵ model, since previous analyses performed by Refs. [116,160] revealed that it is the best one to predict fluid flow for close proximity scenarios. A time step equal to 0.1 s was adopted for all the performed numerical analyses. Finally, numerical simulations were performed adopting the following thermophysical properties of air: specific heat $C_p=1004.5 \text{ J kg}^{-1} \text{ K}^{-1}$, dynamic viscosity $\mu=1.8 \times 10^{-5} \text{ Pa s}$, and Prandtl number $Pr=0.71$.

EULERIAN APPROACH IN SHARED INDOOR ENVIRONMENTS

The investigated shared indoor environment is the university lecture room characterized in Chapter 4; the same assumptions are thus made in the numerical modelling (the reader is referred to Section 4.2.1 for further details). Here it is simply reminded that: (i) the SST k - ω model [78] was adopted to close the continuum equations, since the validation performed in Section 4.3 revealed that it is the best one to predict the fluid flow behaviour inside the lecture room under investigation; (ii) the computed numerical fields were averaged over a proper time interval to reach a quasi-steady state condition. The quasi-steady state flow condition was then employed to transport the IRPs injected by the infected subject over time during speaking activity.

5.2.2 PERSONAL AIR CLEANER IN A CLOSE PROXIMITY SCENARIO

The effectiveness of the portable personal protection device was studied in detail by using the CFD numerical model, described in the previous section and developed by Cortellessa et al. [11], capable of reproducing the velocity, temperature, and pressure fields in a close proximity scenario with high accuracy, in addition to the emission, distribution and inhalation of pathogens received by a susceptible individual.

Figure 5.3 shows the computational domain selected to analyse the performance of the portable personal air cleaner in close proximity scenarios.

The computational domain reproduces an indoor environment in which two subjects are seated, facing each other, at the same table. One of the two subjects is considered infected (the emitter, or speaking subject, in Figure 5.3), while the other (the receiver subject in Figure 5.3) is protected by the device.

The study was conducted in a time-varying regime by faithfully reproducing the respiratory act (inhalation/exhalation of IRPs) and assuming that the infected subject is speaking loudly in the direction of the susceptible subject (which represents the most critical situation). Face-to-face interactions between two subjects (the infected emitter and the susceptible receiver) of the same height, located at a distance of 80 cm, were studied. The susceptible subject was considered as a mouth-breather, thus the IRPs were inhaled through the mouth.

The effectiveness of the personal air cleaner was evaluated by comparing the volume of IRPs inhaled by the susceptible, while the infected is speaking, and expressed as relative reduction among the results obtained from simulations performed with the device turned on and off. In both simulations, the inhalation of IRPs by the receiver through their mouth

was recorded for an exposure time of 900 s. CFD analyses were conducted adopting the boundary conditions available in Table 5.3. The mouths of emitter and receiver were modelled as circular surfaces with a radius of 2 cm [11]. In Figure 5.3, the BC set for the air velocity at the mouths of the emitter and receiver are also illustrated; in particular, a sinusoidal function was adopted at both the emitter and receiver mouths to simulate a real interaction between two subjects [11]. Volumetric flow rates equal to 1 l s^{-1} for speaking and 0.45 l s^{-1} for mouth breathing were imposed as BC [82]. A frequency $f=0.2 \text{ s}^{-1}$ and an amplitude $a=1 \text{ m s}^{-1}$ were selected for the sinusoidal velocity profile applied to the receiver mouth, assuming a temporal range of 5 s for a full breath [11]. For the speaking emitter subject, velocity peaks of 5 m s^{-1} were mounted on the sinusoidal velocity profile [11,82].

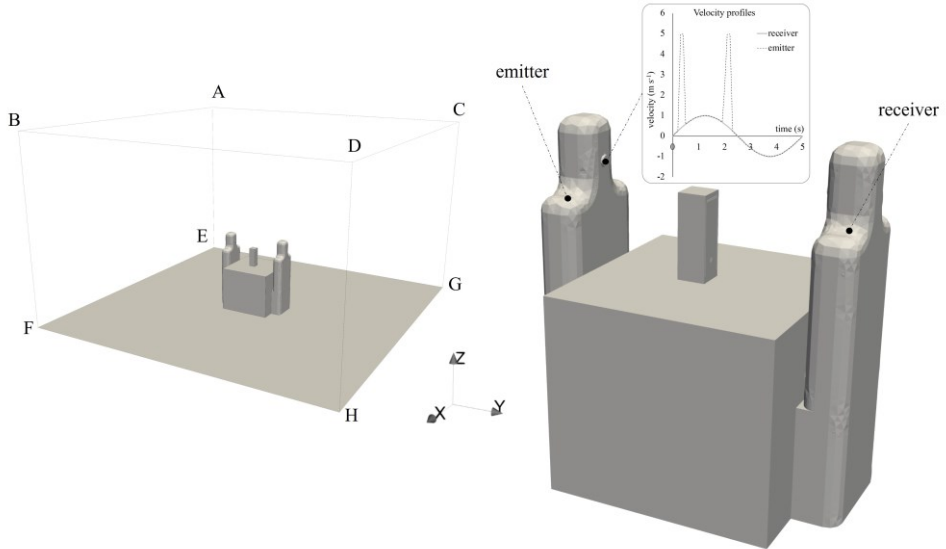


Figure 5.3. Computational domain considered for close proximity simulations: emitter, receiver, air cleaner, and external surfaces are highlighted.

Table 5.3. Boundary conditions adopted for the external surfaces of the computational domain and for the subjects.

Surface	BC for velocity	BC for pressure	BC for temperature
ABEF	$\mathbf{u} = 0$	$\partial p / \partial \mathbf{n} = 0$	$\partial T / \partial \mathbf{n} = 0$
CDGH	$\mathbf{u} = 0$	$\partial p / \partial \mathbf{n} = 0$	$\partial T / \partial \mathbf{n} = 0$
BDFH	$\mathbf{u} = 0$	$\partial p / \partial \mathbf{n} = 0$	$\partial T / \partial \mathbf{n} = 0$
ACEG	$\mathbf{u} = 0$	$\partial p / \partial \mathbf{n} = 0$	$\partial T / \partial \mathbf{n} = 0$
ABCD	$\partial \mathbf{u} / \partial \mathbf{n} = 0$	$p = 101325 \text{ Pa}$	$T = 293.15 \text{ K}$
emitter mouth	see Figure 5.3	$\partial p / \partial \mathbf{n} = 0$	$T = 308.15 \text{ K}$
receiver mouth	$ \mathbf{u} = a \cdot \sin(2\pi ft)$	$\partial p / \partial \mathbf{n} = 0$	$T = 308.15 \text{ K}$

The boundary condition set for the mouth breathing receiver was verified by Cortellessa et al. [11] comparing numerical results with PIV data in terms of velocity profiles obtained at two different distances from the mouth of the emitter. Here four distances are selected for comparison, to provide a more detailed analysis: 10, 15, 20 and 30 cm. This comparison also provided a rough confirmation of the numerical velocity field. Figure 5.4 displays the four validation sections along with the CFD velocity contours obtained within the sagittal plane, by selecting the instant of time for breathing at which the maximum velocity values are reached (peak of the sinusoidal function).

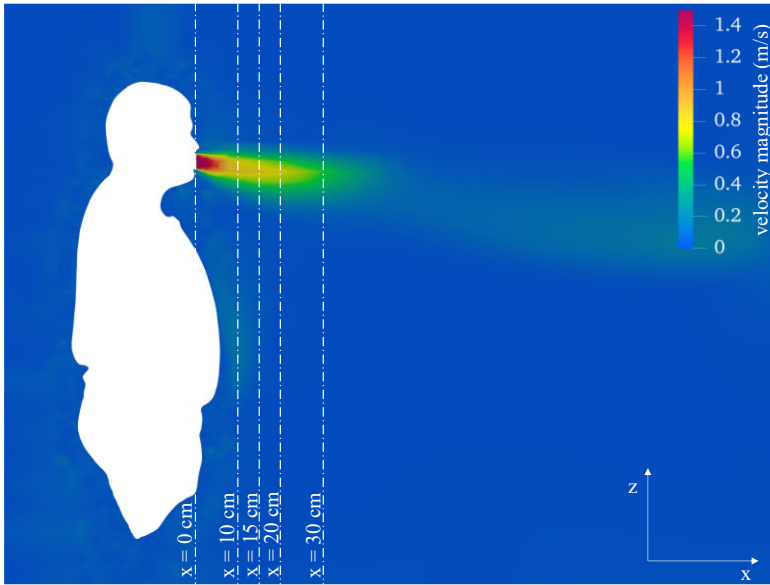


Figure 5.4. CFD velocity contours obtained within the sagittal plane by selecting the instant of time for breathing when the maximum velocity value is reached (peak of the sinusoidal function). The validation sections placed at different distances from the emitter mouth (10, 15, 20 and 30 cm) are also indicated.

Comparison between CFD and PIV vertical velocity profiles is plotted in Figure 5.5: a good agreement was found between the numerical and experimental average and peak velocities, thus validating the numerical solutions obtained through the CFD analyses. The velocity peak of 5 m s^{-1} adopted for the emitter was confirmed as well, by experimental analyses related to the speaking expiratory activity [11].

The IRPs are injected from the emitter's mouth using a conical injection with an angle of 22 deg. This angle, calculated by Abkarian et al. [82], encloses 90% of the IRPs in a cone passing through the mouth exit and was verified to remain stable over time after the initial cycles. The LPT was solved by applying an *escape* boundary condition for IRPs over all the surfaces of the computational domain, including the protection device and the subjects. In that way, the accumulation of viral load in the environment can be avoided. Once again, it is emphasized that in close proximity scenario, the focus of the study is on determining whether the air cleaner can protect the exposed subject from the IRPs directly emitted by the infected subject. Protection from the IRPs accumulated in the indoor environment is investigated separately, as described in Section 5.2.3.

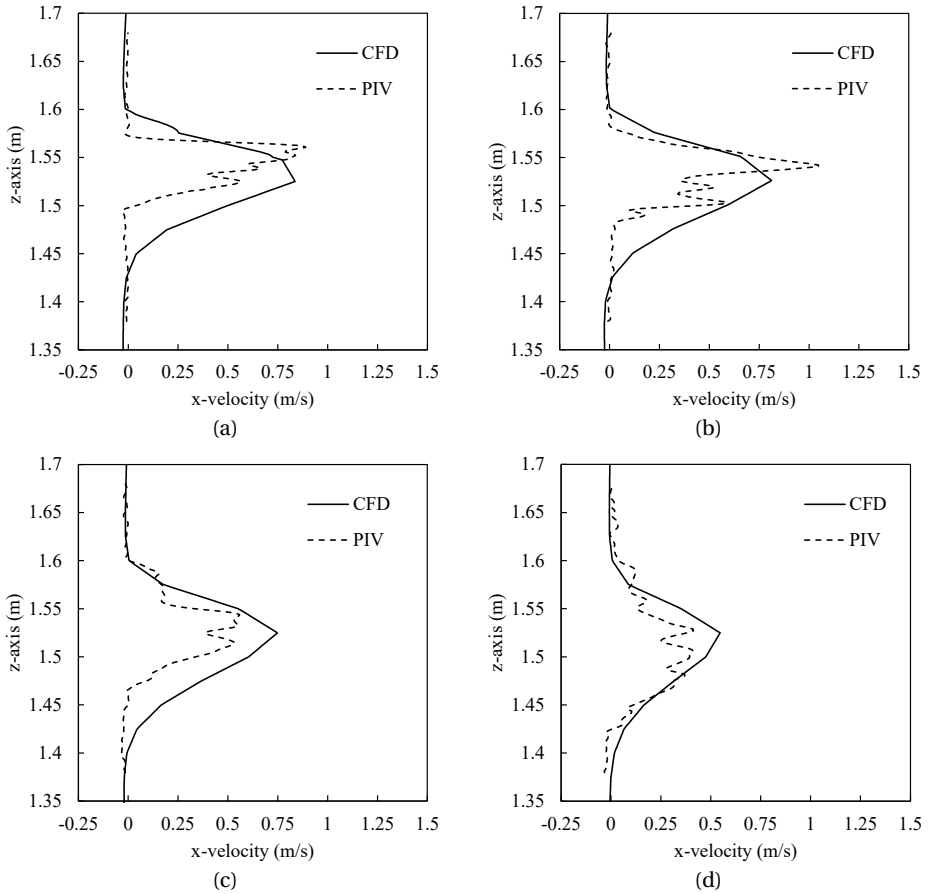


Figure 5.5. Experimental (PIV, dotted lines) and CFD (solid lines) velocity profiles obtained in a sagittal plane at different distances from the emitter's mouth: (a) 0.10 m, (b) 0.15 m, (c) 0.20 m, and (d) 0.30 m.

The computational grids were obtained employing hexahedral-based unstructured elements, by using the opensource *snappyHexMesh* algorithm. Three meshes were tested: Mesh 1 composed of 927,156 elements, Mesh 2 composed of 2,904,623 elements, and Mesh 3 composed of 4,415,668 elements (Figure 5.6). The grids exhibit a maximum non-orthogonality value of about 50 and are refined in correspondence with the solid surfaces, where a boundary layer region is added to better capture the gradients in the viscous region. Spatial and temporal mesh sensitivity analyses were performed to define the optimal grid able to reproduce reliable results for the investigated close proximity scenario. In particular, the spatial sensitivity analysis was performed by selecting the two vertical sections identified in Figure 5.6, located at $y=2.1$ m and $y=2.5$ m along the y - z plane crossing the emitter's mouth at its midpoint along the x -direction. This choice was adopted in order to capture the fluid dynamics phenomena affecting the outgoing air jets from the emitter's mouth and from the outlet surfaces of the personal cleaner. Figure 5.7 shows the comparison of the y -velocity profiles obtained with Mesh 1, 2 and 3 at the two

selected vertical sections ($y=2.1$ m and $y=2.5$ m). The average percent deviation among the velocity fields obtained comparing Mesh 1 and Mesh 2 was equal to 6.5%, while it resulted equal to 2.8% when comparing Mesh 2 and Mesh 3.

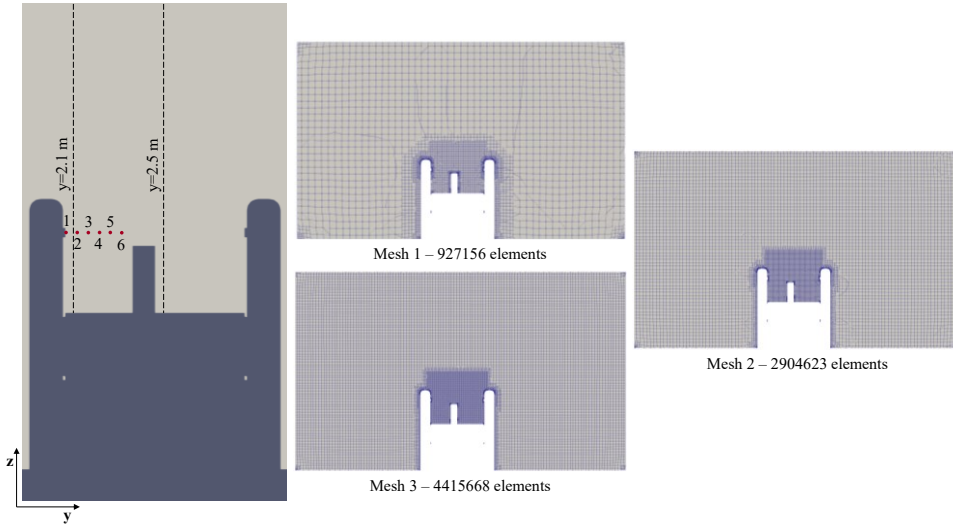


Figure 5.6. Sections and probes selected for the mesh sensitivity analysis (left); computational grids employed to simulate the spread of IRPs in close proximity (right).

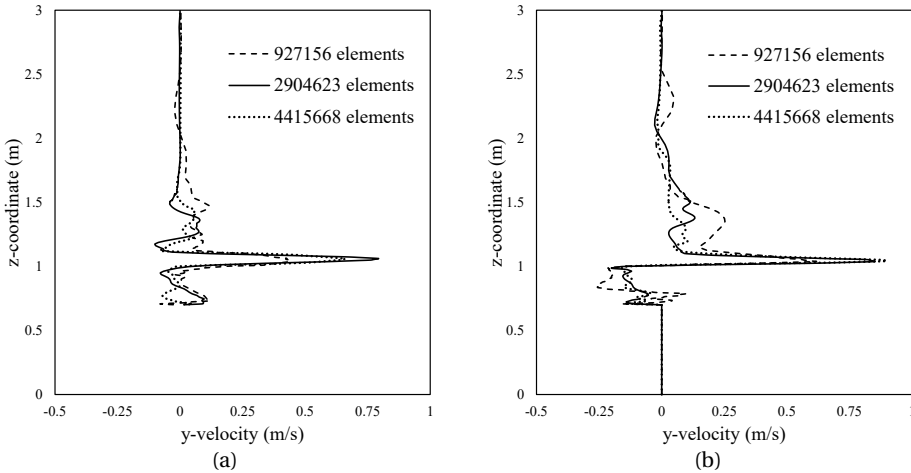


Figure 5.7. y -velocity profiles obtained with Mesh 1, 2 and 3 at two vertical sections located at (a) $y=2.1$ m and (b) $y= 2.5$ m along the y - z plane crossing the emitter’s mouth at its midpoint along the x -direction.

Additionally, a temporal sensitivity analysis was conducted by collecting the y -velocity trends (every 0.1 seconds over a temporal interval of 100 s) at six evenly spaced probes (as indicated in Figure 5.6). These probes were positioned at 5 cm intervals in the y -direction,

starting from the emitting subject's mouth. Table 5.4 summarizes the average y-velocity percent deviations between Mesh 1 and Mesh 2, and between Mesh 2 and Mesh 3, with total averaged deviations of 4.1% and 2.5%, respectively. Since the percent deviations between Mesh 2 and Mesh 3 were lower than 5% for both the sensitivity analyses performed (i.e., spatial and temporal), simulations were carried out adopting Mesh 2.

Table 5.4. Average y-velocity percent deviations between Mesh 1 and Mesh 2, and between Mesh 2 and Mesh 3, calculated for six evenly spaced probes positioned at 5 cm intervals in y-direction starting from the emitting subject's mouth.

Probe number	Probe coordinates (x, y, z)	Average y-velocity percent deviation between Mesh 1 and Mesh 2 (%)	Average y-velocity percent deviation between Mesh 2 and Mesh 3 (%)
1	(2.50, 2.05, 1.06)	4.0	4.0
2	(2.50, 2.10, 1.06)	3.2	1.7
3	(2.50, 2.15, 1.06)	3.1	1.8
4	(2.50, 2.20, 1.06)	3.9	2.1
5	(2.50, 2.25, 1.06)	4.8	2.5
6	(2.50, 2.30, 1.06)	5.6	2.9
Total averaged values (%)		4.1	2.5

5.2.3 PERSONAL AIR CLEANER IN A SHARED INDOOR ENVIRONMENT

The personal air cleaner effectiveness was evaluated, in the case of shared indoor environments, by numerical simulations aimed at investigating the effects of the personal air cleaner on reducing the concentration of IRPs in the breathing area of the air cleaner user during a 2-h lesson delivered by an infected subject (i.e., the teacher). Since the indoor mass transport of IRPs is strongly influenced by natural and mechanical ventilation, great attention was paid to the choice of the indoor environment to be simulated. To this purpose, the university lecture room experimentally and numerically characterised in Chapter 4 was adopted, using the same simulating approach. The spread and distribution of the IRPs within the lecture room during the 2-h lesson was evaluated for the nominal HVAC system operating conditions ($AER=7.5 \text{ h}^{-1}$).

The computational domain is shown in Figure 5.8, where the position of the personal air cleaner is also depicted. The rationale behind this specific placement of the air cleaner will be explained later. The inlet and outlet sections of the computational domain are highlighted in green and red colours in Figure 5.8, while other boundary patches, depicted in transparent grey, are modelled as walls. The teacher's mouth is modelled as a cylinder with a radius of 0.021 m placed at a height of 1.60 m just behind the main desk of the room. A hexahedral-based unstructured grid was employed to simulate the lecture room, as shown in the clipped view in Figure 5.9, realized using the *snappyHexMesh* algorithm. The mesh was generated with the same structure and configuration as in Section 4.3, but with different refinement parameters in the portable personal protection device zone. The mesh used to process the shared environment is composed of 3,351,054 cells (Figure 5.9), with a maximum skewness of 3.42 and a maximum non-orthogonality of 58.3. The selection of this mesh resulted from a sensitivity analysis comparing three grids with

increasing cell numbers; grid independence was achieved with the aforementioned grid (the intermediate one), whose errors were $<5\%$ from the reference. The numerical simulations were conducted in terms of time-averaged velocity fields, following the same approach described in Section 4.3.

The boundary conditions adopted for the different patches of the computational domain considered for the simulation of the lecture room are detailed in Table 5.5. Finally, as concern the boundary conditions of the IRPs, the Lagrangian Particle Tracking was solved by applying an *escape* boundary condition over all the surfaces of the computational domain, except for the entry sections, for which a *rebound* boundary condition was adopted. With such conditions the adhesion of particles to the walls is also modelled, since the particles touching the external surfaces of the domain are assumed to disappear and cannot re-enter the computational domain.

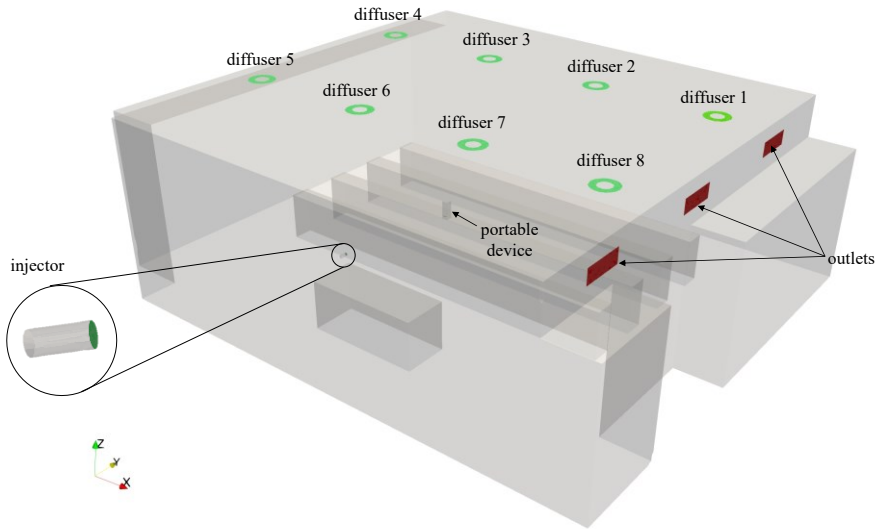


Figure 5.8. 3D model of the lecture room, with patches highlighted, and location of the portable device inside the computational domain.

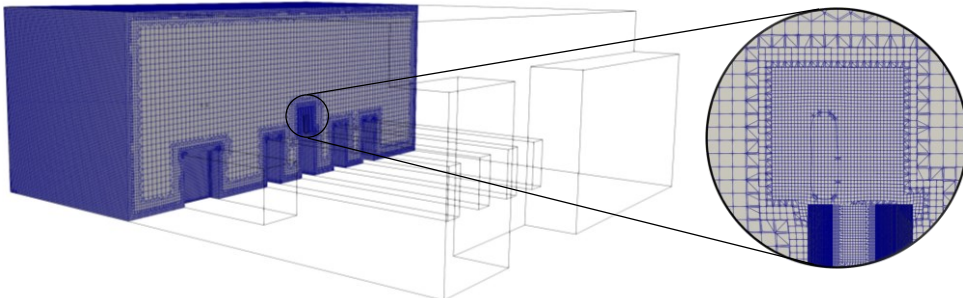


Figure 5.9. Computational grid (composed by 3,351,054 elements) adopted in the numerical analysis of the university lecture room.

Table 5.5. Boundary conditions adopted at the different patches of the computational domain considered for the simulation of the lecture room.

Surface	BC for velocity	BC for pressure	BC for temperature	BC for k	BC for ω	Lagrangian
diffusers	see Table 4.8 (ACH=7.5)	$\partial p / \partial \mathbf{n} = 0$	$T = 293.15 \text{ K}$	$I = 10\%$	$\ell = 0.07 \text{ L}$	<i>rebound</i>
room outlet sections (exhaust grilles)	$\partial \mathbf{u} / \partial \mathbf{n} = 0$	$p = 101325 \text{ Pa}$	$\partial T / \partial \mathbf{n} = 0$	$\partial k / \partial \mathbf{n} = 0$	$\partial \omega / \partial \mathbf{n} = 0$	<i>escape</i>
walls	$\mathbf{u} = 0$	$\partial p / \partial \mathbf{n} = 0$	$\partial T / \partial \mathbf{n} = 0$	standard wall functions		<i>escape</i>
injector	$ \mathbf{u} = 1.11 \text{ m s}^{-1}$	$\partial p / \partial \mathbf{n} = 0$	$T = 308.15 \text{ K}$	$k = 0.1 \text{ m}^2 \text{ s}^{-2}$	$\partial \omega / \partial \mathbf{n} = 0$	<i>rebound</i>
air cleaner jet release sections	see Section 5.2	$\partial p / \partial \mathbf{n} = 0$	$T = 293.15 \text{ K}$	$I = 10\%$	$\ell = 0.07 \text{ L}$	<i>escape</i>

5

The CFD model adopted for the numerical analysis in the shared indoor environment was validated in the preceding chapter by comparing numerical and measured velocities at eight probes placed inside the domain (Figure 4.2): results of the comparison are illustrated in Figure 4.5 and Figure 4.6, where a good agreement between experimental and numerical data is recognizable.

To assess the effectiveness of the personal air cleaner in reducing exposure to IRPs during a 2-h lesson, the IRPs volume concentration in twenty-four boxes (shown in Figure 5.10) was calculated. Each box, measuring $1.00 \text{ m} \times 1.00 \text{ m} \times 0.88 \text{ m}$ (width, height, and depth, respectively), was intended to represent the average IRPs concentration experienced by each student attending the lesson, as they were virtually placed on the students' desks and extend one meter from desk height to analyse the students' breathing areas.

The effectiveness was estimated by comparing the average IRPs volume concentration inside the boxes with and without the air cleaner. Simulations without the air cleaner allowed to identify the box with the highest IRPs volume concentration, as detailed in the results section (5.3.2, Figure 5.14). Subsequently, a simulation with the air cleaner was conducted, positioning it in proximity to the most exposed student/spot previously identified, following the recommended (designed) positioning of about 40 cm from the student.

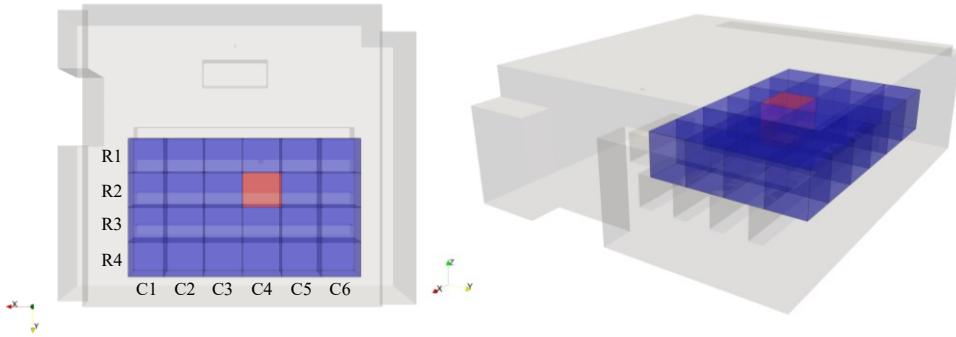


Figure 5.10. Positioning of the twenty-four boxes adopted to estimate the average concentration experienced by the 24 students sitting at their desk during the 2-h lesson in the lecture room. The box characterized by the highest IRPs volume concentration in the simulations without air cleaner is also shown (in red).

5.3 RESULTS

In this section the results obtained from CFD analyses concerning the effectiveness of the personal air cleaner are illustrated and discussed both for the close proximity scenario, described in Section 5.2.2, and for the shared indoor environment, described in Section 5.2.3.

5.3.1 EFFECTIVENESS OF THE AIR CLEANER IN A CLOSE PROXIMITY SCENARIO

The effectiveness of the air cleaner in a close proximity scenario was evaluated comparing the results (in terms of volume of IRPs inhaled by the receiver) obtained from the simulations performed with and without air cleaner for an exposure time of 900 s. The distance between the two subjects sitting at the same table was chosen equal to 80 cm and the air cleaner (when adopted) was placed at the recommended distance of 40 cm from the receiver.

As an illustrative example of the IRPs trajectories and flow fields obtained from the simulations, in Figure 5.11 the velocity streamlines (obtained from the output surfaces of the personal air cleaner) and the IRPs distribution for a breathing period of 5 s (at computational times of 5, 5.5, 6.5, 7.5, 8.5, and 10 s) are shown when the personal purifier is turned on. The figure clearly shows how the high-velocity air flows (both from side and upper sections) provided by the device create a protection zone around the receiving mouth preventing the inhalation of IRPs. In fact, IRPs are deflected upwards and consequently they are removed from the susceptible breathing area. In addition, the low velocity air jet, coming out of the device, ensures the presence of clean air in the breathing zone increasing the level of individual protection. Indeed, IRPs reaching the device protection streams are spread while rising in a vertical direction due to the effect of buoyancy forces. The air flow rate produced by the emitter speaking activity can occasionally produce (at certain time steps) a slight deflection of the high-velocity air flow rates of the air cleaner then leading to slight, but negligible, variations in the protection efficiency of the air cleaner. In Figure 5.12, the volumes of IRPs inhaled by the receiver as a function of time, in both cases of the device being turned off and on, during the 900 s

exposure time are plotted as well as the resulting personal air cleaner effectiveness. The effectiveness is expressed as the relative reduction in the volume of IRPs inhaled by the receiver, evaluated as the percent reduction between the volumes inhaled with the device turned on and off, respectively. The trends show that the device effectiveness is extremely high as the relative reduction of the volume of IRPs inhaled by the receiver is always >92%, with an average reduction during the 900 s exposure scenario equal to 96%.

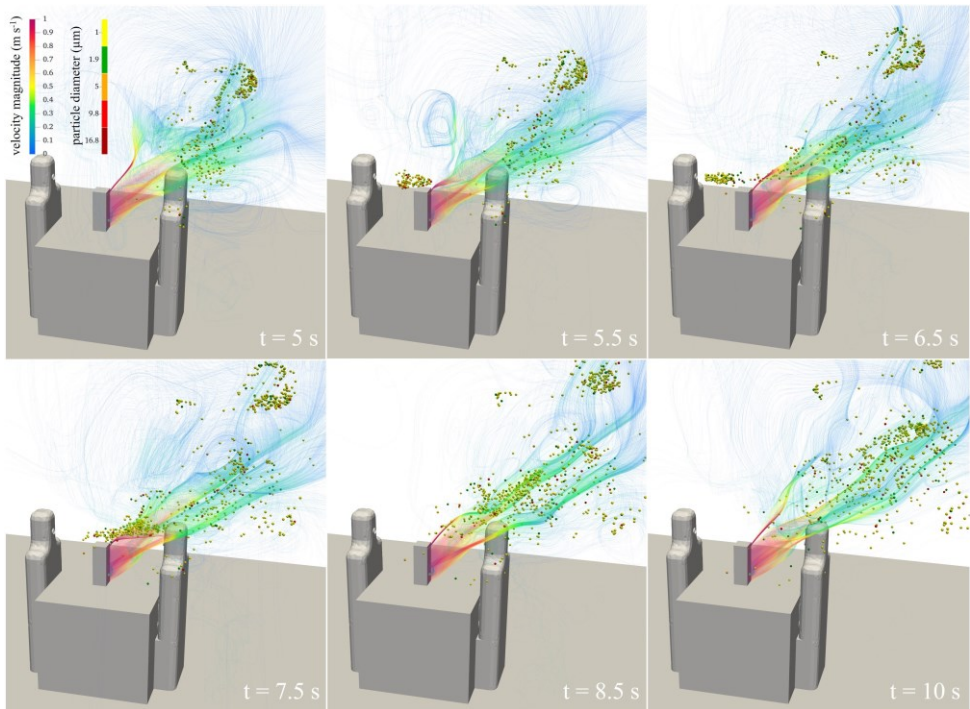


Figure 5.11. Numerical velocity streamlines and IRPs dispersion during a single breath of the emitter subject in the close proximity scenario, obtained from simulations with the portable air cleaner turned on: six selected computational times (5, 5.5, 6.5, 7.5, 8.5, and 10 s) are shown.

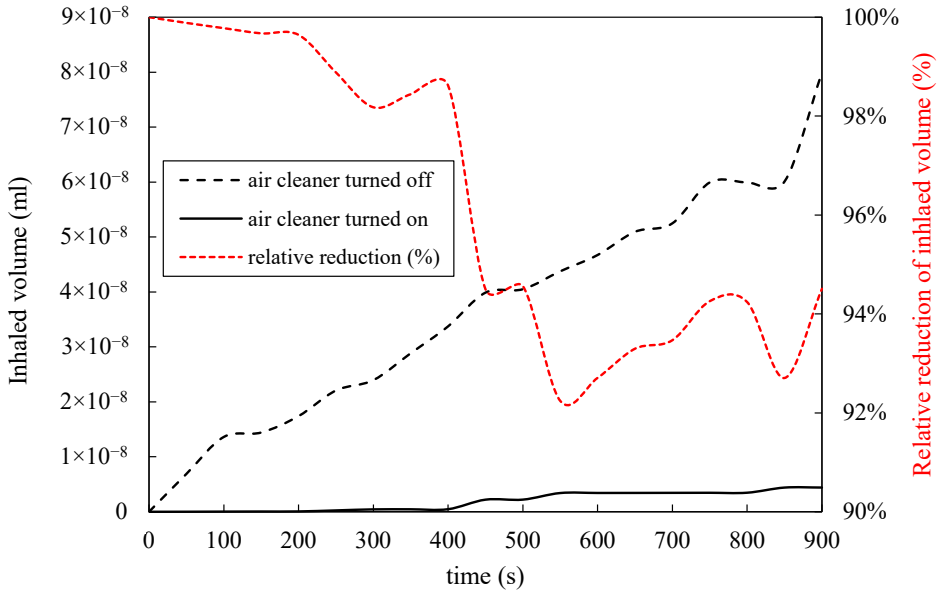


Figure 5.12. Volume of IRPs (ml) inhaled from the receiver subject in the case of personal air cleaner turned off and on during the 900 s close proximity exposure scenario; personal air cleaner effectiveness as a function of time (expressed as the relative reduction of the volume of IRPs inhaled) is also reported.

5.3.2 EFFECTIVENESS OF THE AIR CLEANER IN SHARED INDOOR ENVIRONMENTS

The effectiveness of the air cleaner in the shared indoor environment was assessed by comparing the results obtained from simulations performed with and without air cleaner for a 2-h lesson. The assessment focused on the volume concentration of IRPs inside virtual boxes representing the seats of the students (as identified in Section 5.2.3) while the teacher (i.e., the infected subject) spoke throughout the entire lesson. The air cleaner, when considered, was positioned at the recommended distance of 40 cm from the receiver. Specifically, it was placed inside the box characterized by the highest concentration observed in the simulation without the air cleaner. Figure 5.13 displays the spatial distribution of IRPs in the lecture room as obtained from simulations conducted without and with the air cleaner. In the figure, the box used to compare the IRPs concentrations is highlighted in red, clearly indicating the lower concentration resulting from the simulation with the air cleaner turned on. Anyway, the presence of the portable personal protection device changes radically the motion of the IRPs inside the domain, especially in the working area and ahead of the protection zone. Indeed, the velocity field induced by the personal air cleaner reduces the concentration in the breathing volume of the student using it; meanwhile, IRPs are conveyed by the air cleaner, leading to an increase in concentration in the boxes ahead. This phenomenon is clearly detectable in Figure 5.14 and in Table 5.6. The box characterized by the highest concentration in the scenario without air cleaner is R2C4 (with a volume concentration of $4.07 \times 10^{-7} \text{ ml m}^{-3}$); when the air cleaner is adopted, the concentration in that box is roughly halved ($2.08 \times 10^{-7} \text{ ml m}^{-3}$). The concentrations in the adjacent boxes (R2C3 and R2C5) also

decrease (by roughly 30-35%) when the air cleaner is adopted. However, as mentioned earlier, in the boxes just ahead of the critical one, there is a significant increase in concentration (reaching up to six times the original value) due to the IRPs transport phenomena caused by the air cleaner itself, which draws in and conveys IRPs to the boxes R1C3 and R1C4. Thus, if only one air cleaner is used, the concentration of IRPs experienced by other students can be negatively affected by the presence of the personal air cleaner.

The proposed personal air cleaner may represent a useful solution for indoor spaces where users have a nearly fixed position. Therefore, a personal air cleaner should be installed at each student's spot to protect them and prevent possible increases in IRPs concentration in the breathing zones of adjacent students. The use of multiple air cleaners in the room is not expected to result in negative interactions among them, as, at distances characterizing students' spots, the terminal velocities of the flow exiting the air cleaners are negligible (as shown in Figure 5.11). Nonetheless, it is important to emphasize that the primary objective of this study was to demonstrate that the proposed air cleaner can protect exposed individuals even in shared environments, and indeed, this objective has been achieved. Further studies on real-world applications involving the simultaneous use of multiple air cleaners will be conducted in the future.

5

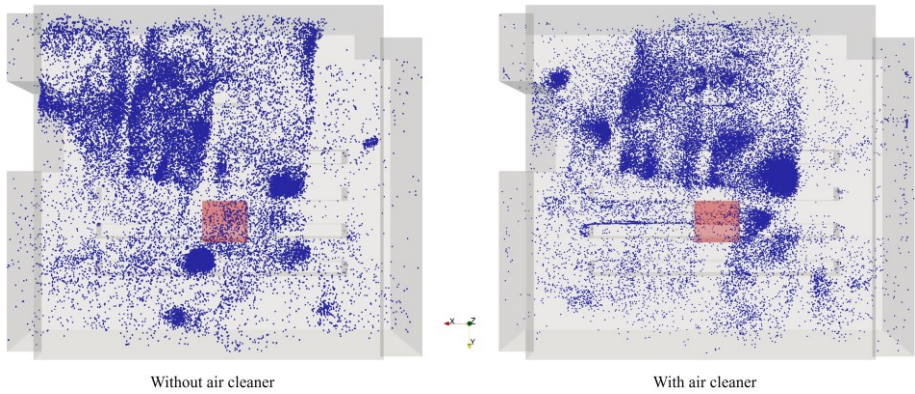


Figure 5.13. Top view of the spatial distribution of IRPs in the lecture room without (left) and with (right) personal air cleaner.

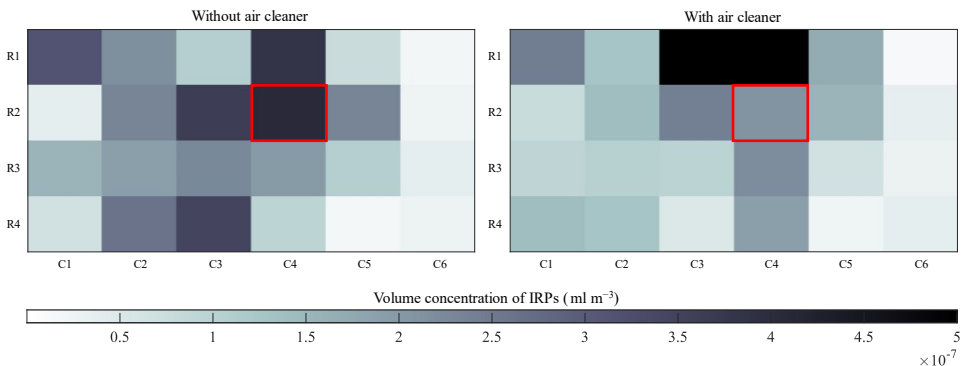


Figure 5.14. Colormaps of the volume concentration of IRPs (ml m^{-3}) inside the 24 boxes, without (left) and with (right) air cleaner.

Table 5.6. Volume concentrations of IRPs in each of the 24 boxes (ml m^{-3}), with and without air cleaner. Concentrations here reported represent the average concentrations during the 2-h exposure period.

Box	Volume concentration of IRPs in each box (ml m^{-3})	
	Without air cleaner	With air cleaner
R1C1	3.16×10^{-7}	2.45×10^{-7}
R1C2	2.16×10^{-7}	1.29×10^{-7}
R1C3	1.07×10^{-7}	6.63×10^{-7}
R1C4	3.82×10^{-7}	6.26×10^{-7}
R1C5	0.76×10^{-7}	1.70×10^{-7}
R1C6	0.21×10^{-7}	0.13×10^{-7}
R2C1	0.39×10^{-7}	0.79×10^{-7}
R2C2	2.32×10^{-7}	1.42×10^{-7}
R2C3	3.63×10^{-7}	2.41×10^{-7}
R2C4	4.07×10^{-7}	2.08×10^{-7}
R2C5	2.32×10^{-7}	1.55×10^{-7}
R2C6	0.24×10^{-7}	0.36×10^{-7}
R3C1	1.54×10^{-7}	0.93×10^{-7}
R3C2	1.90×10^{-7}	1.03×10^{-7}
R3C3	2.25×10^{-7}	0.99×10^{-7}
R3C4	1.95×10^{-7}	2.20×10^{-7}
R3C5	1.07×10^{-7}	0.68×10^{-7}
R3C6	0.38×10^{-7}	0.28×10^{-7}
R4C1	0.67×10^{-7}	1.42×10^{-7}
R4C2	2.61×10^{-7}	1.28×10^{-7}
R4C3	3.47×10^{-7}	0.52×10^{-7}
R4C4	0.97×10^{-7}	1.91×10^{-7}
R4C5	0.19×10^{-7}	0.23×10^{-7}
R4C6	0.27×10^{-7}	0.38×10^{-7}

The use of twenty-four $1.00 \text{ m} \times 1.00 \text{ m} \times 0.88 \text{ m}$ virtual boxes proved to be extremely useful in identifying the student/spot characterized by the highest exposure to IRPs volume concentration; nonetheless, the size of these boxes is significantly larger than the breathing zone of the students and, consequently, larger than the protected zone provided by the air cleaner. In other words, the effectiveness of the air cleaner evaluated with this box size could be extremely underestimated, as it should be determined just considering the actual breathing zone of the student. To address this, a smaller $0.20 \text{ m} \times 0.20 \text{ m} \times 0.20 \text{ m}$ box (referred to as the “reduced box”) located within the device’s airflow outlets was also considered to properly compare the volume concentrations with and without air cleaner. The initial and reduced box size and positioning are highlighted in Figure 5.15, whereas the volume concentrations of IRPs and the corresponding relative reductions

obtained with the two boxes are reported in Table 5.7. When the proper (i.e., the reduced) box is considered, the relative reduction of the student's exposure results equal to 99.5%, indicating that the personal air cleaner can significantly protect the susceptible not only in close proximity scenarios but also in shared indoor environments. Thus, the adoption of a personalized air cleaner could be an interesting solution to support the general ventilation in managing the airborne transmission of respiratory pathogens in shared indoor environments. It is important to emphasize that these findings apply beyond the specific indoor environment considered. They can be generalized to almost all indoor spaces where users have a nearly fixed position: indeed, the protection of the air cleaner can be undermined only if high velocity currents of air are present (e.g., draughts). This is not the case of properly designed HVAC systems, whose terminal velocity at head height, for thermal comfort reasons, is expected to be $<0.5 \text{ m s}^{-1}$.

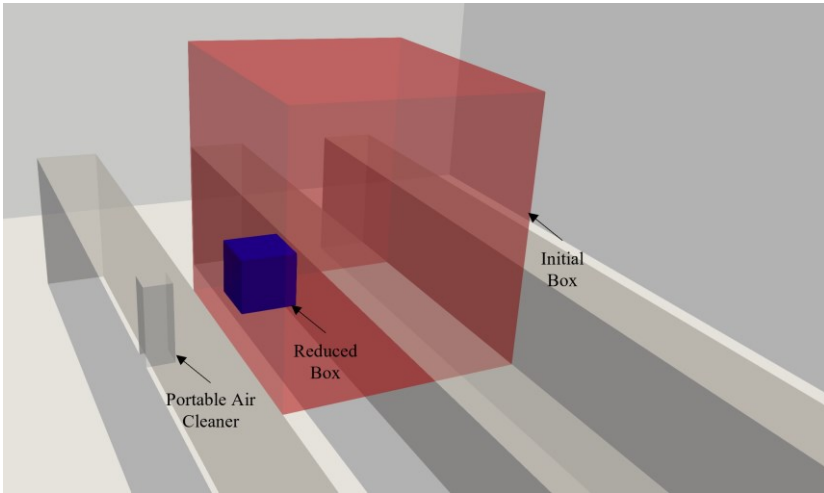


Figure 5.15. Standard and reduced volume applied to the investigation of the personal air cleaner performances.

Table 5.7. Volume concentrations of IRPs (and corresponding relative reductions) obtained from simulations with and without air cleaner, considering both the initial and the reduced box.

Box	Volume concentration of IRPs (ml m^{-3})		Relative reduction of volume concentration
	Without device	With device	
initial box (1.00 m \times 1.00 m \times 0.88 m)	4.07×10^{-7}	2.08×10^{-7}	49.1%
reduced box (0.20 m \times 0.20 m \times 0.20 m)	1.25×10^{-6}	5.95×10^{-9}	99.5%

5.4 CONCLUSIONS

The present chapter evaluated the effectiveness of a newly designed patented portable personal air cleaner in reducing the airborne transmission of respiratory pathogens, including respiratory viruses such as SARS-CoV-2, in two typical exposure scenarios: in

close proximity and in a shared indoor environment. The effectiveness of the portable air cleaner device was investigated by using complex 3D CFD numerical simulations, validated through experimental measurements. The air cleaner under investigation was conceived as a portable battery-operated device and was designed with proper air flow rate velocities and angles able to create a sophisticated fluid-dynamic shield capable of protecting a susceptible from airborne and respiratory particles.

Close proximity simulations were performed considering a typical face-to-face configuration between emitter and receiver, whereas indoor environment simulations were performed considering a university lecture room previously experimentally and numerically characterized in terms of air flows.

Results of the CFD analyses demonstrated that in close proximity scenario the air cleaner was able to reduce, on average, the volume of infectious respiratory particles inhaled by the exposed subject, during a 900 s conversation, by 96% (with instantaneous reductions always >92%).

Results of the simulations performed in the shared indoor environment revealed an average relative reduction of the volume concentration of infectious respiratory particles in the breathing zone of an exposed subject, during a 2-h lesson, equal to 99.5%.

Summarizing, the proposed personal air cleaner is able to provide a significant protection for exposed subjects both in close proximity and in shared indoor environments, then leading to a reduced airborne transmission of respiratory pathogens. This is the reason why future developments of the study will be focused on the prototyping of the air cleaner and on the consequent in-field experimental evaluation of the device performances.

II

INDOOR ENVIRONMENTAL QUALITY: BENCHMARK FOR CFD VALIDATION

6

EXPERIMENTAL CHARACTERISATION OF VENTILATION FLOW IN A REAL CAR CABIN: A BENCHMARK CASE

This chapter presents an experimental investigation of the airflows inside the cabin of a commercially available car aimed at producing a benchmark case for the validation of numerical simulations. The analyses were carried out by operating the front ventilation mode at the four fan flow rates available, with fresh air intake (i.e., without air re-circulation). Firstly, the flow velocity at the exit of the vents was characterised by means of 5-hole pressure probe measurements. Then, the flow velocity fields were measured by Particle Image Velocimetry in three longitudinal sections inside the car cabin, consisting of the car centre longitudinal plane, the driver's seat longitudinal plane, and the passenger's seat longitudinal plane. Although the results focus on the flow field measured at fan speed 3 out of 4, comparisons at specific locations are carried out with the flow fields achieved with the other fan speeds. The time-averaged air velocity is presented and discussed, showing the position of the jet issued by the centre vents and the velocity decay along the jet core. Additionally, the velocity fluctuations are analysed in terms of quadrant analysis, Reynolds stresses and turbulent kinetic energy at the three measured longitudinal planes. Moreover, a detailed uncertainty analysis of the experimental results is presented using the correlation statistics method and linear error propagation. The study provides new insights into the ventilation flow in a car cabin and proposes a new benchmark case for the validation of numerical simulations of energy and mass transport within a car cabin indoor micro-environment.

This chapter is based on the following manuscript (submitted):

Bertone M., Arpino F., Cortellessa G., Grossi G. and Sciacchitano A. (2024). Experimental characterisation of ventilation flow in a real car cabin: a benchmark case.

Keywords: Particle Image Velocimetry (PIV); 5-hole pressure probe; car cabin benchmark; uncertainty analysis; ventilation; indoor environment

6.1 INTRODUCTION

A car cabin is an indoor micro-environment where people spend considerable time, whether for daily commuting or long-distance travel [161,162]. Ensuring the comfort and safety of passengers in this indoor micro-environment requires careful consideration of thermal comfort and air quality [163,164]. To this aim, it is crucial to obtain accurate information regarding the car cabin environment, particularly in terms of ventilation and air velocity distribution [165].

Computational Fluid Dynamics and experimental methods have been widely used in the scientific literature to study the ventilation flow within a car cabin [165,166,75,167–170,80,171–173]. Although CFD can provide useful insights into the car cabin fluid dynamics [174], the obtained results significantly depend on several factors; these include the definition of the computational domain and the boundary conditions, such as vent position and shape, fan strength, cabin geometry and size, alongside with the turbulence models employed (see Chapter 3). Consequently, the availability of measurement data and related uncertainty, useful for boundary conditions definition and numerical results validation, is crucial to ensure numerical investigation reliability [175]. From the experimental perspective, methodologies such as hot-wire anemometry, smoke visualisation and Particle Image Velocimetry have been employed to investigate airflow patterns and velocity distributions. Each method offers valuable insights but comes with certain limitations. For instance, hot-wire anemometry is an intrusive measurement technique and does not allow to measure flow recirculations; being it a pointwise measurement technique, it requires extensive scanning of the domain to achieve measurements in a plane or a volume. Consequently, its application has been mainly restricted to the study of specific aspects of ventilation outlets or HVAC ventilation [171–173]. On the other hand, smoke visualization yields only qualitative data. Ležovič et al. [176], for instance, utilised the latter method to investigate the direction of the airflow outgoing from the vents, revealing that the actual direction of the outflow deviated from the direction of the guiding vanes in the outlet. In contrast, being a non-intrusive measurement technique that provides quantitative flow visualizations, PIV has been identified as a suitable technique for the quantitative characterisation of the airflow distribution within car cabins [170], thus allowing for the validation of numerical simulations by CFD. However, because the optical access to illumination and imaging systems in a car cabin can be limited, in the past, researchers have often used scale-down or simplified car models that, on the one hand, provide high control of the model's geometry and boundary conditions, but, on the other hand, may not accurately represent the real conditions encountered in a car cabin. Moreover, most of the existing studies do not provide relevant information that is essential to the validation of numerical models. Lee and Yoon [165] visualised the airflow and measured the temperature fields inside a 1/10 scale model of a passenger compartment. Lee et al. [167] replaced the roof and the door passenger's seat with tempered glass to perform PIV in longitudinal planes. Similarly, Huera-Huarte et al. [169] removed the two right side doors of the car, which were replaced by two acrylic sheets to carry out PIV measurements in longitudinal and horizontal planes. Yang et al. [75] performed PIV measurements to characterise the airflow inside a car cabin using a scaled model made of acrylic material and a HVAC device to simulate ventilation

conditions. Finally, Ullrich et al. [80] performed PIV measurements in a car removing the HVAC filter to validate a CFD tool; despite the modification made to the cabin is minimal, little information is available concerning the geometry and the boundary conditions, making it unsuitable as a benchmark.

To address the limitations of existing studies, the present chapter provides a comprehensive and exhaustive benchmark for the characterisation of the fluid dynamics fields inside a real car cabin, intended for validating CFD numerical simulations.

The work first characterises the airflow velocity at the outlet of the vents by means of a 5-hole pressure probe; then, PIV measurements are performed to investigate the flow fields inside the car cabin. Through the performed analyses, the time-averaged flow velocity, Reynolds stresses, turbulent kinetic energy (TKE) profiles, and the associated uncertainty of each quantity are presented and discussed. The discussion focuses on the flow field measurements obtained at fan strength 3, out of the 4 levels available, and includes a comparative analysis of the profile quantities (i.e., on time-averaged flow velocity, Reynolds stresses, turbulent kinetic energy) at specific locations, obtained under the other fan strengths. The complete flow field data for all fan speeds are provided in Appendix B. Furthermore, this study offers a comprehensive uncertainty analysis of the experimental results using the correlation statistics method and linear error propagation.

6.2 METHODOLOGY

The experiments were carried out in the Aerodynamics Laboratories of Delft University of Technology using a commercial car, a Peugeot 206. The front ventilation mode was tested using fresh air intake (without re-circulation) and for all four fan velocities available from the on-board regulation panel. In Figure 6.1, the left picture shows the vents enabled during the experiments (representing the front ventilation mode). On the right, the position of the axis system selected as reference for PIV measurements is indicated.



Figure 6.1. The experimental facility. Left: picture of the car dashboard, with the front vents highlighted; right: position of the axis system selected as reference for PIV measurements.

To ensure repeatability, the grille of the vents was fixed in a neutral position using clips, in accordance with previous studies of Adhikari et al. [166] and Piovano et al. [177], which demonstrated that an accurate fixing position of the grille is decisive for the data repeatability during the experiments. In the Peugeot 206 used for the experiment, the vent grilles are equipped with two degrees of freedom, allowing adjustments by means of rotations around both vertical and horizontal axes. To respect the neutral position, the orientation of the vertical grilles was set to ensure airflow exits in the vehicle's longitudinal

direction, resulting in a flow perpendicular to the dashboard. Simultaneously, the horizontal grilles were positioned at an angle that aligned the grille with the dashboard's geometry. No modifications were made to the interior parts of the car cabin, including the seats, side doors, ceiling, and floor. However, reflective surfaces inside the cabin were covered with non-reflecting material (matte black foil) to avoid unwanted laser light reflections.

The flow velocity at the exit of each vent was individually measured using a 5-hole pressure probe, which allowed the definition of the inlet airflow (boundary conditions), while the airflow in the car cabin was studied using the planar PIV technique. In this regard, since the air velocity component in the z (transversal) direction is relatively weak compared to the x (longitudinal) and y (vertical) components [178], the planar PIV method was used.

Additionally, a preliminary investigation was conducted to identify the sections where the air flows out of the car when windows and doors are closed. To this aim, water-glycol droplets of 1 μm median diameter, produced by a SAFEX seeding generator, were introduced into the ventilation system; the resulting flow patterns were observed by visual inspections. This preliminary investigation revealed that, although the vehicle was not hermetic, most of the air exited from the rear area of the passenger compartment near the parcel shelf, which is consistent with the findings of Ullrich et al. [80].

6.2.1 AIRFLOW MEASUREMENTS AT THE VENTS OUTLET

6

A multi-hole pressure probe, the ProCap Compact 5-hole digital probe by Streamwise, was used to measure the airflow velocity at the exit of the vents. The 5-hole probe allowed a 3D measurement of the airflow, measuring velocity, yaw angle and pitch angle based on the pressure differences between the holes on the tip of the probe. The probe is equipped with five differential pressure sensors for the probe tip and one barometric pressure sensor, which is used as a reference pressure for the differential pressure sensors. The pressure sensors have a maximum range of 160 Pa and an estimated accuracy within 0.5% of the full-scale value, allowing air velocity measurements within the range of 1.1–16 m s^{-1} . Additionally, the ProCap Compact is equipped with a motion capture system with three cameras for identifying the exact location of the 5-hole probe with respect to the airflow. A detailed description of the 5-hole probe is available in Refs. [179–181], which the interested reader is referred to. Figure 6.2 shows a schematic of the multi-hole pressure probe (left picture), the actual configuration used for the 5-hole pressure probe (middle picture) and the motion capture system, composed of three cameras, employed to detect the location and orientation of the probe (right picture).

A control volume was defined for each vent. The measurements were carried out with an acquisition frequency of 60 Hz, with a sampling of 20 minutes for each vent. In post-processing, velocity fields were taken on surfaces positioned approximately 1 cm away from the vents. The normal vector of these surfaces, represented as \mathbf{n} in Figure 6.3, lies in the xy plane and is inclined to the y -axis by an angle $\alpha=73$ deg for central vents and $\alpha=60$ deg for lateral vents. The different angles for central and lateral vents are attributed to the specific layout of the Peugeot 206 dashboard.

The uncertainty of the velocity measurement of the 5-hole probe is lower than 0.1 m s^{-1} , as provided by the manufacturer [182].



Figure 6.2. left: ProCap digital multi-hole flow probe and coordinate system convention [183]; middle: actual configuration used of the 5-hole pressure probe; right: actual configuration used of the Trio motion capture system.

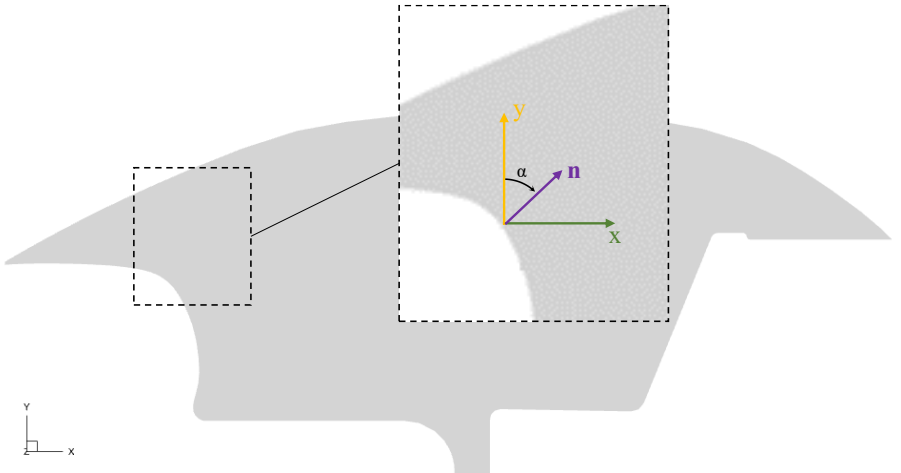


Figure 6.3. Side view, indicating the orientation of the vector \mathbf{n} with respect to the PIV reference system.

6.2.2 PIV EXPERIMENTAL SETUP

Planar PIV measurements at three longitudinal sections were performed: (i) car's centre plane ($z=-0.03$ m), including both the front and rear areas (Figure 6.4, top), referred in the following to as *Measuring Plane 1* (MP1); (ii) driver's seat centre plane ($z=-0.32$ m), only at the front area (Figure 6.4, middle), referred in the following to as *Measuring Plane 2* (MP2); (iii) front passenger's seat centre plane ($z=0.36$ m), only at the front area (Figure 6.4 bottom), referred in the following to as *Measuring Plane 3* (MP3).

Each of these three different setups required specific positioning of the cameras, the laser head and the system calibration. Experiments were conducted in the backyard of the Aerodynamics Laboratories of the Delft University of Technology.

To protect the equipment (seeding generator, laser, cameras, and computer) in case of rain and to confine the laser light, the car and the equipment were placed inside a tent sized $3\text{ m} \times 2.6\text{ m} \times 6\text{ m}$ (width, height and length, respectively). Temperature (T_{out} , °C) and humidity of the environment inside the tent (i.e., outside the car) were measured during all tests, as well as the internal temperature of the cabin (T_{in} , °C). For the latter, a thermocouple was positioned within the vehicle; conversely, the external environmental conditions (i.e., inside the tent) were monitored using an Alecto Weather Station 1500, which ensured a resolution uncertainty of 0.1 K for temperature and 1% for relative humidity. The main characteristic of the employed equipment and information about temperature and humidity during experiments are summarised in Table 6.1.

The seeding was generated using a SAFEX seeding generator placed inside the car cabin, which produces water-glycol droplets of $1\ \mu\text{m}$ median diameter. Particles were illuminated by a dual-cavity Evergreen Laser (Nd:YAG, pulse energy of 200 mJ at 15 Hz, wavelength of 532 nm) and images were taken employing three LaVision sCMOS cameras ($6.5\ \mu\text{m}$ pixel size, 2560×2160 pixels maximum resolution, 16 bit). Depending on the measured section (see Figure 6.4), three, two or one cameras were used. The cameras were equipped with a Nikon objective of 35 mm and 50 mm focal length. The optical aperture (or $f\#$) was set to 4 or 5.6, depending on the camera (see Table 6.1 for further details); these $f\#$ values were selected to ensure a particle image diameter exceeding 1 pixel to avoid peak-locking [124,184]. For the setup used for MP1 (Figure 6.4, top) and MP3 (Figure 6.4, bottom), cameras 1 and 2 were positioned to ensure the overlapping of their fields of view (FOVs), preventing any gaps in the recorded measurement data (see Section 6.3.2). In the overlapping areas, the arithmetic average of the velocities measured by the two cameras was taken. The focal length, optical aperture, field of view and optical magnification factor used in the experiments are summarised in Table 6.1.

The image acquisition was conducted at a frequency of 15 Hz, except for the acquisition at the setup used for MP1 (Figure 6.4, top) with three cameras, in which camera 3 was set at a frequency of 5 Hz. The time intervals between two consecutive particle images varied between 1 and 8 ms, depending on the camera used.

Table 6.1 provides a summary of the main experimental parameters used in each configuration for fan strength 3. Additional details on the experimental parameters used for the other fan strengths can be found in Appendix B. The data sets consist of 500 double-frame images acquired for each experimental condition. The image processing was conducted with the LaVision Davis 8.6 software, using Gaussian interrogation windows of 128×128 pixels with 75% overlap for the initial passes and 32×32 pixels with 75% overlap for the final passes. The resulting instantaneous velocity fields were ensemble-averaged to obtain the spatial distribution of the time-averaged velocity.

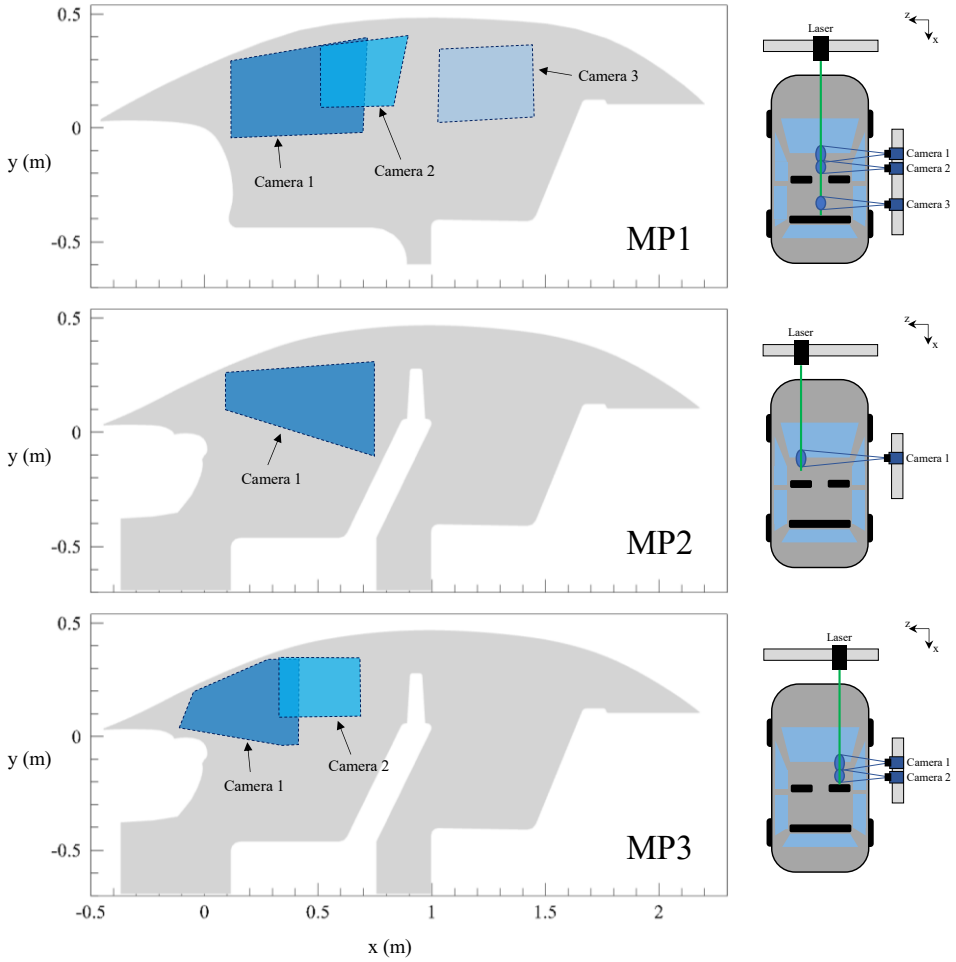


Figure 6.4. FOV covered by the cameras (left) and PIV setup (right). Top: car's centre plane (MP1); middle: driver's centre plane (MP2); bottom: front passenger's seat centre plane (MP3).

Table 6.1. Summary of parameters adopted during the acquisition for fan strength 3.

Camera	f#	Lens objective (mm)	Field of view (mm ²)	Magnification factor	Frequency (Hz)	Δt (ms)	T_{out} (°C)	T_{in} (°C)	Humidity (%)
1	5.6	35	653 × 545	0.025	15	1	30.2	43.6	28
MP1	4	50	454 × 382	0.037	15	1	30.2	43.6	28
3	4.6	35	472 × 397	0.035	5	2	28.4	37.8	25
MP2	1	5.6	35	813 × 688	0.02	8	27.0	39.0	30
1	5.6	35	524 × 437	0.032	15	5	29.1	39.5	33
MP3	2	4	50	351 × 297	0.047	1.7	29.2	39.8	33

PIV DATA UNCERTAINTY QUANTIFICATION

Following Coleman and Steele [185], the combined standard uncertainty is calculated as the square root of the sum of the squares of systematic and random uncertainties:

$$u_r = \sqrt{u_B^2 + u_A^2} \quad (6.1)$$

where u_B is the systematic (bias) uncertainty and u_A is the random standard uncertainty. The systematic uncertainty could arise from peak-locking [184], evaluation of the image magnification and modulation effects due to the limited spatial resolution [186]. However, these were found to be minimal. Peak-locking is negligible since the imaging system parameters (magnification factor and $f\#$) were selected to produce a particle image diameter greater than 1 pixel [124]. Furthermore, the image magnification introduces an uncertainty of 0.1%, which is neglected. Lastly, the uncertainty associated with the spatial modulation is around 1%, thus can be neglected. The random uncertainties of the airflow quantities measured by PIV (i.e., time-averaged velocity, Reynolds stresses and turbulent kinetic energy) have been quantified following Sciacchitano and Wieneke [187].

The expanded random uncertainty of the time-averaged velocity component \bar{u} is expressed as (a similar equation applies to the component \bar{v}):

$$U_{\bar{u}} = \frac{k_c \cdot s_u}{\sqrt{N}} \quad (6.2)$$

where k_c is the coverage factor, s_u is the sample standard deviation of the velocity component u , and N is the number of statistically uncorrelated samples. A coverage factor $k_c = 1.96$ is selected for a confidence level of 95%, assuming a Gaussian distribution of the PIV measurement errors [188].

For the Reynolds normal stresses \mathcal{R}_{xx} , the random uncertainty is quantified following Sciacchitano and Wieneke [187] (a similar equation applies for \mathcal{R}_{yy}):

$$U_{\mathcal{R}_{xx}} = k_c \left(\mathcal{R}_{xx} \sqrt{\frac{2}{N} + \bar{U}_u^2} \right) \quad (6.3)$$

where \bar{U}_u^2 is the mean square of the instantaneous velocity uncertainty, evaluated via the correlation statistics method [189].

For the Reynolds shear stresses \mathcal{R}_{xy} , the random uncertainty is also quantified following Sciacchitano and Wieneke [187]:

$$U_{\mathcal{R}_{xy}} = \sqrt{\mathcal{R}_{xx}\mathcal{R}_{yy} \left(\frac{1 + \rho_{xy}^2}{N - 1} \right)} \quad (6.4)$$

where ρ_{xy} is the cross-correlation coefficient between u and v components and is quantified as follows:

$$\rho_{xy} = \frac{\mathcal{R}_{xy}}{\sqrt{\mathcal{R}_{xx}\mathcal{R}_{yy}}} \quad (6.5)$$

The turbulent kinetic energy TKE is quantified as:

$$TKE = \frac{1}{2} (\mathcal{R}_{xx} + \mathcal{R}_{yy}) \quad (6.6)$$

whereas its random uncertainty is extracted via linear error propagation [190]:

$$U_{TKE} = \sqrt{U_{\mathcal{R}_{xx}}^2 + U_{\mathcal{R}_{yy}}^2} \quad (6.7)$$

6.3 RESULTS AND DISCUSSIONS

The experimental results are presented in two distinct sections. The first section highlights the results obtained from the 5-hole pressure probe to characterise the airflow exiting the vents, while the second section discusses the results of the PIV technique applied to the investigated measurement planes.

6.3.1 AIRFLOW MEASUREMENTS AT THE VENTS OUTLET, 5-HOLE PRESSURE PROBE

Figure 6.5 shows the mean velocity fields of the outlet flow from the four vents opened in the front ventilation mode.

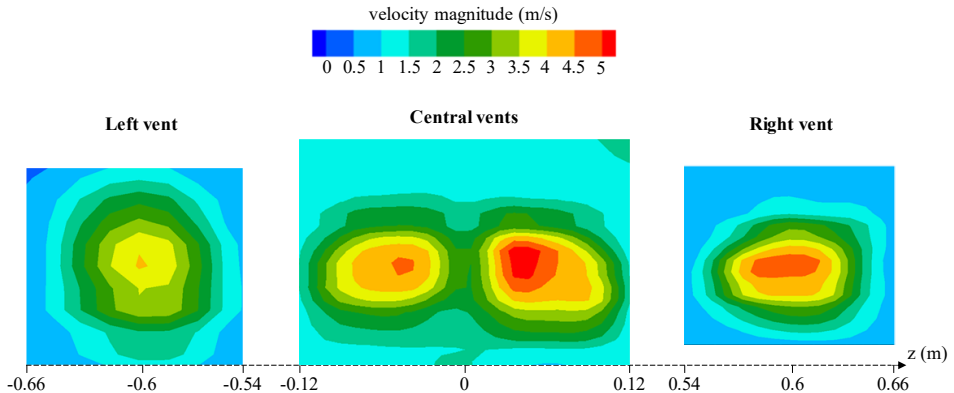


Figure 6.5. Mean velocity fields measured at the vents exits in front ventilation mode. All measurements are conducted at fan speed 3 out of 4.

The observed velocity has a Gaussian distribution across all the vents, suggesting a smooth and symmetrical airflow pattern. However, a notable variance in the maximum jet velocity between the left (driver's side) and right (passenger's side) is evident. In particular, the peak velocity reaches approximately 4 m s^{-1} on the driver's side, while the passenger's side records a higher peak of around 5 m s^{-1} . This asymmetry in the ventilation flow could be a direct consequence of the design of the Peugeot 206 car, where the air intake duct is located on the right of the car's hood, potentially causing a higher air flow rate through the vent of the passenger's side. Furthermore, the flow shape diverges distinctly between the driver's side vent and the others. The centre and right vents show a horizontal elongation in their shapes, contrasting with the nearly circular shape on the driver's side. This

phenomenon could be attributed to the presence of the steering wheel, which could impose flow restrictions and introduce perturbations to the velocity field on the driver's side. The steering wheel's presence could cause turbulence or deflections in the airflow, thereby altering the shape and intensity of the emanating jet.

These findings underscore the impact of vehicle design on airflow characteristics within the cabin. The spatial configuration and component placement, such as the air intake duct and steering wheel, play significant roles in the distribution and strength of airflow from the ventilation system.

6.3.2 PIV MEASUREMENTS

In this section, the experimental results of PIV measurements are described in terms of the four main parameters: (i) time-averaged velocity field; (ii) distribution of turbulent kinetic energy; (iii) Reynolds shear stress; (iv) uncertainty bounds of the measured quantities.

TIME-AVERAGED VELOCITY FIELDS AND MEASUREMENT UNCERTAINTY

The experimental time-averaged flow field measured at the centre plane of the car (MP1) is illustrated in Figure 6.6 for the case of fan speed 3 out of 4. It should be noted that the region of the velocity field near the inlet section ($x \sim 0.15$ m, $y \sim 0.1$ m) was affected by reflections from the steering wheel and was then excluded and blanked out.

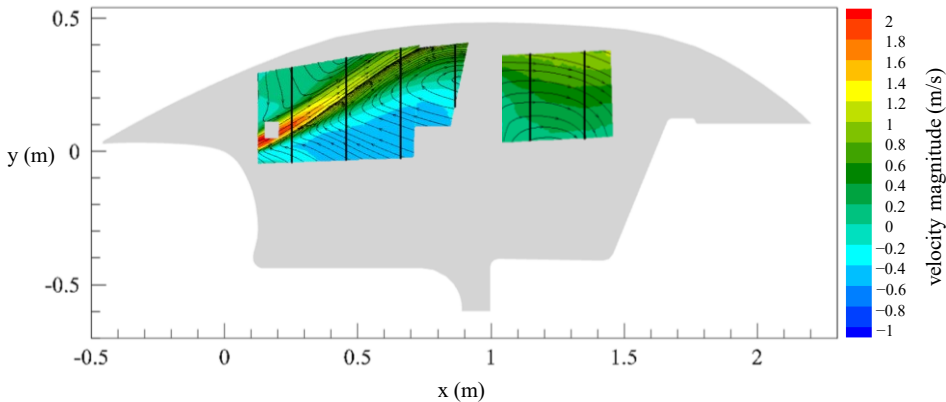


Figure 6.6. Experimental time-averaged velocity fields in the x-y plane at the car centre plane (MP1) for fan speed 3 out of 4.

Despite the measurement planes capturing only a portion of the cabin's space, a large-scale spanwise vortex is prominently visible, characterizing the airflow within the observed section. The jet stream issued from the central dashboard vents is directly observed thanks to the measurement plane aligned with the centre of the two central panel vents. It can be noticed that the jet stream at the vent exit is rather narrow, featuring a width of about 7 cm. The jet stream remains clearly visible up to its interaction with the cabin's ceiling, where the jet width increases to 16 cm due to the adverse pressure gradient caused by stagnation on the ceiling. On average, the magnitudes of the velocity vectors at the front of the car cabin are larger than those at the rear, which is clearly because the jet,

emitted from the vents at the front, loses momentum when moving downstream, especially after the interaction with the cabin's ceiling. Within the jet stream region, a maximum x -velocity of 2 m s^{-1} is measured, but this velocity decreases considerably from section $x=0.4 \text{ m}$. It is noticed that the maximum velocity measured by PIV is about half of that measured with the 5-hole probe (Section 6.3.1) because the PIV plane is located at the middle between the two vents. The airflow emitted from the vents impinges on the vehicle ceiling, forming a large-scale clockwise vortex that encompasses both the front and rear areas. In the rear measurement plane, it seems that part of the airflow takes part to the recirculation towards the front, whereas the remaining part is directed towards the back (parcel shelf), identified as the flow exit from the cabin in the preliminary investigation. The PIV measurements confirmed that, as highlighted in the preliminary analysis, the airflow mainly goes out of the parcel shelf; therefore, it can be regarded as the outlet section of the airflow from the car.

The velocity field pattern at fan strength 3 exhibits consistency across all fan strengths, as evidenced in Figure B.1, Figure B.5 and Figure B.9 (see Appendix B). Obviously, a difference is observed in the maximum magnitude of the velocity vectors, but all the flow fields exhibit a high degree of self-similarity.

Figure 6.7 and Figure 6.8 show the comparison between the measured velocity profiles, for the horizontal component (Figure 6.7) and the vertical component (Figure 6.8), at four fan speeds, within the central longitudinal plane (MP1) at seven different sections, indicated with black vertical lines in Figure 6.6. The velocity profiles at different fan strengths are observed to be proportional to each other, supporting the hypothesis of self-similarity of the flow fields at the different fan strengths; indeed, the fan operating at strength 4 registers a maximum speed of 2.9 m s^{-1} for the horizontal component and 1.6 m s^{-1} for the vertical component at section $x=0.25 \text{ m}$, while all other velocity profiles exhibit proportionally lower values. Furthermore, the development of the flow pattern is clearly visible, with the jet moving towards the cabin ceiling.

Figure 6.9 shows a more detailed analysis of the jet core and maximum velocity. The figure is divided into two key graphs. On the left, the graph shows the positions (x, y) of maximum velocities within the car cabin at varying fan speeds for the MP1 plane, specifically the region characterized by the jet. The jets propagate almost linearly at an angle of about 20 degrees with respect to the horizon, which is influenced by the orientation angle of the horizontal grille of the vents. It can be noticed that, up to $x \sim 0.4 \text{ m}$, the jet cores at the different fan speeds are approximately superimposed. For larger values of x , they depart from each other, with the jets from the lower fan speeds moving upwards. This trend suggests that natural convection, induced by high cabin air temperatures, plays a role in influencing the air flow, especially at low speeds. On the right, the graph demonstrates how the maximum outflow velocity from the central vents decreases as the distance from the vents increases, highlighting a gradual reduction in the air jet speed as it moves away from the source. Moreover, the speeds achieved at various fan speeds appear to be proportional to each other.

The mean velocity fields for the driver's seat plane (MP2) are presented in Figure 6.10. Despite the limited area of the measurement planes, the flow within this sector exhibits a clear separation, with one vortex directed towards the windscreen and another directed towards the seat. It is noticed that the velocity magnitudes in this area are comparatively small compared to the central plane (Figure 6.6), with the peak of velocity magnitude reaching about 0.5 m s^{-1} in the top-right region. This difference in velocity is ascribed to the fact that the plane analysed in Figure 6.10 is in the middle of the driver's seat, hence it

exhibits a relatively large distance (0.32 m) from the vents on the left and at the middle of the car.

The velocity field pattern at fan strength 3 exhibits consistency with the velocity field at fan strength 4, as illustrated in Figure B.9, and differs from the velocity field at fan strengths 1 and 2, in which four distinct vortices appear, as observed in Figure B.1 and Figure B.5, due to the lower penetration of the jets that causes the formation of two additional recirculation regions close to the ceiling.

Figure 6.11 and Figure 6.12 provide a comparison between the measured velocity profiles, for the streamwise component (Figure 6.11) and the vertical component (Figure 6.12), at the four fan speeds within the driver seat plane at three different sections (i.e., $x=0.25$ m, $x=0.45$ m and $x=0.65$ m); the locations where the profiles are extracted are shown with three black vertical lines in Figure 6.10. Contrary to what was discussed for the cabin's median plane, the velocity profiles are not proportional to each other at the different fan strengths. This is particularly evident for the streamwise component in the two upstream sections ($x=0.25$ m and $x=0.45$ m), where at fan speeds 1 and 2 the flow is mainly directed towards the windshield (negative x-velocity), whereas for the higher fan speeds the flow is at least partly directed towards the back of the car (positive x-velocity).

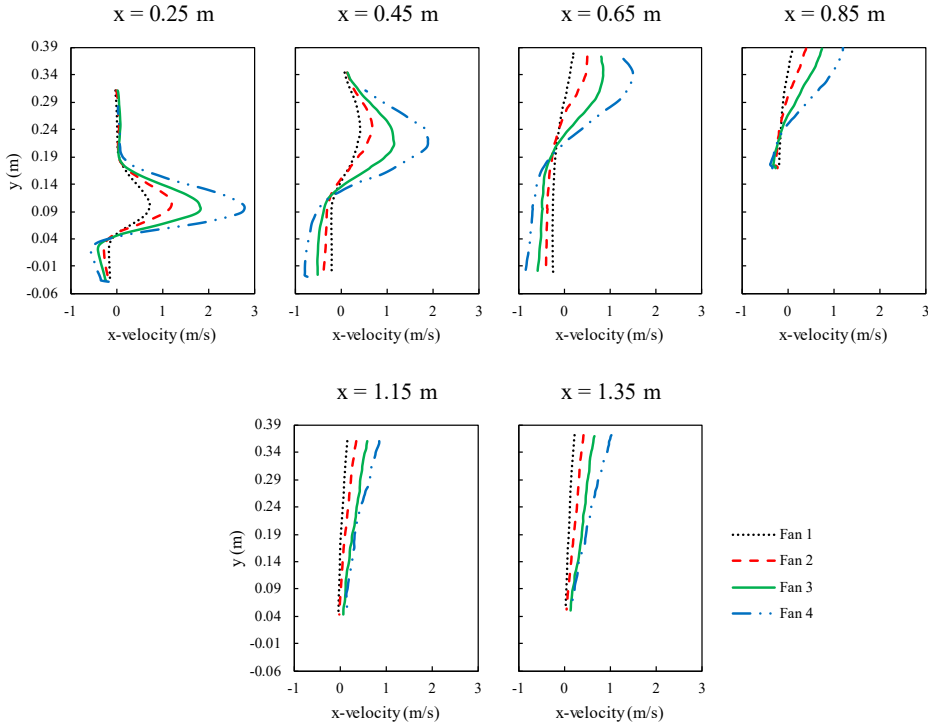


Figure 6.7. Comparison between experimental time-averaged streamwise velocity profiles for all four fan strengths at different locations within the car centre plane (MP1).

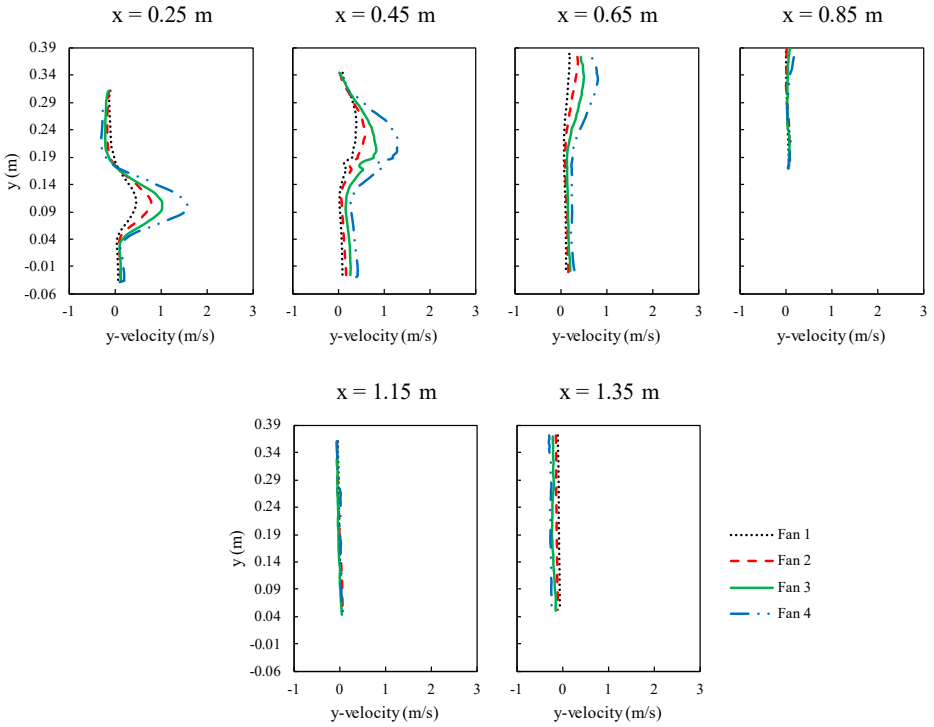


Figure 6.8. Comparison between experimental time-averaged vertical velocity profiles for all four fan strengths at different locations within the car centre plane (MP1).

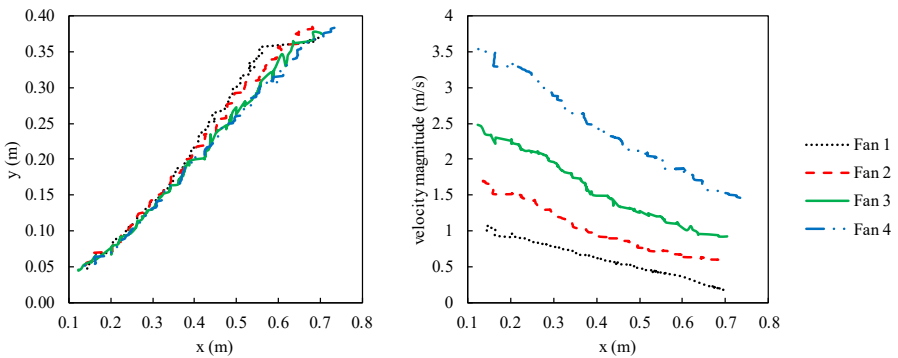


Figure 6.9. Analysis of jet behaviour from central vents. Left: position (x, y) where maximum velocity is reached at varying fan speeds. Right: maximum velocity at different fan speeds.

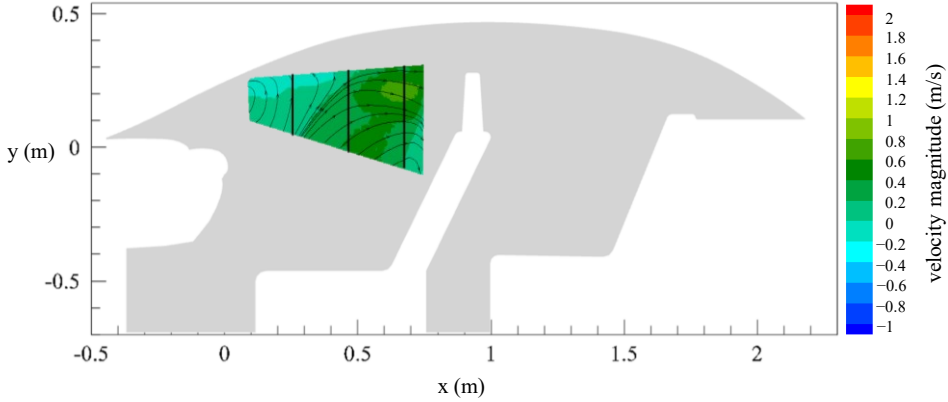


Figure 6.10. Experimental time-averaged velocity fields in the x-y plane at the driver seat plane (MP2) for fan speed 3 out of 4.

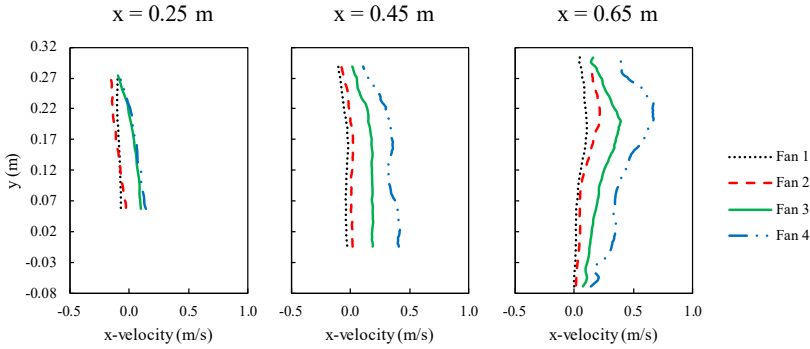


Figure 6.11. Comparison between experimental time-averaged streamwise velocity profiles for all four fan strengths at different locations within the driver seat plane (MP2).

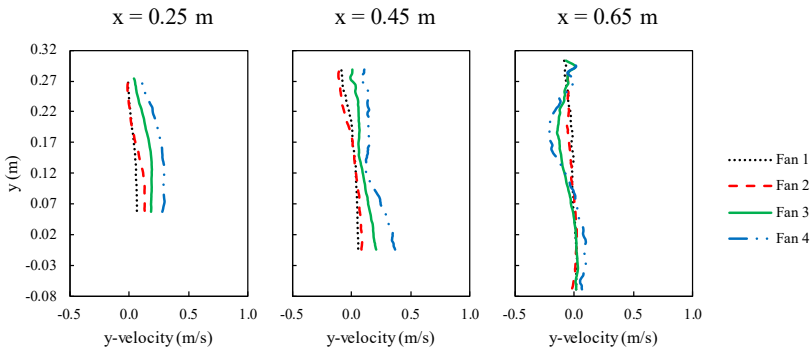


Figure 6.12. Comparison between experimental time-averaged vertical velocity profiles for all four fan strengths at different locations within the driver seat plane (MP2).

Figure 6.13 shows the mean velocity fields for the passenger seat plane (MP3). The velocity magnitude is larger than that observed in the driver's seat plane and smaller than that observed in the central plane. This discrepancy could result from the non-symmetric layout of the vehicle dashboard, which causes different geometries of the car cabin at the driver and passenger locations, such as the presence of the steering wheel that might obstruct ventilation airflow or distort the flow direction. The observed asymmetry could also result from the difference in velocity flow magnitude between the right and left sides of the outlet vents, as discussed in paragraph 6.3.1. The maximum velocity magnitude is approximately 1 m s^{-1} and is reached in the top right corner of the measurement domain. Similarly, the high speed in the upper right area is also notable in the other fan speeds, as shown in Figure B.1, Figure B.5 and Figure B.9.

Figure 6.14 and Figure 6.15 illustrate a comparison of the measured velocity profiles, for the streamwise component (Figure 6.14) and the vertical component (Figure 6.15), at the four fan speeds within the passenger longitudinal plane (MP3) at three different sections (i.e., $x=0.10 \text{ m}$, $x=0.30 \text{ m}$ and $x=0.50 \text{ m}$); the locations where the profiles are extracted are shown with three black vertical lines in Figure 6.13. At sections $x=0.10 \text{ m}$ and $x=0.30 \text{ m}$, the velocity profiles exhibit close proximity and appear to overlap due to their very low velocity. In contrast, the velocity profiles are distinct and proportional to each other at section $x=0.50 \text{ m}$, where the velocity is notably higher than that on the rest of the plane.

Figure 6.16 shows the uncertainty of the time-averaged velocity components at 95% confidence level. The highest uncertainty levels ($U > 0.06 \text{ m s}^{-1}$, equivalent to 3% of the jet velocity) are observed for both components in the jet stream region, mainly due to the flow's high velocity and unsteady behaviour. In addition, a high degree of uncertainty exists in the top right area of both the passenger and driver planes, possibly caused by the out-of-plane particle motion associated with a lateral airflow motion.

The uncertainty of the vertical velocity component, presented on the right of Figure 6.16, shows a similar spatial distribution as that of the horizontal velocity component, with uncertainty values comparable in the passenger and driver planes (middle and bottom pictures, respectively) and lower in the central plane (top picture) as a consequence of the lower velocity in the vertical direction.

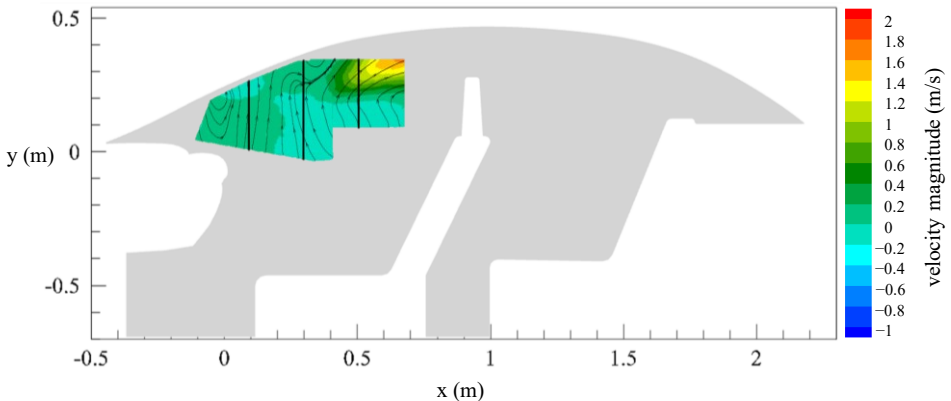


Figure 6.13. Experimental time-averaged velocity fields in the x-y plane at the passenger seat plane (MP3) for fan speed 3 out of 4.

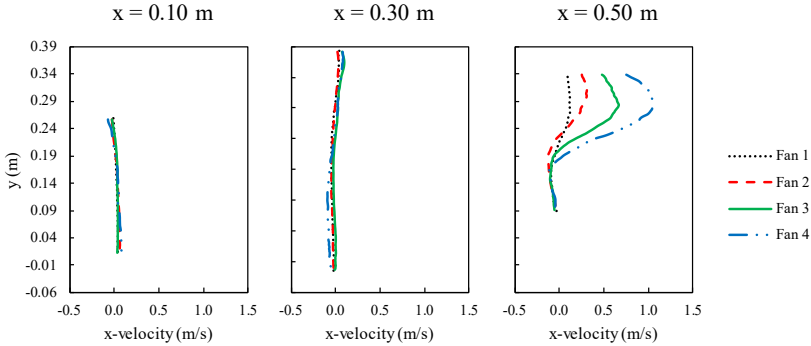


Figure 6.14. Comparison between experimental time-averaged streamwise velocity profiles for all four fan strengths at different locations within the passenger seat plane (MP3).

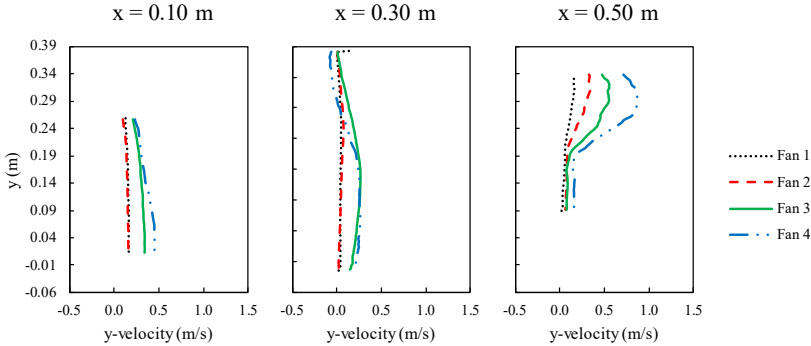


Figure 6.15. Comparison between experimental time-averaged vertical velocity profiles for all four fan strengths at different locations within the passenger seat plane (MP3).

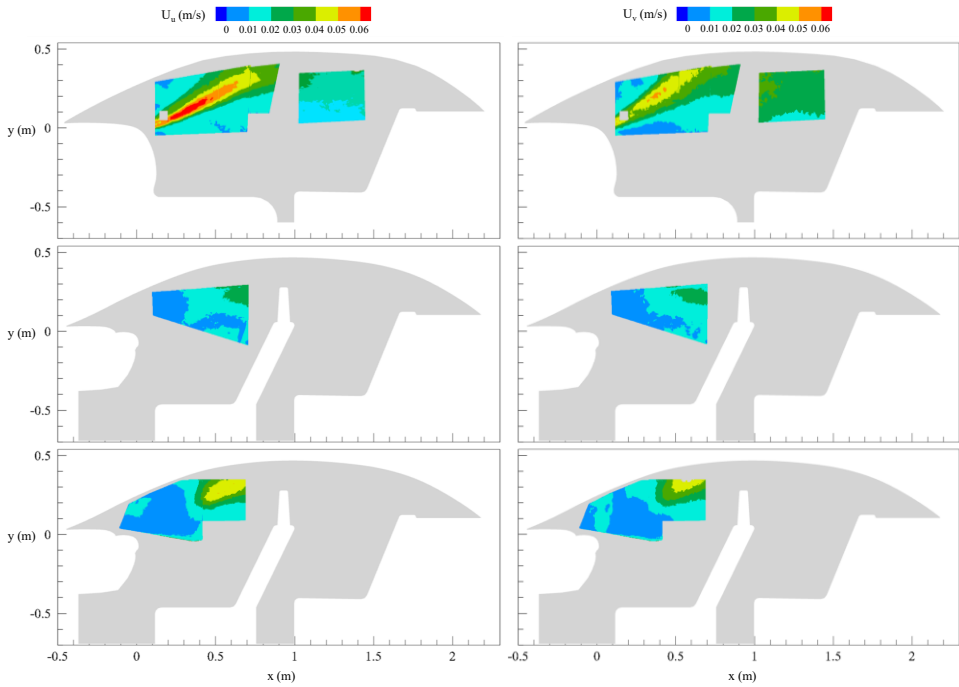


Figure 6.16. Measurement uncertainty at 95% confidence level for streamwise velocity component (left) and vertical velocity component (right). Top: car's centre plane (MP1); middle: driver's seat centre plane (MP2); bottom: passenger's seat centre plane (MP3).

FLOW FLUCTUATIONS AND THEIR UNCERTAINTIES

In this section, the focus is initially placed on the velocity scatter plots at three locations in the flow field, represented by points A, B, and C in Figure 6.17, corresponding to the region outside the jet, the shear layer and the jet core, respectively. This is followed by the analysis of the turbulent kinetic energy and Reynolds shear stresses, along with their associated uncertainties.

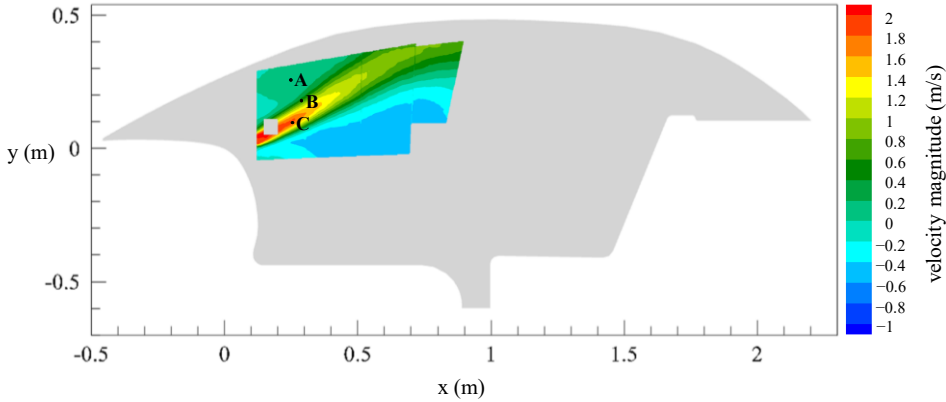


Figure 6.17. Experimental time-averaged velocity fields in the x-y plane at the car centre plane (MP1) for fan speed 3 out of 4. Locations of points A (outer region), B (shear layer region), and C (jet core) are indicated.

For each point highlighted in Figure 6.17, a quadrant analysis [191] is performed via the velocity scatter plots shown in Figure 6.18, Figure 6.19 and Figure 6.20. Each of these plots incorporates data taken within a $1.4 \times 1.4 \text{ mm}^2$ box surrounding the specific point's location as shown in Figure 6.17. Concerning the morphology of the scatter plots, point A, located in the free stream region, exhibits a data distribution that is compact: this is expected, because in the region outside the jets the flow fluctuations are minor. Conversely, the distribution becomes more dispersed for point B, which is situated in the shear layer region. Here, most of the events occur in the first quadrant ($u' > 0, v' > 0$) and in the third quadrant ($u' < 0, v' < 0$), which is associated with oscillations of the jet. In fact, when the jet oscillates upwards, both velocity components at point B increase, yielding an event in the first quadrant; instead, when the jet oscillates downwards, both velocity components at point B decrease, leading to an event in the third quadrant. Clearly, the scatter of the data points progressively increases when moving from fan level 1 to level 4, which is consistent with the increased jet exit velocity. In the inner region, represented by point C, the distribution is notably broader and approximately isotropic, indicating a low degree of correlation between the fluctuations along x and y.

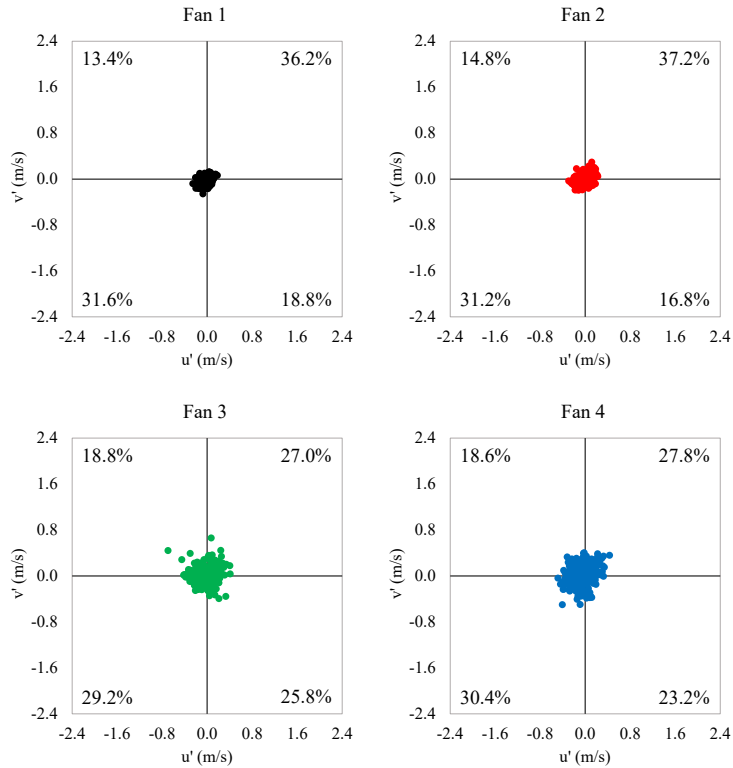


Figure 6.18. Scatter plot of u' and v' components at point A, located in the free stream region. The percentages indicate the number of events (u' , v') in each of the four quadrants.

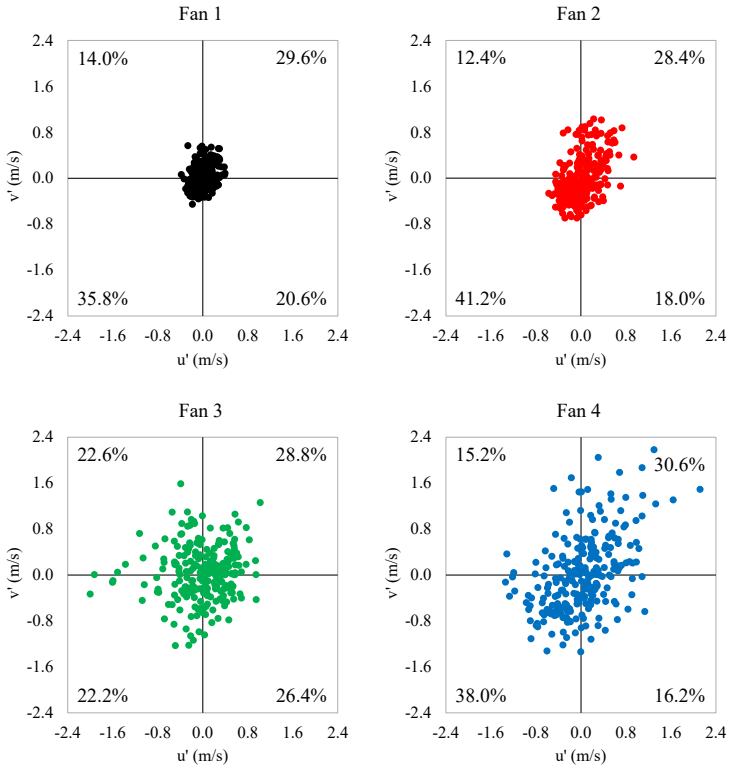


Figure 6.19. Scatter plot of u' and v' components at point B, located in the shear layer region. The percentages indicate the number of events (u' , v') in each of the four quadrants.

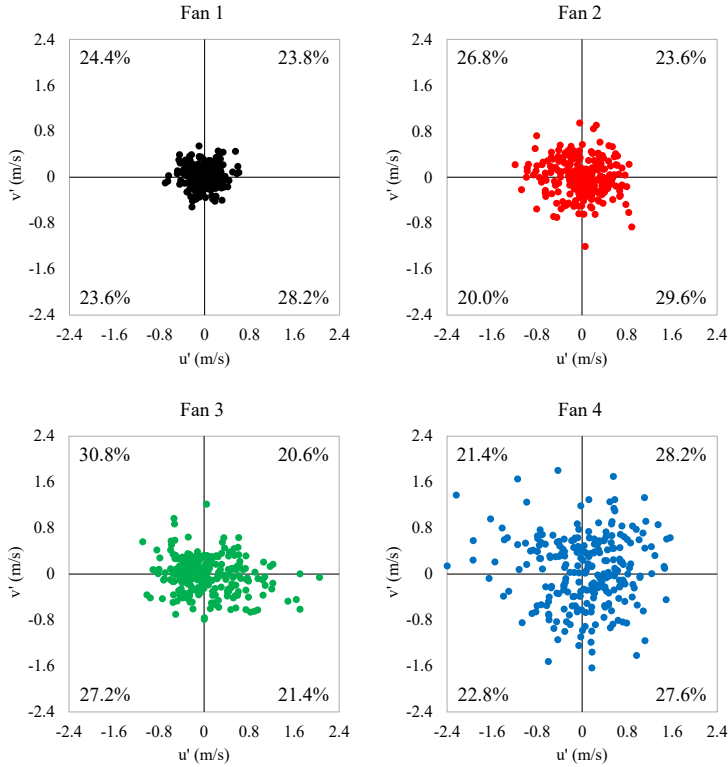


Figure 6.20. Scatter plot of u' and v' components at point C, located in the inner region. The percentages indicate the number of events (u' , v') in each of the four quadrants.

Figure 6.21 illustrates the turbulent kinetic energy (TKE) measured experimentally at the three different planes (left picture) and the corresponding uncertainty at 95% confidence level (right picture). Clear differences can be seen between the centre plane (MP1, top) and the driver (MP2, middle) and passenger (MP3, bottom) planes. Indeed, at MP1 the jet stream exhibits large velocity fluctuations, leading to TKE values larger than $0.4 \text{ m}^2 \text{ s}^{-2}$. Conversely, in the two other planes, the velocity fluctuations are lower, except in the top right of the longitudinal passenger plane (MP3), where higher velocity fluctuations (TKE up to $0.15 \text{ m}^2 \text{ s}^{-2}$ at MP2 and up to $0.35 \text{ m}^2 \text{ s}^{-2}$ at MP3) are ascribed to a lateral airflow motion (also seen in the preceding subsection). The uncertainty affecting TKE follows the same pattern observed for the uncertainties of the streamwise and vertical velocity components, as presented in the preceding subsection. High uncertainties in the TKE are observed in the jet stream region and the top right area of MP3 due to the relatively higher unsteady fluctuations. In contrast, lower uncertainties are found in the MP2, which exhibits the slightest fluctuations in the flow. The maximum uncertainty of the TKE remains below $0.05 \text{ m}^2 \text{ s}^{-2}$ or 12% of the maximum TKE value.

Figure 6.22, Figure 6.23 and Figure 6.24 present a comparison of TKE profiles at four fan speeds in the three longitudinal planes at different sections. Figure 6.22 shows the comparison for the central longitudinal plane (MP1) at seven distinct sections indicated with black lines in Figure 6.6. Figure 6.23 illustrates the comparison for the driver's seat

centre plane (MP2) at sections indicated with black lines in Figure 6.10. Figure 6.24 compares the TKE profiles at the passenger's seat centre plane (MP3), at sections indicated with black lines in Figure 6.13. The TKE profiles across different fan strengths show a proportional relationship, as observed for the velocity. For instance, the fan operating at strength 4 exhibits a peak TKE of $1.4 \text{ m}^2 \text{ s}^{-2}$ for MP1 at section $x=0.25 \text{ m}$, while all other TKE profiles exhibit proportionally lower values. This proportionality also manifests itself in the other two planes, MP2 and MP3.

The Reynolds shear stress fields for the three different setups (left picture) and their uncertainties at 95% confidence level (right picture) are illustrated in Figure 6.25. As noted for the TKE fields, the discrepancies between the central plane (MP1, top) and the driver (MP2, middle) and passenger planes (MP3, bottom) are notable, with the Reynolds shear stress being much more pronounced (up to about $0.05 \text{ m}^2 \text{ s}^{-2}$) in the central plane, giving clear indications that this is the region where most of the turbulence is produced. The highest uncertainty of the Reynolds shear stress is about $0.015 \text{ m}^2 \text{ s}^{-2}$, or 30% of the Reynolds shear stress value, indicating that the accurate measurement of this flow property remains a challenge.

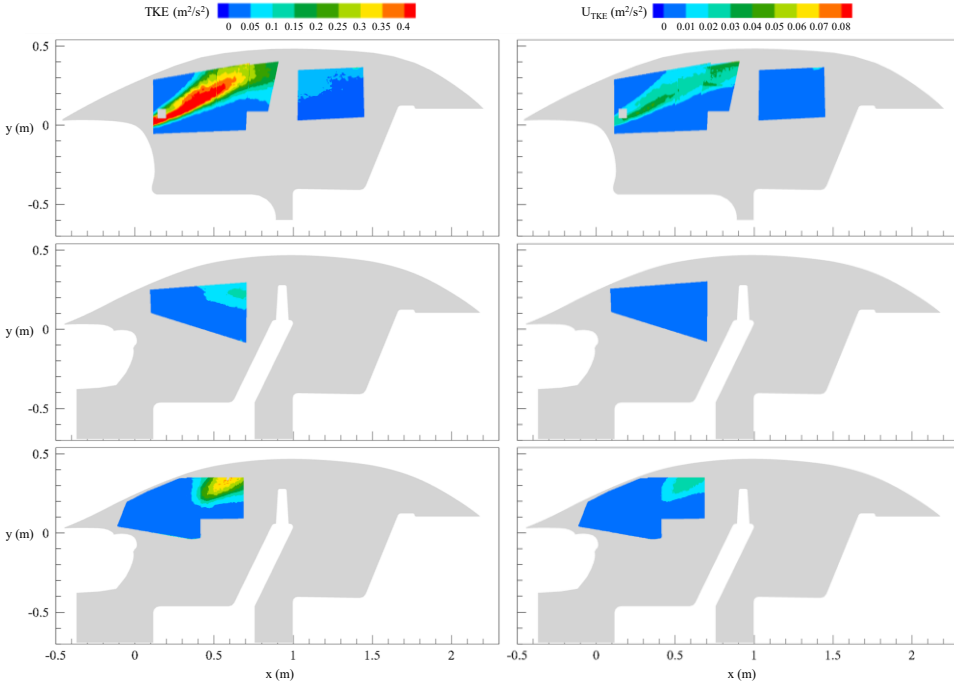


Figure 6.21. Experimental TKE (left) and corresponding measurement uncertainty at 95% confidence level (right). Top: car's centre plane (MP1); middle: driver's seat centre plane (MP2); bottom: passenger's seat centre plane (MP3).

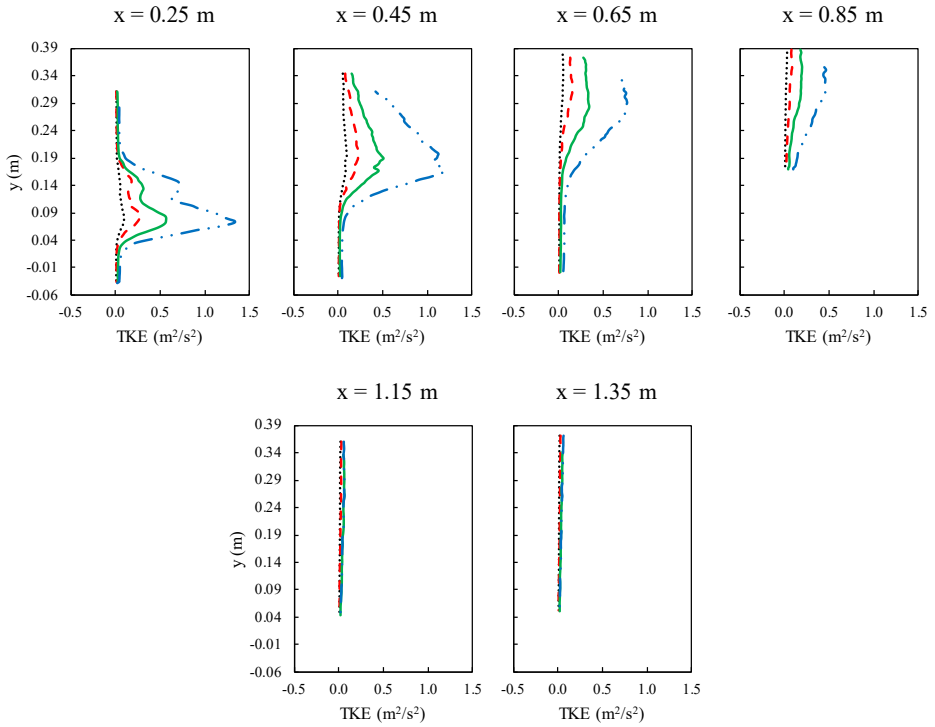


Figure 6.22. Comparison between TKE profiles for all four fan strengths at different locations within the car centre plane (MP1).

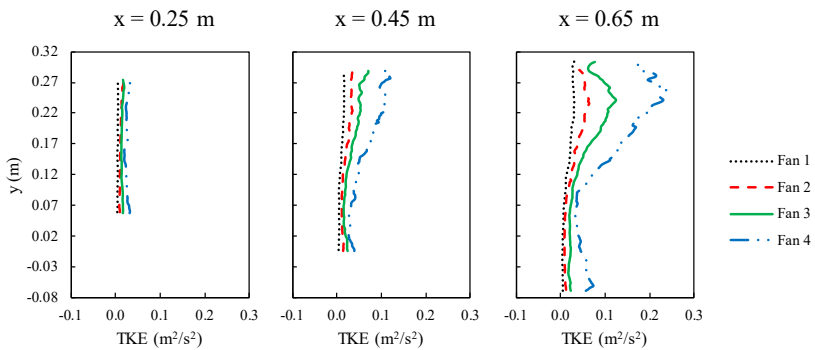


Figure 6.23. Comparison between TKE profiles for all four fan strengths at different locations within the driver seat plane (MP2).

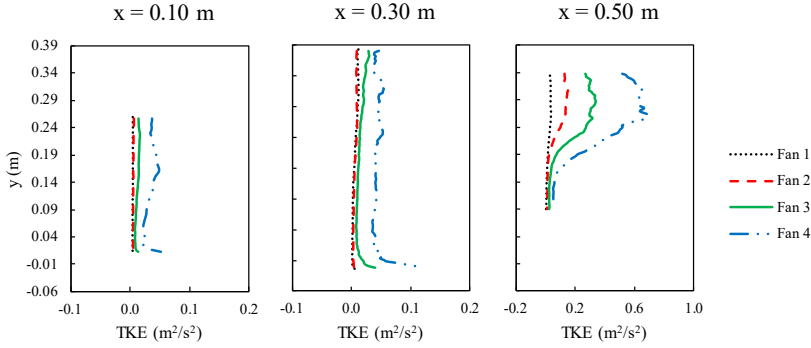


Figure 6.24. Comparison between TKE profiles for all four fan strengths at different locations within the passenger seat plane (MP3).

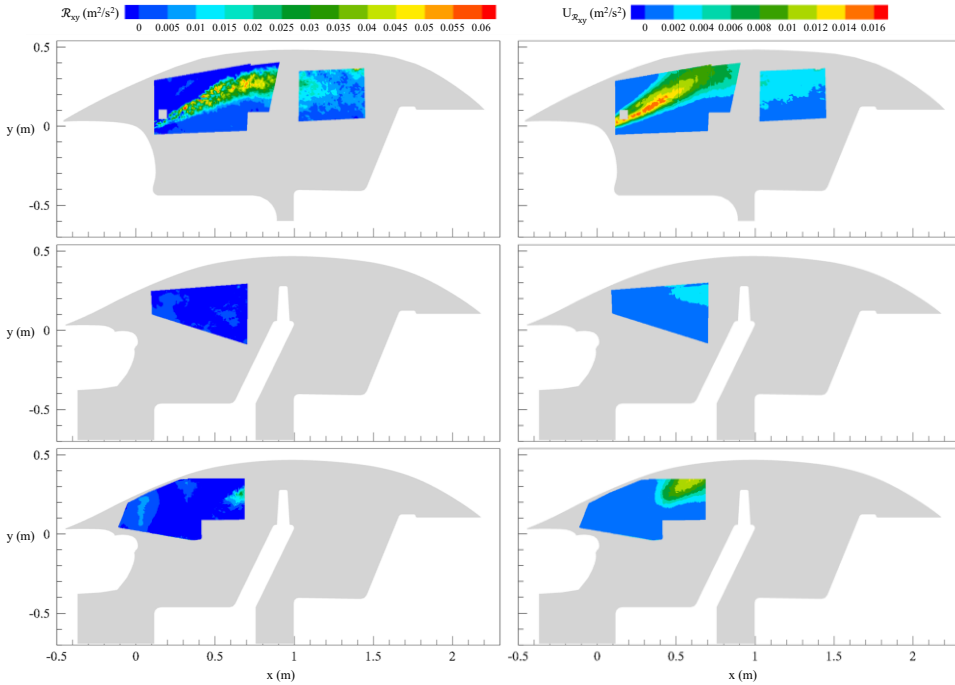


Figure 6.25. Experimental Reynolds shear stress R_{xy} and corresponding measurement uncertainty at 95% confidence level. Top: car's centre plane (MP1); middle: driver's seat centre plane (MP2); bottom: passenger's seat centre plane (MP3).

Figure 6.26, Figure 6.27 and Figure 6.28 present a comparison of R_{xy} profiles at four fan speeds in the three longitudinal planes at different sections: $x = 0.25$ m, 0.45 m, 0.65 m, 0.85 m, 1.15 m and 1.35 m for the central longitudinal plane MP1 (Figure 6.26); $x = 0.25$ m, 0.45 m and 0.65 for the driver's seat plane MP2 (Figure 6.27); $x = 0.1$ m, 0.3 m and 0.5 m for the passenger's seat plane MP3 (Figure 6.28).

In all cases, the \mathcal{R}_{xy} profiles show a proportional relationship to each other, as has been observed in the case of TKE profiles. However, at the MP2 and MP3 planes, this proportionality is less evident due to the lower values of \mathcal{R}_{xy} and the relatively high uncertainty, which increases the noise in the \mathcal{R}_{xy} profiles.

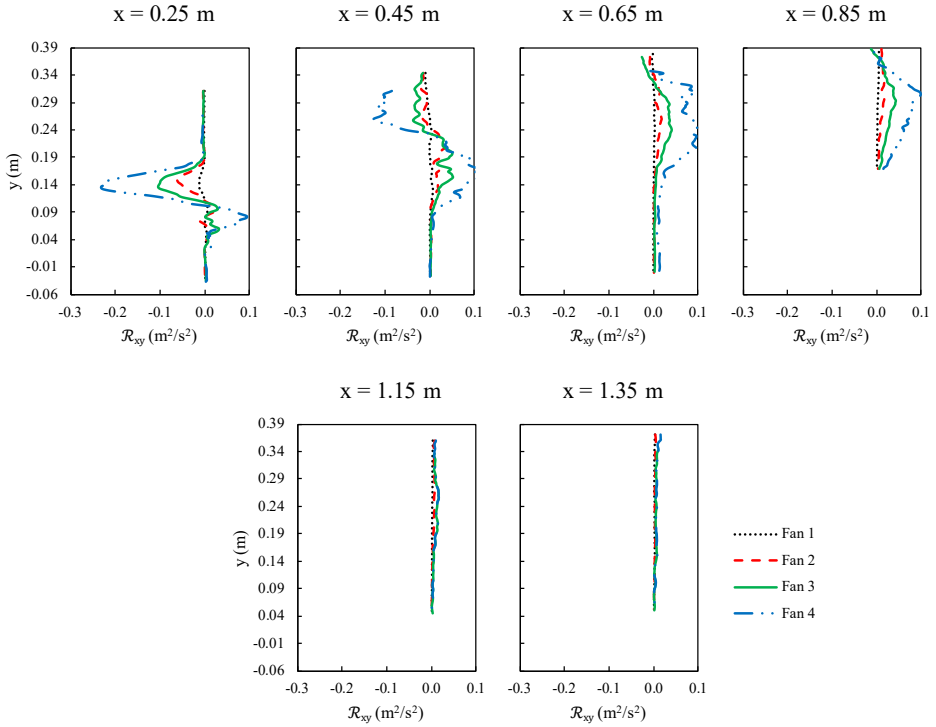


Figure 6.26. Comparison between \mathcal{R}_{xy} profiles for all four fan strengths at different locations within the car centre plane (MP1).

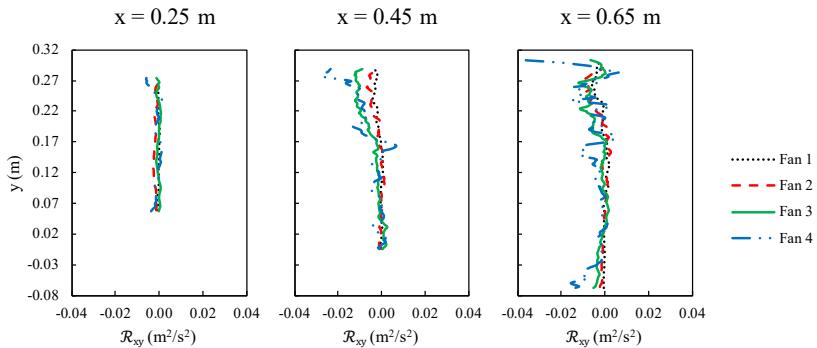


Figure 6.27. Comparison between \mathcal{R}_{xy} profiles for all four fan strengths at different locations within the driver seat plane (MP2).

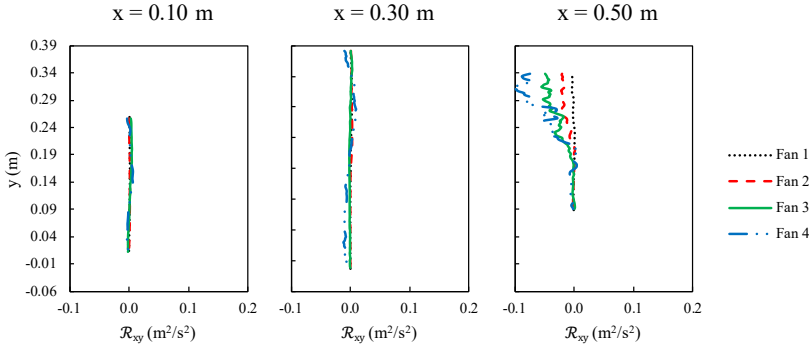


Figure 6.28. Comparison between \mathcal{R}_{xy} profiles for all four fan strengths at different locations within the passenger seat plane (MP3).

6.4 CONCLUSIONS

This chapter presented the results of an experimental investigation of the ventilation flow in a real car cabin using a 5-hole pressure probe and Particle Image Velocimetry. The investigation focused on the analysis of the flow structure at three longitudinal planes inside the car cabin when the vents were operated in the front ventilation mode. While measurements were conducted at all four fan speeds, the primary discussion is focused on the flow fields obtained at fan speed 3. A comparative analysis across the different fan speeds has also been conducted, specifically along designated vertical lines. The complete flow fields at the different fan speeds are reported in Appendix B.

The study reveals significant differences in the air flow issued from the four vents opened in the front ventilation mode, resulting in an asymmetry in the flow structure between the longitudinal planes at the driver and passenger locations. In particular, the jet exit velocity from the right vent is about 20% higher than that from the left vent. This asymmetry is likely due to the specific design of the Peugeot 206 car, where the air intake duct is located on the right of the car hood, and is accentuated by the asymmetry of the internal geometry of the car cabin, such as the presence of the steering wheel, which might obstruct the ventilation airflow or distort the flow direction.

The experimental investigation by Particle Image Velocimetry revealed a large-scale clockwise vortex in the longitudinal centre plane; such vortex encompasses both the front and rear areas of the car cabin and is caused by the jet stream issued from the central vents, which is deflected backwards by the presence of the vehicle ceiling. The analysis of the data at different fan speeds shows that mild buoyancy effects are present, for which the jets at the lower fan speeds tend to deflect upwards towards the ceiling. The highest velocity, exceeding 2 m s^{-1} , is reached in the car cabin's centre plane, especially in the jet core; in front of the passenger's and driver's headers, lower velocities are obtained of about 2 m s^{-1} and 1 m s^{-1} , respectively. The comparison of velocity profiles at various fan strengths indicates a proportionality among them, demonstrating the concept of self-similarity in the flow fields across different fan speeds.

From the inspection of the velocity fluctuations via the quadrant analysis, it is shown that, in the shear layer, most of the fluctuation events occur in the first ($u' > 0, v' > 0$) and third ($u' < 0, v' < 0$) quadrants, which is ascribed to vertical oscillations of the jets. The largest

velocity fluctuations are encountered in the median plane and especially in the jet core, with TKE exceeding $0.4 \text{ m}^2 \text{ s}^{-2}$; conversely, lower fluctuations take place in front of the passenger's and driver's headers (TKE less than $0.35 \text{ m}^2 \text{ s}^{-2}$ and $0.2 \text{ m}^2 \text{ s}^{-2}$, respectively). The Reynolds shear stresses, similar to the TKE fields, are significantly more pronounced (up to about $0.05 \text{ m}^2 \text{ s}^{-2}$) in the central plane, indicating that this is the region where most of the turbulence is generated.

The experimental results presented in this work provide valuable insights into the ventilation flow in a real car cabin, with detailed descriptions of the boundary conditions and measurement uncertainties. Additionally, the data presented in this chapter serve as a benchmark for the validation of CFD numerical models. In the next chapter, PIV measurements here discussed are employed to assess the accuracy of URANS and LES approaches in predicting airflow patterns inside real car cabins.

7

ON THE EFFECTIVENESS OF REYNOLDS–AVERAGED AND SUBGRID SCALE MODELS IN PREDICTING FLOWS INSIDE CAR CABINS

The aim of the present chapter is to analyse the performances of URANS and LES approaches in predicting airflow patterns inside car cabins and to provide insights into the design of CFD simulations of a real car cabin. For this purpose, one eddy viscosity-based turbulence model (SST $k-\omega$) and two subgrid scale models (WALE and dynamic KE) were tested, and numerical results were compared with the PIV measurements presented in the preceding chapter, carried out on a commercial car. The URANS model exhibited great accuracy in predicting the mean flow behaviour and was appreciably outperformed by the LES models only far from the inlet sections (i.e., where jet fluctuations are more pronounced). For this reason, it was deemed suitable for conducting further analyses, aimed at characterizing the airflow patterns in winter and summer conditions and performing a thermal comfort analysis. The thermal regime was found to have a very little effect on the air flow patterns, once the quasi-steady state regime is achieved; in fact, both in winter and in summer the temperature field is fairly uniform within the car cabin, making the contribution of buoyancy negligible and velocity fields to be very similar in the two seasons. Findings also reveal that thermal comfort sensation can be different for passengers sharing the same car but sitting on different seats; this aspect should be considered when designing and operating the HVAC system, since the minimum comfort requirements should be met for all the occupants.

This chapter is based on the following manuscript:

Grossi G., Arpino F., Bertone M., Cortellessa G. and Sciacchitano A. (2024). On the effectiveness of Reynolds–averaged and subgrid scale models in predicting flows inside car cabins. Accepted to *Physics of Fluids* (DOI: 10.1063/5.0180823).

Keywords: Computational Fluid Dynamics (CFD); Particle Image Velocimetry (PIV); indoor environment; airflow; thermal comfort; transportation

7.1 INTRODUCTION

Computational Fluid Dynamics has undergone significant developments in the last years, becoming a suitable tool for investigating velocity, pressure and temperature fields in various indoor microenvironments including aircraft cabins [192–208], trains [209–211], buses [212–219] and cars [80,83,220–232]. Despite its versatility, if not properly validated, numerical modelling may be affected by large errors and produce misleading results, thereby eliminating all the advantages deriving by its employment (i.e., reduced costs and times with respect to experiments). These errors could be induced by several factors: definition and discretisation of the domain (oversimplification of the geometry and bad quality cells in the computational grid), selection of the boundary conditions, wrong assumptions in the mathematical modelling (i.e., choice of the governing equations to be solved and models for the fluid and solid properties). Therefore, before applying any numerical tool to engineering problems, a verification and validation procedure is required to ensure the reliability and accuracy of the results [99]. In this regard, the Particle Image Velocimetry technique can be used to provide accurate data for the validation of numerical simulations. Looking at the scientific literature, several studies rely on PIV data for the validation of numerical codes. Among others, You et al. [193,200] employed PIV data to validate the CFD models adopted to investigate the impact of gaspers on the airflow patterns inside an aircraft cabin; Yang et al. [195] conducted large eddy simulations to investigate the airflow characteristics in a simplified Boeing 737-200 cabin model, validating numerical results against PIV measurements. While a considerable amount of research was dedicated to achieving a better understanding of airflow patterns inside aircraft, buses and trains, very few properly validated numerical studies are available concerning car cabins. Chang et al. [83] developed a CFD model to study the effects of the ventilation rate on the air quality inside a car cabin and to establish the amount of fresh air required for each occupant in a vehicle; however, validation of the numerical model is provided by comparing simulated and experimental CO₂ concentrations in the cabin and not in terms of velocity fields. Khatoon and Kim [221] and Yang et al. [220] performed CFD simulations to investigate passenger comfort inside car cabins; even in these cases, validation was not provided in terms of velocity fields but comparing temperature values at specific points of the domain. Zhang et al. [222,223] evaluated the influence of different factors on the thermal comfort and the energy consumption in a car cabin, comparing measured and predicted transient temperatures. Dehne et al. [224] presented three vertical ventilation concepts for car cabins, comparing them to common dashboard ventilation using both experimental and numerical approaches; the analyses were carried out on a simplified cabin prototype and the CFD model was validated with mean temperature and velocity values taken at multiple points of the cabin. Ullrich et al. [80] conducted a numerical study, validated with PIV measurements, in order to optimize the HVAC system and reduce its energy consumption; unfortunately, detailed information about the geometry is not available, making the reproduction of the numerical setup not possible. Danca et al. [228,229] carried out experimental and numerical analyses to investigate the air distribution and the thermal comfort inside a car cabin mock-up; a simplified geometry was used to reproduce the in-vehicle environment, which may be not representative of life-like scenarios.

Mathai et al. [226] performed RANS simulations to study the aerosol distribution inside a vehicle cabin, for different combinations of open and closed windows; Sen and Singh [227] also used a CFD model to analyse the droplets dispersion inside a moving car with the windows open, by adopting a Eulerian-Lagrangian approach. Both these studies, however, make use of an extremely simplified geometry and do not provide a quantitative validation of the numerical results. More recently, Sip et al. [171] provided a benchmark for the characterization of the flow immediately downstream of automotive vents, comparing two theoretical approaches and validating them with measurements acquired with the constant temperature anemometry technique. Finally, Djeddou et al. [225] analysed the performances of five RANS turbulence models in predicting the airflow inside a passenger car cabin, providing validation against mean velocities and turbulence intensity profiles obtained with hot-wire anemometers; as claimed by the authors themselves, the PIV technique would have been more suitable since it is non-intrusive and provides information about the direction of the flow.

In Chapter 3, a transient, non-isothermal numerical model able to predict airborne droplet dispersion inside car cabins has been presented; the tool was validated against PIV measurements carried out on a glass-made scaled model and then applied to quantify the risk of infection from SARS-CoV-2 of passengers sharing a car with an infected subject for a 30 min journey. Findings revealed that CFD approaches are needed to properly describe the airflow patterns in such confined spaces and can be used to design new ventilation strategies for the purpose of improving the indoor air quality and the comfort of the occupants. The results obtained by CFD analyses, however, may be considerably influenced by the geometry adopted for reproducing the in-vehicle environment; hence, a situation as realistic as possible is desirable. For this reason, on the wave of previous numerical investigations, transient non-isothermal CFD simulations are herein performed and compared with PIV measurements carried out on a commercial car (presented in the preceding chapter). Both URANS and LES approaches are employed, assessing the performance of one eddy viscosity-based model, the SST $k-\omega$, and two subgrid scale (SGS) models, the wall-adapting local eddy-viscosity (WALE) and the dynamic kinetic energy (KE) models.

The URANS model, owing to the very good agreement with the experimental results and to the reduced computational time with respect to LES, was selected to conduct further numerical analyses, aimed at characterizing the thermal-fluid dynamics fields inside the car cabin in summer and winter conditions. A thermal comfort analysis is also conducted, calculating the evolution over time of the Predicted Mean Vote (PMV) and the Predicted Percentage Dissatisfied (PPD) [21,233] at multiple significant points of the cabin. For the scenarios here presented the car cabin is assumed to be empty, since the PIV measurements were carried out in the absence of occupants. The main objective of the present work is, in fact, to numerically reproduce the experiments and to provide insights into the design of CFD simulations of a real car cabin (from the creation of the geometry model to the selection of the boundary conditions and of the most convenient approach for turbulence modelling). The focus is also on the comparison between URANS and LES approaches, particularly useful in the modern scientific landscape. The increasing computational resources available to researchers and industries worldwide are indeed expanding the use of LES in pursuit of more accurate and reliable results. However, this comes with higher complexity and computational costs, making it necessary to define when such complications are required. Future works, relying on the numerical tool here validated, will include the presence of the occupants and explore broader scenarios, with

the purpose of improving the IAQ and the comfort of the passengers as well as reducing the energy consumption by the car HVAC system.

The chapter is organized as follows: Section 7.2 outlines the methodology, briefly recalls the experimental setup and defines the case study; details on the numerical setup are provided in Section 7.3; Section 7.4 shows the comparison of URANS and LES results with PIV data; in Section 7.5, the discussion of numerically predicted velocity and temperature fields in winter and summer conditions is provided, together with a thermal comfort analysis; finally, conclusions are drawn in Section 7.6.

7.2 METHODOLOGY

The HVAC system produces a highly transient, three-dimensional and turbulent flow pattern inside the car cabin, which is influenced by several factors: position and shape of the vents, inlet air velocity, geometry and size of the interior [176]. A careful design of the numerical analyses is thus required; in the present study, particular attention was paid to the reproduction of the in-vehicle environment, identification of inlet and outlet sections and to the proper definition of the boundary conditions.

The experimental facility is represented by a Peugeot 206, as described in the preceding chapter (a picture is available in Figure 6.1). Highlighted in the left picture are the vents enabled during the experiments (representing the front ventilation mode). On the right, the position of the axis system selected as reference for PIV measurements is shown; it has been placed in the middle of the central vents to ensure the repeatability of the experimental conditions.

PIV measurements, and so the numerical simulations, were carried out for the case of front ventilation mode, fresh air intake (i.e., no air recirculation) and HVAC system's fan strength set at level 3 out of the 4 available for mass flowrate adjustments.

7

7.2.1 PIV EXPERIMENTAL SETUP

Experiments were conducted in the backyard of the Aerodynamics Laboratories of the Delft University of Technology; for security reasons, the car and all the equipment employed were placed inside a tent 3 m wide, 2.6 m high and 6 m long. Temperature and humidity inside and outside the car (i.e., inside the tent) were monitored during the experiments with an Alecto Weather Station 1500, ensuring a resolution uncertainty of 0.1 K for temperature and 1% for relative humidity. Planar PIV measurements were taken on the xy plane at $z=-0.03\text{m}$ (with reference to the axis system shown in Figure 6.1). Two cameras were used to have a wider area for the acquisition of velocity fields, able to capture the tail of the jet coming out of the central vents. The measuring area is displayed in the right image of Figure 7.1, whereas on the left the arrangement of cameras and laser is sketched. The measuring plane is the one denoted as MP1 in the preceding chapter. The laser sheet gains access to the cabin through the windshield and enlightens the flow field, seeded with micrometric water-glycol droplets produced by a SAFEX seeding generator placed inside the car cabin; the optical access is provided to the cameras, placed on the right of the car, by the side windows (which were kept closed during the tests). A set of 500 uncorrelated image pairs was recorded for each camera; in the overlap area, the arithmetic average of the acquired flow fields was computed. The parameters of the experiments are reported in Section 6.2.2, to which the reader is referred for further details.

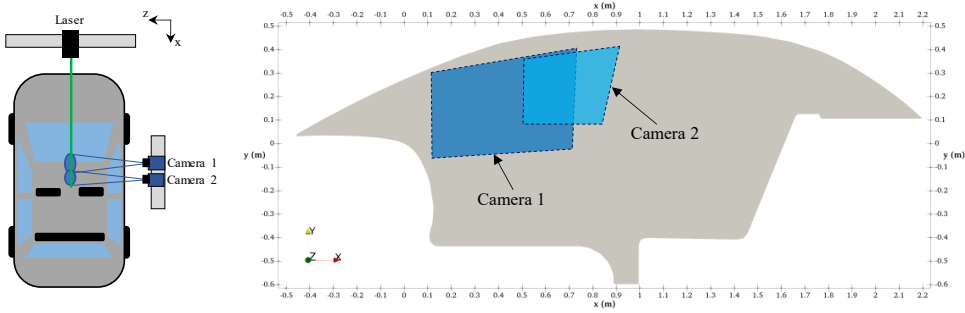


Figure 7.1. Sketch of the PIV measurements setup. Left: arrangement of cameras and laser; right: measuring area covered by the cameras.

7.2.2 GEOMETRY MODELLING

To facilitate the analyses and save computational resources, a simplified model of the Peugeot 206 car has been reproduced while keeping the main geometric characteristics of the passenger compartment; in fact, an overly detailed geometry would require an excessive grid refinement with unreasonable CPU times, which is beyond the scope of the present study. The cabin, whose internal volume is 2.05 m^3 , has 4 inlet vents (2 in the center and 1 at each side); only these vents have been considered for the computational domain definition, since in the experimental campaign only the front ventilation mode has been investigated) and one outlet section as shown in Figure 7.2.

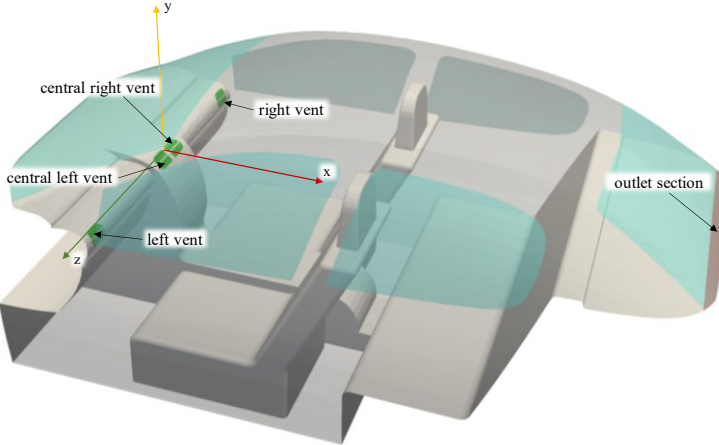


Figure 7.2. Computational domain with boundary patches.

Specific analyses were conducted to identify the output: the flow induced by the ventilation system was seeded with micrometric water-glycol droplets produced by a SAFEX seeding generator (the same used for PIV measurements), observing the flow patterns within the cabin and visually detecting where the air leaves the passenger compartment; these investigations revealed that the air exits the cabin at multiple

locations, being the vehicle not perfectly air-tight, but the main flow is directed back to the parcel shelf; this last finding was later confirmed by PIV measurements, described with a greater detail in Section 6.3.2, and for these reasons the exit section has been defined as depicted in Figure 7.2. To reproduce the inlet vents, only the section available to the air flow stream has been considered. For what concerns the walls, glazed surfaces (i.e., windshield, side windows and rear window) have been distinguished from non-glazed ones to ensure an accurate definition of the boundary conditions.

7.2.3 DEFINITION OF THE INLET MEAN VELOCITY BOUNDARY CONDITION

Being the air flow patterns within the car cabin strongly affected by the velocity at the inlet sections, a proper definition of such boundary condition is desirable to ensure a trustable reproduction of actual operating conditions. For this purpose, 3D measurements of the airflow exiting the front vents were performed by using the ProCap Compact 5-hole digital probe by Streamwise; a detailed description of the experimental apparatus is available in Section 6.2.1. The measured mean velocity data were fitted with the 2D Gaussian function represented by Equation (7.1), employing the Excel Evolutionary solver. Gaussian fitting for velocity profile at the inlet allows to have a simplified expression, which can be implemented with more ease as boundary condition in the code.

$$u_G(y, z) = u_{max} \cdot \exp\left(-\left(\frac{(z - z_0)^2}{2\sigma_z^2} + \frac{(y - y_0)^2}{2\sigma_y^2}\right)\right) \quad (7.1)$$

The parameters of the Gaussian function implemented in the numerical simulations are listed in Table 7.1 for the different boundary patches, whereas in Figure 7.3 a visual comparison among measured and numerically reproduced velocity fields is provided. The asymmetry of the HVAC system has been reproduced in order to have an accurate reproduction of the thermal-fluid dynamics fields inside the car cabin. The experimental fields of Figure 7.3, as already discussed in Section 6.2.1, are taken on surfaces whose normal vector lies in the xy plane and is inclined to the y-axis by 73deg for central vents and 60deg for lateral vents (see Figure 6.3).

Table 7.1. Parameters for the gaussian function imposing the mean velocity magnitude at the inlet.

Surface	$u_{max} \text{ (m s}^{-1}\text{)}$	$z_0 \text{ (m)}$	$y_0 \text{ (m)}$	$\sigma_z \text{ (m)}$	$\sigma_y \text{ (m)}$
central right vent	4.900	-0.05261	-0.01222	0.0244	0.0106
central left vent	4.240	0.05261	-0.01222	0.0244	0.0106
right vent	4.520	-0.57865	-0.04192	0.0244	0.0159
left vent	3.675	0.57865	-0.04192	0.0244	0.0159

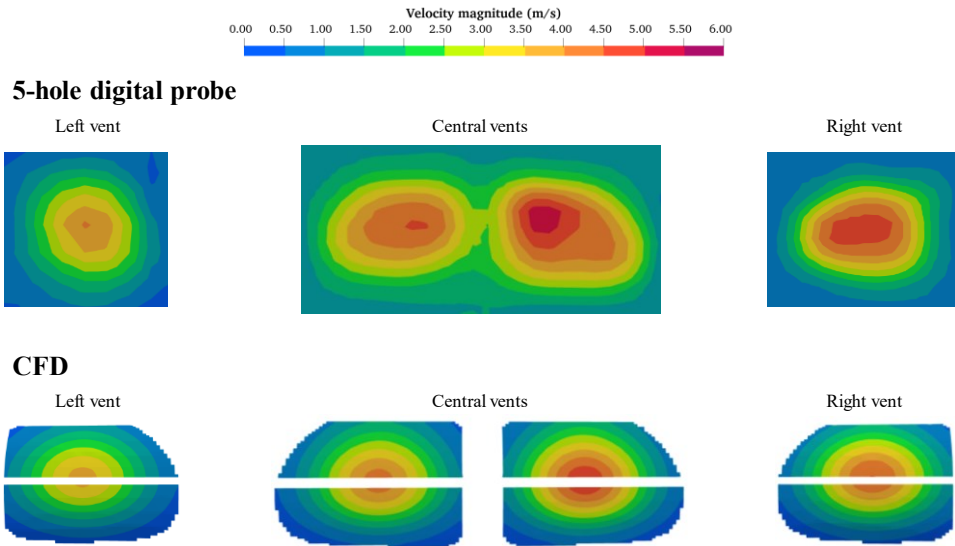


Figure 7.3. Measured (top) and numerically reproduced (bottom) mean velocity fields at the inlet vents, in case of HVAC system's fan strength set at level 3.

7.2.4 CASE STUDY

The main objective of this chapter is to assess the accuracy of URANS and LES approaches in predicting the characteristics of flow patterns arising inside car cabins, and to point out the main criticalities that may affect the CFD modelling of these indoor micro-environments. This is achieved through a careful analysis of all numerical aspects (Section 7.3) and a comparison with PIV measurements (extensively described in Section 7.4). The URANS model is then employed to study the airflow characteristics in winter and summer conditions, bringing up the main aspects affecting the well-being of the passengers. The following reference temperatures have been assumed: for winter scenario, the internal temperature is set to 20°C and the external to 10°C; for summer scenario, internal and external temperatures are 25°C and 30°C, respectively. Such outdoor temperature values were selected as representative of the typical Mediterranean climate, as claimed by Golasi et al. [234].

7.2.5 METHODOLOGY FOR THERMAL COMFORT ASSESSMENT

Despite the existence of more advanced methods for thermal comfort predictions [235–238], in this study the PMV and PPD indices (recommended by the international standards [21,233,239]) are selected as reference parameters, due to the relatively easy implementation and to the easy-to-grasp information provided about the well-being of the passengers. Their usage to assess thermal comfort in transient environments is allowed if the operative temperature does not change more than ~2 °C during a 1 h period [21,233]; however, if these temperature variations are induced by adjustments by the users (as in the scenarios here investigated) higher values may be acceptable [233].

The PMV and PPD indices have been calculated according to the ISO 7730 Standard [21] and their evolution over time has been monitored in correspondence of five points inside the domain, as explained in Section 7.5; for this purpose the *pythermalcomfort* package developed by Tartarini and Schiavon [240] was employed.

The PMV is an index allowing to predict the mean value of votes of a large group of people exposed to same environment on the 7-point thermal sensation scale given in Table 7.2, based on the heat balance of the human body.

Table 7.2. Seven-point thermal sensation scale.

+3	Hot
+2	Warm
+1	Slightly warm
0	Neutral
-1	Slightly cool
-2	Cool
-3	Cold

The PMV can be calculated using Equations (7.2) to (7.7):

$$\begin{aligned}
 PMV = & [0.303 \cdot \exp(-0.036 \cdot M) + 0.028] \\
 & \cdot \{(M - W) - 3.05 \cdot 10^{-3} \cdot [5733 - 6.99 \cdot (M - W) - p_a] \\
 & - 0.42 \cdot [(M - W) - 58.15] - 1.7 \cdot 10^{-5} \cdot M \cdot (5867 - p_a) \\
 & - 0.0014 \cdot M \cdot (34 - t_a) - 3.96 \cdot 10^{-8} \cdot f_{cl} \\
 & \cdot [(t_{cl} + 273)^4 - (\bar{t}_r + 273)^4] - f_{cl} \cdot h_c \cdot (t_{cl} - t_a)\}
 \end{aligned} \quad (7.2)$$

$$\begin{aligned}
 t_{cl} = & 35.7 - 0.028 \cdot (M - W) - I_{cl} \\
 & \cdot \{3.96 \cdot 10^{-8} \cdot f_{cl} \cdot [(t_{cl} + 273)^4 - (\bar{t}_r + 273)^4] + f_{cl} \cdot h_c \\
 & \cdot (t_{cl} - t_a)\}
 \end{aligned} \quad (7.3)$$

$$h_c = \begin{cases} 2.38 \cdot |t_{cl} - t_a|^{0.25}, & 2.38 \cdot |t_{cl} - t_a|^{0.25} > 12.1 \cdot \sqrt{v_{ar}} \\ 12.1 \cdot \sqrt{v_{ar}}, & 2.38 \cdot |t_{cl} - t_a|^{0.25} < 12.1 \cdot \sqrt{v_{ar}} \end{cases} \quad (7.4)$$

$$v_{ar} = v + v_{ag} \quad (7.5)$$

$$v_{ag} = \begin{cases} 0, & M \leq 58.2 \text{ W m}^{-2} \\ 0.3 \cdot \left(\frac{M}{58.2} - 1\right), & M > 58.2 \text{ W m}^{-2} \end{cases} \quad (7.6)$$

$$f_{cl} = \begin{cases} 1.00 + 1.290I_{cl}, & I_{cl} \leq 0.078 \text{ m}^2 \text{ K W}^{-1} \\ 1.05 + 0.645I_{cl}, & I_{cl} > 0.078 \text{ m}^2 \text{ K W}^{-1} \end{cases} \quad (7.7)$$

where M is the metabolic rate (W m^{-2}); W is the effective mechanical power (W m^{-2}); I_{cl} is the clothing insulation ($\text{m}^2 \text{ K W}^{-1}$); f_{cl} is the clothing surface area factor; t_a is the air temperature ($^{\circ}\text{C}$); \bar{t}_r is the mean radiant temperature ($^{\circ}\text{C}$); v_{ar} is the relative air velocity

combining the average air speed of the environment v plus the relative air speed resulting from the body movement v_{ag} (m s^{-1}); p_a is the water vapor partial pressure (Pa); h_c is the convective heat transfer coefficient ($\text{W m}^{-2} \text{K}^{-1}$); t_{cl} is the clothing surface temperature. On the other hand, the PPD predicts the percentage of thermally dissatisfied people who feel too cool or too warm. According to the ISO 7730 Standard, thermally dissatisfied people are those who will vote hot, warm, cool or cold on the 7-point thermal sensation scale of Table 7.2; the rest of the group will feel thermally neutral, slightly warm or slightly cool. With the PMV value determined, the PPD is calculated using Equation (7.8):

$$PPD = 100 - 95 \cdot \exp(-0.03353 \cdot PMV^4 - 0.2179 \cdot PMV^2) \quad (7.8)$$

An environment satisfying all the occupants is not possible due to the individual thermal sensation; for this reason standards specify particular criteria to be met [241]. The ISO 7730 defines three classes: (i) class A, requiring $-0.2 < PMV < 0.2$ ($PPD < 6\%$), represents a high level of expectation and is intended for spaces occupied by very sensitive and fragile persons with particular requirements; (ii) class B, with $-0.5 < PMV < 0.5$ ($PPD < 10\%$), is the level commonly adopted for design and operation; (iii) class C, with $-0.7 < PMV < 0.7$ ($PPD < 15\%$), which ensures an environment that is still considered acceptable but presents some risk of reduced occupants performance [241]. In the present study the class B is taken as reference, since this is the same level defined as acceptable by the American national standard ASHRAE 55-2020 [233].

7.3 NUMERICAL SETUP

URANS and LES simulations were performed employing the open-source OpenFOAM code, based on the finite volume formulation. Air density is assumed to vary linearly with temperature, according to the Boussinesq approximation, due to the small temperature gradients in the computational domain (see Section A.1.1 for more details).

7.3.1 SETUP FOR URANS SIMULATIONS

For URANS simulations, the SST $k-\omega$ model was selected since studies on a simplified car cabin (described in Chapter 3) revealed its better performance with respect to other eddy viscosity-based models. Transient simulations were carried out using the PIMPLE algorithm, processing the overall transient phenomenon as consecutive steady-state time steps; a time step of 0.01s was adopted and as requirement for time step convergence the scaled residuals were set $< 10^{-3}$ for pressure and $< 10^{-5}$ for velocity.

To ensure the independence of the URANS solution from the adopted grid, a mesh sensitivity analysis has been performed. Three unstructured hex-dominant meshes have been employed, generated using the *snappyHexMesh* algorithm. An x-y plane at $z=0$ (see Figure 7.4a) is available in Figure 7.4b–d for the different grids, while details of the computational meshes are summarized in Table 7.3.

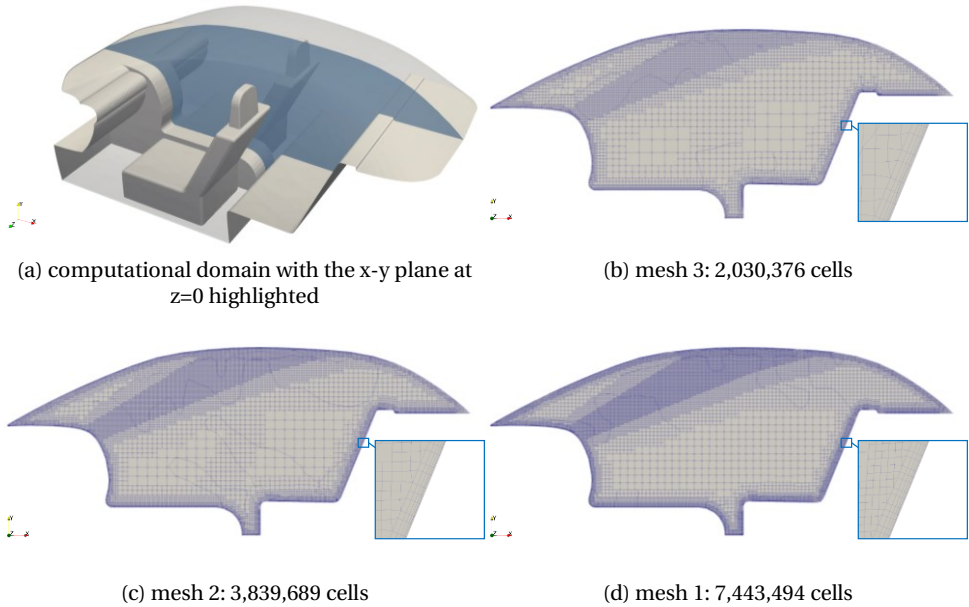


Figure 7.4. Computational domain with the x-y plane at $z=0$ highlighted (a); slices at $z=0$ of the computational grids employed for mesh sensitivity analysis (b)-(d).

Table 7.3. Details of the computational meshes.

Mesh #	Number of Cells	Skewness max	Non orthogonality max	y^+ max	y^+ min	y^+ avg
3	2,030,376	4.52	50	25.94	5.78×10^{-4}	1.45
2	3,839,689	4.77	65	24.19	3.46×10^{-4}	1.31
1	7,443,494	3.56	65	19.32	2.84×10^{-4}	1.28

All grids were refined in the jet zone (upper area of the passenger compartment) and in correspondence of solid walls, where a boundary layer region composed of 5 layers has been defined; this construction strategy allowed accurate description of the gradients of the solution and led to the maximum, minimum and average y^+ values reported in Table 7.3. Grid convergence tests were performed considering the Richardson error estimation procedure [242]. According to such criterion, the average error in a fine grid solution and in a coarse grid solution is determined by:

$$E_{Mesh1}^{fine} = \frac{f_2 - f_1}{1 - r_f^p} \quad (7.9)$$

$$E_{Mesh2}^{coarse} = \frac{r_f^p (f_2 - f_1)}{1 - r_f^p} \quad (7.10)$$

where P is the formal order of accuracy of the algorithm, calculated as follows:

$$P = \frac{\ln \left(\frac{f_3 - f_2}{f_2 - f_1} \right)}{\ln(r_f)} \quad (7.11)$$

In the expressions above f_1 , f_2 and f_3 are numerical solutions obtained with grid spacing equal to h_1 , h_2 and h_3 respectively (with subscript 1 indicating the finest grid in the present notation) and $r_f = h_i/h_{i-1} > 1$ is the refinement factor adopted for the generation of the different grids. A constant refinement factor equal to 1.3 was adopted here, and the average formal order of accuracy of the algorithm is equal to 3.36. Figure 7.5 shows the velocity profiles compared for the sensitivity analysis, obtained with the three selected grids at $x=0.25$ m and $z=-0.03$ m (i.e., the measuring plane of the PIV experiment). The location where the profiles are extracted is highlighted in yellow colour on the right picture in Figure 7.5, portraying the abovementioned x-y plane at $z=-0.03$ m. The average error obtained for Mesh 2, E_{Mesh2}^{coarse} , is equal to 4.03% while the average error obtained for Mesh 1 E_{Mesh1}^{fine} is equal to 2.85%. Being the error below the 5%, it can be concluded that Mesh 2 provides nearly grid-independent results and has been selected for numerical investigations. Since the flow field is affected by periodic temporal fluctuations in the jet region, grid convergence study and numerical versus experimental comparison were conducted in terms of time-averaged velocity fields. Targeted analyses were conducted to establish the proper averaging time interval, finding that 25 seconds are needed to have a deviation of less than 1% among the predicted mean velocity profiles.

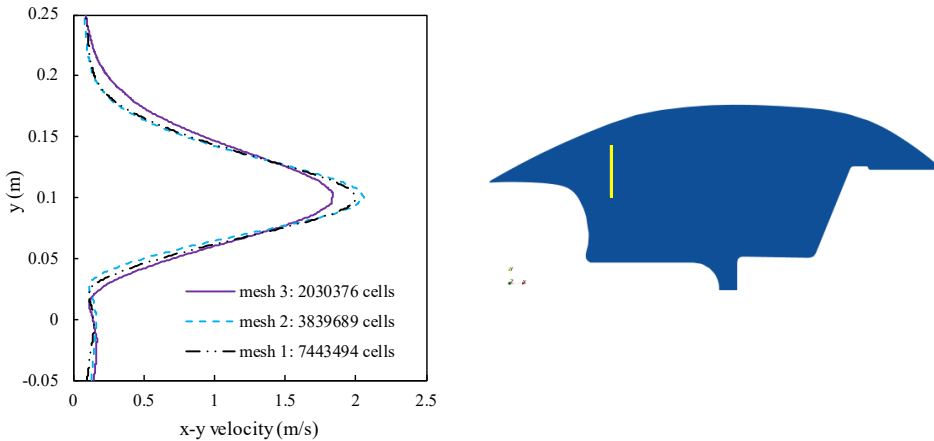


Figure 7.5. Velocity profiles obtained at $x=0.25$ m and $z=-0.03$ m (measuring plane, shown on the right), for the three grids considered in the sensitivity analysis.

7.3.2 SETUP FOR LES SIMULATIONS

The LES simulations were initialized with the results from the URANS simulation and carried out on the finest grid (i.e., Mesh 1). Pressure-velocity coupling was solved with the

PISO algorithm, setting the maximum Courant number $Co=5$ (corresponding to a time step of 0.0002 s).

Two different subgrid scale (SGS) models were tested: the WALE model with default coefficients [243] and the dynamic KE model [244]. Simulations have included a start-up phase equal to five flow-through times $T_{FT}=0.61$ s (to make the flow develop and reach a condition of stable fluctuations) and then a time-averaging phase (to get the mean solution) equal to 12 s. T_{FT} has been calculated as the ratio of the extension of the computational domain in the x-direction to the mean flow velocity at the inlet vents.

To assess the suitability of Mesh 1 for LES computations, the LES index of quality LES_{IQ} is calculated according to the following expression by Celik et al. [245]:

$$LES_{IQ} = \frac{k_{resolved}}{k_{total}} = \frac{1}{1 + 0.05 \cdot \left(\frac{\nu + \nu_{SGS}}{\nu}\right)^{0.53}} \quad (7.12)$$

where ν is the molecular viscosity and ν_{SGS} is the SGS viscosity; this parameter, representing the ratio of the resolved to the total turbulent kinetic energy, must be greater than 80% for a well-resolved computation [246]. Figure 7.6 shows the contours of LES_{IQ} on the x-y plane at $z=-0.03$ m, for the WALE model; the minimum value is 79.4% whereas the average on the plane is 92.5%, therefore it can be argued that the LES computations resolve a large fraction of the total turbulent kinetic energy and that the adopted grid is suitable for the investigations.

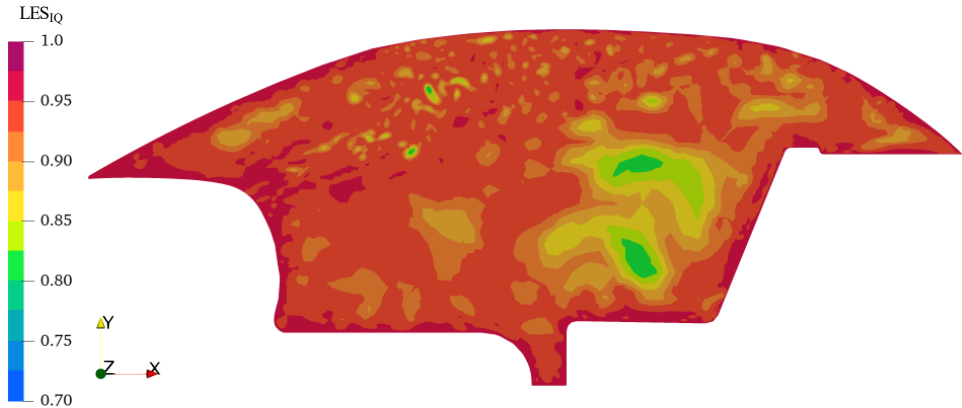


Figure 7.6. Contours of LES_{IQ} on the x-y plane at $z=-0.03$ m (PIV measuring plane) for the WALE model.

7.4 NUMERICAL MODEL VALIDATION AGAINST PIV MEASUREMENTS

In this section, the validation of the numerical model is presented by comparing measured and predicted velocity fields within the longitudinal plane at $z=-0.03$ m (PIV measuring plane). The boundary conditions imposed for the validation of the numerical model are available in Table 7.4; I indicates the turbulence intensity, ℓ (m) is the turbulent length scale, L (m) is the characteristic length, assumed equal to the width of the inlet sections.

Patches not specified in Figure 7.2 have been modelled as walls and distinguished between glazed (highlighted in light-blue colour in Figure 7.2) and non-glazed surfaces (highlighted in grey colour in Figure 7.2). Regarding temperature, non-glazed walls have been modelled as adiabatic while at glazed surfaces a fixed value has been imposed, equal to the temperature of the measurement environment during the experiments (see Section 7.2.1). In URANS simulations, a Gaussian function was imposed for velocity at the inlet, defined by experimentally fitted coefficients (see Section 7.2.3); in LES simulations, the Divergence Free Synthetic Eddy Method (DFSEM) boundary condition was adopted for the generation of synthetic turbulence, imposing the same Gaussian function for the mean velocity and mapping the Reynolds stresses and the turbulent length scale from the RANS solution [247,248]. Overall, the HVAC system provides an air change per hour of 60 h^{-1} .

In Figure 7.7 the experimental (bottom picture) and URANS (top picture) mean velocity contours are shown; the experimental field of view is superimposed on the CFD field to display its extent in comparison with the whole computational domain. Figure 7.8, instead, depicts the instantaneous velocity field predicted with the WALE model after 5 seconds; from this picture, it is possible to observe the jet destabilization and the turbulent mixing, aspects that cannot be captured by URANS.

In Figure 7.9 mean velocity profiles in five different sections (i.e., $x=0.25 \text{ m}$, $x=0.35 \text{ m}$, $x=0.45 \text{ m}$, $x=0.55 \text{ m}$ and $x=0.65 \text{ m}$) are outlined; the locations where the profiles are extracted are shown in Figure 7.7 with yellow-coloured vertical lines.

Table 7.4. Boundary conditions set for comparison with PIV measurements.

Surface	BC for mean velocity	BC for pressure	BC for temperature	BC for k	BC for ω
inlet sections	see Section 7.2.3	$\frac{\partial p}{\partial \mathbf{n}} = 0$	$T = 43.6 \text{ }^\circ\text{C}$	$I = 15\%$	$\ell = 0.07L$
outlet section	$\frac{\partial \mathbf{u}}{\partial \mathbf{n}} = 0$	$p = 101325 \text{ Pa}$	$\frac{\partial T}{\partial \mathbf{n}} = 0$	$\frac{\partial k}{\partial \mathbf{n}} = 0$	$\frac{\partial \omega}{\partial \mathbf{n}} = 0$
glazed walls	$\mathbf{u} = 0$	$\frac{\partial p}{\partial \mathbf{n}} = 0$	$T = 30.2 \text{ }^\circ\text{C}$	standard wall functions	
non-glazed walls	$\mathbf{u} = 0$	$\frac{\partial p}{\partial \mathbf{n}} = 0$	$\frac{\partial T}{\partial \mathbf{n}} = 0$	standard wall functions	

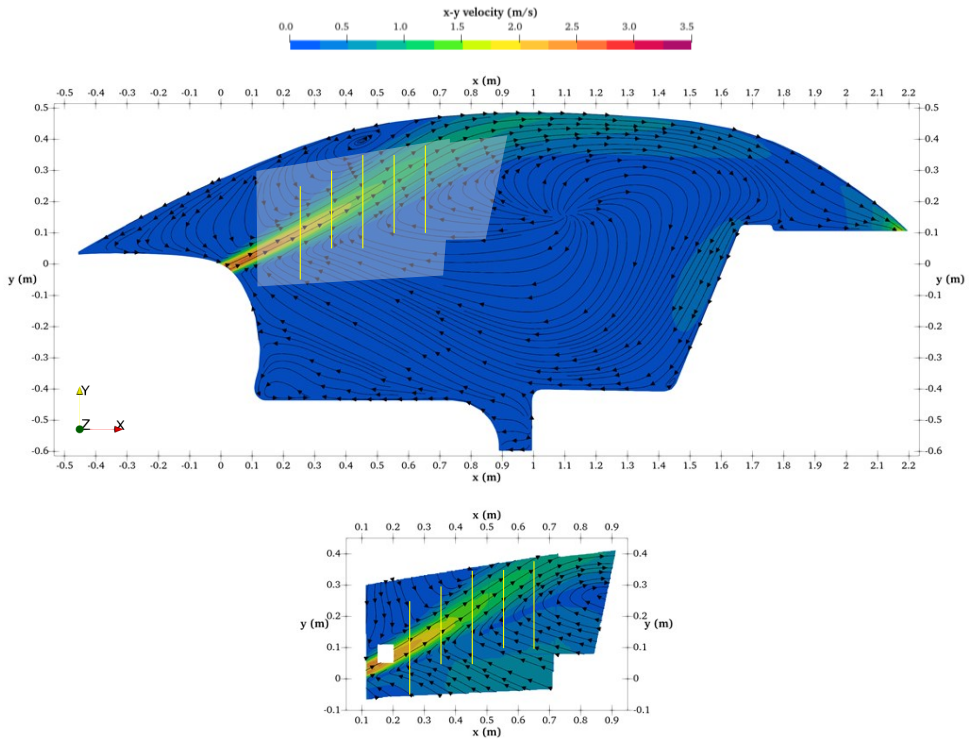


Figure 7.7. URANS (top) and PIV (bottom) velocity contours on the longitudinal plane at $z = -0.03$ m (measuring plane), together with the 2D streamlines. The experimental field of view is superimposed on the CFD field.

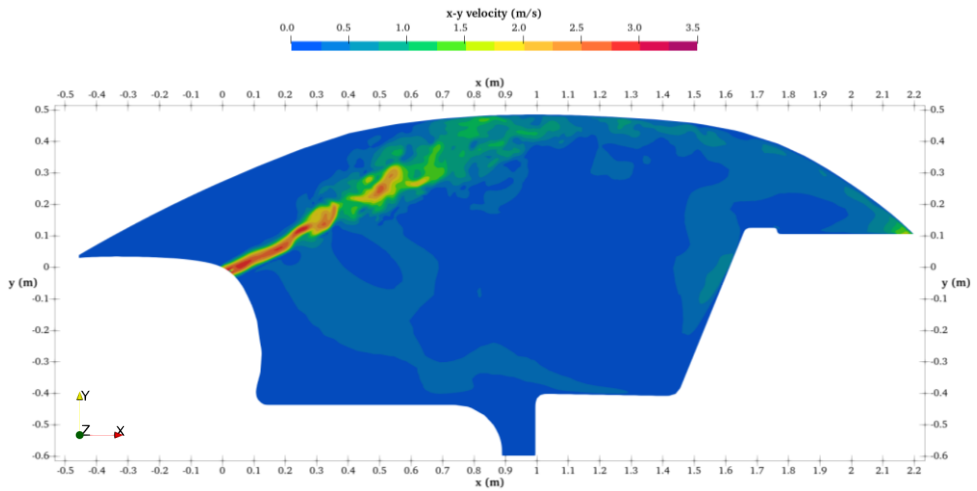


Figure 7.8. Instantaneous velocity contours predicted with the WALE model, on the longitudinal plane at $z = -0.03$ m (measuring plane), after 5 seconds of simulated time.

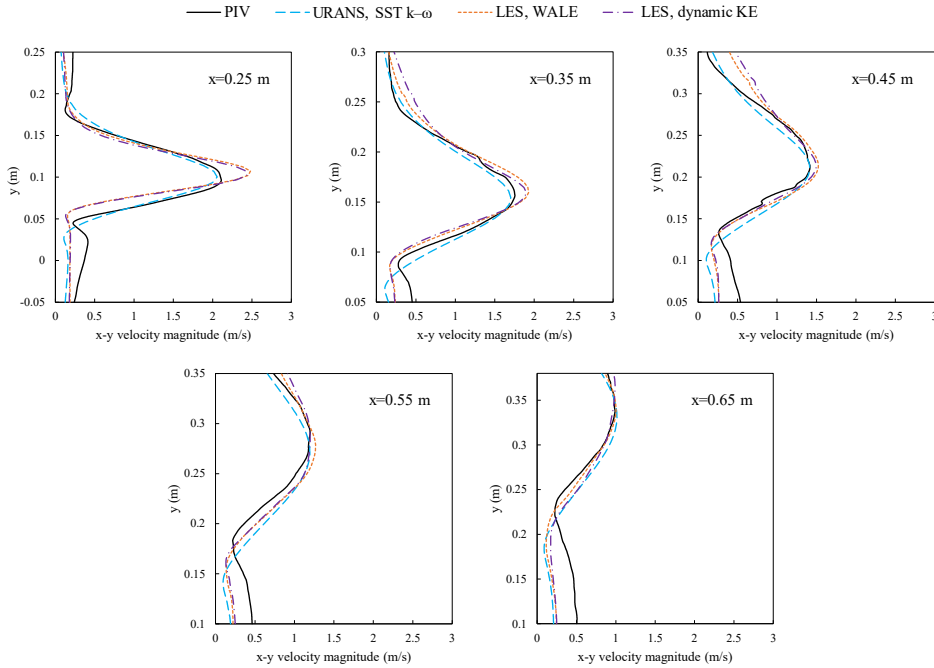


Figure 7.9. Experimental and predicted velocity profiles comparison in five different sections within the selected plane at $z=-0.03\text{m}$: $x=0.25\text{m}$, $x=0.35\text{m}$, $x=0.45\text{m}$, $x=0.55\text{m}$ and $x=0.65\text{m}$.

The capability of the URANS and LES models to reproduce the experiments was assessed quantitatively by calculating the RMSE between the predicted and measured data (Equation (3.7)). In addition, the Normalized RMSE (NRMSE) was calculated dividing the RMSE by the maximum velocity value measured along each profile, namely 2.11 m s^{-1} , 1.76 m s^{-1} , 1.42 m s^{-1} , 1.20 m s^{-1} and 0.99 m s^{-1} for $x=0.25\text{ m}$, $x=0.35\text{ m}$, $x=0.45\text{ m}$, $x=0.55\text{ m}$ and $x=0.65\text{ m}$ respectively. The results, summarized in Table 7.5, show a very good agreement existing between predicted and measured velocity fields with errors below the order of 0.25 m s^{-1} ($\sim 5\%$ of the maximum velocity at the vent exit). In addition to the errors calculated for the five sections of interests, Table 7.5 also provides the global errors considering the entire region where PIV measurements are available. In this case, NRMSEs are obtained dividing the RMSE by the maximum experimental velocity within the plane, which is equal to 2.49 m s^{-1} . Global values confirm the close agreement between the simulations and the experiments.

On the whole, the shape of the flow is well predicted by the CFD models; buoyancy effects are properly described as well, with profiles shifting upwards when the distance from the inlet vents increases, in accordance with the experimental data.

Both LES models initially overestimate the velocity peak; this is probably because the Reynolds stresses given as input to the DFSEM boundary conditions are not measured but mapped from the URANS simulations. One solution to improve the accuracy of LES results could thus be measuring the Reynolds stress tensor at the inlet sections; this would provide a more precise description of the turbulence anisotropy and help minimize discrepancies with the PIV data. However, performing such measurements poses challenges due to the non-planar surface of the inlet vents and requires a targeted

experimental campaign, which is beyond the scope of the present work. In the profiles extracted at a greater distance from the inlet, the WALE SGS model outperforms the SST $k-\omega$, especially at $x=0.55$ m and $x=0.65$ m. On the other hand, the dynamic KE SGS model exhibits the worst behaviour and has a better agreement with PIV data only at $x=0.55$ m and $x=0.65$ m, probably due to the initialization of the turbulent kinetic energy from precursor URANS simulation. In general, both WALE and dynamic KE models better describe the shape of the jet at the bottom; however, all models underestimate the velocity value in the area below the bulk of the jet flow. This can be primarily attributed to the simplifications made for the reproduction of the in-vehicle environment, which are more substantial in the lower part of the domain (first among all, not having modelled the presence of the steering wheel and of the gearshift, which can create disturbances to the flow field in their surroundings). Overall, URANS SST $k-\omega$ model is sufficiently accurate in predicting the airflow patterns (if proper attention is given to the design of the CFD simulation) and is appreciably outperformed by LES only in the turbulent mixing region.

Table 7.5. RMSE and NRMSE between predicted and measured velocity values, for the five sections of interest and for the entire region where PIV measurements are available.

	RMSE (NRMSE)					
	x=0.25 m	x=0.35 m	x=0.45 m	x=0.55 m	x=0.65 m	Global
URANS	0.142 m s ⁻¹	0.131 m s ⁻¹	0.176 m s ⁻¹	0.181 m s ⁻¹	0.189 m s ⁻¹	0.203 m s ⁻¹
SST $k-\omega$	(6.7%)	(7.5%)	(12.4%)	(15.1%)	(19.1%)	(8.17%)
LES WALE	0.242 m s ⁻¹	0.130 m s ⁻¹	0.167 m s ⁻¹	0.143 m s ⁻¹	0.161 m s ⁻¹	0.207 m s ⁻¹
	(11.5%)	(7.4%)	(11.8%)	(11.9%)	(16.2%)	(8.34%)
LES	0.234 m s ⁻¹	0.158 m s ⁻¹	0.182 m s ⁻¹	0.133 m s ⁻¹	0.155 m s ⁻¹	0.206 m s ⁻¹
dynamic KE	(11.1%)	(9.0%)	(12.8%)	(11.1%)	(15.6%)	(8.29%)

A more careful comparison between the simulated and measured mean flow fields can be made considering the distributions of the mean z -vorticity (Ω_z , s⁻¹) shown in Figure 7.10, where the positive z direction is oriented away from the x - y plane. The numerical fields are represented on the PIV measuring plane for a more effective visualization.

The mean z -vorticity contours in Figure 7.10 emphasize the capability of all the adopted models in predicting the mean flow structures, both inside and outside the main bulk of the jet. In fact, the strong vortices at the edges of the jet (arising from the interaction of the moving jet with the still surroundings) are well reproduced as well as the vorticity distribution away from the jet core.

The close agreement between the experimental and numerical data is confirmed when looking at Figure 7.11, which displays the difference between the predicted and measured z -vorticity. Outside of the jet core, the absolute difference is almost everywhere below 10 s⁻¹; the largest differences are located in the bottom-left corner, confirming that the simplification of the geometry in the lower part of the domain can reduce the accuracy of the numerical models in reproducing the flow characteristics in that area.

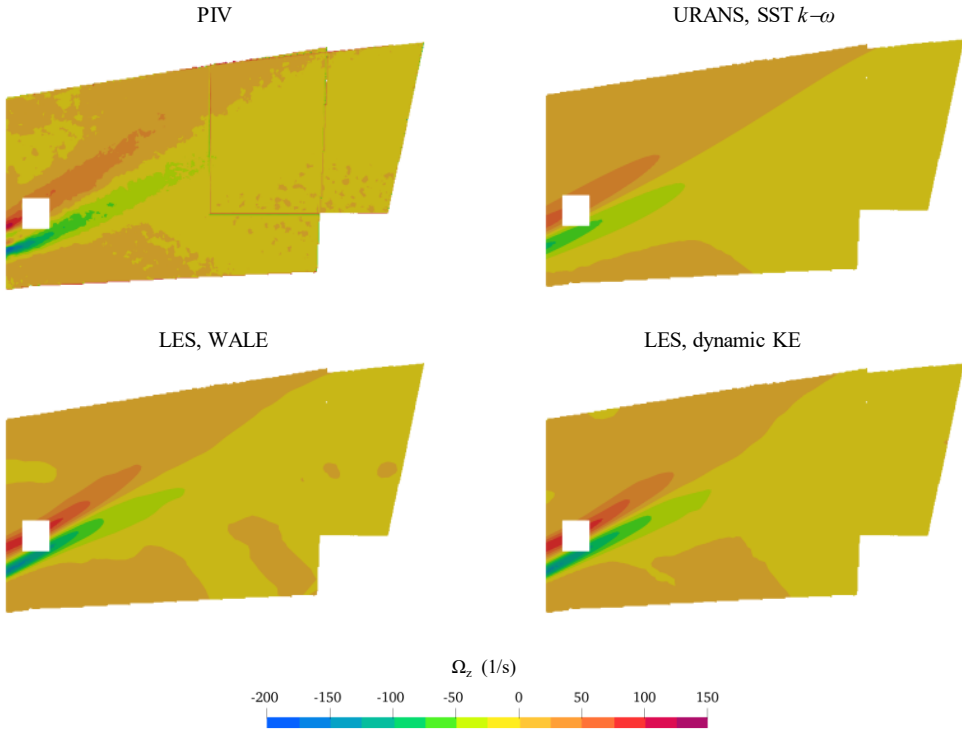


Figure 7.10. Experimental and numerical distribution of the mean z-vorticity. The numerical fields are represented on the PIV measuring plane for a more effective visualization.

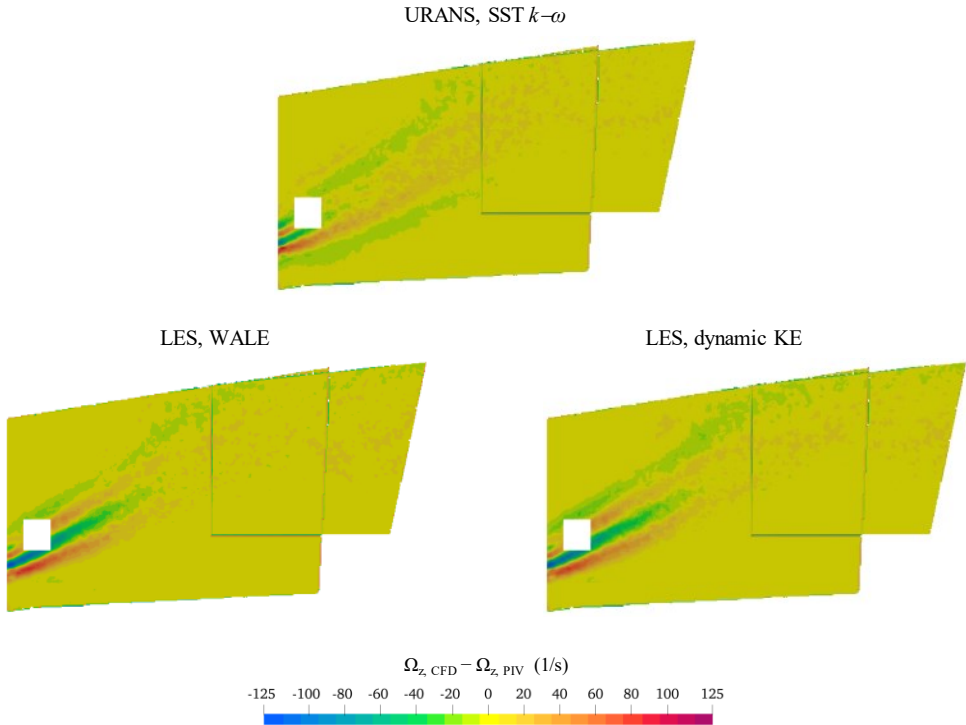


Figure 7.11. Spatial distribution of the difference between the predicted and measured z -vorticity, obtained with the different turbulence models.

To assess the performance of the adopted CFD models in predicting not only the mean flow behavior but also the fluctuations in the velocity fields, a comparison between numerical and PIV data is made in terms of turbulent kinetic energy (TKE). Figure 7.12 displays the measured and predicted TKE fields (with the latter represented on the PIV measuring plane for effective visualization), while Figure 7.13 presents a comparison across the same five sections previously analyzed (i.e., $x=0.25$ m, $x=0.35$ m, $x=0.45$ m, $x=0.55$ m and $x=0.65$ m). Overall, the LES simulations yield higher TKE values than URANS simulations, resulting in better agreement with the measured values except at $x=0.25$ m. In this section, the LES models exhibit higher RMSEs than URANS, attributed to upward shifts in the profiles (as observed in Figure 7.9 for the velocity profiles). Nevertheless, the LES models provide a better prediction of the profile shape. Table 7.6 summarizes the RMSE and NRMSE values obtained for the different sections of interest and for the entire region where PIV measurements are available. NRMSE values are calculated by dividing the RMSE by the maximum experimental value along each profile (namely $0.563 \text{ m}^2 \text{ s}^{-2}$, $0.603 \text{ m}^2 \text{ s}^{-2}$, $0.509 \text{ m}^2 \text{ s}^{-2}$, $0.444 \text{ m}^2 \text{ s}^{-2}$ and $0.337 \text{ m}^2 \text{ s}^{-2}$ for $x=0.25$ m, $x=0.35$ m, $x=0.45$ m, $x=0.55$ m and $x=0.65$ m respectively) for errors calculated for each profile, and the maximum within the whole measuring plane for global values (i.e., $0.637 \text{ m}^2 \text{ s}^{-2}$).

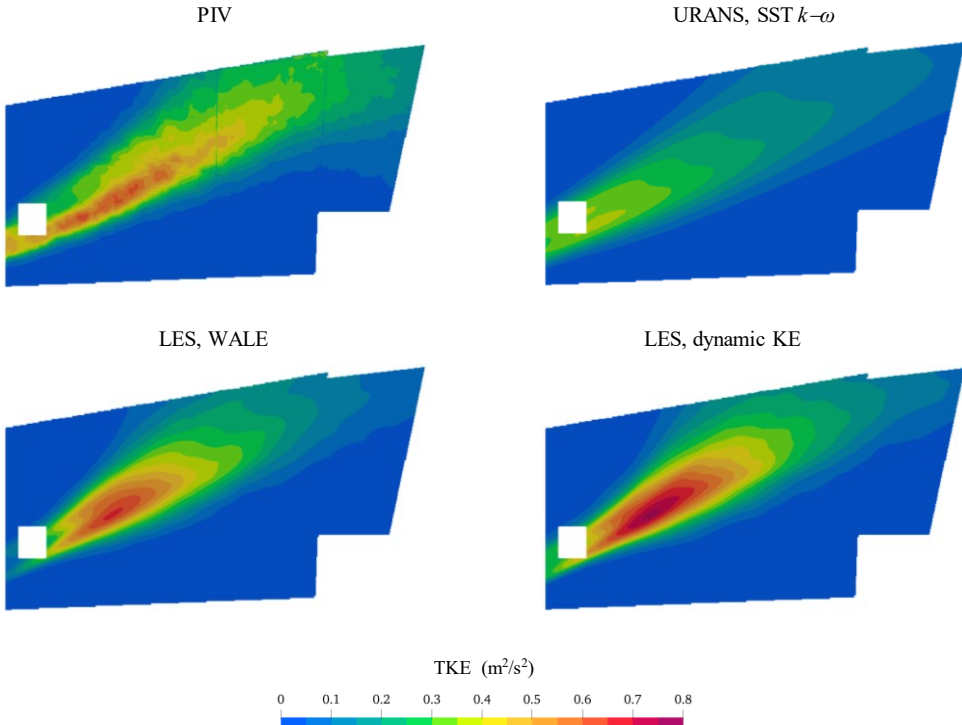


Figure 7.12. Experimental and numerical distribution of the turbulent kinetic energy. The numerical fields are represented on the PIV measuring plane for a more effective visualization.

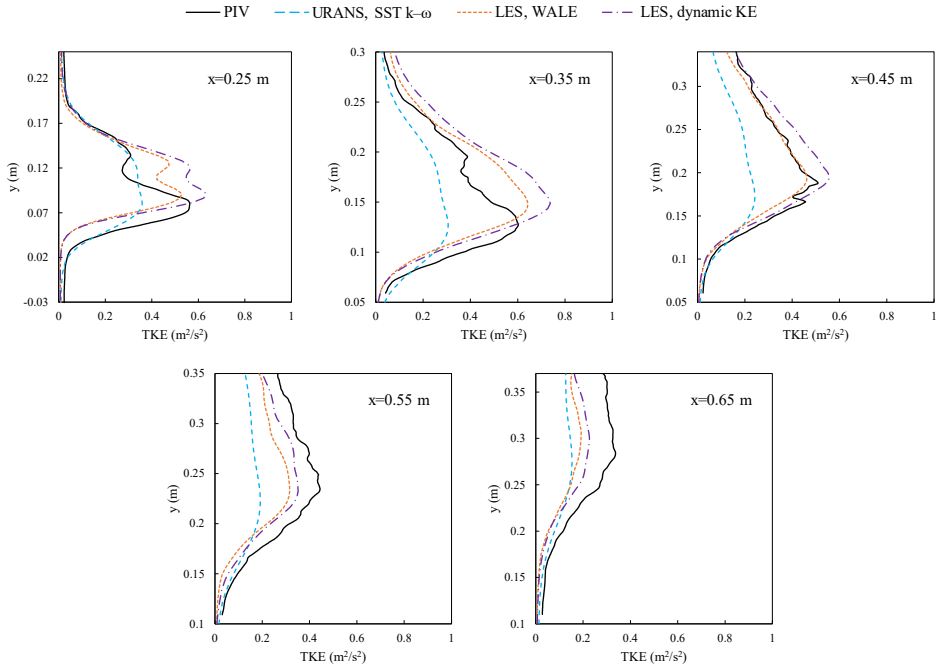


Figure 7.13. Experimental and predicted turbulent kinetic energy profiles comparison in five different sections within the selected plane at $z=-0.03\text{m}$: $x=0.25\text{m}$, $x=0.35\text{m}$, $x=0.45\text{m}$, $x=0.55\text{m}$ and $x=0.65\text{m}$.

7

Table 7.6. RMSE and NRMSE between predicted and measured TKE values, for the five sections of interest and for the entire region where PIV measurements are available.

	RMSE (NRMSE)					
	$x=0.25\text{ m}$	$x=0.35\text{ m}$	$x=0.45\text{ m}$	$x=0.55\text{ m}$	$x=0.65\text{ m}$	Global
URANS SST $k-\omega$	$0.067\text{ m}^2\text{ s}^{-2}$ (11.98%)	$0.140\text{ m}^2\text{ s}^{-2}$ (23.16%)	$0.133\text{ m}^2\text{ s}^{-2}$ (26.18%)	$0.158\text{ m}^2\text{ s}^{-2}$ (35.61%)	$0.118\text{ m}^2\text{ s}^{-2}$ (34.96%)	$0.101\text{ m}^2\text{ s}^{-2}$ (15.90%)
LES WALE	$0.097\text{ m}^2\text{ s}^{-2}$ (17.30%)	$0.098\text{ m}^2\text{ s}^{-2}$ (16.26%)	$0.035\text{ m}^2\text{ s}^{-2}$ (6.81%)	$0.092\text{ m}^2\text{ s}^{-2}$ (20.64%)	$0.101\text{ m}^2\text{ s}^{-2}$ (29.85%)	$0.085\text{ m}^2\text{ s}^{-2}$ (13.27%)
LES dynamic KE	$0.120\text{ m}^2\text{ s}^{-2}$ (21.24%)	$0.133\text{ m}^2\text{ s}^{-2}$ (22.07%)	$0.053\text{ m}^2\text{ s}^{-2}$ (10.38%)	$0.062\text{ m}^2\text{ s}^{-2}$ (13.85%)	$0.078\text{ m}^2\text{ s}^{-2}$ (23.16%)	$0.080\text{ m}^2\text{ s}^{-2}$ (12.55%)

Although the dynamic KE model shows worse agreement with experiments than the WALE model in the five investigated sections, it has lower global errors. This can be explained by examining Figure 7.14, which displays the difference between predicted and measured TKE for all turbulence models. In the jet core, the dynamic KE exhibits worse agreement, while the WALE model demonstrates a poorer performance in the bottom-left region (closer to the inlet sections), resulting in a slightly worse overall agreement with the experiments. Figure 7.14 also highlights that the URANS SST $k-\omega$ underestimates the TKE in the jet core, and all models underestimate the TKE in the bottom-left region.

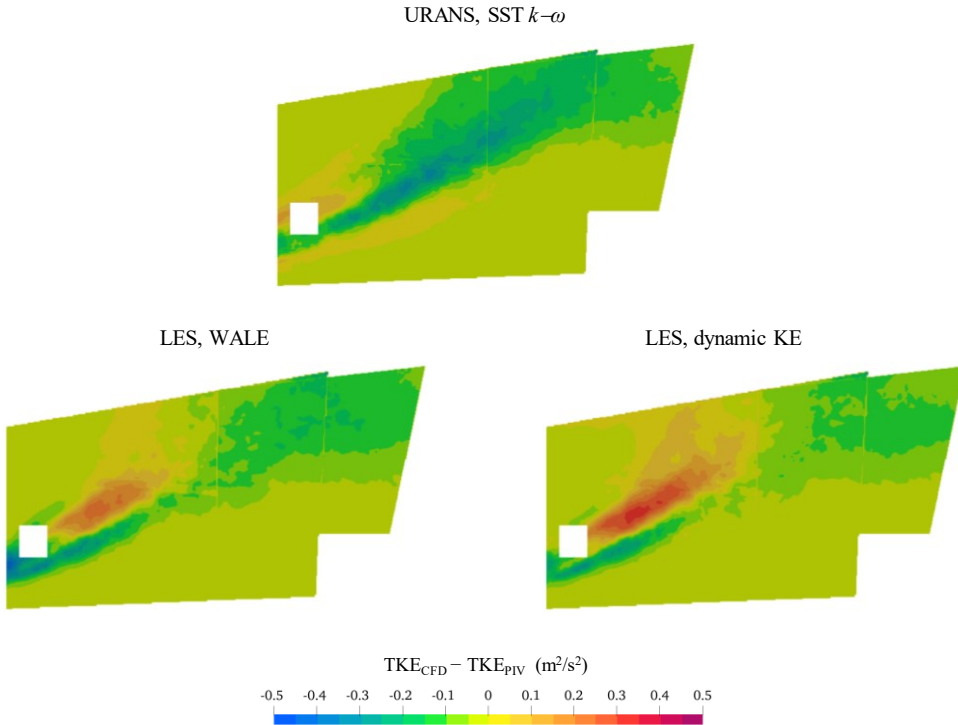


Figure 7.14. Spatial distribution of the difference between the predicted and measured turbulent kinetic energy, obtained with the different turbulence models.

The simulations were performed on a Dell Precision 7920 Rack with 104 CPUs and 64 GB RAM. URANS computations took 4.7 days to complete on the finest grid; LES took about twice the time required by URANS. Due to the less computational resources required, URANS approach has been selected for the numerical investigations presented in the next section.

7.5 DISCUSSION OF VELOCITY AND TEMPERATURE FIELDS, AND THERMAL COMFORT ANALYSIS

The validated URANS model is here applied to study the thermal-fluid dynamics fields inside the car cabin in winter and summer conditions. The same boundary conditions as the validation scenario were adopted, except for the temperature values at the inlet sections and at the glazed walls, listed in Table 7.7 and selected according to the climatic conditions outlined in Section 0. Since the thermal resistance of windows and windshield is negligible (due to their fine thickness and to the large convection heat transfer coefficients in forced convection), it is reasonable to assume the glazed walls temperature equal to the outdoor temperature.

Table 7.7. Subset of boundary conditions imposed for temperature in winter and summer scenarios.

Surface	Winter scenario	Summer scenario
inlet sections	$T = 20\text{ }^{\circ}\text{C}$	$T = 25\text{ }^{\circ}\text{C}$
glazed walls	$T = 10\text{ }^{\circ}\text{C}$	$T = 30\text{ }^{\circ}\text{C}$

Investigated scenarios cover 10 minutes of simulated time, which are sufficient to achieve a quasi-steady state condition (as discussed in Section 7.5.1). Five virtual probes were placed in the computational domain as shown in Figure 7.15, representing the position of the passengers, to monitor the evolution over time of PMV and PPD indices; such an approach allows to find out whether the thermal comfort of the passengers is ensured and to determine the amount of time required to achieve acceptable thermo-hygro-metric conditions. Mean temperature and velocity fields are also discussed by comparing winter and summer scenarios.

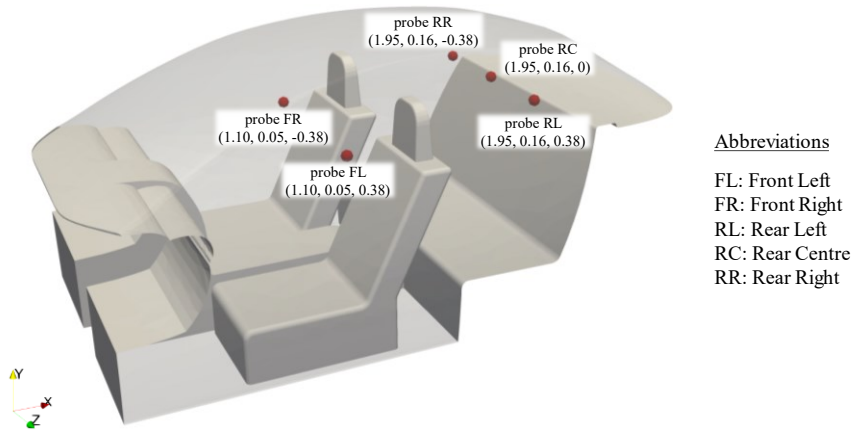


Figure 7.15. Positions inside the domain, with coordinates expressed in meters, of the virtual probes placed to monitor the evolution over time of PMV and PPD.

7.5.1 NUMERICAL MEAN VELOCITY AND TEMPERATURE FIELDS

In the present section, mean velocity and temperature fields are discussed by comparing winter and summer scenarios.

In Figure 7.16 the trend over time of temperature and velocity values in correspondence of the five virtual probes is depicted. After 60 seconds the velocity field already has stable fluctuations whereas, as expected, thermal phenomena have a longer evolution time and 300 seconds are required to reach a steady state. The averaging time interval was selected accordingly, discarding the first minutes and considering from the fifth minute (i.e., 300 s) onward; in so doing, the mean temperature fields are not affected by the initial transients and the mean velocity fields are not affected by the initial thermal instabilities.

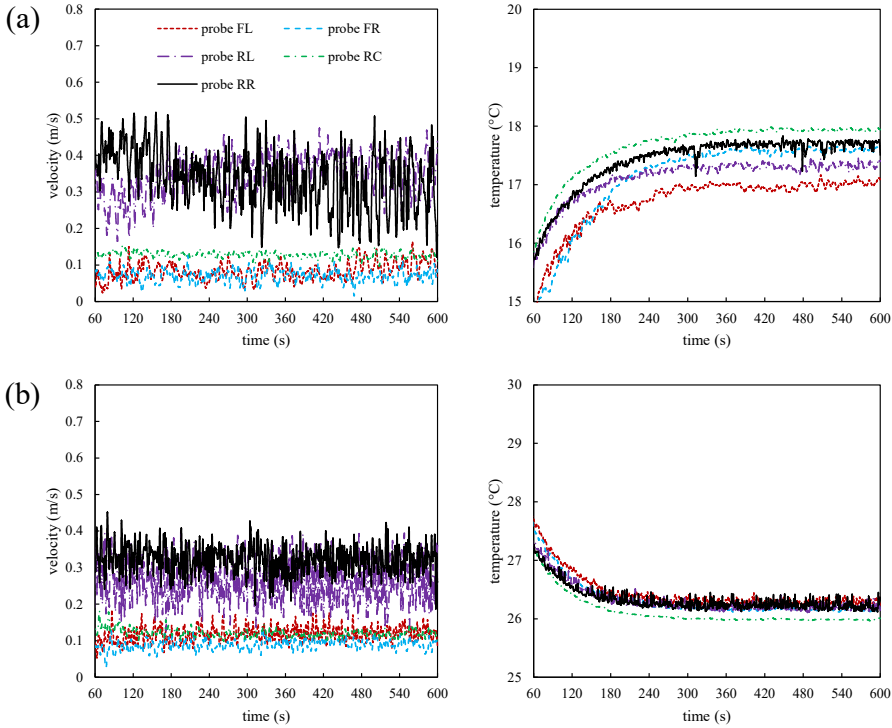


Figure 7.16. Trend over time of velocity and temperature values in correspondence of the five virtual probes placed in the domain, for (a) winter and (b) summer conditions.

Figure 7.17 shows the streamlines of the airflow entering the domain from the inlet vents, coloured by mean velocity, in winter and summer scenarios. Motion structures are very similar, with the jet flows directed towards the rear compartment without being deflected and creating a recirculating zone near the rear seats; the different thermal regime has a very little effect on the velocity fields, since the temperature field is fairly uniform as can be seen by Figure 7.18 and Figure 7.19, where temperature contours are displayed on the x-y slices intersecting the driver and passenger seats respectively. Only a small difference can be observed in the direction of the central jets, that in winter scenario are slightly shifted upwards owing to the buoyancy forces.

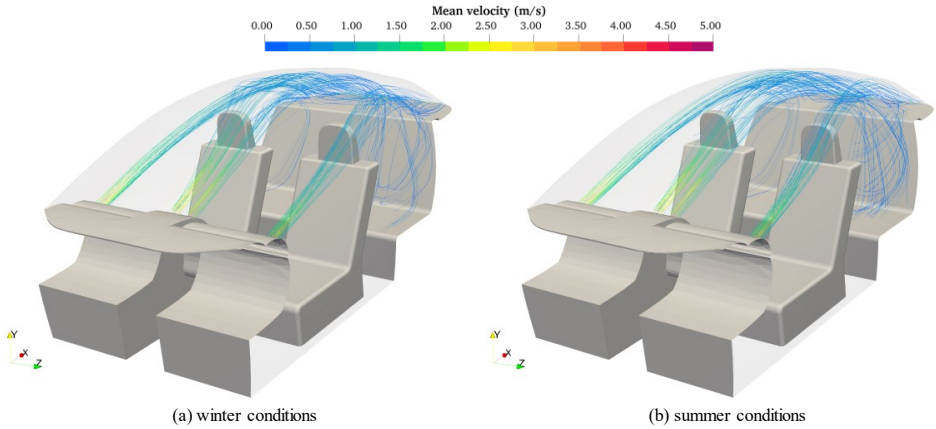


Figure 7.17. Streamlines of the airflows entering the domain from the inlet vents, coloured by mean velocity magnitude, for (a) winter and (b) summer conditions.

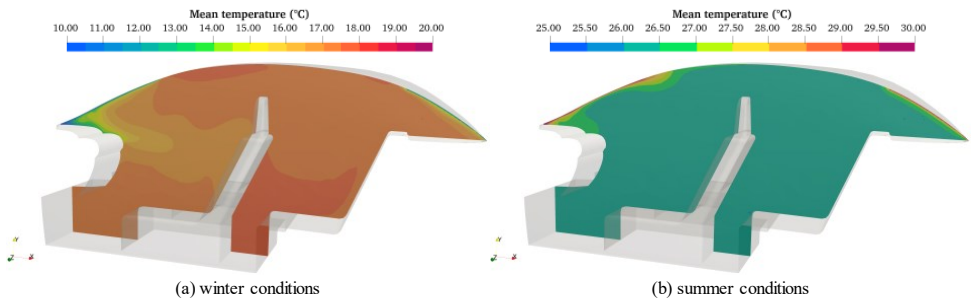


Figure 7.18. Mean temperature contours on the driver side (x-y slice at $z=0.38$ m, i.e., driver's seat) for (a) winter and (b) summer conditions.

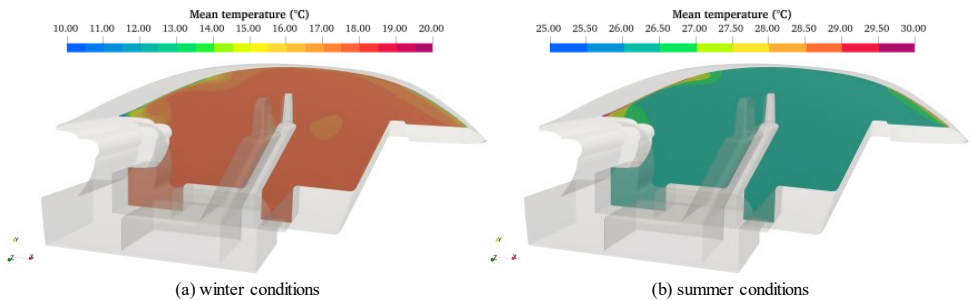


Figure 7.19. Mean temperature contours on the passenger side (x-y slice at $z=-0.38$ m, i.e., passenger's seat) for (a) winter and (b) summer conditions.

The small influence of temperature field on the airflow patterns is confirmed by comparing velocity contours and streamlines in winter and summer on the driver (Figure 7.20) and passenger side (Figure 7.21). Flow patterns are very similar, with the air directed towards the parcel shelf and a recirculating zone being created in the rear compartment. A further aspect which must be addressed is the influence of the asymmetric air supply by the HVAC system on the velocity fields. By comparing Figure 7.20a with Figure 7.21a (winter conditions) and Figure 7.20b with Figure 7.21b (summer conditions), it is possible to observe that the passenger side is characterized by higher velocities, and this is due by the higher velocity of the air supplied by the right vents with respect to the left vents (see Figure 7.3 and Table 7.1). However, this asymmetry does not affect the thermal comfort of the occupants dramatically, as discussed in Section 7.5.2, since such differences are confined to the upper part of the passenger compartment.

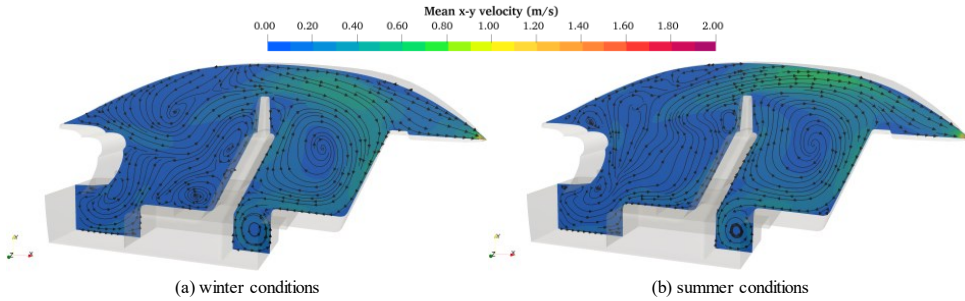


Figure 7.20. Mean x-y velocity contours and 2D streamlines on the driver side (x-y slice at $z=0.38$ m) for (a) winter and (b) summer conditions.

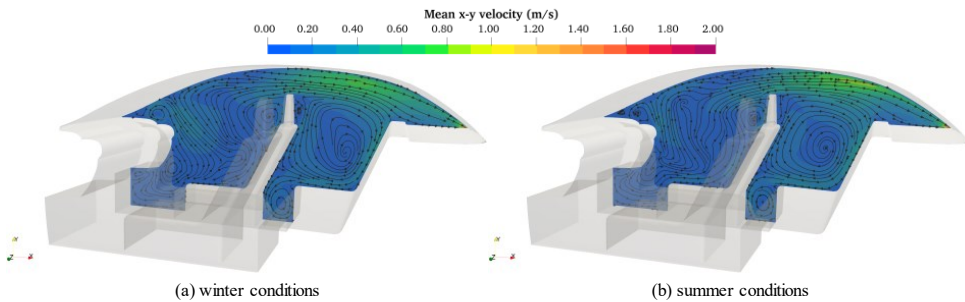


Figure 7.21. Mean x-y velocity contours and 2D streamlines on the passenger side (x-y slice at $z=-0.38$ m) for (a) winter and (b) summer conditions.

Finally, in Figure 7.22 the mean z velocity contours are shown, together with the 2D streamlines, for the x-z plane intersecting the mouth of possible passengers (i.e., at $y=0.1$ m), for winter and summer scenarios. In this case, important differences can be highlighted both in flow patterns and velocity values. On the other hand, in both conditions the velocity component in the z direction is not negligible and there are significant recirculation zones in the rear seats; in addition, in the front seats the streamlines are directed from the two sides towards the centre. All these three features may be decisive in the transmission of respiratory viruses, thus posing a risk for the occupants.

It must be pointed out that the presence of the passengers would affect the air flow patterns inside the car cabin and their contribution inside a real cabin environment will be studied in future works. The main scope of the present study is, in fact, to numerically reproduce the experiments (so developing a reliable validated tool to be used for many purposes) and to provide insights into the design of CFD simulations of a real car cabin. Since the PIV measurements were taken in the absence of occupants, the latter were not included in the numerical simulations. In addition, such an approach allows to isolate the only contribution of the HVAC system, which has been proven to have a strong influence on the distribution of exhaled respiratory droplets inside car cabins (see Chapter 3).

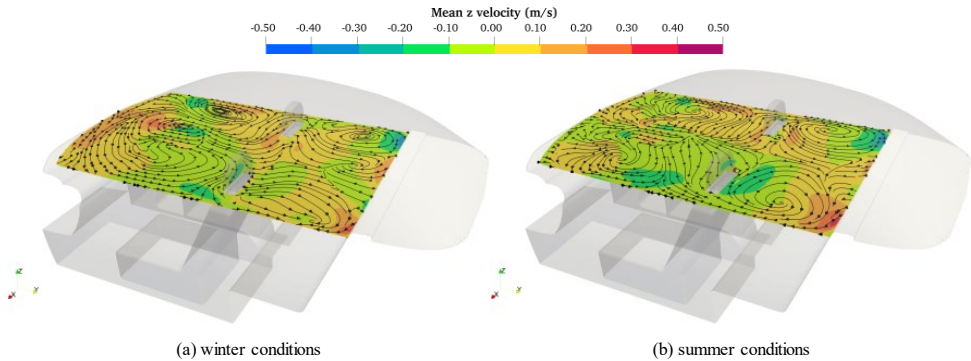


Figure 7.22. Mean z velocity contours and 2D streamlines on the x - z slice at $y=0.1$ m for (a) winter and (b) summer conditions.

7

7.5.2 THERMAL COMFORT ASSESSMENT

As explained in Section 7.2.5, PMV and PPD indices were evaluated according to the ISO 7730 Standard using the *pythermalcomfort* package [240]. The mean radiant temperature was calculated as the average walls temperature; the relative humidity was determined according to the model developed in Ref. [249], based on the moisture balance; the metabolic rate was set to 1.5 met (1 metabolic unit = 1 met = 58.2 W m^{-2}) for the driver and to 1.2 met for other passengers [240], and the clothing insulation set to 0.5 clo (1 clothing unit = 1 clo = $0.155 \text{ m}^2 \text{ K W}^{-1}$) for typical summer garment and to 1 clo for typical winter garment [240]. Results are presented in graphical form in Figure 7.23 and Figure 7.24 where the comfort region (PMV in the range -0.5 to 0.5 , resulting in a PPD under 10%) is highlighted in green colour.

In winter conditions (Figure 7.23a and Figure 7.24a) the negative values of the PMV mean that the occupants are cold; after initial unacceptable values, the operation of the HVAC system allows to improve the thermal sensation of the people in the cabin and after 5 minutes a quasi-steady state regime is achieved. Due to the higher metabolic activity, the driver (probe FL) experiences the best condition, with a PMV well above the lower limit of -0.5 (PPD well below 10%); a good condition is also experienced by the passengers sitting next to the driver (probe FR) and on the central back seat (probe RC). For what concerns the passengers sitting on the left back seat (probe RL) and right back seat (probe RR), the comfort indices exceed the bounds owing to the higher air speeds (see Figure 7.20 and Figure 7.21); however, the comfort indices fall in the lowest class (i.e., class C) and the environment can still be considered acceptable. In summer (Figure 7.23b and Figure

7.24b), the occupants share a hot environment as evidenced by the positive values of the PMV. In such scenario, the higher metabolic activity disadvantages the driver, who experiences the worst condition ($PMV > 0.7$, $PPD > 15\%$) followed by the passengers sitting next to the driver (probe FR) and on the central back seat (probe RC). In this case, the higher velocities improve the comfort sensation of passengers sitting on the left back seat (probe RL) and right back seat (probe RR), which have $PMV < 0.5$ ($PPD < 10\%$). Despite the asymmetry of the fan strengths and the different air velocities, the PMV in correspondence of probes RL and RR are close to each other both in winter and summer.

A general consideration, referred to both scenarios, is that thermal comfort sensation can be quite different for passengers sitting on different seats, as a function of different temperature and velocity values as well as of the different metabolic activity; this aspect should be duly taken into account when designing and operating the HVAC system, since the minimum comfort requirements should be met for all occupants sharing the car. In this respect, validated CFD tools can be very useful since they allow to predict and design the airflow patterns inside the car cabin.

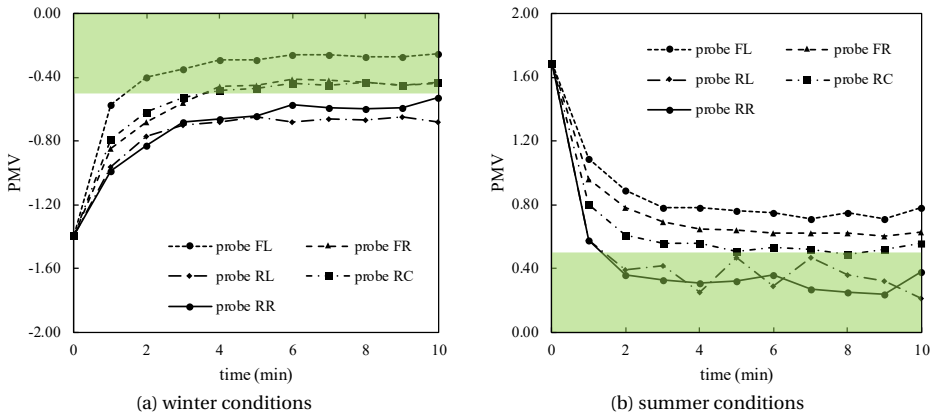


Figure 7.23. PMV in correspondence of the virtual probes, for (a) winter and (b) summer conditions.

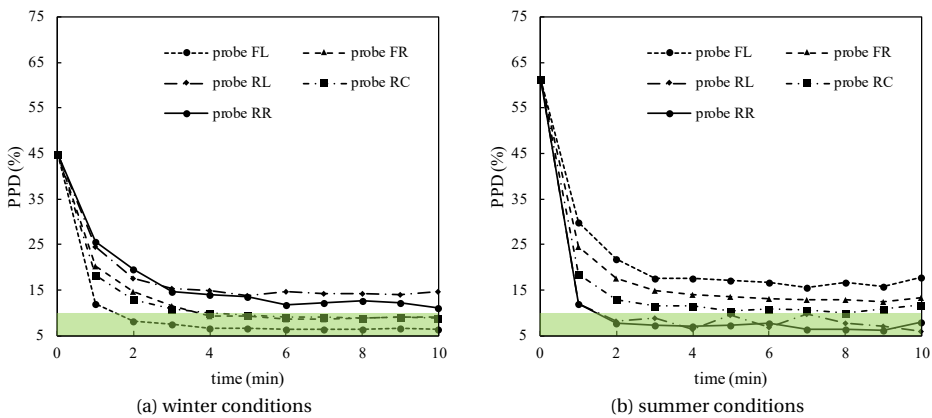


Figure 7.24. PPD in correspondence of the virtual probes, for (a) winter and (b) summer conditions.

7.6 CONCLUSIONS

In the present chapter, a transient non-isothermal CFD tool, able to predict the airflow patterns inside a real car cabin, has been developed and validated against PIV measurements. The main objective is to give insights in the design of CFD simulations of such indoor microenvironments and to produce a reliable tool to be used for many purposes, including the improvement of IAQ and comfort of the occupants and the reduction of the energy consumption by the HVAC system. Numerical analyses have been carefully designed, giving attention to the reproduction of the in-vehicle environment, identification of inlet and outlet sections and to the proper definition of the boundary conditions; all this led to a very good numerical-experimental agreement, with errors kept below 0.25 m s^{-1} for the mean velocity.

A comparison is made between URANS (with the SST $k-\omega$ model) and LES (with the WALE and dynamic KE models) approaches, evidencing that the URANS produces satisfactory results and is suitable for studying the thermal-fluid dynamics fields inside real car cabins. The URANS model, owing to the less computational resources required, is applied to characterize the mean thermal-fluid dynamics fields in winter and summer conditions, and to assess the evolution over time of the PMV and the PPD indices at multiple points of the cabin representing the position of the passengers. In quasi-steady state conditions, the temperature is fairly uniform inside the cabin, and therefore has a little influence on the velocity fields; the direct consequence is that the mean flow structures in summer and winter are very similar.

On the other hand, the analysis of the well-being of the occupants here performed led to the conclusion that passengers sharing the same car may have contrasting comfort perceptions. This point must be considered in the design and operation of the HVAC systems, since the environment must meet the minimum comfort requirements for all the occupants; to this end, validated CFD tools become essential as they allow to faithfully predict the airflow patterns in this and other indoor environments.

In this study the presence of the passengers in the car cabin was not modelled, since the experiments were conducted in the absence of occupants; this aspect will be addressed in future studies, relying on the CFD tool here validated.

III

ENERGY CONVERSION SYSTEMS AND DECARBONIZATION

8

GREEN HYDROGEN FOR ENERGY STORAGE AND NATURAL GAS SYSTEM DECARBONIZATION

The increase of the electricity production from non-programmable and intermittent renewable energy sources generates criticalities in the balance between the energy supply and demand, requiring significant energy storage capabilities for the next future. The exploitation of the available NG Transmission Network (NGTN) by implementing the Power to Gas (PtG) technology is particularly promising since it allows a massive energy storage capability and the decarbonization of the NGTN by the green hydrogen injection into the grid with growing percentages up to 100%. The objective of this chapter is to analyse the actual feasibility of distributed green hydrogen generation and its injection into the national NGTN. A mathematical model has been developed to assess the dynamic operation of a PtH₂ integrated system to produce green hydrogen using photovoltaic-powered electrolyser and to inject it into the NGTN, upstream of a Regulating and Measuring Station (RMS) located in central Italy. Three different surface sizes are considered for the installation of PV panels (100 m², 300 m² and 500 m²) and the optimal hydrogen accumulation size has been calculated to ensure the uniformity of the supplied mixture throughout the year. Obtained results show that employing the optimal accumulation size, hydrogen percentage in the NG-H₂ mixture ranges between 0% and 0.90% by volume. In the best-case scenario (i.e., when considering a surface area of 500 m²), the cost of hydrogen production is 5.10 EUR kg⁻¹ and the PtH₂ plant allows to save 32.348 tonnes of CO₂ emissions every year.

This chapter is based on the following published article:

Arpino F., Canale C., Cortellesa G., Dell'Isola M., Ficco G., Grossi G. and Moretti L. (2024). Green hydrogen for energy storage and natural gas system decarbonization: An Italian case study. *International Journal of Hydrogen Energy*, 49, 586-600.

Keywords: decarbonization; green hydrogen; Power to Hydrogen (PtH₂); natural gas transmission network; photovoltaic/electrolyser system

8.1 INTRODUCTION

Renewable energy sources (RESs) are the keystone of the energy policy of European Union to replace fossil fuels and consequently, to fulfil the target of a carbon neutral economy by 2050. Due to the decrease in costs, non-programmable RESs (i.e., wind and solar) are expected to be the most promising renewable power sources. According to the future scenarios developed by the main Italian Transmission System Operators (TSOs), it is expected that between 40% and 60% of national electricity production will be constituted by non-programmable RESs by 2040 [250]. The increase of power generation from RESs poses serious challenges to the stability of the energy system because the supply and demand of power are intermittent and random. On the supply side, non-programmable RESs exhibit strong short and long-term variations. On the demand side, hourly, daily, weekly, monthly, and seasonal variations are also significant, especially in the building sector. Therefore, the integration of a significant share of RESs will require to store large energy quantities over weeks, months and seasons, to match the intermittent renewable supply with the pattern of energy consumption. In addition, the direct electrification is not a viable option for all end-use sectors yet; owing to technological, logistical and economic barriers, it is particularly challenging for the so-called Hard-to-Abate sectors (e.g., heavy transport, building heating, high-grade industry heat). In this context, green hydrogen could play a crucial role as an energy vector in the transition to RESs by providing a mechanism to flexibly transfer energy across sectors, in time and space. Hydrogen, in fact, provides several key benefits for the whole energy system, due to its versatility and integrability with other clean technologies for the production and consumption of energy. Specifically, hydrogen offers the possibility of decarbonizing the final consumption sectors on a large scale: it can use existing assets and infrastructures, such as the natural gas (NG) transmission and distribution networks, existing heaters, industrial assets, and fuel retail networks to decarbonize the NG grid, heavy transport, and high-grade heat. Green hydrogen, as well as Carbon Capture and Storage (CCS) technologies, allows to reduce the carbon footprint of industry feedstock, especially in the production of steel and chemicals [251], so accelerating the decarbonization process in the sectors for which electrification is not an efficient solution, such as heavy industry, long-distance and heavy goods transport, non-electrified rail transport and residential sector. Green hydrogen can also be employed to ensure the storage capabilities required to efficiently meet the future large energy production from RES by employing the Power to Hydrogen (PtH₂) technology. In fact, the electrical energy surplus from renewables can be employed to produce green hydrogen to be injected in the natural gas distribution network, that offers huge line-pack storage capabilities. Injection of green hydrogen into the available NG network allows to connect production and demand sites, thus reducing supply costs and providing at the same time security and continuity of supplies through the development of an international market. Finally, in the next years the production costs of hydrogen are expected to decrease reaching competitive cost levels compared to other alternatives, due to the development of green hydrogen production technologies and to the increasing availability of renewable electricity. Despite the governments drive towards the uptake of green hydrogen, multiple barriers are challenging the scale-up of electrolyzers and hydrogen transport infrastructures. Obstacles include high costs, sustainability issues,

unclear future and lack of demand, unfit power system structures, and lack of technical and commercial standards [252,253]. There is no doubt that the high costs are the main obstacle to the development of a “Hydrogen economy”. Even though costs have been decreasing over the last decades, mainly due to the reduction of renewable power generation costs, the green hydrogen still costs 2 – 3 times more than blue hydrogen (i.e., hydrogen produced from fossil fuels with CCS systems) [254]. On the other hand, the low cost of power supply is a necessary but not sufficient condition to produce hydrogen at competitive prices. An expense reduction is also needed for the electrolysis facilities, which are the second highest cost element of hydrogen production, as well as of transportation and storage ones, that can make the green hydrogen up to 15 times more costly than the hydrogen produced and used on-site [255]. One possible strategy to decrease costs related to green hydrogen production is the development of a decentralized hydrogen production system, constituted by multiple downsized hydrogen production sites allocated more densely across a specific region [255–257]. In fact, the latter could contribute to reduce the off-site hydrogen costs curtailing the transportation and storage expenses or could even erase ones in the case of the whole hydrogen production is dispatched to end-users in loco. Several studies have been devoted to the analysis of the decentralised hydrogen production as effective strategy to decarbonize the energy system. Prince-Richard et al. [258] developed a cost model in order to provide a tool that allows to identify the most competitive position for the decentralized electrolytic hydrogen production for fuel cell vehicles, demonstrating that the decentralized hydrogen production can be competitive with other fossil fuel in locations where electricity costs are low and/or fuel taxes are high.

Barhouni et al. [259] analysed the feasibility of three different photovoltaic-based systems to produce green hydrogen for a small-scale refuelling station for fuel cells vehicles; they found that a PV grid-connected system was more promising than stand-alone PV systems with batteries or fuel cells, ensuring a Levelized Cost of Hydrogen (LCOH) of 5.5 EUR kg⁻¹. A LCOH in the range of 7.526–7.866 USD kg⁻¹ was calculated in [260] instead, where the authors performed a techno-economic analysis to design a hydrogen refuelling station intended to refuel 25 fuel cell vehicles on a daily basis.

Okundamiya [261] carried a study to determine the optimal configuration of a hydrogen-based hybrid system intended for supplying the electric load demand of a university laboratory, in order to move towards a more sustainable energy supply system. Caravantes et al. [262] assessed the potential to produce green hydrogen in the Piura region (northern Peru), realizing that solar energy source is more promising than wind and biomass sources and that green hydrogen can potentially replace the energy sources currently exploited in the region. Di Micco et al. [263] analysed the performances of two Renewable Multi-Energy Systems configurations, finding that the simultaneous production of different energy streams (i.e., electricity, thermal energy and hydrogen) allows to reduce their levelized costs considerably. Zhou et al. [264] proposed a configuration optimisation model for an integrated energy system exploiting different energy sources and carriers such as photovoltaic, wind, natural gas and hydrogen; the annual comprehensive cost and the annual carbon emissions were simultaneously optimized considering different optimisation strategies.

Zare Oskouei and Mehrjerdi [265] addressed the problem related to the optimal allocation of PtH₂ plants in the regional electricity grids, taking into account the high wind energy penetration. Specifically, the authors proposed a stochastic security-constrained optimal power flow (SSC-OPF) model with the aim to maximize the earnings of electricity grid operators through the sale of the hydrogen produced in the local hydrogen market.

Simulation results showed that PtH₂ plants supplied by RESs make electrical grids more profitable, also improving the grid technical parameters. Moreover, the study revealed that the optimal site and size of PtH₂ plants strongly depend on the RESs share, in addition to the system loads model. In Ref. [255], a new methodology to arrange the distributed hydrogen production system minimizing the total cost in supplying hydrogen to demand was proposed. A hypothetical case in which the hydrogen request comes from three stations was analysed using the proposed methodology. The assessment demonstrated that the expenses of a decentralized production system greatly reduce compared to the centralized production system if the optimal configuration identified by the methodology is adopted. Bhandari et al. [266] addressed the potential of PtH₂ using a decentralized approach. A case study sited in Cologne, Germany, was assessed. In detail, the potential of the PtH₂ process supplied by photovoltaic systems was evaluated considering both alkaline and proton exchange membrane (PEM) electrolysis technologies. The economic performance of the PtH₂ plant was evaluated for six scenarios. The analysis found that the hydrogen produced with the grid-connected solar photovoltaics system coupled with alkaline electrolyzers is the most competitive option among those analysed, with the LCOH being equal to 6.23 EUR kg⁻¹. Cavana et al. [267] presented a methodology to model the electricity and NG sectors coupling by the PtH₂ technology. The impact of hydrogen blending under increasing distributed photovoltaic generation on an urban NG network, specifically at a local level, was quantified. The results showed that in the summertime, the hydrogen percentage in the NG mixture, directly following the photovoltaic overproduction, reaches peaks around 20–30% when the photovoltaic penetration is equal to 40%, not complying with the quality standard imposed by the NG Distribution System Operator (DSO). Furthermore, the analysis also underlined the relevance of the choice of the hydrogen injection point to minimise the effects on the NG distribution grid. Cheli et al. [268] developed a steady-state model to analyse the capacity of a NG distribution network to store the renewable energy surplus generated by a close RES plant. In detail, the main thermodynamic properties and fluid dynamics parameters of the NG mixtures were analysed, with the aim to understand the feasibility of hydrogen injection into a NG distribution network. The model was applied to a hypothetical NG urban grid supposed to be located in Tuscany (central Italy), and a typical winter day was investigated. The authors concluded that the hydrogen injection mainly impacts on the Wobbe Index and the most critical situation occurs in correspondence with the peaks of electricity surplus generated by RESs. Besides, the injection node has to be carefully chosen in order to avoid non-compliance with quality standards of NG mixtures. Jarosch et al. [257] provided a thorough analysis about the hydrogen production in decentralized energy systems, as well as possible operation modes (i.e., hydrogen generation or system flexibility). The analysis was carried out using a linear optimization model in the open-source framework OEMOF for the current situation and the year 2050 in five German municipalities, highlighting that the required flexibility to succeed in the energy transition could be promoted by changes in the regulatory, market and technical frameworks.

The objective of the present work is to assess for the first time the feasibility of PtH₂ integrated energy systems, installed in correspondence of the Regulating and Measuring Stations (RMSs) of the national NG network, as a strategy for small-scale distributed green hydrogen production and energy storage. The employment of RMSs for decentralized green hydrogen production could represent a very interesting opportunity to facilitate the hydrogen implementation into the energy mix in a cost-effective way due to the capillary presence of RMSs on the national territory. Besides, experimentations carried out by

SNAM on its transmission network at Contursi Terme [269], demonstrated that limited technological adaptations are required to include hydrogen in the natural gas mixture. Specifically, in this study, a mathematical model has been developed to simulate the daily operation of an integrated plant for green hydrogen production via photovoltaic-powered electrolyzers and its injection downstream of an RMS. The model relies on hourly radiation data and on the daily natural gas consumption of a NG transmission network stretch located in central-southern Italy. Different scenarios in terms of installed photovoltaic power and green hydrogen local storage have been investigated from both technical and economical points of view.

8.2 DESCRIPTION OF THE PtH₂ INTEGRATED ENERGY SYSTEM

The investigated PtH₂ plant consists of three main sections: (i) electricity production unit based on a photovoltaic system; (ii) hydrogen generation unit based on an asymmetric PEM electrolyser, delivering hydrogen at the operating pressure of the RMS downstream of the plant; (iii) hydrogen storage unit based on the pressure vessels technology. The operating strategy of the proposed PtH₂ integrated energy system is shown in Figure 8.1; the electricity produced by the PV system is entirely absorbed by the electrolysis unit to produce hydrogen, which is then stored in pressurized vessels. When the PV production is below the minimum input power required by the electrolyser (i.e., 5% of the nominal capacity), electricity is taken from the network to keep it in operation at the minimum load. According to the natural gas demand by the transmission network, the stored hydrogen is then sent to the RMS, where it is blended with NG and injected into the NG transmission grid. The hydrogen storage unit has been introduced to decouple the operation of the electrolysis unit, depending on the random electricity production by the PV system, by the operation of NG transmission grid that is regulated by the end-users consumption; in this way, a fixed and known hydrogen percentage is ensured in the NG-H₂ mixture. The technical specifications and the costs of each component of the PtH₂ integrated energy system are summarized in Table 8.1.

The lifetime of the project (R_{proj}) is set to 20 years. The limit of hydrogen content in natural gas pipelines is actually set to 2% vol. by the authorities [270]; however, since it is generally agreed that 10% vol. of hydrogen in the NG-H₂ is acceptable [271], in the current study the maximum hydrogen content allowed (δ_{max}) is set to 10%.

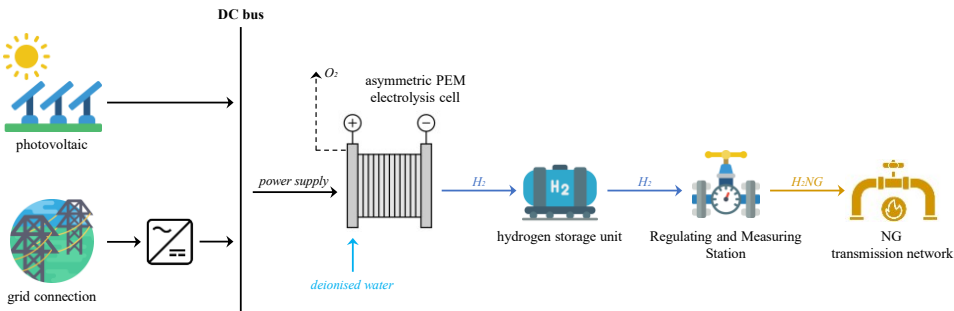


Figure 8.1. Layout of the PtH₂ integrated energy system.

Table 8.1. Technical specifications of the components of the PtH₂ integrated energy system.

PV system		
Panel model	Trina Solar Vertex Backsheet Module TSM-DE21	
Panel type	Monocrystalline	
P_{RPV} (W)	670	[272]
α_p (°C ⁻¹)	-0.0034	
NOCT (°C)	43	
Single PV panel footprint (m ²)	3.2	
f_{PV}	0.9	[273]
Lifespan (year)	20	[264,274]
Capital costs (EUR kW ⁻¹)	908	
O&M costs (EUR kW ⁻¹ per year)	13.62	[275]
Available surface area for PV plant (m ²)	100, 300, 500	
PEM electrolysis unit		
Nominal capacity of single power module (kW)	2	[276]
Load flexibility (% of nominal load)	5–100	[264,277]
H ₂ delivery pressure (bar)	24	
Specific energy consumption w_{EL} (kWh kg ⁻¹)	46.673	[278]
Water consumption (kg/kg H ₂)	18.04	[279]
Lifespan (year)	15	[264,274]
Capital costs (EUR kW ⁻¹)	1036	
O&M costs (EUR kW ⁻¹ per year)	43.82	[280]
AC/DC converter		
Nominal capacity of single module (kW)	1	
Efficiency (%)	95	[281]
Lifespan (year)	15	[282]
Capital costs (EUR kW ⁻¹)	527.87	
O&M costs (EUR kW ⁻¹ per year)	7.54	[281]
H₂ storage unit		
$SOC_{HST,min}$	0	
$SOC_{HST,max}$	0.9	[264]
Storage pressure (bar)	24	
Storage temperature (°C)	12	
Lifespan (year)	20	[264,274]
Capital costs (EUR m ⁻³)	3802.73	
O&M costs (EUR m ⁻³ per year)	38.03	[264]
HHV of H ₂ (kWh kg ⁻¹)	39.4	[283]
NG network		
Operating pressure (bar)	24	
NG Temperature (°C)	12	
δ_{max} (%)	10	

8.3 PtH₂ INTEGRATED ENERGY SYSTEM MODEL

The developed mathematical model allows to evaluate the annual operation of the PtH₂ integrated energy system with a daily resolution; the model is based on a block modelling approach with lumped parameters, allowing to evaluate the overall behaviour of the system and to assess the feasibility of the proposed solution. The electricity production by the PV system and the hydrogen production by electrolysis is determined on hourly basis; conversely, since only daily data were available for natural gas consumption, the PtH₂ plant operation is predicted on daily basis. In order to simplify the modelling process, the following assumptions have been made: (i) efficiencies of electrolyser and AC/DC converter are assumed to be constant; (ii) the start-up, shutdown and operating times in off-design conditions are neglected; (iii) device failures are not expected during the operation of the system and replacements of the equipment are only due to the end of the useful life.

8.3.1 PHOTOVOLTAIC SYSTEM

The hourly electricity production by the photovoltaic system has been modelled as a function of the actual solar radiation per unit surface G (W m⁻²), using the following expression [264,284]:

$$P_{PV}(t_i) = n_{PV} \cdot P_{RPV} \cdot f_{PV} \cdot \left(\frac{G}{G_{STC}} \right) \cdot [1 + \alpha_p (T_{PV} - T_{PV,STC})] \quad (8.1)$$

where the actual temperature of the PV panel, T_{PV} (°C), at time t_i is calculated as a function of the ambient temperature, T_a (°C), and of the actual solar radiation, G , as follows [285–288]:

$$T_{PV} = T_a + \frac{NOCT - T_{a,NOCT}}{G_{NOCT}} \cdot G \quad (8.2)$$

The hourly data of the actual solar radiation, G , and the ambient temperature, T_a , have been retrieved from the Photovoltaic Geographical Information System (PVGIS) database, freely accessible online at <https://ec.europa.eu/jrc/en/PVGIS/tools/hourly-radiation>. PVGIS provides information about solar radiation and PV system performance for any location in Europe and Africa, as well as a large part of Asia and America, allowing to estimate the power produced by a PV system optimizing its parameters, including orientation (azimuth angle) and tilt angle of the solar panels, according to the specific characteristics of the installation site. The tool's reliability has been proven in a significant number of scientific papers [289–295], to which the interested reader could refer for more information on the functionality of the tool and on the mathematical model behind it. To ensure the accuracy of solar radiation estimates, at least ten years of time series are needed [291]; therefore, sixteen-year averages of the period 2005–2020 (entire dataset available on the PVGIS database) are provided as input to the model for the solar radiation and the ambient temperature.

Figure 8.2 shows hourly values for sixteen-year averaged ambient temperature and the calculated photovoltaic panels temperature (according to Equation (8.2)); on the other hand, Figure 8.3 shows hourly data for sixteen-year averaged solar irradiance and the power output of the single PV module (calculated according to Equation (8.1)).

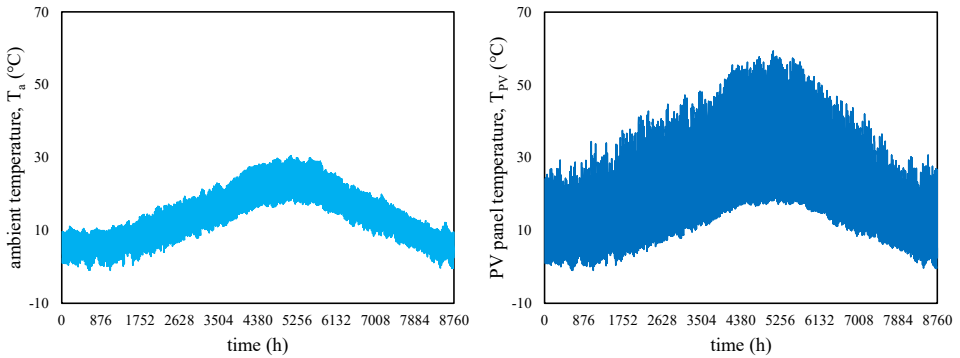


Figure 8.2. Hourly data for sixteen-year averaged ambient temperature (left) and PV panel temperature (right).

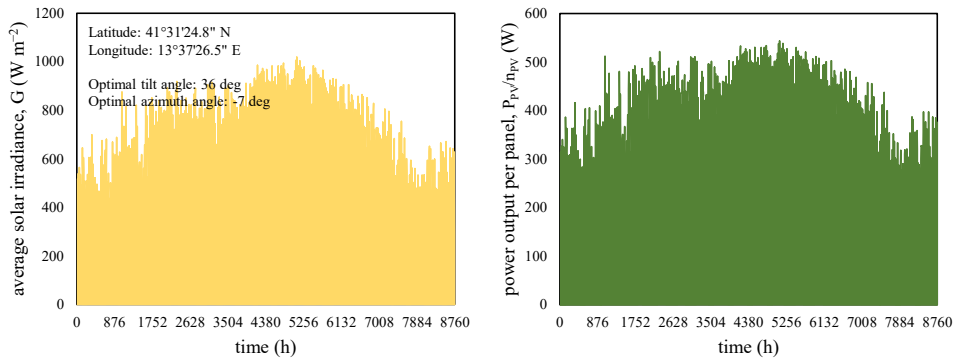


Figure 8.3. Hourly data for sixteen-year averaged solar irradiance (left) and power output of the single module (right).

8.3.2 ELECTROLYSIS UNIT

Three main technologies are nowadays available for hydrogen production by water electrolysis: Alkaline Electrolyser (AEL), Polymer Electrolyte Membrane Electrolyser (PEMEL) and Solid Oxide (SOEL). Compared to other solutions, PEM technology appears to be the most suitable to couple with highly intermittent energy sources (i.e., solar and wind) owing to the capability to follow the fluctuations of the electric load, to start-up in few minutes and to operate in a wide load range (5 – 100% of rated power) [277]. Another advantage of the PEM electrolysis is the possibility to operate at a differential pressure between the anode and cathode sections (called *asymmetric* or *unbalanced* setup), that is the solution adopted in this study; in fact, a study conducted by Bensmann et al. [278] revealed that this is the most energy-efficient solution for hydrogen delivery pressures of up to 40 bar.

The cell is fed with water at atmospheric pressure and delivers hydrogen at 24 bar, that is the operating pressure of the RMS coupled with the PtH₂ system. The mass of hydrogen produced in the electrolysis process over a specified time interval, $m_{H_2,EL}$ (kg), is given by [288]:

$$m_{H_2,EL} = \frac{P_{EL} \cdot \Delta\theta}{w_{EL}} \quad (8.3)$$

with

$$P_{EL} = \begin{cases} P_{PV}, & P_{PV} \geq P_{EL,min} \\ P_{PV} + P_{grid}, & P_{PV} < P_{EL,min} \end{cases} \quad (8.4)$$

$$P_{grid} = \begin{cases} 0, & P_{PV} \geq P_{EL,min} \\ P_{EL,min} - P_{PV}, & P_{PV} < P_{EL,min} \end{cases} \quad (8.5)$$

Equations (8.4) and (8.5) show the logic behind the handling of the input power to the electrolyser P_{EL} (kW): the power produced by the PV system, P_{PV} , is entirely absorbed by the electrolysis unit to produce hydrogen; when the PV production is below the minimum input power required by the electrolyser ($P_{EL,min}$, that is 5% of its rated capacity), part of the energy is taken from the electrical grid, P_{grid} , to keep the electrolyser in operation at the minimum allowed load, so avoiding losses of production and improving the dynamic response of the system (especially in case of unforeseen climatic conditions).

The specific energy consumption by the electrolyser, w_{EL} (kWh kg⁻¹), in Equation (8.3) is retrieved from Bensmann et al. [278].

The volume of hydrogen produced by the electrolyser, $V_{H_2,EL}$ (m³), has been evaluated as the ratio of the mass of product hydrogen to the density of hydrogen, as shown below:

$$V_{H_2,EL} = \frac{m_{H_2,EL}}{\rho_{H_2}} \quad (8.6)$$

The hydrogen density ρ_{H_2} (kg m⁻³) is calculated with the following formula:

$$\rho_{H_2} = \frac{M_{mol,H_2} \cdot p}{Z \cdot R_g \cdot T_{H_2}} \quad (8.7)$$

where hydrogen supply pressure and temperature are assumed to be equal to the operating values of the NG transmission network stretch analysed (see Table 8.1), and the calculated values for the compressibility factor and the density of hydrogen are $Z=1.015$ and $\rho_{H_2} = 2.0115$ kg m⁻³, respectively.

8.3.3 STORAGE UNIT

The green hydrogen produced in the electrolysis process is stored in pressurized vessels at the outlet pressure of the electrolyser (i.e., 24 bar), prior to be injected in the natural gas network. The storage temperature is assumed to be 12 °C, that is the operating temperature of the NG pipeline under study (Table 8.1). The hydrogen volume stored at time t_i , $V_{H_2,st}(t_i)$ (m³), is given by:

$$V_{H_2,st}(t_i) = V_{H_2,st}(t_i - 1) + V_{H_2,EL}(t_i) - V_{H_2,inj}(t_i) \quad (8.8)$$

where the volume of hydrogen injected into the NG network, $V_{H_2,inj}(t_i)$, at time t_i is evaluated in accordance with the following equation:

$$V_{H_2,inj}(t_i) = \delta \cdot V_{NG}(t_i) \quad (8.9)$$

with the NG volume that flows in the NG network, $V_{NG}(t_i)$, depending on the end-users' consumption.

Finally, following Zhou et al. [264], a State of Charge for the hydrogen storage tank (SOC_{HST}) has been defined as the ratio of the hydrogen volume present in the tank at time t_i , $V_{H_2,st}(t_i)$ (m^3), to the nominal storage capacity $V_{H_2,rated}$ (m^3):

$$SOC_{HST}(t_i) = \frac{V_{H_2,st}(t_i)}{V_{H_2,rated}} \quad (8.10)$$

This parameter is considered when determining the optimal size of the hydrogen storage tank.

8.3.4 NATURAL GAS NETWORK CONSUMPTION

The amount of hydrogen that can be injected into the natural gas network depends on the NG volume circulating in the grid, and thus on the users NG consumption. In order to generate reliable estimates of the potential of the proposed solution, for the present study real data of daily NG consumption of a RMS located in central-southern Italy have been employed. Real consumptions were provided by the TSO of the specific stretch of the network supplied by the RMS, for the period from 2015 to 2018; such data have been then averaged to get the daily mean consumption (see Figure 8.4), provided as input for calculations.

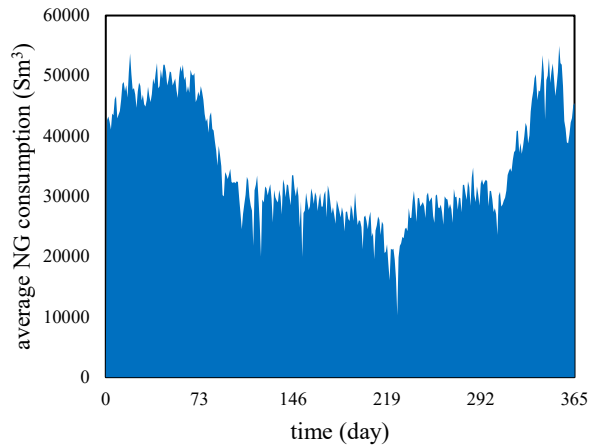


Figure 8.4. Daily average NG consumption of a specific stretch of the transmission network located in central-southern Italy.

8.3.5 AVOIDED CARBON DIOXIDE EMISSIONS CALCULATION

The objective of the present analysis is the maximization of the avoided carbon dioxide emissions, taking into account the available space for the PtH₂ plant installation and the

economic constraints. Avoided emissions are evaluated as the difference between the yearly amount of CO₂ emitted when the users' energy demand is met by supplying NG (tCO_{2NG}) and the yearly mass of CO₂ emitted when the NG-H₂ blend is supplied (tCO_{2NG-H_2}), according to the following equation:

$$\text{avoided } CO_2 = tCO_{2NG} - tCO_{2NG-H_2} \quad (8.11)$$

To calculate the CO₂ emissions the following equation has been introduced:

$$tCO_2 = m_f \cdot EF_f \cdot 10^{-3} \quad (8.12)$$

Assuming stoichiometric combustion, the emission factor is evaluated as:

$$EF_f = X_C \cdot d_f \cdot MM_{CO_2} \quad (8.13)$$

Problem constraints are expressed by equations (8.14)–(8.17) below. In particular, the input power to the electrolyser should not fall below the minimum allowed power (see Table 8.1):

$$P_{EL} \geq P_{EL,min} \quad (8.14)$$

The equivalent State of Charge of the HST, defined in Section 8.3.3, should meet the upper and lower limit constraints:

$$SOC_{HST,min} \leq SOC_{HST} \leq SOC_{HST,max} \quad (8.15)$$

Finally, concerning the hydrogen injection in the natural gas pipelines, the H₂ fraction in the blend should not exceed the 10% by volume:

$$0 \leq \delta \leq 0.1 \quad (8.16)$$

and to ensure the uniformity of the mixture throughout the year the following constraint has been imposed:

$$\frac{\text{days with injection}}{365 \text{ days}} \geq \chi = 0.5 \quad (8.17)$$

The value selected for the χ coefficient prevents supplied gas composition from varying too much throughout the year and provides the lowest costs, as discussed in Section 8.6.2.

8.4 ECONOMIC ASSESSMENT METHODOLOGY

Following the methodology adopted by other works available in the scientific literature [274,296–301], the three main parameters identified to assess the economic effectiveness of the proposed solutions are: (i) the net present cost or life-cycle cost (*LCC*); (ii) the total annualized cost ($C_{ann,tot}$); (iii) the levelized cost of hydrogen (*LCOH*).

The life-cycle cost is given by:

$$LCC = \sum_{ny=1}^{R_{proj}} f_d \cdot (ICC + RC + OM - S) \quad (8.18)$$

where the Operation and Maintenance cost (OM) includes the costs for the deionised water supplied to the electrolyser and for the electricity purchased from the grid; the unit price of deionised water is assumed to be 0.59 EUR m^{-3} [264], while the electricity grid price is set to 0.22 EUR kWh^{-1} (that is the non-households average price in Italy for December 2021, retrieved from www.globalpetrolprices.com).

The discount rate, f_d , can be evaluated as follows:

$$f_d = \frac{1}{(1+i)^{ny}} \quad (8.19)$$

where i is the real discount rate, calculated as a function of the nominal discount rate i' and of the expected inflation rate ir :

$$i = \frac{i' - ir}{1 + ir} \quad (8.20)$$

The nominal discount rate and the inflation rate were assumed to be equal to 7% and 2%, respectively, resulting in a real discount rate of 4.9% [302].

The salvage value is the value remaining in a component of the system at the end of the project lifetime. It can be expressed by Equations (8.21)–(8.23), assuming a linear depreciation of the components [303].

$$S = C_{rep} \cdot \frac{R_{rem}}{R_{comp}} \quad (8.21)$$

$$R_{rem} = R_{comp} - (R_{proj} - R_{rep}) \quad (8.22)$$

$$R_{rep} = R_{comp} \cdot INT \left(\frac{R_{proj}}{R_{comp}} \right) \quad (8.23)$$

The total annualised cost is computed multiplying the life-cycle cost by the capital recovery factor (CRF), as follows:

$$C_{ann,tot} = CRF \cdot LCC \quad (8.24)$$

$$CRF = \frac{i(1+i)^{R_{proj}}}{(1+i)^{R_{proj}} - 1} \quad (8.25)$$

Finally, the levelized cost of hydrogen is calculated as the ratio of the life-cycle cost to the total mass of hydrogen produced during the useful life of the system, $M_{hydrogen}$ (kg).

$$LCOH = \frac{LCC}{M_{hydrogen}} \quad (8.26)$$

8.5 CASE STUDY

The Italian natural gas network is divided in two main parts: the transmission network and the distribution network. The transmission network consists of a *national pipelines network* and a *regional pipelines network*. The former, with a total length of 9600 km, conveys the natural gas from the entry points (i.e., the import points connected to foreign pipelines, regasification plants and the national production sites) to the regional interconnections and the storage sites; the latter, with a total length of 23100 km, has the purpose of moving natural gas on an interregional, regional and local scale to supply gas to industrial users and distribution companies. The industrial users and distribution companies are connected to the *regional network* through several RMSs at a minimum pressure of 24 bar, where the natural gas is filtered, pre-heated, decompressed and odorized. Finally, the distribution system is responsible for natural gas supply to final costumers [304]. The main objective of the present work is to evaluate the effectiveness of distributed small-scale photovoltaic-based PtH₂ systems (with the layout shown in Section 8.2) next to the available RMSs of the NG transmission network, producing green hydrogen to be injected in the grid. The case study is represented by a RMS located in central-southern Italy (depicted in Figure 8.5), operated at an absolute pressure of 24 bar and feeding industrial facilities. Figure 8.6 shows the layout of the RMS. The concept is to install photovoltaic panels on the roof of the cabin (highlighted in orange colour), with an available surface area of 300 m², and place the remaining equipment (i.e., electrolyzers and hydrogen storage tanks) within the enclosure surrounding the station (borders highlighted in yellow).



Figure 8.5. Overview of the RMS.



Figure 8.6. Layout of the RMS, with the surface area available for PV panels installation highlighted in orange colour.

In order to have more general findings, a survey has been conducted on a significant number of RMSs in Italy with the aim to determine the space typically available for installing PV panels on the roofs of the cabins. The results are shown in the chart of Figure 8.7: most of the RMSs have a surface area under 150 m², while very few have areas above 300 m². According to the distribution shown in Figure 8.7, two further scenarios have been analysed considering an available surface area of 100 m² and 500 m² for the installation of the PV panels to cover the whole range of surfaces available. It could be anyway underlined that additional surface for PV panels installation could be obtained on the available land within the RMS area.

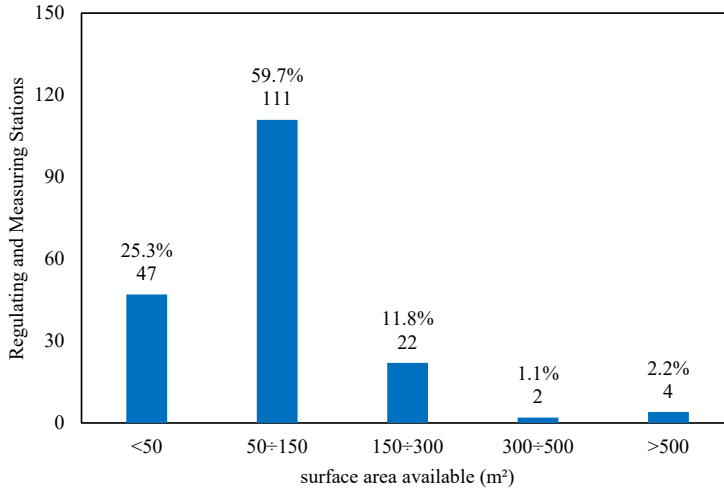


Figure 8.7. Surface area available on the roof of the Regulating and Measuring Stations considered in the survey.

8.6 RESULTS AND DISCUSSIONS

The optimal system architecture is presented in Table 8.2 for the investigated scenarios, hereinafter referred to as *case a* (surface area of 100 m²), *case b* (surface area of 300 m²) and *case c* (surface area of 500 m²). The number of photovoltaic panels is determined according to the sizes and spacing of each PV unit (see Table 8.1), assuming to exploit the whole available surface on the cabin roof. The installed capacity of the electrolysis unit depends on the actual energy production capability of the photovoltaic subsystem (i.e., it is calculated to match the maximum hourly photovoltaic production); for instance, for *case b*, the maximum hourly PV production is $P_{PV,max} = 543.41 \text{ W} \cdot n_p \approx 50.5 \text{ kW}$, leading to a PEM installed capacity of 52 kW. Finally, the converter is sized on the maximum power taken from the electric grid and the size of the hydrogen storage unit is found respecting the constraints expressed by Equation (8.15).

Depicted in Figure 8.8 are the daily trends for the hydrogen produced and stored for *case b*. Similar patterns are found under *case a* and *case c*. The maximum value of the hydrogen produced is equal to 8.892 kg and occurs in the month of August, due to the higher solar irradiance; on the other hand, the minimum value, equal to 4.016 kg, is foreseen for November. The hydrogen storage profile shows a jagged shape (Figure 8.8, right chart), underlying that a continuous injection of hydrogen in the natural gas pipelines is not possible owing to the patterns and values in the natural gas consumption with respect to the producing capability of the photovoltaic unit and confirming the need for a hydrogen buffer. The greater continuity in the storage occurring in days 218–234 is due to the reduction in the NG consumption (see Figure 8.4) and thus in the hydrogen injection, being its fraction in the blend set to a fixed value.

One of the key aspects for the integrated PtH₂ system proposed is the evaluation of the properties of the supplied NG-H₂ blend and the estimation of the saved carbon dioxide emissions. Details of the mixtures, together with the total mass of hydrogen injected into

the NG pipelines and the avoided CO₂ emissions, are provided in Table 8.3 for the three case studies.

Findings reveal that even when increasing the H₂ fraction to almost 1% vol. (*case c*), the Wobbe Index of the NG-H₂ mixture is still close to the NG value (i.e., 50.367 MJ Sm⁻³); the quality of the supplied gas is therefore preserved and the fuels are interchangeable, with no consequence for the end-users. The volume increase factor is calculated as the ratio of the HHV of natural gas to the HHV of the NG-H₂ mixture and points out that, considering the same amount of energy, larger volumes are needed as the hydrogen content increases in the NG-H₂ mixture. As concerns the carbon dioxide emissions, the proposed system allows to save 19.249 tonnes of CO₂ every year for *case b* (that is the base-case scenario) arriving up to 32.348 tonnes for *case c*. To further increase the avoided carbon dioxide emissions, the space intended for photovoltaic panels may be extended and thus the power generation enhanced; the RMS under study, like the other stations spread across the country, is in an industrial area, therefore one solution could be to use the space available on the roofs of the surrounding industrial facilities that would otherwise remain unused or, alternatively, the available land within the RMS area.

Table 8.2. Installed capacity for the scenarios under investigation.

PV system			
	Surface area (m ²)		
	100 (<i>case a</i>)	300 (<i>case b</i>)	500 (<i>case c</i>)
Number of panels	31	93	156
Installed nominal capacity (kW)	20.77	62.31	104.52
System footprint (m ²)	99.2	297.6	499.2
PEM Electrolysis Unit			
	Surface area (m ²)		
	100 (<i>case a</i>)	300 (<i>case b</i>)	500 (<i>case c</i>)
Number of power modules	9	26	43
Installed capacity (kW)	18	52	86
Converter			
	Surface area (m ²)		
	100 (<i>case a</i>)	300 (<i>case b</i>)	500 (<i>case c</i>)
Installed units	1	3	5
Installed capacity (kW)	1	3	5
H₂ Storage Unit			
	Surface area (m ²)		
	100 (<i>case a</i>)	300 (<i>case b</i>)	500 (<i>case c</i>)
Installed capacity (m ³)	5	13	21

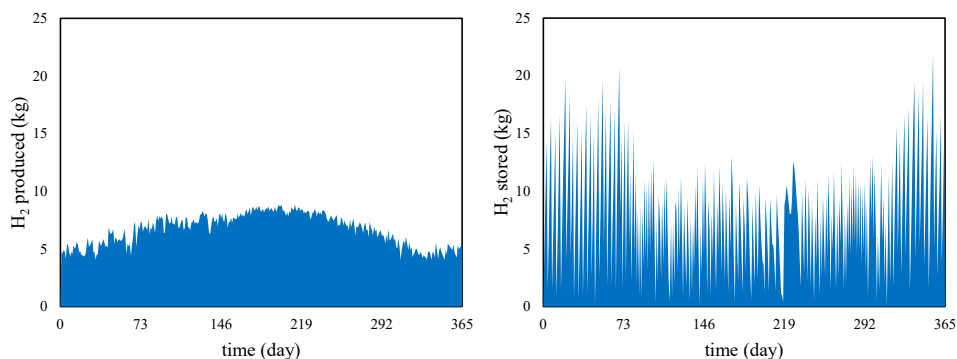


Figure 8.8. Daily trends for the hydrogen produced (left) and stored (right), with an available surface area for PV panels installation of 300 m².

Table 8.3. Details of NG-H₂ mixtures with avoided CO₂ emissions.

Surface area (m ²)	H ₂ fraction (% vol.)	Density (kg Sm ⁻³)	Wobbe Index (MJ Sm ⁻³)	Volume increase factor	Total mass of H ₂ injected per year (tonne)	CO ₂ avoided per year (tonne)
100 (<i>case a</i>)	0.18	0.7515	50.344	1.001	0.815	6.398
300 (<i>case b</i>)	0.54	0.7491	50.298	1.004	2.434	19.249
500 (<i>case c</i>)	0.90	0.7467	50.252	1.006	4.077	32.348

8.6.1 ECONOMIC EVALUATIONS

The main financial indicators are summarised in Table 8.4 for the analysed scenarios.

Table 8.4. Summary of the economic analysis.

Surface area (m ²)	Financial indicators		
	LCC (million EUR)	$C_{ann,tot}$ (EUR/year)	LCOH (EUR kg ⁻¹)
100 (<i>case a</i>)	0.088	7040.58	5.43
300 (<i>case b</i>)	0.252	20051.02	5.18
500 (<i>case c</i>)	0.416	33118.23	5.10

The growth of life-cycle costs and total annualized costs is nearly linear with the increase of the surface area available for the installation of the PV panels (and thus with the size of the PtH₂ system); on the other hand, the levelized costs of hydrogen production decrease and are comparable to ranges available in the scientific literature (2.5–6.4 EUR kg⁻¹) [305]. One of the main advantages of the proposed solution is the absence of transportation costs, since the hydrogen is produced, temporarily stored in vessels and then injected in the NG grid at one location. Finally, a cost comparison is shown in Figure 8.9 among the different components of the PtH₂ system for *case b*; a similar cost sharing has been found for the other scenarios but is not presented for the sake of brevity. The major contribution to the life-cycle cost is given by the PEM electrolyser (53%), followed by the PV system (25%) and the hydrogen storage tank (21%); the converter accounts only for 1% of the total.

Replacement costs are expected only for the converter and the electrolyser since their lifespan is lower than the project lifetime (see Table 8.1). Concerning the operation and maintenance costs, for the PEMEL the expenses for demineralized water and for the electricity purchased from the grid are included; such selection justifies the O&M repartition of Figure 8.9. The cost sharing just outlined in Figure 8.9 opens up to relevant prospects when considering that the costs of PEM electrolysers are expected to decrease significantly in the next years (i.e., at an annual rate of 4.77%) [306]. The LCOH will then be reduced, making the proposed solution even more competitive.

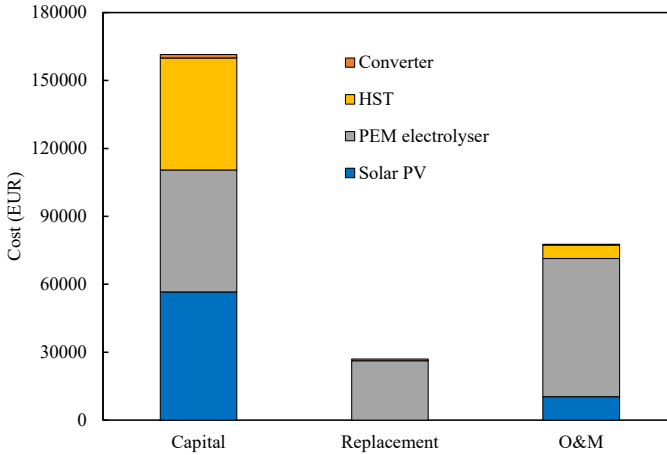


Figure 8.9. Cost comparison for the scenario with 300 m² of available surface (*case b*).

8.6.2 SENSITIVITY ANALYSIS TO THE χ COEFFICIENT

In the present section a sensitivity analysis is performed varying the value of the χ coefficient appearing in Equation (8.17), fixed to 0.5 in the calculations previously shown. χ is here varied in the range 0.1–0.9; maximum and minimum bounding values (i.e., 0 and 1) have not been considered since they do not represent technically feasible constraints. The values obtained for the LCOH, saved CO₂ emissions and required H₂ storage capacity are listed in Table 8.5, Table 8.6, Table 8.7 for *case a*, *b* and *c* respectively; they are also displayed in graphical form in Figure 8.10. Results show that a value of $\chi=0.5$ gives the lowest LCOHs for all the considered scenarios. When decreasing χ , higher values can be obtained for the avoided CO₂ emissions (however, with negligible relative gains); this is achieved with higher H₂ fractions in the NG-H₂ mixtures and larger storage capacities required, since longer time is needed to reach the optimal amount of hydrogen to be injected. As a direct consequence, LCOH increases making values of $\chi<0.5$ not suitable. On the other hand, for values of $\chi>0.5$, smaller hydrogen fractions must be mixed with the NG to accommodate the increased injection frequency. Being the amount of hydrogen produced the same, the required storage capacity increases, thus raising the costs. At the same time, avoided CO₂ emissions are reduced since less hydrogen is contained in the supplied gas.

The above considerations allow to establish that the optimal value for χ is 0.5, justifying the selection of this value for the analyses presented in the previous sections.

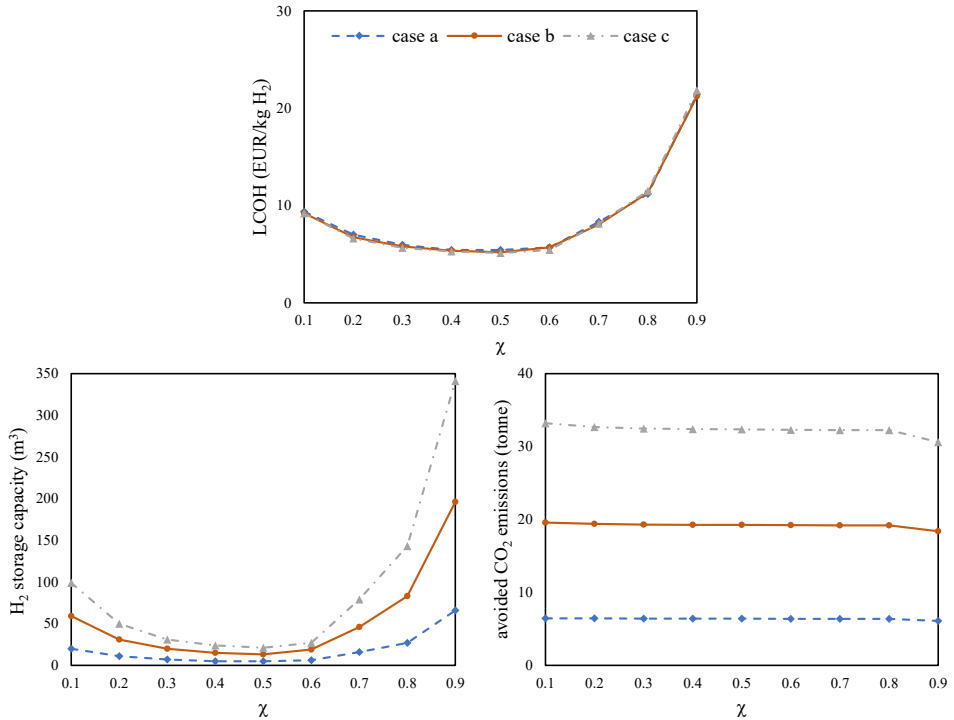


Figure 8.10. LCOH (top), required hydrogen storage capacity (bottom left) and avoided CO₂ emissions (bottom right) for different values of the χ coefficient.

Table 8.5. LCOH, required hydrogen storage capacity and avoided CO₂ emissions for different values of the χ coefficient (*case a*).

χ	<i>Case a</i>		
	LCOH (EUR kg ⁻¹)	CO ₂ avoided per year (tonne)	H ₂ storage capacity (m ³)
0.1	9.35	6.460	20
0.2	7.00	6.437	11
0.3	5.95	6.419	7
0.4	5.43	6.408	5
0.5	5.43	6.398	5
0.6	5.69	6.387	6
0.7	8.31	6.376	16
0.8	11.19	6.368	27
0.9	21.39	6.083	66

Table 8.6. LCOH, required hydrogen storage capacity and avoided CO₂ emissions for different values of the χ coefficient (*case b*).

<i>Case b</i>			
χ	LCOH (EUR kg ⁻¹)	CO ₂ avoided per year (tonne)	H ₂ storage capacity (m ³)
0.1	9.20	19.569	59
0.2	6.75	19.387	31
0.3	5.79	19.308	20
0.4	5.35	19.273	15
0.5	5.18	19.249	13
0.6	5.70	19.224	19
0.7	8.07	19.206	46
0.8	11.31	19.194	83
0.9	21.21	18.374	196

Table 8.7. LCOH, required hydrogen storage capacity and avoided CO₂ emissions for different values of the χ coefficient (*case c*).

<i>Case c</i>			
χ	LCOH (EUR kg ⁻¹)	CO ₂ avoided per year (tonne)	H ₂ storage capacity (m ³)
0.1	9.18	33.191	99
0.2	6.62	32.681	50
0.3	5.63	32.474	31
0.4	5.26	32.402	24
0.5	5.10	32.348	21
0.6	5.42	32.293	27
0.7	8.14	32.264	79
0.8	11.48	32.244	143
0.9	21.84	30.616	341

8.7 CONCLUSIONS

In order to contribute to the energy systems decarbonization, the present study investigated the feasibility of distributed small-scale PtH₂ systems, coupled with PV plants and installed next to the RMSs available in the national natural gas transmission and distribution network. In particular, a mathematical model has been developed to analyse the daily operation of a small-scale PtH₂ plant producing green hydrogen to be injected upstream of a real RMS located in central-southern Italy. The investigated PtH₂ plant is composed of three main subsections: (i) electricity production unit based on a PV system, with the panels installed on the roof of the RMS; (ii) hydrogen generation unit based on an asymmetric PEM electrolysis cell, delivering hydrogen at the operating pressure of the

RMS; (iii) hydrogen storage unit based on the pressure vessels technology. The developed model is based on hourly irradiation data retrieved by the PVGIS database and on real NG consumption of the analysed transmission network stretch, provided by the TSO. Three different scenarios have been investigated, considering three surface sizes for the installation of PV panels: 100 m² (*case a*), 300 m² (*case b*) and 500 m² (*case c*) and evaluating the effects on the NG infrastructure in terms of characteristics of the supplied gas, saved carbon dioxide emissions and costs of the project.

Obtained results reveal that a continuous injection of hydrogen in the natural gas transmission network is not possible, due to the patterns and values in the NG consumption with respect to the producing capability of the photovoltaic plant; this confirms the need of a hydrogen buffer to decouple the operation of the electrolysis unit, depending on the random electricity production by the PV system, by the operation of the NG transmission grid that is regulated by the end-users' consumption. Hydrogen fractions achievable in the blend are 0.18% vol. for *case a*, 0.54 % vol. for *case b* and 0.90 % vol. for *case c*; the Wobbe Index of the NG-H₂ mixture is always close to the NG value, meaning that the quality of the supplied gas is preserved and the supplied fuels are interchangeable. In the best-case scenario (i.e., *case c*), the cost of hydrogen production is 5.10 EUR kg⁻¹ (compatible with the ranges available in the scientific literature) and the PtH₂ plant allows to save 32.348 tonnes of CO₂ emissions per year.

Future developments may involve the integration of different kinds of renewable sources and the implementation of a multi-objective optimization tool allowing to select the best configurations for the PtH₂ plant according to the characteristics of the installation site.

EPILOGUE

9

CONCLUSIONS AND OUTLOOK

9.1 CONCLUDING REMARKS AND FUTURE PERSPECTIVES

The work in this dissertation can be divided into three parts, seemingly disparate yet brought together by a single objective: ensuring a sustainable future. The significance of this research lies, in fact, in the pursuit of novel solutions that address the immediate need for healthier indoor spaces and the long-term goal of achieving a carbon-neutral energy landscape. Both aspects are essential to consider for a sustainable future, as evidenced by the *sustainable development goals* established by the United Nations in 2015.

The conclusions and final recommendations for the different parts comprising this booklet are reported in the subsections below.

9.1.1 PART I

The first part of this dissertation (*Indoor environmental quality: applications*) analysed the spread and distribution of virus-laden droplets, emitted by an infected subject, in three distinct situations occurring in indoor environments: a car journey, a university lecture and a close-distance conversation between two people. These scenarios were chosen for their representation of commonplace situations in our daily lives. The car cabin represents a confined indoor micro-environment, while the university lecture room exemplifies a crowded, spacious indoor setting with prolonged human interaction. Both micro and large environments warrant thorough investigation, as particle dynamics can vary significantly, consequently influencing the exposure and risks faced by susceptible individuals.

The methodology adopted is consistent across the chapters and is based on both experimental and CFD investigations. The numerical model is based on a Eulerian-Lagrangian approach, solving the mass, momentum and energy conservation equations for the air flow (continuous phase) and Newton's equation of motion for each droplet (discrete phase).

Chapter 3 combines a validated CFD transient model and a predictive emission-to-risk approach to estimate the SARS-CoV-2 Delta variant risk of infection in a car cabin under different conditions in terms of ventilation (ventilation mode and airflow rate of the HVAC system) and emission scenarios (expiratory activity, such as breathing vs. speaking, and position of the infected subject within the car cabin). The results are compared with those obtained adopting a zero-dimensional approach, which is based on the simplified assumption of complete and instantaneous mixing of emissions to achieve a uniform spatial concentration within the environment. Findings of the study demonstrated the necessity of using CFD approaches to properly assess individual risks in such confined spaces, as fluid-dynamic conditions significantly influence the airflow patterns and, consequently, the spatial distribution of the virus-laden particles within the cabin. In contrast, simplified zero-dimensional approaches, which evaluate the average risk of susceptible individuals without considering the specific flow patterns possibly arising in confined spaces, can lead to miscalculations, particularly for ventilation modes not designed for mixing. The well-mixed solutions for a speaking infected subject presented here are roughly comparable to the CFD results only in case of very low flow rates (10% of the maximum flow rate), that is, when the reduced airflow rates do not effectively clean the breathing zone of the exposed subjects and the virus-laden concentrations are likely homogenous within the car cabin. While the CFD results provided in this chapter are specific to the configuration analysed and are not directly transferable to other cars (due

to the case-specific geometry, vent positions, etc.), they emphasize the importance of the approach adopted and suggest that ad-hoc designing of closed environments is achievable, especially when the spatial locations of the occupants are fixed. One limitation of this study is the simplified geometry adopted for the numerical analyses; this is addressed in Part II of this thesis, where future development of this research activity are implemented.

In Chapter 4, 3D CFD simulations have been performed to explore the movement and distribution of droplets emitted by a particles source, replicating the scenario of an infected individual (e.g., a professor) speaking for 2 hours in a university lecture room. The study aims to evaluate the usefulness of validated CFD tools in three key areas: (i) facilitating the proper design of HVAC systems; (ii) optimizing the system's efficiency in evacuating pollutants and pathogens from the room; (iii) assisting HVAC system management, by analysing the aerosol distribution in the room as a function of the AER. The numerical model was validated against measurement data collected inside a lecture room located in the Department of Engineering of the University of Naples "Parthenope" and was then employed to evaluate the influence of three different air supply rates (3.75 ACH, 7.5 ACH and 15 ACH) on particles age, distribution throughout the room and concentration within selected control volumes surrounding the rows of benches. Obtained results reveal that increasing the air supply rate does not always lead to improved indoor air quality (assuming it is related to the droplet concentration). In fact, while the overall number of droplets in the room decreases, at a local level the increased air flow produces adverse effects, raising the risk of exposure in many of the selected control volumes. These findings emphasize the need to consider local air flow patterns when designing ventilation systems and evaluating the risk of exposure to airborne diseases. They also underscore the essential role of CFD in investigating the intricate thermo-fluid dynamics of indoor environments and highlight that the AER alone is insufficient for assessing HVAC system effectiveness. The primary limitation of this study lies in the absence of occupants in the room, which will be addressed in future research. The objective of this work is to analyse droplet distribution as it relates to HVAC design and operation while excluding other influential parameters. While it is acknowledged that occupants, with their thermal plume, impact airflow and particle transport, modelling their presence without prior knowledge of their positions or in situations where positions may change would weaken the generalizability of results rather than strengthen it.

Chapter 4 highlighted a crucial issue: the need for better control of local airflow patterns in indoor environments, since increasing the air flow rate provided by HVAC systems might have adverse local effects. Consequently, Chapter 5 introduces the design of a portable personal air cleaner intended to control local airflow patterns in large indoor spaces and reduce the airborne transmission of respiratory pathogens. The effectiveness of the device is evaluated using complex 3D CFD simulations, validated through experimental measurements, in two common exposure scenarios: close proximity and shared indoor environments. The air cleaner under investigation was conceived as a portable battery-operated device and was designed with proper air flow rate velocities and angles able to create a sophisticated fluid-dynamic shield capable of protecting a susceptible from airborne and respiratory particles. Close proximity simulations were performed considering a typical face-to-face configuration between emitter and receiver, whereas indoor environment simulations were performed considering the university lecture room experimentally and numerically characterized in Chapter 4. Results of the

CFD analyses demonstrated that in close proximity scenario the air cleaner was able to reduce, on average, the volume of infectious respiratory particles inhaled by the exposed subject, during a 900 s conversation, by 96% (with instantaneous reductions always >92%). Results of the simulations performed in the shared indoor environment revealed an average relative reduction of the volume concentration of infectious respiratory particles in the breathing zone of an exposed subject, during a 2-h lesson, equal to 99.5%.

In summary, the proposed personal air cleaner provides significant protection to exposed individuals in both close proximity and shared indoor environments, leading to a reduced airborne transmission of respiratory pathogens. Future research will focus on prototyping the air cleaner and conducting in-field experimental evaluations of its performances.

9.1.2 PART II

Part II (*Indoor environmental quality: benchmark for CFD validation*) continues the research introduced in Chapter 3, underlying the significance of CFD in studying and designing airflow patterns in indoor microenvironments like car cabins.

As already pointed out in this dissertation, the results obtained by CFD analyses may be considerably influenced by the geometry adopted for reproducing the in-vehicle environment; therefore, achieving a situation as realistic as possible is desirable. To address this need, this section provides a comprehensive benchmark that offers valuable insights into the ventilation flow in a real car cabin through experimental analyses; additionally, it provides guidance on the design of CFD simulations of such indoor microenvironments. To the best of author's knowledge, as of the time of writing, no study of this kind and with this level of detail exists in the scientific literature.

Chapter 6 detailed the experimental campaign, carried out on a commercial car in the Aerodynamics Laboratories at Delft University of Technology. Firstly, the flow velocity at the exit of the vents was characterised by means of 5-hole pressure probe measurements, to provide accurate inlet velocity boundary conditions for the CFD model. Then, the flow velocity fields were measured by Particle Image Velocimetry (PIV) at three longitudinal sections inside the car cabin. The time-averaged air velocity fields were presented and discussed, as well as the velocity fluctuations in terms of quadrant analysis, Reynolds stresses and turbulent kinetic energy. Moreover, a detailed uncertainty analysis of the experimental results was presented.

In Chapter 7, a transient non-isothermal CFD tool was developed and validated against the PIV measurements discussed in Chapter 6. The numerical analyses were carefully designed, giving attention to the reproduction of the in-vehicle environment, identification of inlet and outlet sections and to the proper definition of the boundary conditions (based on the measurements presented in Chapter 6). This approach yielded a very good numerical-experimental agreement, with errors kept below 0.25 m s^{-1} . A comparison was made between URANS (with the SST $k-\omega$ model) and LES (with the WALE and dynamic KE models) approaches, evidencing that the URANS produces satisfactory results and is suitable for studying the thermal-fluid dynamics fields inside real car cabins. The URANS model, owing to the less computational resources required, was applied to characterize the mean thermal-fluid dynamics fields in winter and summer conditions, and to assess the evolution over time of the PMV and the PPD indices in multiple points of the cabin representing the position of the passengers. In quasi-steady state conditions, the temperature is fairly uniform inside the cabin, and therefore has a little influence on the

velocity fields; the direct consequence is that the mean flow structures in summer and winter are very similar.

On the other hand, the analysis of the well-being of the occupants led to the conclusion that passengers sharing the same car may have contrasting comfort perceptions. This point must be considered in the design and operation of the HVAC systems, since the environment must meet the minimum comfort requirements for all the occupants; to this end, validated CFD tools become essential as they allow to faithfully predict the airflow patterns in this and other indoor environments.

It is worth noting that the presence of passengers in the car cabin was not modelled in this study, as the experiments were conducted in the absence of occupants; this aspect will be addressed in future studies, relying on the CFD tool here validated. Future research will also aim at identifying innovative ventilation solutions capable of ensuring the well-being of passengers while reducing energy consumption by the HVAC system.

9.1.3 PART III

The last part (*Energy conversion systems and decarbonization*) is dedicated to seeking innovative solutions for decarbonizing the current energy landscape.

Green hydrogen has emerged as a pivotal energy carrier in the transition to RESs. It can, in fact, be employed to address the storage demands essential for efficiently managing the future large energy production from RES through the Power to Hydrogen (PtH₂) technology. This approach involves using surplus electrical energy from renewables to produce green hydrogen, which can then be injected into the natural gas transmission network, offering huge line-pack storage capabilities.

Chapter 8 investigated the feasibility of distributed small-scale PtH₂ systems, coupled with PV plants and installed next to the RMSs available within the national natural gas transmission and distribution network. A mathematical model has been developed to analyse the daily operation of a small-scale PtH₂ plant producing green hydrogen to be injected upstream of a real RMS located in central-southern Italy. The proposed PtH₂ plant is composed of three main subsections: (i) electricity production unit based on a PV system, with the panels installed on the roof of the RMS; (ii) hydrogen generation unit based on an asymmetric PEM electrolysis cell, delivering hydrogen at the operating pressure of the RMS; (iii) hydrogen storage unit based on the pressure vessels technology. The developed model is based on hourly irradiation data retrieved by the PVGIS database and on real NG consumption of the analysed transmission network stretch, provided by the TSO. Three different scenarios have been investigated, considering three surface sizes for the installation of PV panels: 100 m² (case a), 300 m² (case b) and 500 m² (case c) and evaluating the effects on the NG infrastructure in terms of characteristics of the supplied gas, saved carbon dioxide emissions and costs of the project.

Obtained results reveal that a continuous injection of hydrogen in the natural gas transmission network is not possible, due to the patterns and values in the NG consumption with respect to the producing capability of the photovoltaic plant; this confirms the need of a hydrogen buffer to decouple the operation of the electrolysis unit, depending on the random electricity production by the PV system, by the operation of the NG transmission grid that is regulated by the end-users' consumption. Hydrogen fractions achievable in the blend are 0.18% vol. for case a, 0.54 % vol. for case b and 0.90 % vol. for case c; the Wobbe Index of the NG-H₂ mixture is always close to the NG value, meaning that the quality of the supplied gas is preserved and the supplied fuels are interchangeable.

In the best-case scenario (i.e., case c), the cost of hydrogen production is 5.10 EUR kg⁻¹ (compatible with the ranges available in the scientific literature) and the PtH₂ plant allows to save 32.348 tonnes of CO₂ emissions per year.

Future developments may entail the integration of different kinds of renewable sources and the implementation of a multi-objective optimization tool allowing to select the best configurations for the PtH₂ plant according to the characteristics of the installation site.

A

APPENDIX A

A.1 GOVERNING EQUATIONS OF FLUID DYNAMICS

The equations governing the motion of a fluid represent mathematical statements of the conservation of mass, momentum, and energy [100,122,307].

For a viscous Newtonian, homogeneous and isotropic fluid the *conservative form* of the governing equations can be expressed as:

$$\frac{\partial \rho}{\partial t} + \operatorname{div}(\rho \mathbf{u}) = 0 \quad (\text{A.1})$$

$$\frac{\partial(\rho u)}{\partial t} + \operatorname{div}(\rho u \mathbf{u}) = -\frac{\partial p}{\partial x} + \mu \left(\frac{\partial^2 u}{\partial x^2} + \frac{\partial^2 u}{\partial y^2} + \frac{\partial^2 u}{\partial z^2} \right) + \mu \frac{\partial}{\partial x} \left[\left(1 + \frac{\lambda}{\mu} \right) \operatorname{div}(\mathbf{u}) \right] + \sum b_x \quad (\text{A.2})$$

$$\frac{\partial(\rho v)}{\partial t} + \operatorname{div}(\rho v \mathbf{u}) = -\frac{\partial p}{\partial y} + \mu \left(\frac{\partial^2 v}{\partial x^2} + \frac{\partial^2 v}{\partial y^2} + \frac{\partial^2 v}{\partial z^2} \right) + \mu \frac{\partial}{\partial y} \left[\left(1 + \frac{\lambda}{\mu} \right) \operatorname{div}(\mathbf{u}) \right] + \sum b_y \quad (\text{A.3})$$

$$\frac{\partial(\rho w)}{\partial t} + \operatorname{div}(\rho w \mathbf{u}) = -\frac{\partial p}{\partial z} + \mu \left(\frac{\partial^2 w}{\partial x^2} + \frac{\partial^2 w}{\partial y^2} + \frac{\partial^2 w}{\partial z^2} \right) + \mu \frac{\partial}{\partial z} \left[\left(1 + \frac{\lambda}{\mu} \right) \operatorname{div}(\mathbf{u}) \right] + \sum b_z \quad (\text{A.4})$$

$$\frac{\partial \rho e_i}{\partial t} + \operatorname{div}(\rho e_i \mathbf{u}) = -p \operatorname{div}(\mathbf{u}) + \kappa \left(\frac{\partial^2 T}{\partial x^2} + \frac{\partial^2 T}{\partial y^2} + \frac{\partial^2 T}{\partial z^2} \right) + \Phi + S_{e_i} \quad (\text{A.5})$$

Φ is the dissipation function, accounting for the effects due to viscous stresses, whereas the term S_{e_i} represents a source of energy per unit volume per unit time.

Equations (A.1)–(A.5) constitute a set of five partial differential equations involving seven unknown field variables: u , v , w , p , ρ , e_i , T . The two missing equations, required to close the system, can be obtained by determining the relationships existing between the thermodynamic variables (p , ρ , e_i , T) based on the assumption of thermodynamic equilibrium [308]. These relationships are referred to as *equations of state*, and provide a mathematical connection between two or more *point functions* (i.e., thermodynamic variables) [309]. In most of engineering problems, it is reasonable to assume that the investigated gas behaves as a perfect gas with constant specific heats, for which the following relations hold: $p = \rho \cdot R_{\text{specific}} \cdot T$ and $de_i = C_v dT$.

A.1.1 SIMPLIFIED MATHEMATICAL MODELS

The conservation equations for mass and momentum are non-linear and strongly coupled, making them challenging to solve. Analytical solutions of the Navier-Stokes equations can be obtained only in a limited number of cases and for very simple geometries with limited practical relevance [122]. In most situations numerical methods must be employed, demanding significant computational resources. To address this issue, simplifications can be made to reduce the computing efforts. Two commonly adopted

simplifications are the incompressible flow assumption and the Boussinesq approximation, described below.

INCOMPRESSIBLE FLOW

In many applications the fluid density may be assumed as constant, leading to the assumption of *incompressible flow*. Such approximation is acceptable if the Mach number is below 0.3. In that case, governing equations reduce to:

$$\text{div}(\mathbf{u}) = 0 \quad (\text{A.6})$$

$$\rho \left[\frac{\partial u}{\partial t} + \text{div}(u\mathbf{u}) \right] = -\frac{\partial p}{\partial x} + \mu \left(\frac{\partial^2 u}{\partial x^2} + \frac{\partial^2 u}{\partial y^2} + \frac{\partial^2 u}{\partial z^2} \right) + \sum b_x \quad (\text{A.7})$$

$$\rho \left[\frac{\partial v}{\partial t} + \text{div}(v\mathbf{u}) \right] = -\frac{\partial p}{\partial y} + \mu \left(\frac{\partial^2 v}{\partial x^2} + \frac{\partial^2 v}{\partial y^2} + \frac{\partial^2 v}{\partial z^2} \right) + \sum b_y \quad (\text{A.8})$$

$$\rho \left[\frac{\partial w}{\partial t} + \text{div}(w\mathbf{u}) \right] = -\frac{\partial p}{\partial z} + \mu \left(\frac{\partial^2 w}{\partial x^2} + \frac{\partial^2 w}{\partial y^2} + \frac{\partial^2 w}{\partial z^2} \right) + \sum b_z \quad (\text{A.9})$$

$$\rho \left[\frac{\partial e_i}{\partial t} + \text{div}(e_i\mathbf{u}) \right] = \kappa \left(\frac{\partial^2 T}{\partial x^2} + \frac{\partial^2 T}{\partial y^2} + \frac{\partial^2 T}{\partial z^2} \right) + \Phi + S_{e_i} \quad (\text{A.10})$$

The energy equation is no longer coupled with other equations (assuming that fluid properties do not change with temperature, otherwise all equations are coupled as for compressible flows). Therefore, we can first solve the continuity and momentum conservation equations to find velocity and pressure fields and then solve the energy equation to yield the temperature distribution. For buoyancy-driven flows, where variations in density due to temperature changes are accounted for in the body force term of the momentum equation (Boussinesq approximation, see below) all conservation equations again become coupled.

BOUSSINESQ APPROXIMATION

In flows involving heat transfer, fluid properties typically depend on temperature. Even minor variations in temperature can cause the fluid motion. If the change in density is small, it is possible to treat the density as constant in the unsteady and convection terms and treat it as variable only in the gravitational term. This simplification is referred to as the *Boussinesq approximation*, and assumes that density varies linearly with temperature:

$$\rho = \rho_0 [1 - \beta(T - T_0)] \quad (\text{A.11})$$

where ρ_0 is a reference density, T_0 a reference temperature and β is the coefficient of volumetric expansion. This approximation introduces errors of the order of 1% if the temperature differences are below 15 °C for air [122].

A.2 PHYSICS OF TURBULENT FLOWS

Most flows of engineering interest are turbulent in nature [122,246,307]. Turbulence is characterized by unsteadiness and three-dimensionality and causes the appearance in the flow of rotational structures, so-called *turbulent eddies*, with a broad range of length and time scales. In the study of turbulent flows, it is common to refer to an energy cascade, a process where the kinetic energy of larger eddies is transferred to smaller eddies. The cascade starts with the largest eddies (of size l), extracting energy from the mean flow and having the highest level of turbulent kinetic energy per unit mass, as illustrated in the energy spectrum graph below (Figure A.1). These large eddies are identified by the *turbulence Reynolds number* $Re_l = \sqrt{\kappa}l/\nu$. In Figure A.1, the horizontal axis is the wave number, representing the number of eddies per unit length (i.e., $\propto r^{-1}$, where r is the eddy size). The kinetic energy of eddies between the wave numbers κ and $\kappa+d\kappa$ is $E(\kappa)d\kappa$ [310].

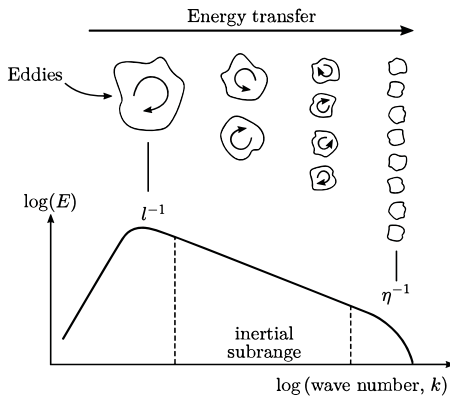


Figure A.1. Energy spectrum for a turbulent flow [310].

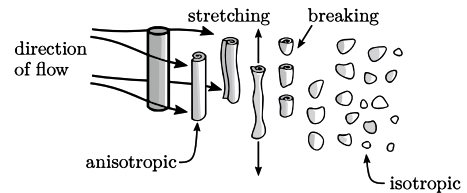


Figure A.2. Process of large eddies becoming smaller [310].

Large eddies are usually anisotropic due to the way turbulence is generated; their behaviour is dictated by the geometry of the problem domain, the boundary conditions and body forces [100]. For instance, when a fluid flows past a cylinder, it causes the shedding of vortices having a shape similar to the cylinder, i.e., they are elongated in the direction of the cylinder axis (see Figure A.2).

When moving downstream, through open space, eddies quickly stretch, bend, rotate and break, eventually becoming “blobs” of vorticity. The *turn-over* time of the eddies (i.e., the time for one revolution) decreases with their size. The smaller eddies are nearly isotropic, and have a universal behaviour, dominated by the viscosity ν and by the rate of energy transferred from the large scales ε . The smallest relevant length scales are known as the *Kolmogorov length scale* (η) and are responsible for dissipation. If the Reynolds number is sufficiently high, an intermediate range of scale exists ($\eta \ll r \ll l$, known as the *inertial subrange*) which transfers the energy from the large scales down the cascade (however, negligible dissipation occurs in this range).

There are several numerical methods to model the behaviour of turbulence flows.

These methods can be grouped into three main categories: (i) turbulence models for Reynolds-averaged Navier-Stokes (RANS) equations; (ii) large eddy simulation (LES); (iii) direct numerical simulation (DNS) [100].

The latter consists in directly numerically solving the governing equations over the whole range of turbulent scales (both temporal and spatial). This results in prohibitive computational costs owing to the mesh and time step requirements: the total number of grid points required is of the order of $Re_l^{9/4}$, whereas the time step should be of the order of η/u_l (where u_l is the large-scale velocity) [311]. For this reason, this approach is mainly used for benchmarking and academic purposes.

With LES, the largest scales of turbulent motion are directly simulated whereas the smaller scales are filtered out and modelled by the so-called subgrid scale models. The underlying principle of this approach is that, while largest scales are affected by the flow conditions and domain boundaries, the smaller scales tend only to be aware of their immediate surroundings and have common characteristic, being thus easier to model. LES reduces the computational cost compared to DNS, and its use is gradually expanding thanks to the advances in computing hardware and parallel algorithms [308].

The method that demands the least computational resources, and for this reason widely applied in both industry and research, is RANS. Here, the governing equations are time-averaged, giving rise to new terms that must be correlated with the mean flow variables through turbulence models. These models are semi-empirical, based on experimental data acquired for simple and controlled flow configurations; as a result, a general-purpose model does not exist and several models have been developed over the years, each suitable for investigating specific categories of fluid flow problems.

A schematic representation of the length scales solved with the different approaches described above is provided in Figure A.3.

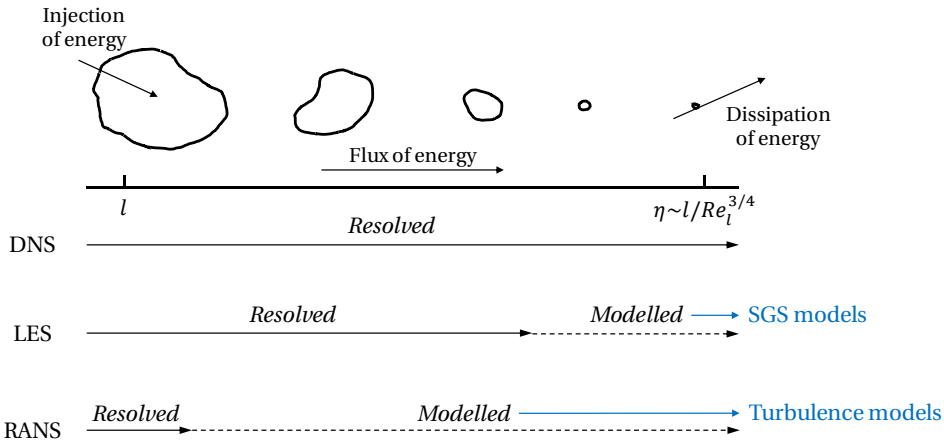


Figure A.3. Schematic representation of the scales of turbulent motion solved with DNS, LES and RANS approaches (adapted from Bakker [312]).

A.2.1 REYNOLDS-AVERAGED NAVIER-STOKES (RANS) SIMULATIONS

According to the Reynolds decomposition, every flow variable can be written as the sum of a mean (i.e., time-averaged) part $\bar{\varphi}$ and a time-dependent fluctuating part φ' [246]:

$$\varphi(\mathbf{x}, t) = \bar{\varphi}(\mathbf{x}) + \varphi'(\mathbf{x}, t) \quad (\text{A.12})$$

The time-average of the fluctuating value is zero $\overline{\varphi'} = 0$, and the mean value defined as:

$$\bar{\varphi}(\mathbf{x}) = \lim_{T \rightarrow \infty} \frac{1}{T} \int_t^{t+T} \varphi(\mathbf{x}, t) dt \quad (\text{A.13})$$

Here, T represents the averaging interval. This interval must be large compared to the typical time scales of the fluctuations; thus, we are interested in the limit $T \rightarrow \infty$ [122] (see Figure A.4, left picture).

If the mean flow $\bar{\varphi}$ varies slowly over time, an unsteady approach (URANS) must be employed. Equations (A.12) and (A.13) modify as follows:

$$\varphi(\mathbf{x}, t) = \bar{\varphi}(\mathbf{x}, t) + \varphi'(\mathbf{x}, t) \quad (\text{A.14})$$

$$\bar{\varphi}(\mathbf{x}, t) = \frac{1}{T} \int_t^{t+T} \varphi(\mathbf{x}, t) dt \quad , \quad T_1 \ll T \ll T_2 \quad (\text{A.15})$$

where T_1 is the time scale of the rapid fluctuations and T_2 the time scale of the slow variations in the flow, respectively (Figure A.4, right picture).

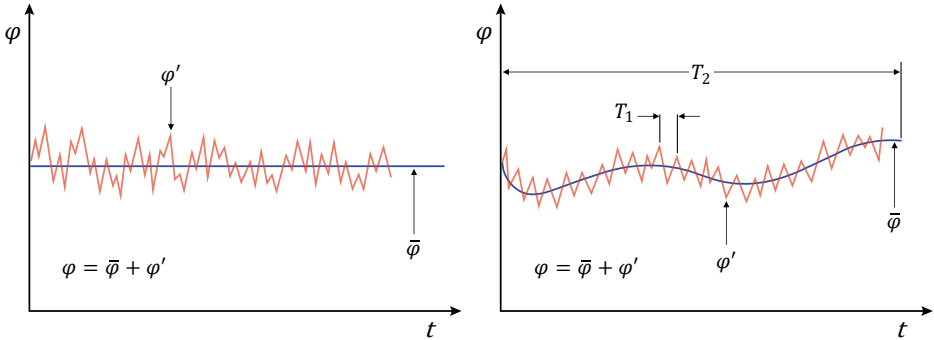


Figure A.4. Time averaging for a statistically steady turbulent flow (left) and time averaging for an unsteady turbulent flow (right), adapted from Guerrero [308].

Let us now consider the continuity and momentum equations for incompressible flows without body forces:

$$\text{div}(\mathbf{u}) = 0 \quad (\text{A.16})$$

$$\frac{\partial \rho u}{\partial t} + \text{div}(\rho \mathbf{u} \mathbf{u}) = -\frac{\partial p}{\partial x} + \mu \left(\frac{\partial^2 u}{\partial x^2} + \frac{\partial^2 u}{\partial y^2} + \frac{\partial^2 u}{\partial z^2} \right) \quad (\text{A.17})$$

$$\frac{\partial \rho v}{\partial t} + \text{div}(\rho v \mathbf{u}) = -\frac{\partial p}{\partial y} + \mu \left(\frac{\partial^2 v}{\partial x^2} + \frac{\partial^2 v}{\partial y^2} + \frac{\partial^2 v}{\partial z^2} \right) \quad (\text{A.18})$$

$$\frac{\partial \rho w}{\partial t} + \text{div}(\rho w \mathbf{u}) = -\frac{\partial p}{\partial z} + \mu \left(\frac{\partial^2 w}{\partial x^2} + \frac{\partial^2 w}{\partial y^2} + \frac{\partial^2 w}{\partial z^2} \right) \quad (\text{A.19})$$

Reynolds decomposition of the flow variables returns:

$$\mathbf{u}(\mathbf{x}, t) = \bar{\mathbf{u}}(\mathbf{x}) + \mathbf{u}'(\mathbf{x}, t) \quad (\text{A.20})$$

$$p(\mathbf{x}, t) = \bar{p}(\mathbf{x}) + p'(\mathbf{x}, t) \quad (\text{A.21})$$

Substituting expressions (A.20) and (A.21) in equations (A.16)–(A.19), time averaging and rearranging, the incompressible RANS equations are obtained:

$$\text{div}(\bar{\mathbf{u}}) = 0 \quad (\text{A.22})$$

$$\text{div}(\rho \bar{u} \bar{\mathbf{u}}) + \text{div}(\rho \overline{u' \mathbf{u}'}) = -\frac{\partial \bar{p}}{\partial x} + \mu \left(\frac{\partial^2 \bar{u}}{\partial x^2} + \frac{\partial^2 \bar{u}}{\partial y^2} + \frac{\partial^2 \bar{u}}{\partial z^2} \right) \quad (\text{A.23})$$

$$\text{div}(\rho \bar{v} \bar{\mathbf{u}}) + \text{div}(\rho \overline{v' \mathbf{u}'}) = -\frac{\partial \bar{p}}{\partial y} + \mu \left(\frac{\partial^2 \bar{v}}{\partial x^2} + \frac{\partial^2 \bar{v}}{\partial y^2} + \frac{\partial^2 \bar{v}}{\partial z^2} \right) \quad (\text{A.24})$$

$$\text{div}(\rho \bar{w} \bar{\mathbf{u}}) + \text{div}(\rho \overline{w' \mathbf{u}'}) = -\frac{\partial \bar{p}}{\partial z} + \mu \left(\frac{\partial^2 \bar{w}}{\partial x^2} + \frac{\partial^2 \bar{w}}{\partial y^2} + \frac{\partial^2 \bar{w}}{\partial z^2} \right) \quad (\text{A.25})$$

The term $\overline{u'_i u'_j}$ (in suffix notation), arising from the time-averaging operation, is the so-called *Reynolds stress tensor* \mathcal{R}_{ij} ². It is clearly symmetric and represents the momentum transfer by the fluctuating velocity field. From Equations (A.22)–(A.25) it is observed that the number of unknown quantities (pressure, three velocity components and six stresses) is larger than the number of equations. As a result, the system of equations is not closed, and the Reynolds stresses need to be appropriately modelled. A common approach used to resolve the problem of closure is the Boussinesq hypothesis, which relates the Reynolds stresses to the mean velocity gradients through an eddy (or turbulent) viscosity μ_T :

$$-\rho \overline{u'_i u'_j} = \mu_T \left(\frac{\partial \bar{u}_i}{\partial x_j} + \frac{\partial \bar{u}_j}{\partial x_i} \right) - \frac{2}{3} \rho \delta_{ij} k \quad (\text{A.26})$$

where δ_{ij} is the Kronecker delta and $k = \frac{1}{2} \overline{u'_i u'_i}$ is the turbulent kinetic energy per unit mass. The isotropic part of the Reynolds stress tensor is absorbed normally into the pressure term as $\bar{p} = \bar{p} + 2k/3$ [189]. The turbulent viscosity is a property of the flow field

² A check of the dimensions will show that \mathcal{R}_{ij} is not actually a stress. It must be multiplied by the density ρ to have dimensions corresponding to the stresses.

and not a physical property of the fluid. The missing equations, required to balance the number of unknowns and yield the solution, are provided by the so-called *turbulence models*.

A.2.2 LARGE EDDY SIMULATIONS (LES)

Instead of time-averaging, large eddy simulation involves the use of a spatial filter to separate the larger eddies (to be resolved) from the smaller ones (to be modelled).

For a general property φ , the filtering operation is usually defined as:

$$\tilde{\varphi}(\mathbf{x}, t) = \int_{\mathcal{D}} \mathcal{G}(\mathbf{x}, \mathbf{x}', \Delta) \varphi(\mathbf{x}', t) dx' dy' dz' \quad (\text{A.27})$$

where $\tilde{\varphi}(\mathbf{x}, t)$ is the filtered function; \mathcal{D} is the flow domain; \mathcal{G} is the filter function (usually a Gaussian filter); \mathbf{x}' is the variable moving in the points surrounding \mathbf{x} , that is instead the vector coordinate of the position.

Δ is the cutoff width (only eddies with a length scale greater than the cutoff width are resolved), and is often taken as the cube root of the grid cell volume:

$$\Delta = \sqrt[3]{\Delta x \Delta y \Delta z} \quad (\text{A.28})$$

Δx , Δy , Δz are the grid lengths in the x, y and z directions respectively.

Let us now focus our attention on incompressible flows, for the sake of simplicity. The filtered continuity and momentum conservation equations for a Newtonian fluid are the following (body forces are also neglected):

$$\text{div}(\rho \tilde{\mathbf{u}}) = 0 \quad (\text{A.29})$$

$$\frac{\partial(\rho \tilde{u})}{\partial t} + \text{div}(\rho \tilde{u} \tilde{\mathbf{u}}) = -\frac{\partial \tilde{p}}{\partial x} + \mu \left(\frac{\partial^2 \tilde{u}}{\partial x^2} + \frac{\partial^2 \tilde{u}}{\partial y^2} + \frac{\partial^2 \tilde{u}}{\partial z^2} \right) \quad (\text{A.30})$$

$$\frac{\partial(\rho \tilde{v})}{\partial t} + \text{div}(\rho \tilde{v} \tilde{\mathbf{u}}) = -\frac{\partial \tilde{p}}{\partial y} + \mu \left(\frac{\partial^2 \tilde{v}}{\partial x^2} + \frac{\partial^2 \tilde{v}}{\partial y^2} + \frac{\partial^2 \tilde{v}}{\partial z^2} \right) \quad (\text{A.31})$$

$$\frac{\partial(\rho \tilde{w})}{\partial t} + \text{div}(\rho \tilde{w} \tilde{\mathbf{u}}) = -\frac{\partial \tilde{p}}{\partial z} + \mu \left(\frac{\partial^2 \tilde{w}}{\partial x^2} + \frac{\partial^2 \tilde{w}}{\partial y^2} + \frac{\partial^2 \tilde{w}}{\partial z^2} \right) \quad (\text{A.32})$$

Equations (A.29)–(A.32) must be solved to yield the filtered velocity (\tilde{u} , \tilde{v} , \tilde{w}) and pressure (\tilde{p}) fields. However, the convective terms $\text{div}(\rho \tilde{u} \tilde{\mathbf{u}})$, $\text{div}(\rho \tilde{v} \tilde{\mathbf{u}})$ and $\text{div}(\rho \tilde{w} \tilde{\mathbf{u}})$ requires further manipulation to get the solution. One can write:

$$\text{div}(\rho \tilde{u}_i \tilde{\mathbf{u}}) = \text{div}(\rho \tilde{u}_i \tilde{\mathbf{u}}) + (\text{div}(\rho \tilde{u}_i \tilde{\mathbf{u}}) - \text{div}(\rho \tilde{u}_i \tilde{\mathbf{u}})) \quad (\text{A.33})$$

The difference $\tilde{u}_i \tilde{\mathbf{u}} - \tilde{u}_i \tilde{\mathbf{u}}$ is modelled as:

$$\tau_{SGS} = -\rho(\tilde{u}_i \tilde{\mathbf{u}} - \tilde{u}_i \tilde{\mathbf{u}}) \quad (\text{A.34})$$

providing the momentum equations solved in LES:

$$\frac{\partial(\rho\tilde{u})}{\partial t} + \text{div}(\rho\tilde{u}\tilde{\mathbf{u}}) = -\frac{\partial\tilde{p}}{\partial x} + \mu\left(\frac{\partial^2\tilde{u}}{\partial x^2} + \frac{\partial^2\tilde{u}}{\partial y^2} + \frac{\partial^2\tilde{u}}{\partial z^2}\right) + \text{div}(\tau_{SGS}) \quad (\text{A.35})$$

$$\frac{\partial(\rho\tilde{v})}{\partial t} + \text{div}(\rho\tilde{v}\tilde{\mathbf{u}}) = -\frac{\partial\tilde{p}}{\partial y} + \mu\left(\frac{\partial^2\tilde{v}}{\partial x^2} + \frac{\partial^2\tilde{v}}{\partial y^2} + \frac{\partial^2\tilde{v}}{\partial z^2}\right) + \text{div}(\tau_{SGS}) \quad (\text{A.36})$$

$$\frac{\partial(\rho\tilde{w})}{\partial t} + \text{div}(\rho\tilde{w}\tilde{\mathbf{u}}) = -\frac{\partial\tilde{p}}{\partial z} + \mu\left(\frac{\partial^2\tilde{w}}{\partial x^2} + \frac{\partial^2\tilde{w}}{\partial y^2} + \frac{\partial^2\tilde{w}}{\partial z^2}\right) + \text{div}(\tau_{SGS}) \quad (\text{A.37})$$

τ_{SGS} stresses are called the *subgrid-scale Reynolds stresses* and represent the momentum flux caused by the action of the unresolved scales [122]; they are approximated by the so-called *subgrid-scale models*.

A.3 THE FINITE VOLUME METHOD (FVM)

The governing equations described in the preceding sections are converted into linear algebraic equations and solved using the open-source code OpenFOAM, which is based on the finite volume formulation.

The Finite Volume Method is a widely employed technique in computational fluid dynamics, known for its inherent conservation properties and its ability to be used on arbitrary computational grids [313]. Like other numerical methods, the FVM transforms the set of partial differential equations into a system of algebraic equations; however, the discretisation process is different and is based on integrating the governing equations over control volumes that discretise the computational domain [100].

The starting point for applying the FVM is the convection-diffusion equation, which for a general property per unit mass φ appears as follows [100]:

$$\underbrace{\frac{\partial(\rho\varphi)}{\partial t}}_{\text{transient term}} + \underbrace{\text{div}(\rho\varphi\mathbf{u})}_{\text{convective term}} = \underbrace{\text{div}(\Gamma \text{grad}\varphi)}_{\text{diffusive term}} + \underbrace{S_\varphi}_{\text{source term}} \quad (\text{A.38})$$

This equation can take the form of the equation of conservation of mass, momentum or energy by appropriately choosing φ , the diffusion coefficient Γ and the source term S_φ .

Integration of Equation (A.38) over a three-dimensional control volume (CV) returns:

$$\int_{CV} \frac{\partial(\rho\varphi)}{\partial t} dV + \int_{CV} \text{div}(\rho\varphi\mathbf{u}) dV = \int_{CV} \text{div}(\Gamma \text{grad}\varphi) dV + \int_{CV} S_\varphi dV \quad (\text{A.39})$$

The convective and diffusive terms are rewritten as integrals over the entire bounding surface of the CV (A), by using the Gauss's divergence theorem, which for a generic vector \mathbf{a} states:

$$\int_{CV} \text{div}(\mathbf{a}) dV = \int_A \mathbf{n} \cdot \mathbf{a} dA \quad (\text{A.40})$$

where $\mathbf{n} \cdot \mathbf{a}$ is the component of vector \mathbf{a} in the direction of the vector \mathbf{n} normal to the surface element dA .

Applying Gauss's divergence theorem, Equation (A.39) can be thus written as:

$$\frac{\partial}{\partial t} \int_{CV} \rho \varphi dV + \int_A \mathbf{n} \cdot (\rho \varphi \mathbf{u}) dA = \int_A \mathbf{n} \cdot (\Gamma \text{grad} \varphi) dA + \int_{CV} S_\varphi dV \quad (\text{A.41})$$

In words:

$$\begin{array}{ccccccc} \text{Rate of increase of} & & \text{Net rate of} & & \text{Net rate of increase} & & \text{Net rate of creation} \\ \varphi \text{ inside the CV} & + & \text{decrease of } \varphi \text{ due} & = & \text{of } \varphi \text{ due to} & + & \text{of } \varphi \text{ inside the CV} \\ & & \text{to convection} & & \text{diffusion across} & & \\ & & \text{across the CV} & & \text{the CV boundaries} & & \\ & & \text{boundaries} & & & & \end{array}$$

Equation (A.41) is thus a statement of the conservation of property φ for a finite size CV.

A.3.1 FVM FOR DIFFUSION PROBLEMS

The governing equation for diffusion problems can be derived from the general transport equation (A.38) for a property φ by deleting the convective term. This gives:

$$\text{div}(\Gamma \text{grad} \varphi) + S_\varphi = \frac{\partial(\rho \varphi)}{\partial t} \quad (\text{A.42})$$

In the present discussion, the numerical techniques to discretise the governing equations are introduced for the sake of simplicity with reference to a steady state 1D case; however, the methodology adopted here has general validity and can be easily extended to 2D and 3D problems. Figure A.5 displays a generic 1D domain with the terminology commonly adopted in the finite volume formulation.

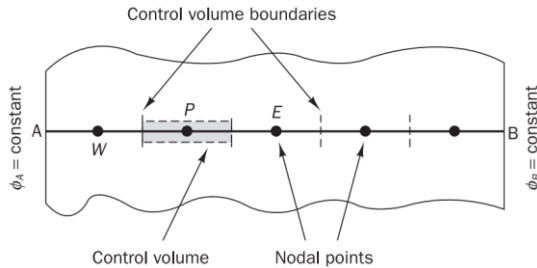


Figure A.5. Generic 1D computational domain [100].

For steady state, one-dimensional problems, Equation (A.42) modifies as follows:

$$\frac{d}{dx} \left(\Gamma \frac{d\varphi}{dx} \right) + S = 0 \quad (\text{A.43})$$

The first step for the discretisation of the governing equation is the definition of the computational grid, obtained by dividing the domain into discrete control volumes. For a general nodal point P , the control volume is depicted in Figure A.6. The left and right nodes are identified by the letters W and E , respectively; faces of the control volume are referred to by the letters w and e . Distances of interest for the analysis, and the width of the CV, are indicated in Figure A.6 as well.

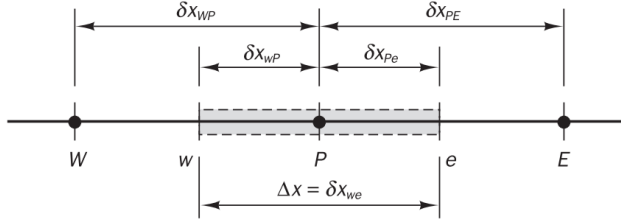


Figure A.6. Usual convention of CFD methods [100].

The next step is the integration over the CV of the terms from Equation (A.43) and the application of Gauss's theorem:

$$\int_{\Delta V} \frac{d}{dx} \left(\Gamma \frac{d\varphi}{dx} \right) dV + \int_{\Delta V} S dV = \left(\Gamma A \frac{d\varphi}{dx} \right)_e - \left(\Gamma A \frac{d\varphi}{dx} \right)_w + \bar{S} \Delta V = 0 \quad (\text{A.44})$$

Here A is the cross-sectional area of the CV face, ΔV is the volume and \bar{S} is the average value of source S over the CV.

Assuming that the generic property φ is continuous, differentiable, with bounded and continuous derivatives, it is possible to expand the function $\varphi(x)$ into a Taylor series and express φ_E and φ_P in terms of φ_e :

$$\varphi_E = \varphi_e + \left. \frac{d\varphi}{dx} \right|_e \delta x_{eE} + \left. \frac{d^2\varphi}{dx^2} \right|_e \frac{\delta x_{eE}^2}{2} + o(\delta x^3) \quad (\text{A.45})$$

$$\varphi_P = \varphi_e - \left. \frac{d\varphi}{dx} \right|_e \delta x_{Pe} + \left. \frac{d^2\varphi}{dx^2} \right|_e \frac{\delta x_{Pe}^2}{2} + o(\delta x^3) \quad (\text{A.46})$$

where the symbol $o(\delta x^3)$ indicates that the order of magnitude of the remaining terms is δx^3 . Subtracting expressions (A.45) and (A.46) term by term yields:

$$\varphi_E - \varphi_P = \left. \frac{d\varphi}{dx} \right|_e (\delta x_{eE} + \delta x_{Pe}) + o(\delta x^2) \quad (\text{A.47})$$

from which, considering that $\delta x_{eE} + \delta x_{Pe} = \delta x_{PE}$ and neglecting the term $o(\delta x^2)$, the approximation of the differential operator using the central differencing scheme, second-order accurate³, is obtained:

$$\left. \frac{d\varphi}{dx} \right|_e = \frac{\varphi_E - \varphi_P}{\delta x_{PE}} \quad (\text{A.48})$$

A similar expression is obtained for the derivative at the interface w :

$$\left. \frac{d\varphi}{dx} \right|_w = \frac{\varphi_P - \varphi_W}{\delta x_{WP}} \quad (\text{A.49})$$

By substituting equations (A.48) and (A.49) into equation (A.44), the discretised form of equation (A.43) is obtained, which is valid for the general internal node P :

$$\Gamma_e A_e \frac{\varphi_E - \varphi_P}{\delta x_{PE}} - \Gamma_w A_w \frac{\varphi_P - \varphi_W}{\delta x_{WP}} + \bar{S} \Delta V = 0 \quad (\text{A.50})$$

Discretised expressions of the form of equation (A.50) must be derived for each node of the computational grid in order to solve the problem. For control volumes adjacent to the domain boundaries, equation (A.50) is modified to embed boundary conditions. This results in a system of linear algebraic equations that is solved to obtain the values of the property φ at the nodes of the computational grid.

A.3.2 FVM FOR CONVECTION-DIFFUSION PROBLEMS

To solve problems involving the presence of a moving fluid, it is necessary to consider both the effects of transport and diffusion. Let us consider the steady-state convection-diffusion equation for the general quantity φ , derived from equation (A.38) by deleting the transient term:

$$\text{div}(\rho \varphi \mathbf{u}) = \text{div}(\Gamma \text{grad} \varphi) + S_\varphi \quad (\text{A.51})$$

Simultaneously, due to the presence of a velocity field, the continuity equation must also be upheld:

$$\text{div}(\rho \mathbf{u}) = 0 \quad (\text{A.52})$$

To simplify the analysis, the 1D scenario in a steady-state condition without generation is here considered. It is assumed that the velocity field is known (some methods for solving the velocity field are described in Section A.4).

³ It is second-order accurate because the neglected term in equation (A.47), i.e., the truncation error, is proportional to δx^2 . This enables greater accuracy in the solution with coarser grids.

Equations (A.51) and (A.52) are modified as follows:

$$\frac{d}{dx}(\rho\varphi\mathbf{u}) = \frac{d}{dx}\left(\Gamma\frac{d\varphi}{dx}\right) \quad (\text{A.53})$$

$$\frac{d(\rho\mathbf{u})}{dx} = 0 \quad (\text{A.54})$$

Let us now focus on the control volume in Figure A.7, with particular attention to the general internal node P .

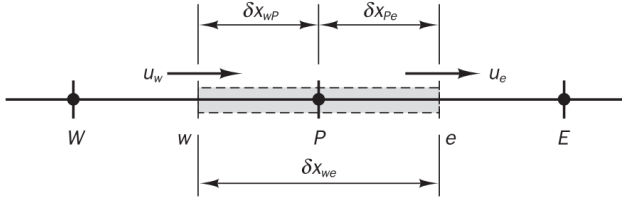


Figure A.7. A control volume around node P [100].

The integration of equation (A.53) over the control volume yields the following expression:

$$(\rho u A \varphi)_e - (\rho u A \varphi)_w = \left(\Gamma A \frac{d\varphi}{dx}\right)_e - \left(\Gamma A \frac{d\varphi}{dx}\right)_w \quad (\text{A.55})$$

Integration of the mass conservation equation (A.54) yields the following:

$$(\rho u A)_e - (\rho u A)_w = 0 \quad (\text{A.56})$$

To derive the discretised equations, it is necessary to approximate the terms within equation (A.55). In this instance, not only the gradient but also the value of φ itself needs to be evaluated at the interface. The derivatives at the interfaces (e , w) can still be approximated according to equations (A.48) and (A.49), respectively.

Let us introduce the two terms:

$$F = \rho u A; \quad D = \frac{\Gamma A}{\delta x} \quad (\text{A.57})$$

and thus

$$F_e = (\rho u A)_e \quad F_w = (\rho u A)_w \quad (\text{A.58})$$

$$D_e = \frac{\Gamma_e A_e}{\delta x_{PE}} \quad D_w = \frac{\Gamma_w A_w}{\delta x_{WP}} \quad (\text{A.59})$$

Hence, equations (A.55) and (A.56) can be rewritten as:

$$F_e \varphi_e - F_w \varphi_w = D_e(\varphi_E - \varphi_P) - D_w(\varphi_P - \varphi_W) \quad (\text{A.60})$$

$$F_e - F_w = 0 \quad (\text{A.61})$$

The values of φ_e and φ_w still need to be evaluated, and there are several possibilities to consider: (i) central differencing scheme, (ii) constant upwinding, and (iii) linear upwinding.

THE CENTRAL DIFFERENCING SCHEME

In the central differencing scheme, φ values at the control volume faces are computed using linear interpolation of nodal values:

$$\varphi_e = (\varphi_E + \varphi_P)/2 \quad (\text{A.62})$$

$$\varphi_w = (\varphi_W + \varphi_P)/2 \quad (\text{A.63})$$

The substitution of the above relationships into equation (A.60) leads to the following expression:

$$F_e \left(\frac{\varphi_E + \varphi_P}{2} \right) - F_w \left(\frac{\varphi_W + \varphi_P}{2} \right) = D_e(\varphi_E - \varphi_P) - D_w(\varphi_P - \varphi_W) \quad (\text{A.64})$$

Rearranging equation (A.64) and also considering the continuity equation (A.61), we obtain the discretised expression (according to the central differencing scheme) of the convection-diffusion equation for the general internal node P:

$$a_P \varphi_P = a_E \varphi_E + a_W \varphi_W \quad (\text{A.65})$$

where $a_P = a_E + a_W$, $a_E = D_e - \frac{F_e}{2}$, $a_W = D_w + \frac{F_w}{2}$.

By deriving expressions similar to (A.65) for all nodes, a system of linear algebraic equations is obtained, which, when solved, yields the distribution of the property φ inside the computational domain.

PROPERTIES OF DISCRETISATION SCHEMES

The central differencing scheme, which was used in the previous section for the discretisation of convective terms, exhibits stability issues when the convective term becomes more significant compared to the diffusive term. To understand the reasons behind this, it is necessary to introduce the properties that discretisation schemes must possess for the numerical results obtained from solving the approximate equations to accurately describe physical reality. The most important properties are: (i) conservativeness; (ii) boundedness; (iii) transportiveness.

i. Conservativeness

A numerical scheme must be *conservative*. The integration of the convection-diffusion equation over a finite number of control volumes leads to a set of discretised equations where the fluxes of the property φ through the control volume faces appear. To ensure the conservation of φ throughout the solution domain, the flux of φ leaving the control volume through a face must be equal to the flux entering the adjacent volume through the same face. Therefore, the flux through a common face must be consistently expressed in the same manner across adjacent elements.

ii. Boundedness

A numerical scheme must be *bounded*. To ensure *boundedness*, it is desirable for the discretisation scheme to produce coefficients in compliance with the Scarborough criterion⁴ [100,314]:

$$\frac{|a_p|}{\sum |a_{nb}|} \begin{cases} \geq 1 & \text{at all nodes} \\ > 1 & \text{at one node at least} \end{cases} \quad (\text{A.66})$$

Here a_p is the coefficient of the central node P and the summation in the denominator is taken over all the neighbouring nodes (*nb*). If the condition expressed by equation (A.66) is verified, then the resulting matrix of coefficients is said to be *diagonally dominant*. From a physical perspective, this implies that, for example, in a steady-state conduction problem with no sources and boundary temperatures of 500°C and 200°C, all internal temperature values must be less than 500°C and greater than 200°C. In this sense, the problem is bounded: it has an upper and lower limit.

Another fundamental requirement for *boundedness* is that the coefficients of the discretised equations must all have the same sign (usually all positive). Physically, this means that an increase in the variable φ at one node results in an increase in nearby nodes. If the discretisation scheme does not satisfy the boundedness condition, it is possible that the solution may contain small oscillations or may not converge at all.

iii. Transportiveness

A numerical scheme should be capable of properly handling transport and taking into account the actual direction from which the flow originates. This property can be illustrated by considering the effect of two nearby sources, located at nodes *W* and *E*, on a generic node *P* (Figure A.8).

To accomplish this, we introduce the *Peclet number*, which represents a measure of the relative strength of convection and diffusion:

$$Pe = \frac{F}{D} = \frac{\rho u \delta x}{\Gamma} \quad (\text{A.67})$$

where δx is the characteristic length (cell width).

The contour lines in Figure A.8 represent the contours of constant φ in the cases of pure diffusion (Figure A.8a) and increasing convection (Figure A.8b). In the first case ($Pe \rightarrow 0$,

⁴ This criterion represents a sufficient condition for a convergent iterative method, not a necessary one. There are instances where convergence can still be achieved despite violating the criterion [314].

pure diffusion), points W and E influence point P in the same way; conversely, in the case of a non-negligible convective contribution (increasing Pe), the influence of the upstream point becomes more pronounced. In this case, it is therefore crucial for the numerical scheme to consider the direction of the flow.

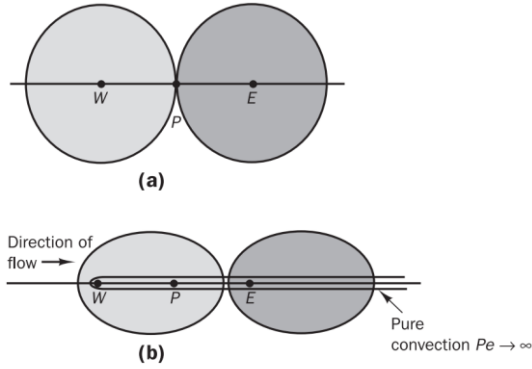


Figure A.8. Distribution of ϕ in the vicinity of two sources at different Peclet numbers: (a) pure diffusion, $Pe \rightarrow 0$; (b) diffusion and convection [100].

In light of the considerations just made, it is possible to assess the applicability of the central differencing scheme to convection-diffusion problems.

- *Conservativeness*: the scheme is conservative because it employs consistent expressions to evaluate convective and diffusive fluxes at the control volume faces.
- *Boundedness*: taking into consideration the discretised equation (A.65), the scheme is bounded if a_E is positive and hence:

$$\frac{F_e}{D_e} = Pe_e < 2 \quad (\text{A.68})$$

This is why the method encounters stability issues when convection dominates over diffusion: Pe increases and exceeds the limit just identified. To accommodate higher inlet velocities, it is necessary to refine the computational grid so as to satisfy the condition expressed by equation (A.68).

- *Transportiveness*: the scheme does not possess the transportiveness property because it does not account for the flow direction. The fluxes through the faces are computed as the average of values upstream and downstream of the face itself.

CONSTANT UPWINDING

One of the main limitations of the central differencing scheme is its inability to identify the flow direction: the value of the property ϕ is always influenced by the nodes upstream and downstream. The *upwinding* method overcomes this limitation and considers the convective effects, by approximating the values of the unknown variable ϕ on the faces with the upstream value of ϕ :

$$\phi_e = \phi_P \quad (\text{A.69})$$

$$\varphi_w = \varphi_W \quad (\text{A.70})$$

A

The convection-diffusion equation for the generic internal node P , discretised using the *upwinding* scheme, is presented below:

$$a_P \varphi_P = a_E \varphi_E + a_W \varphi_W \quad (\text{A.71})$$

where $a_P = a_W + a_E$, $a_E = D_e$, $a_W = D_w + F_w$.

The *upwinding* method is *conservative*, possesses the *transportiveness* property (as it accounts for the flow direction) and *bounded* (the coefficients of the discretised equation are always positive, thus satisfying the condition expressed by equation (A.68)). However, it is first-order accurate and has the drawback of introducing artificial diffusion (*false diffusion*) that tends to dampen the gradients in the solution.

LINEAR UPWINDING

Linear upwinding is a second-order accurate discretisation scheme that addresses the issues of artificial diffusion introduced by constant upwinding. It takes into account the Peclet number for evaluating the property φ on the control volume faces.

A.4 PRESSURE-VELOCITY COUPLING: SIMPLE, PISO AND PIMPLE ALGORITHMS

In the preceding section, the process of discretising and solving the convection-diffusion equation for a general property φ , given the velocity field, was demonstrated. However, in general, this velocity field is not initially known but emerges as part of the overall solution along with other variables. To obtain the velocity field of a fluid system, the continuity and momentum conservation equations must be solved. However, solving these equations is challenging due to: (i) their strong coupling (each velocity component appears in each equation); (ii) the absence of an explicit equation to determine the pressure; (iii) the presence of nonlinear terms in the momentum conservation equation. For incompressible flows, the calculation is further complicated by the strong coupling between pressure and velocity (if the correct pressure field is applied in the conservation of momentum, the resulting velocity field must satisfy mass conservation) and the fact that pressure does not appear as a primary variable in the equations of momentum conservation nor continuity. The issues associated with nonlinearity in the system of equations and the pressure-velocity coupling can be addressed by adopting iterative solution strategies. Among the most used solvers are the so-called *pressure-based* algorithms, which involve determining the velocity field by solving the momentum conservation equation and calculating the pressure field by solving a pressure-correction equation (obtained by manipulating the equations of mass and momentum conservation and taking the form of a Poisson equation). *Pressure-based* algorithms can be categorized as *segregated* and *coupled*; with the former, the governing equations are solved separately and sequentially, while with the latter, they are solved simultaneously. In OpenFOAM, the segregated solvers SIMPLE, PISO, and PIMPLE are implemented, and these are described in more detail in the following sections.

A.4.1 SIMPLE ALGORITHM

The SIMPLE algorithm (Semi-Implicit Method for Pressure-Linked Equations), developed by Patankar and Spalding in 1972 [315], is a steady-state solver for both compressible and incompressible flows. Over the years, many variations of this algorithm have been proposed, making it one of the most extensively studied algorithms in the field of computational fluid dynamics.

The algorithm, whose flowchart is depicted in Figure A.9, involves an iterative sequence of steps ($i = 1, 2, \dots, i_{end}$) until convergence is reached. It starts by constructing a matrix equation for energy, which is under-relaxed⁵ by a factor α_T . This equation is solved for temperature T , which is then used to update the density $\rho(T, p)$ according to an equation of state. A matrix equation denoted as $\mathbf{A} \cdot \mathbf{u} - \mathbf{b}$ (momentum matrix) is then built using all terms from the momentum conservation equation except ∇p ; this matrix equation is under-relaxed by a factor α_u before being equated to $-\nabla p$ and solved for the velocity vector \mathbf{u} (momentum predictor). Starting from the matrix equation $\mathbf{A} \cdot \mathbf{u} - \mathbf{b}$, the terms $\mathbf{A}\mathbf{u}$ and $\mathbf{H}(\mathbf{u})$ are determined, where \mathbf{A} is a diagonal matrix (see Figure A.10).

These derived terms are employed to formulate the pressure equation and calculate p . The new pressure is then used to correct the mass flux ϕ_f to ensure with greater accuracy the adherence to the mass conservation equation (flux corrector). Finally, it is under-relaxed by a factor α_p before correcting the velocity value (momentum corrector).

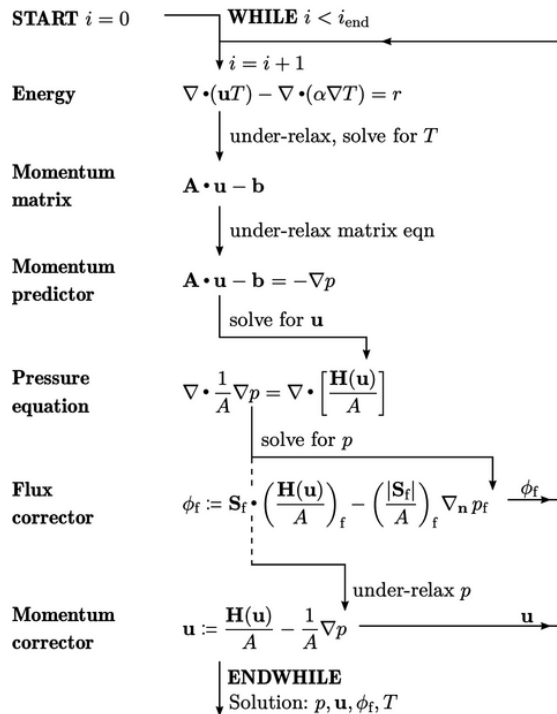


Figure A.9. Implementation of the SIMPLE algorithm in OpenFOAM [310].

⁵ Under-relaxation is a method used to improve the convergence of the solution, by limiting the amount of variation of a variable during a solution step.

$$\begin{array}{c}
 \mathbf{A} \cdot \mathbf{u} - \mathbf{b} \\
 \downarrow \\
 \begin{bmatrix} \square & * & * \\ * & \square & * \\ * & * & \square \end{bmatrix} \begin{bmatrix} u \\ v \\ w \end{bmatrix} - \begin{bmatrix} * \\ * \\ * \end{bmatrix} \\
 \downarrow \qquad \qquad \downarrow \\
 \underbrace{\begin{bmatrix} \square & & & \\ & \square & & \\ & & \square & \\ & & & \square \end{bmatrix} \begin{bmatrix} u \\ v \\ w \\ p \end{bmatrix}}_{\mathbf{A}\mathbf{u}} + \underbrace{\begin{bmatrix} * & * & * \\ * & * & * \\ * & * & * \end{bmatrix} \begin{bmatrix} u \\ v \\ w \end{bmatrix} - \begin{bmatrix} * \\ * \\ * \end{bmatrix}}_{-\mathbf{H}(\mathbf{u})}
 \end{array}$$

Figure A.10. Splitting of the starting matrix equation $\mathbf{A} \cdot \mathbf{u} - \mathbf{b}$ [310].

A.4.2 PISO ALGORITHM

The PISO algorithm (Pressure Implicit with Splitting of Operators), introduced by Issa in 1986 [316], is a non-iterative method for solving the coupled equations arising from the implicit discretisation of the time-varying fluid motion equations. It can be seen as a transient version of SIMPLE, with the significant modification that the momentum corrector is executed more than once for each time step (PISO loop).

The equations are solved over successive time intervals Δt between an initial time instant t_{start} and a final time instant t_{end} (Figure A.11). The time step must be relatively small to maintain sufficient accuracy in describing transient phenomena, condition that is expressed in terms of the maximum allowable Courant number ($Co < 1$).

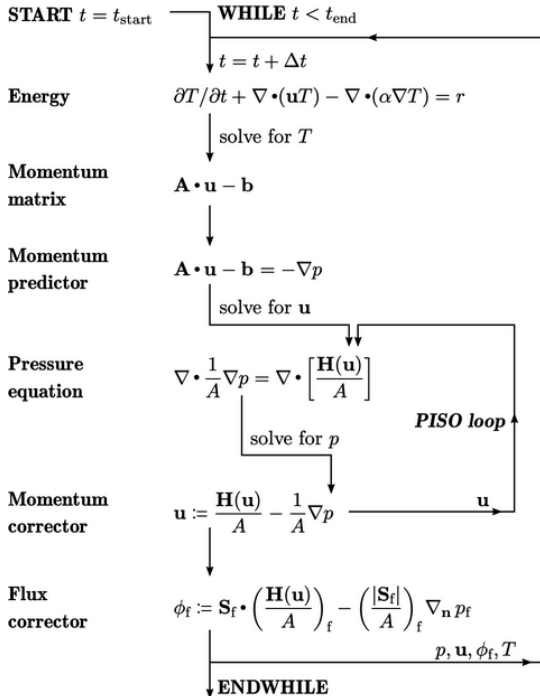


Figure A.11. Implementation of the PISO algorithm in OpenFOAM [310].

A.4.3 PIMPLE ALGORITHM

The algorithms for pressure-velocity coupling previously presented can be combined into an algorithm known as PIMPLE. It blends the controls of both PISO and SIMPLE (hence the merged acronym), particularly the iterative cycles and under-relaxation. It can be viewed as the application of SIMPLE at each time step, iterating until convergence or a maximum number of iterations is reached. The advantage of PIMPLE over PISO is its increased stability, even with $Co > 1$. Figure A.12 illustrates the flowchart of the PIMPLE solver, as implemented in OpenFOAM [310].

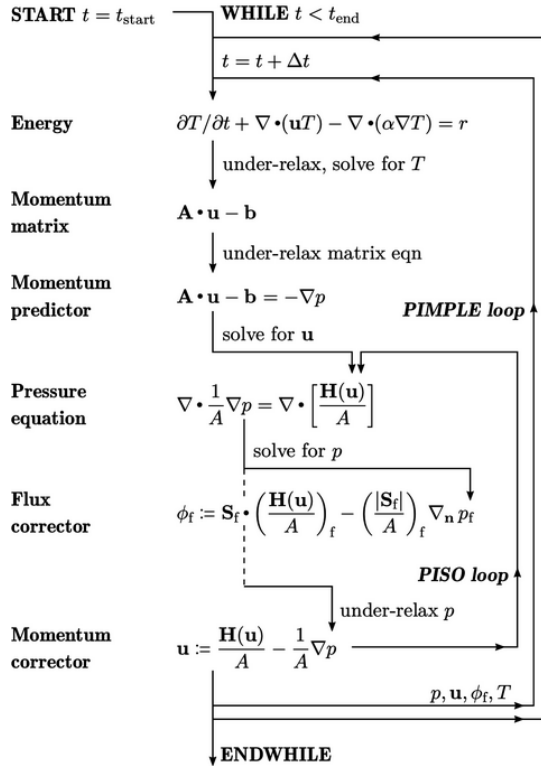


Figure A.12. Implementation of the PIMPLE algorithm in OpenFOAM [310].

B

APPENDIX B

This appendix reports the supplementary material to the study presented in Chapter 6.

B.1 FAN STRENGTH: LEVEL 1

Table B.1. Summary of parameters adopted during the acquisition for fan strength 1.

Camera	#	Lens objective (mm)	Field of view (mm ²)	Magnification factor	Frequency (Hz)	Δt (ms)	T_{out} (°C)	T_{in} (°C)	Humidity (%)	
MP1	1	5.6	35	653 × 545	0.025	5	4	31.1	42.1	25
	2	4	50	454 × 382	0.037	5	4	31.1	42.1	25
	3	5,6	35	472 × 397	0.035	5	6	28.4	38.4	26
MP2	1	5,6	35	813 × 688	0.02	5	12	24.0	31.4	31
MP3	1	5,6	35	524 × 437	0.032	15	1	22.4	37.4	33
	2	4	50	351 × 297	0.047	15	3	29.5	40.0	34

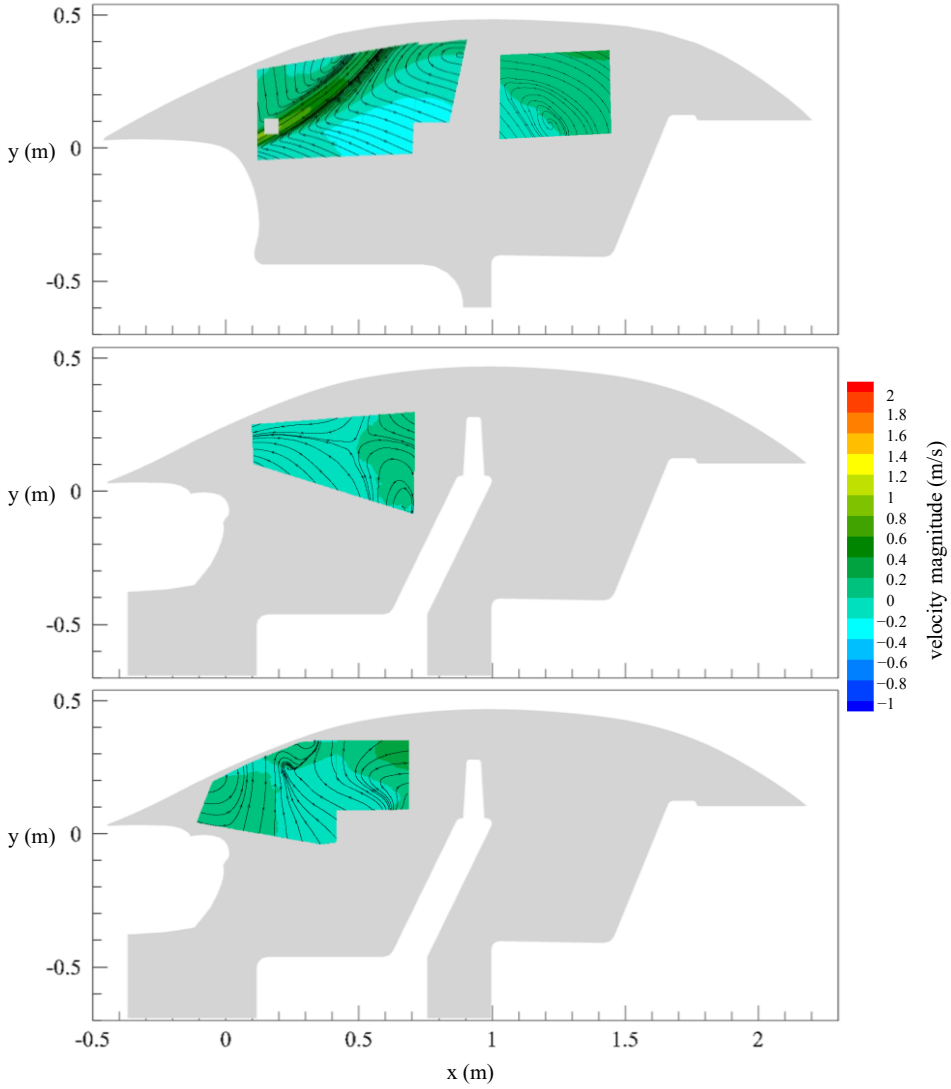


Figure B.1. Experimental time-averaged velocity fields in the x-y plane. Top: MP1; middle: MP2; bottom: MP3.

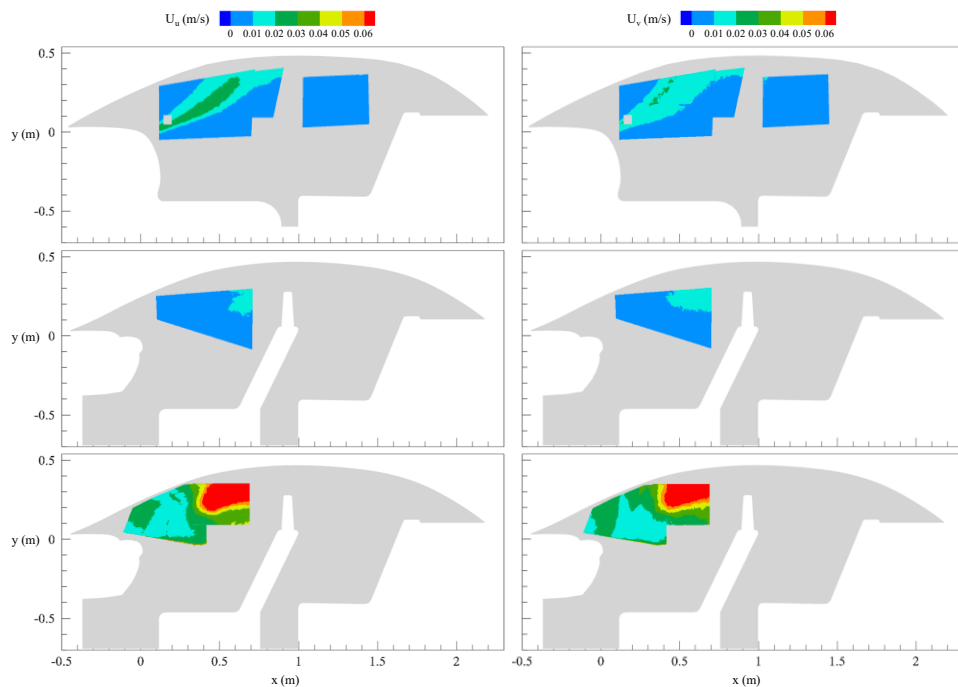


Figure B.2. Measurement uncertainty at 95% confidence level for streamwise (left) and vertical (right) velocity component. Top: MP1; middle: MP2; bottom: MP3.

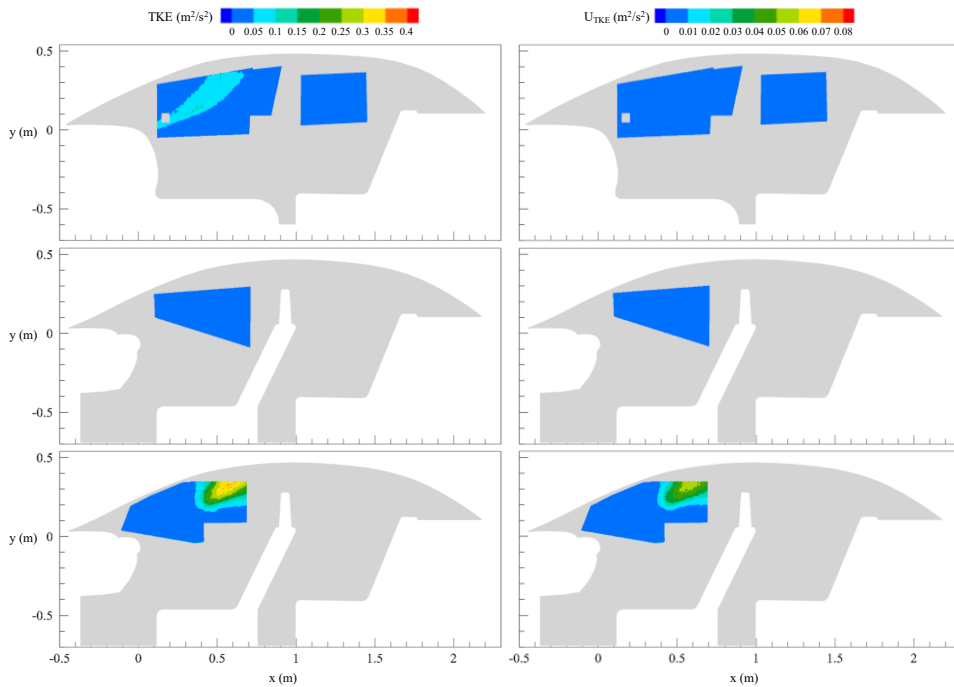


Figure B.3. Experimental TKE (left) and corresponding measurement uncertainty (right).
Top: MP1; middle: MP2; bottom: MP3.

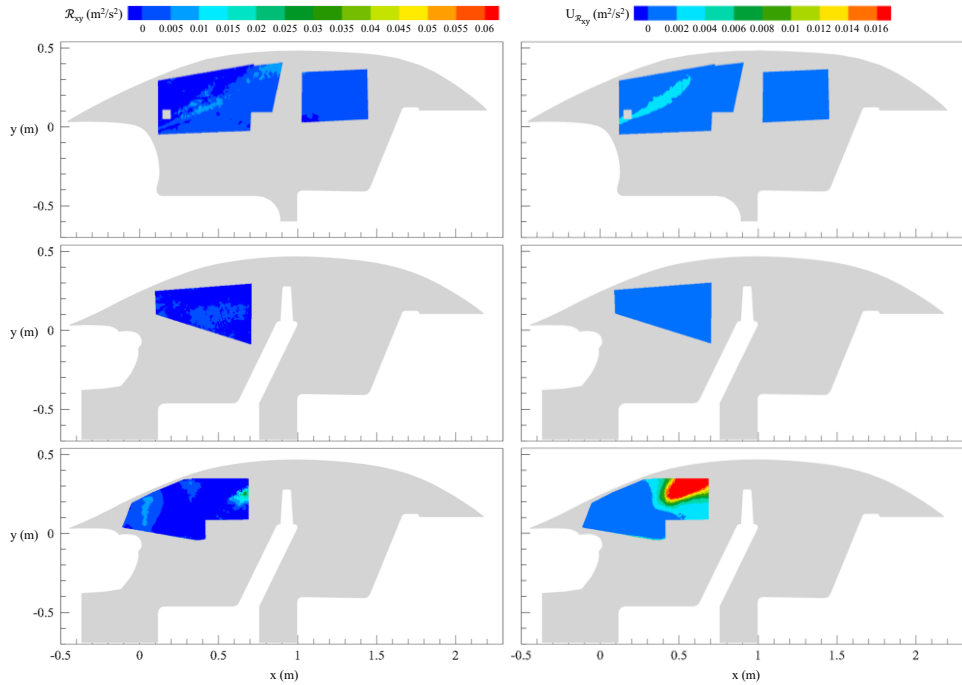


Figure B.4. Experimental Reynolds shear stress \mathcal{R}_{xy} (left) and corresponding measurement uncertainty (right). Top: MP1; middle: MP2; bottom: MP3.

B.2 FAN STRENGTH: LEVEL 2

Table B.2. Summary of parameters adopted during the acquisition for fan strength 2.

Camera	f#	Lens objective (mm)	Field of view (mm ²)	Magnification factor	Frequency (Hz)	Δt (ms)	T_{out} (°C)	T_{in} (°C)	Humidity (%)	
MP1	1	5.6	35	653 × 545	0.025	5	2	30.3	42.3	28
	2	4	50	454 × 382	0.037	5	2	30.3	42.3	28
	3	4.6	35	472 × 397	0.035	5	4	28.1	38.7	26
MP2	1	5.6	35	813 × 688	0.02	5	10	24.5	32.0	32
MP3	1	5.6	35	524 × 437	0.032	15	1	23.2	36.0	34
	2	4	50	351 × 297	0.047	15	2.25	29.0	39.0	34

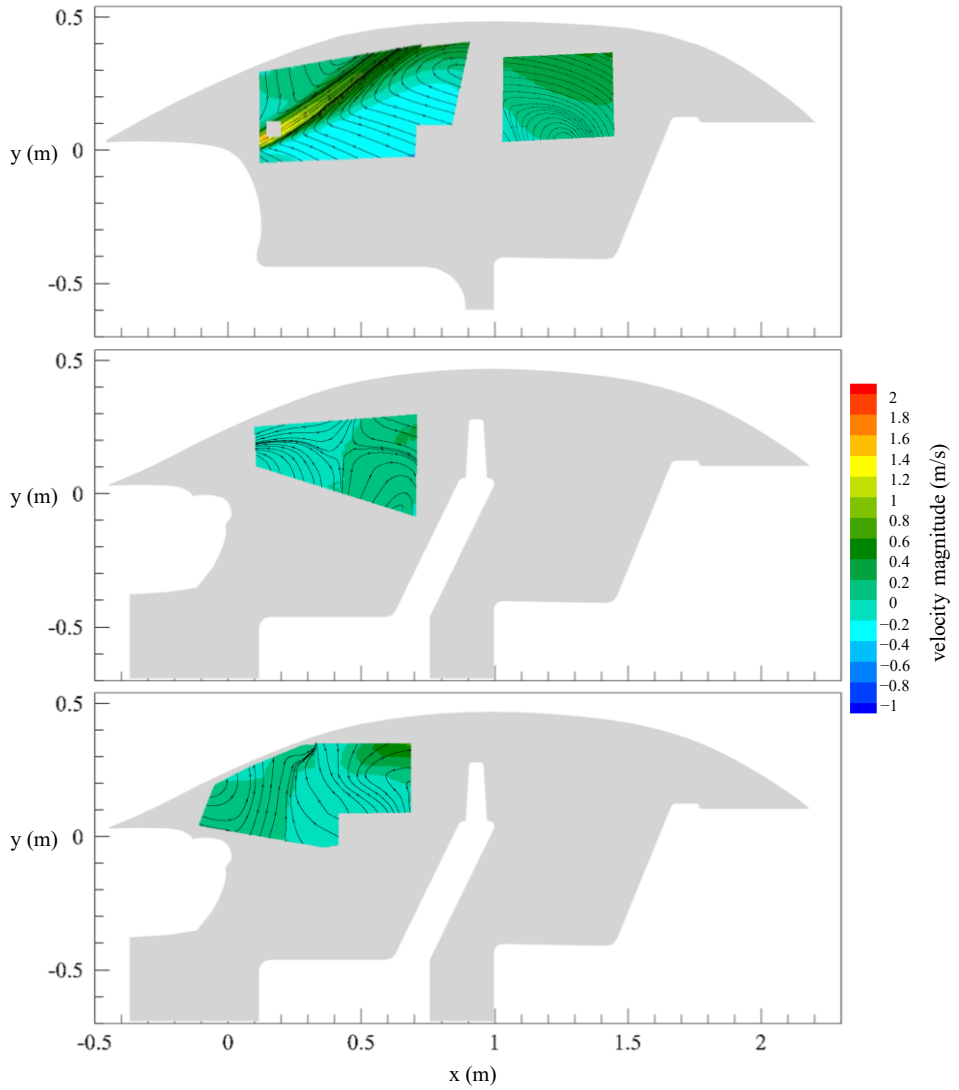


Figure B.5. Experimental time-averaged velocity fields in the x-y plane.
Top: MP1; middle: MP2; bottom: MP3.

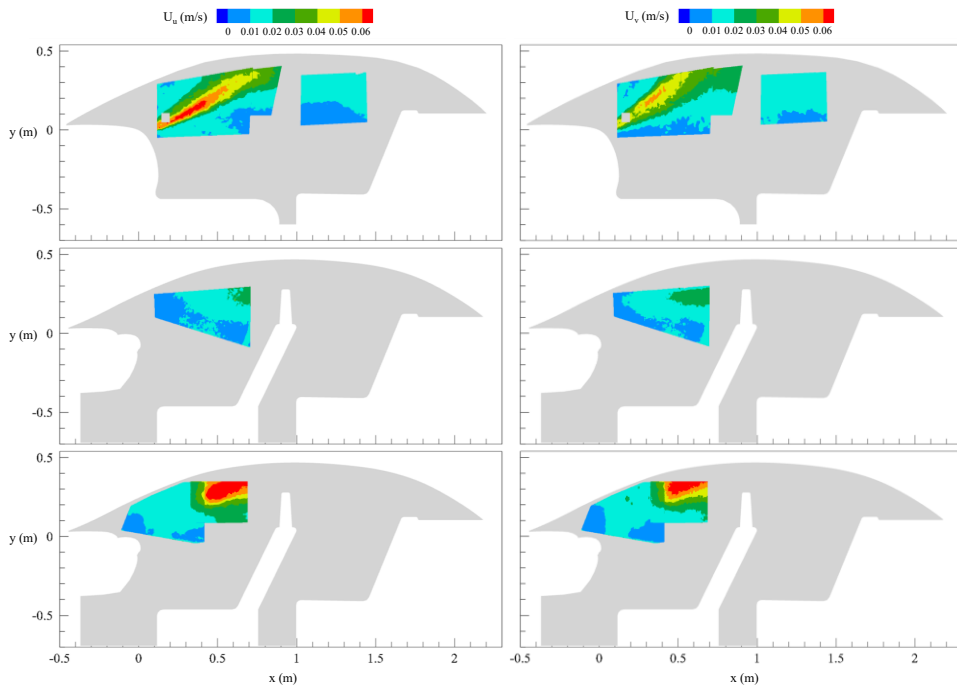


Figure B.6. Measurement uncertainty at 95% confidence level for streamwise (left) and vertical (right) velocity component. Top: MP1; middle: MP2; bottom: MP3.

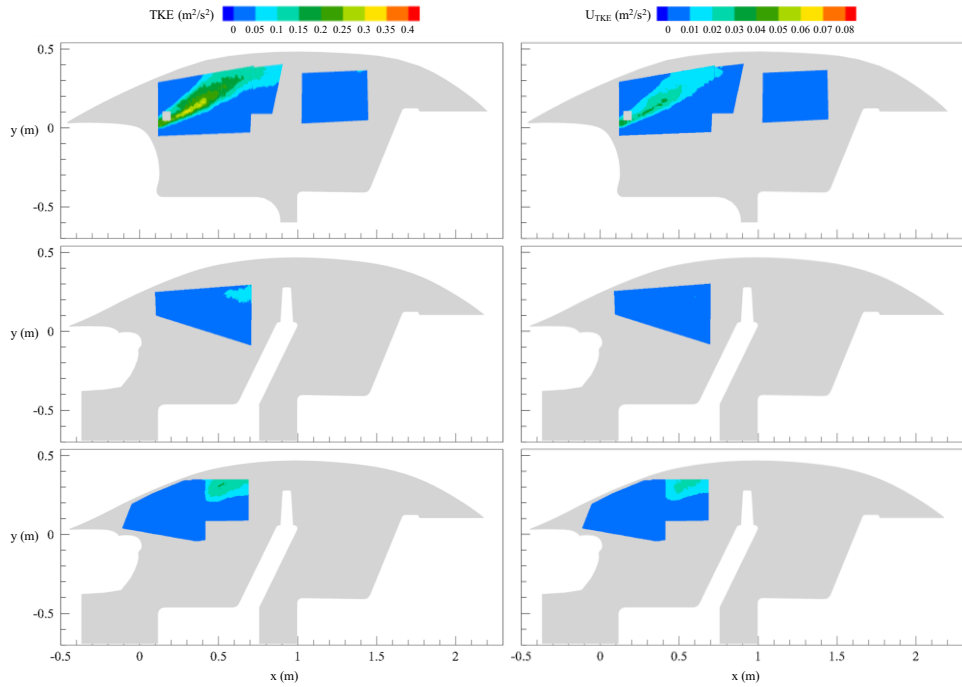


Figure B.7. Experimental TKE (left) and corresponding measurement uncertainty (right).
Top: MP1; middle: MP2; bottom: MP3.

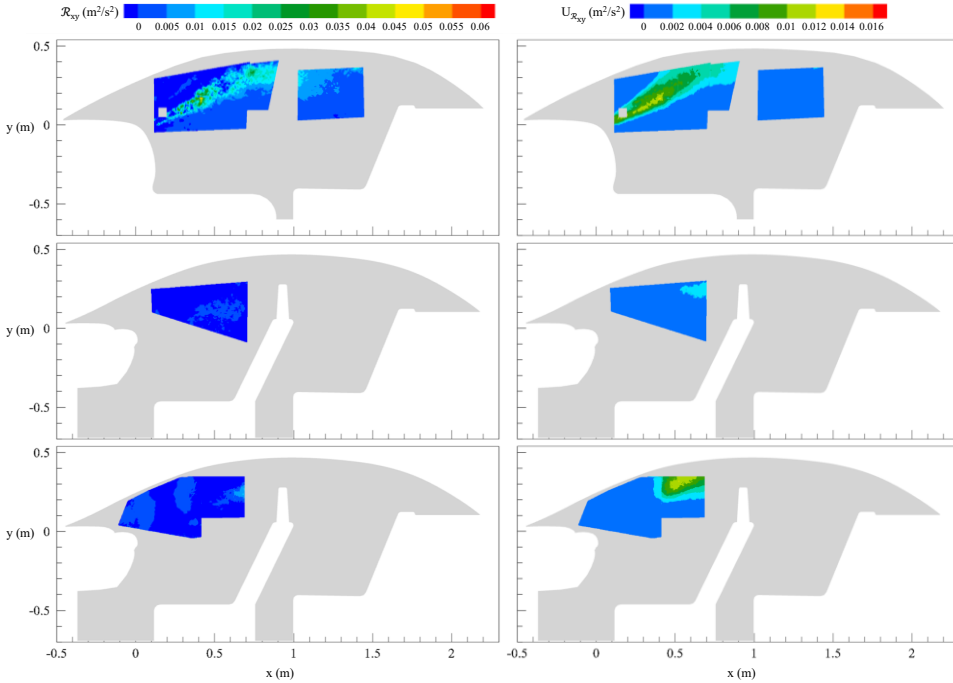


Figure B.8. Experimental Reynolds shear stress \mathcal{R}_{xy} (left) and corresponding measurement uncertainty (right). Top: MP1; middle: MP2; bottom: MP3.

B.3 FAN STRENGTH: LEVEL 4

Table B.3. Summary of parameters adopted during the acquisition for fan strength 4.

Camera	f#	Lens objective (mm)	Field of view (mm ²)	Magnification factor	Frequency (Hz)	Δt (ms)	T_{out} (°C)	T_{in} (°C)	Humidity (%)	
MP1	1	5.6	35	653 × 545	0.025	15	0.75	30.3	42.3	28
	2	4	50	454 × 382	0.037	15	0.75	30.3	42.3	28
	3	4.6	35	472 × 397	0.035	15	1.5	28.1	40.3	26
MP2	1	5.6	35	813 × 688	0.02	15	6	29.0	41.0	30
MP3	1	5.6	35	524 × 437	0.032	15	2.5	29.0	40.3	33
	2	4	50	351 × 297	0.047	15	0.7	29.0	39.0	33

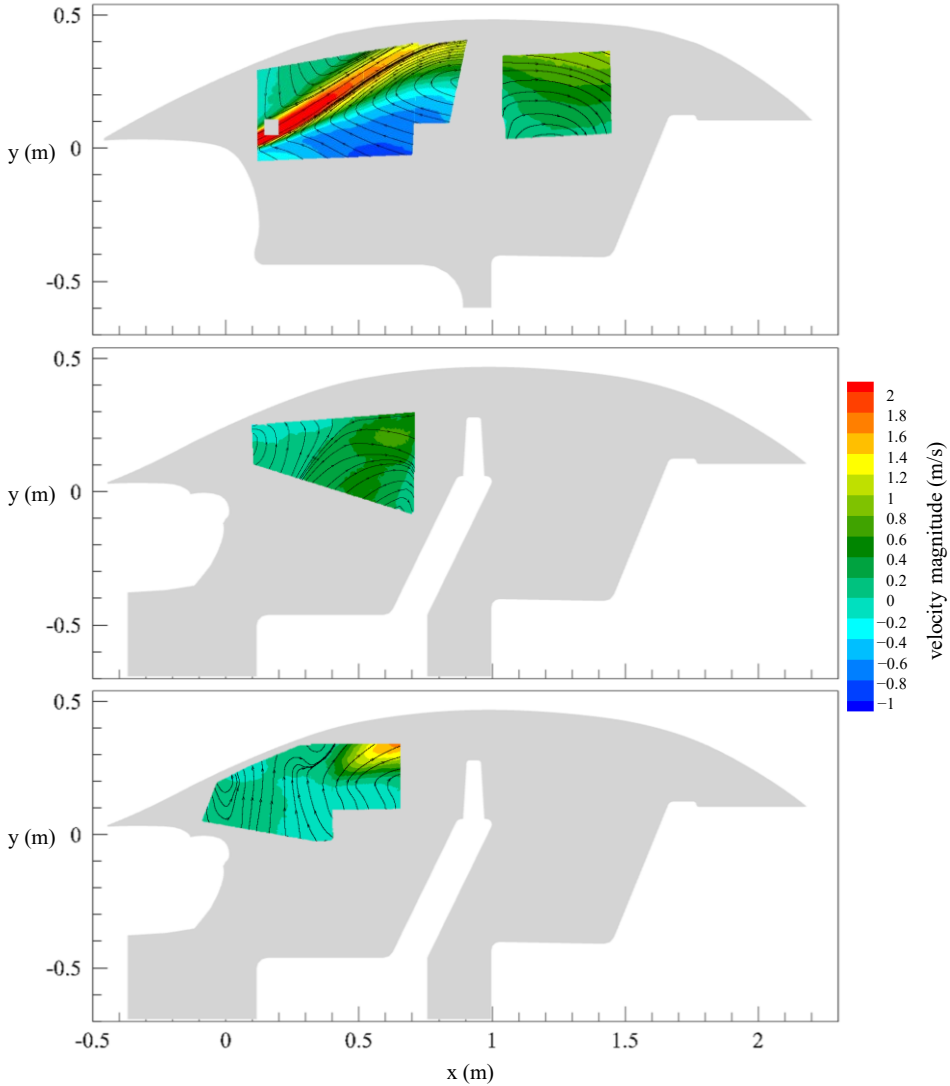


Figure B.9. Experimental time-averaged velocity fields in the x-y plane. Top: MP1; middle: MP2; bottom: MP3.

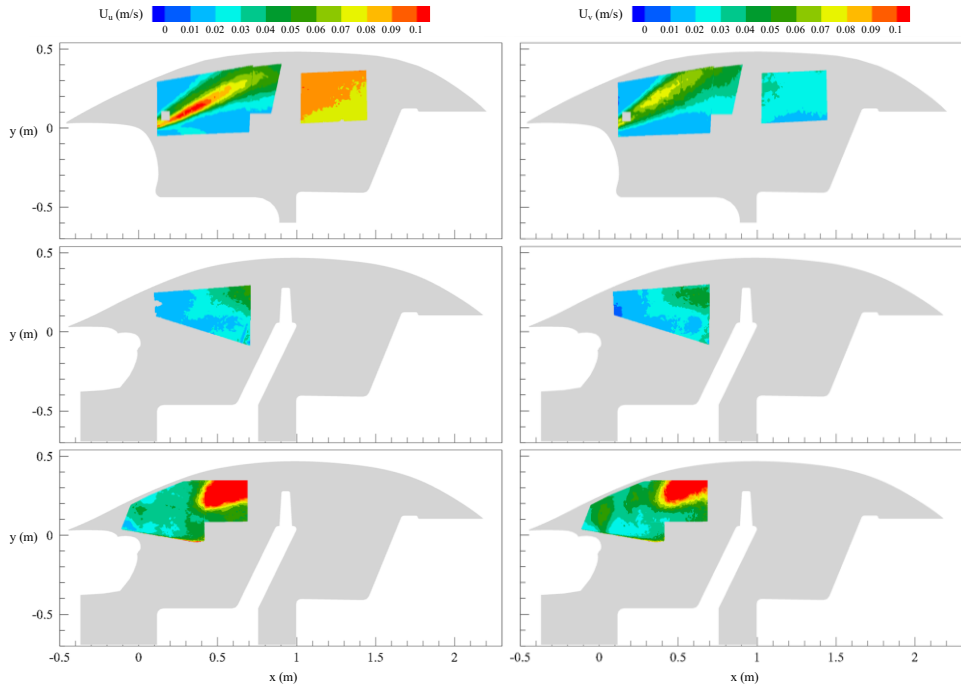


Figure B.10. Measurement uncertainty at 95% confidence level for streamwise (left) and vertical (right) velocity component. Top: MP1; middle: MP2; bottom: MP3.

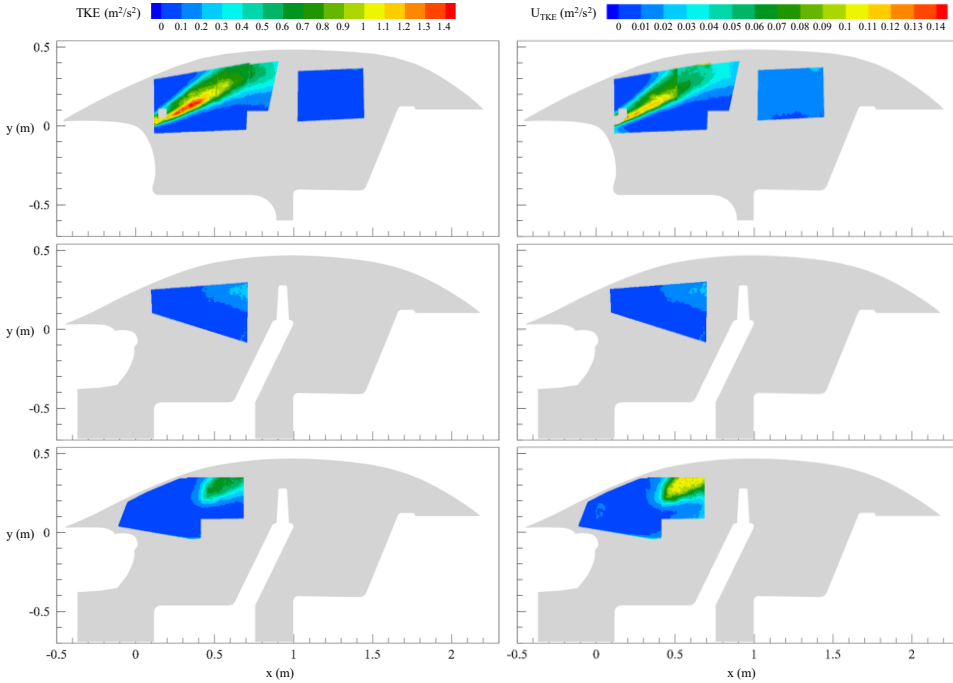


Figure B.11. Experimental TKE (left) and corresponding measurement uncertainty (right).
Top: MPI; middle: MP2; bottom: MP3.

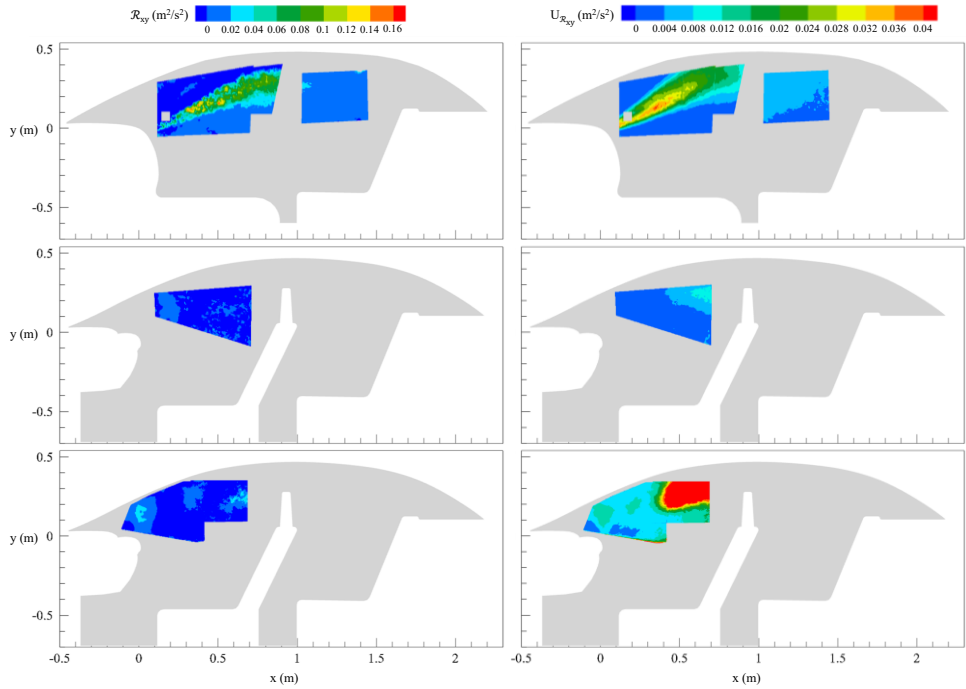


Figure B.12. Experimental Reynolds shear stress \mathcal{R}_{xy} (left) and corresponding measurement uncertainty. Top: MP1; middle: MP2; bottom: MP3.

REFERENCES

- [1] M. Hastings, *Sustainable Development: The Challenge of Transition*, 1st ed., Cambridge University Press, 2000. <https://doi.org/10.1017/CBO9780511536021>.
- [2] United Nations, Department of Economic and Social Affairs, Population Division, *World Population Prospects 2022*, Online Edition, (2022).
- [3] United Nations, *Transforming our World: The 2030 Agenda for Sustainable Development*, (2015).
- [4] N.E. Klepeis, W.C. Nelson, W.R. Ott, J.P. Robinson, A.M. Tsang, P. Switzer, J.V. Behar, S.C. Hern, W.H. Engelmann, The National Human Activity Pattern Survey (NHAPS): a resource for assessing exposure to environmental pollutants, *J Expo Sci Environ Epidemiol* 11 (2001) 231–252. <https://doi.org/10.1038/sj.jea.7500165>.
- [5] H. Tang, X. Liu, Y. Geng, B. Lin, Y. Ding, Assessing the perception of overall indoor environmental quality: Model validation and interpretation, *Energy and Buildings* 259 (2022) 111870. <https://doi.org/10.1016/j.enbuild.2022.111870>.
- [6] I.L. Niza, A.M. Bueno, E.E. Broday, Indoor Environmental Quality (IEQ) and Sustainable Development Goals (SDGs): Technological Advances, Impacts and Challenges in the Management of Healthy and Sustainable Environments, *Urban Science* 7 (2023) 96. <https://doi.org/10.3390/urbansci7030096>.
- [7] F. Zhang, S. Liu, W. Hu, M. Yadav, Editorial: Effects of indoor environmental quality on human performance and productivity, *Front. Built Environ.* 8 (2022) 1095443. <https://doi.org/10.3389/fbuil.2022.1095443>.
- [8] P.M. Falcone, M. Hiete, A. Sapiro, Hydrogen economy and sustainable development goals: Review and policy insights, *Current Opinion in Green and Sustainable Chemistry* 31 (2021) 100506. <https://doi.org/10.1016/j.cogsc.2021.100506>.
- [9] M.S. Akhtar, H. Khan, J.J. Liu, J. Na, Green hydrogen and sustainable development – A social LCA perspective highlighting social hotspots and geopolitical implications of the future hydrogen economy, *Journal of Cleaner Production* 395 (2023) 136438. <https://doi.org/10.1016/j.jclepro.2023.136438>.
- [10] Y. Li, Basic routes of transmission of respiratory pathogens—A new proposal for transmission categorization based on respiratory spray, inhalation, and touch, *Indoor Air* 31 (2021) 3–6. <https://doi.org/10.1111/ina.12786>.
- [11] G. Cortellessa, L. Stabile, F. Arpino, D.E. Faleiros, W. van den Bos, L. Morawska, G. Buonanno, Close proximity risk assessment for SARS-CoV-2 infection, *Science of The Total Environment* 794 (2021) 148749. <https://doi.org/10.1016/j.scitotenv.2021.148749>.
- [12] G. Buonanno, A. Robotto, E. Brizio, L. Morawska, A. Civra, F. Corino, D. Lembo, G. Ficco, L. Stabile, Link between SARS-CoV-2 emissions and airborne concentrations: Closing the gap in understanding, *Journal of Hazardous Materials* 428 (2022) 128279. <https://doi.org/10.1016/j.jhazmat.2022.128279>.
- [13] T. Greenhalgh, J.L. Jimenez, K.A. Prather, Z. Tufekci, D. Fisman, R. Schooley, Ten scientific reasons in support of airborne transmission of SARS-CoV-2., *Lancet* 397 (2021) 1603–1605. [https://doi.org/10.1016/S0140-6736\(21\)00869-2](https://doi.org/10.1016/S0140-6736(21)00869-2).

- [14] W.W. Nazaroff, Indoor aerosol science aspects of SARS-CoV-2 transmission, *Indoor Air* 32 (2022). <https://doi.org/10.1111/ina.12970>.
- [15] A.C. D'Alicandro, N. Massarotti, A. Mauro, Aerosol hazards in operating rooms: A review of numerical and experimental studies, *Journal of Aerosol Science* 158 (2021) 105823. <https://doi.org/10.1016/j.jaerosci.2021.105823>.
- [16] M. Abuhegazy, K. Talaat, O. Anderoglu, S.V. Poroseva, Numerical investigation of aerosol transport in a classroom with relevance to COVID-19, *Physics of Fluids* 32 (2020) 103311. <https://doi.org/10.1063/5.0029118>.
- [17] G.K. Rencken, E.K. Rutherford, N. Ghanta, J. Kongoletos, L. Glicksman, Patterns of SARS-CoV-2 aerosol spread in typical classrooms, *Building and Environment* 204 (2021) 108167. <https://doi.org/10.1016/j.buildenv.2021.108167>.
- [18] W. Li, A. Chong, T. Hasama, L. Xu, B. Lasternas, K.W. Tham, K.P. Lam, Effects of ceiling fans on airborne transmission in an air-conditioned space, *Building and Environment* 198 (2021) 107887. <https://doi.org/10.1016/j.buildenv.2021.107887>.
- [19] Y. Wang, F.-Y. Zhao, J. Kuckelkorn, D. Liu, J. Liu, J.-L. Zhang, Classroom energy efficiency and air environment with displacement natural ventilation in a passive public school building, *Energy and Buildings* 70 (2014) 258–270. <https://doi.org/10.1016/j.enbuild.2013.11.071>.
- [20] N. Massarotti, A. Mauro, S. Mohamed, A.J. Nowak, D. Sainas, Fluid dynamic and thermal comfort analysis in an actual operating room with unidirectional airflow system, *Build. Simul.* 14 (2021) 1127–1146. <https://doi.org/10.1007/s12273-020-0713-3>.
- [21] ISO, ISO 7730 - Ergonomics of the thermal environment — Analytical determination and interpretation of thermal comfort using calculation of the PMV and PPD indices and local thermal comfort criteria, (2005).
- [22] C.T. Crowe, J.D. Schwarzkopf, M. Sommerfeld, Y. Tsuji, *Multiphase Flows with Droplets and Particles*, 0 ed., CRC Press, 2011. <https://doi.org/10.1201/b11103>.
- [23] M.R.R.S. van Beest, F. Arpino, O. Hlinka, E. Sauret, N.R.T.P. van Beest, R.S. Humphries, G. Buonanno, L. Morawska, G. Governatori, N. Motta, Influence of indoor airflow on particle spread of a single breath and cough in enclosures: Does opening a window really 'help'?, *Atmospheric Pollution Research* 13 (2022) 101473. <https://doi.org/10.1016/j.apr.2022.101473>.
- [24] C. Kleinstreuer, *Two-phase flow: theory and applications*, Taylor & Francis, New York, 2003.
- [25] C. Kleinstreuer, Y. Feng, Computational Analysis of Non-Spherical Particle Transport and Deposition in Shear Flow With Application to Lung Aerosol Dynamics—A Review, *Journal of Biomechanical Engineering* 135 (2013) 021008. <https://doi.org/10.1115/1.4023236>.
- [26] R.M. McCombs, W.E. Rawls, Density Gradient Centrifugation of Rubella Virus, *J Virol* 2 (1968) 409–414. <https://doi.org/10.1128/jvi.2.5.409-414.1968>.
- [27] M. Pattison, D.J. Alexander, J.W. Harkness, Purification and preliminary characterisation of a pathogenic strain of infectious bursal disease virus, *Avian Pathology* 4 (1975) 175–187. <https://doi.org/10.1080/03079457509353864>.
- [28] A.E. Ritchie, D.R. Deshmukh, C.T. Larsen, B.S. Pomeroy, Electron Microscopy of Coronavirus-Like Particles Characteristic of Turkey Bluecomb Disease, *Avian Diseases* 17 (1973) 546. <https://doi.org/10.2307/1589153>.
- [29] G.R. Johnson, L. Morawska, Z.D. Ristovski, M. Hargreaves, K. Mengersen, C.Y.H. Chao, M.P. Wan, Y. Li, X. Xie, D. Katoshevski, S. Corbett, Modality of human expired

- aerosol size distributions, *Journal of Aerosol Science* 42 (2011) 839–851. <https://doi.org/10.1016/j.jaerosci.2011.07.009>.
- [30] L. Morawska, G.R. Johnson, Z.D. Ristovski, M. Hargreaves, K. Mengersen, S. Corbett, C.Y.H. Chao, Y. Li, D. Katoshevski, Size distribution and sites of origin of droplets expelled from the human respiratory tract during expiratory activities, *Journal of Aerosol Science* 40 (2009) 256–269. <https://doi.org/10.1016/j.jaerosci.2008.11.002>.
- [31] K.P. Fennelly, Particle sizes of infectious aerosols: implications for infection control, *The Lancet Respiratory Medicine* 8 (2020) 914–924. [https://doi.org/10.1016/S2213-2600\(20\)30323-4](https://doi.org/10.1016/S2213-2600(20)30323-4).
- [32] S.L. Bixler, C.P. Stefan, A. Jay, F. Rossi, K.M. Ricks, C.J. Shoemaker, A.M. Moreau, X. Zeng, J.W. Hooper, D. Dyer, O. Frick, J.W. Koehler, B. Kearney, N. DiPinto, J. Liu, S. Tostenson, T.L. Clements, J.M. Smith, J.A. Johnson, K. Berrier, H. Esham, K.L. Delp, S.R. Coyne, H. Bloomfield, P. Kuehnert, K. Akers, K. Gibson, T.D. Minogue, A. Nalca, M.L.M. Pitt, Aerosol Exposure of Cynomolgus Macaques to SARS-CoV-2 Results in More Severe Pathology than Existing Models, *bioRxiv* (2021) 2021.04.27.441510. <https://doi.org/10.1101/2021.04.27.441510>.
- [33] S. Balachandar, S. Zaleski, A. Soldati, G. Ahmadi, L. Bourouiba, Host-to-host airborne transmission as a multiphase flow problem for science-based social distance guidelines, *International Journal of Multiphase Flow* 132 (2020) 103439. <https://doi.org/10.1016/j.ijmultiphaseflow.2020.103439>.
- [34] X. Xie, Y. Li, A.T.Y. Chwang, P.L. Ho, W.H. Seto, How far droplets can move in indoor environments? revisiting the Wells evaporation-falling curve, *Indoor Air* 17 (2007) 211–225. <https://doi.org/10.1111/j.1600-0668.2007.00469.x>.
- [35] K. Luo, Z. Lei, Z. Hai, S. Xiao, J. Rui, H. Yang, X. Jing, H. Wang, Z. Xie, P. Luo, W. Li, Q. Li, H. Tan, Z. Xu, Y. Yang, S. Hu, T. Chen, Transmission of SARS-CoV-2 in Public Transportation Vehicles: A Case Study in Hunan Province, China., *Open Forum Infect Dis* 7 (2020) ofaa430. <https://doi.org/10.1093/ofid/ofaa430>.
- [36] Y. Shen, C. Li, H. Dong, Z. Wang, L. Martinez, Z. Sun, A. Handel, Z. Chen, E. Chen, M.H. Ebell, F. Wang, B. Yi, H. Wang, X. Wang, A. Wang, B. Chen, Y. Qi, L. Liang, Y. Li, F. Ling, J. Chen, G. Xu, Community Outbreak Investigation of SARS-CoV-2 Transmission Among Bus Riders in Eastern China, *JAMA Internal Medicine* 180 (2020) 1665–1671. <https://doi.org/10.1001/jamainternmed.2020.5225>.
- [37] Q. Lv, D. Kong, Y. He, Y. Lu, L. Chen, J. Zhao, S. Feng, Y. Chen, J. Wan, Y. Wen, W. Gao, Z. Chen, X. Tang, S. Mei, X. Zou, T. Feng, A SARS-CoV-2 Delta variant outbreak on airplane: vaccinated air passengers are more protected than unvaccinated, *Journal of Travel Medicine* (2021) taab161. <https://doi.org/10.1093/jtm/taab161>.
- [38] M.R. Kasper, J.R. Geibe, C.L. Sears, A.J. Riegodedios, T. Luse, A.M. Von Thun, M.B. McGinnis, N. Olson, D. Houskamp, R. Fenequito, T.H. Burgess, A.W. Armstrong, G. DeLong, R.J. Hawkins, B.L. Gillingham, An Outbreak of Covid-19 on an Aircraft Carrier, *N Engl J Med* 383 (2020) 2417–2426. <https://doi.org/10.1056/NEJMoa2019375>.
- [39] E. Dahl, Coronavirus (Covid-19) outbreak on the cruise ship Diamond Princess., *Int Marit Health* 71 (2020) 5–8. <https://doi.org/10.5603/MH.2020.0003>.
- [40] A.J. Ing, C. Cocks, J.P. Green, COVID-19: in the footsteps of Ernest Shackleton, *Thorax* 75 (2020) 693. <https://doi.org/10.1136/thoraxjnl-2020-215091>.
- [41] H. Speake, A. Phillips, T. Chong, C. Sikazwe, A. Levy, J. Lang, B. Scalley, D. Speers, D. Smith, P. Effler, S. McEvoy, Flight-Associated Transmission of Severe Acute Respiratory Syndrome Coronavirus 2 Corroborated by Whole-Genome Sequencing,

- Emerging Infectious Disease Journal 26 (2020) 2872. <https://doi.org/10.3201/eid2612.203910>.
- [42] N. Yang, Y. Shen, C. Shi, A.H.Y. Ma, X. Zhang, X. Jian, L. Wang, J. Shi, C. Wu, G. Li, Y. Fu, K. Wang, M. Lu, G. Qian, In-flight transmission cluster of COVID-19: a retrospective case series, *Null* 52 (2020) 891–901. <https://doi.org/10.1080/23744235.2020.1800814>.
- [43] L. Morawska, J.W. Tang, W. Bahnfleth, P.M. Bluyssen, A. Boerstra, G. Buonanno, J. Cao, S. Dancer, A. Floto, F. Franchimon, C. Haworth, J. Hogeling, C. Ison, J.L. Jimenez, J. Kurnitski, Y. Li, M. Loomans, G. Marks, L.C. Marr, L. Mazzeo, A.K. Melikov, S. Miller, D.K. Milton, W. Nazaroff, P.V. Nielsen, C. Noakes, J. Peccia, X. Querol, C. Sekhar, O. Seppänen, S. Tanabe, R. Tellier, K.W. Tham, P. Wargocki, A. Wierzbicka, M. Yao, How can airborne transmission of COVID-19 indoors be minimised?, *Environment International* 142 (2020) 105832. <https://doi.org/10.1016/j.envint.2020.105832>.
- [44] L. Morawska, J. Cao, Airborne transmission of SARS-CoV-2: The world should face the reality, *Environment International* 139 (2020) 105730. <https://doi.org/10.1016/j.envint.2020.105730>.
- [45] J.L. Santarpia, D.N. Rivera, V.L. Herrera, M.J. Morwitzer, H.M. Creager, G.W. Santarpia, K.K. Crown, D.M. Brett-Major, E.R. Schnaubelt, M.J. Broadhurst, J.V. Lawler, S.P. Reid, J.J. Lowe, Aerosol and surface contamination of SARS-CoV-2 observed in quarantine and isolation care, *Scientific Reports* 10 (2020) 12732. <https://doi.org/10.1038/s41598-020-69286-3>.
- [46] R.A. Stern, P. Koutrakis, M.A.G. Martins, B. Lemos, S.E. Dowd, E.M. Sunderland, E. Garshick, Characterization of hospital airborne SARS-CoV-2, *Respiratory Research* 22 (2021) 73. <https://doi.org/10.1186/s12931-021-01637-8>.
- [47] J.A. Lednický, M. Lauzardo, Z.H. Fan, A. Jutla, T.B. Tilly, M. Gangwar, M. Usmani, S.N. Shankar, K. Mohamed, A. Eiguren-Fernandez, C.J. Stephenson, Md.M. Alam, M.A. Elbadry, J.C. Loeb, K. Subramaniam, T.B. Waltzek, K. Cherabuddi, J.G. Morris, C.-Y. Wu, Viable SARS-CoV-2 in the air of a hospital room with COVID-19 patients, *International Journal of Infectious Diseases* 100 (2020) 476–482. <https://doi.org/10.1016/j.ijid.2020.09.025>.
- [48] N. Van Doremalen, T. Bushmaker, D.H. Morris, M.G. Holbrook, A. Gamble, B.N. Williamson, A. Tamin, J.L. Harcourt, N.J. Thornburg, S.I. Gerber, J.O. Lloyd-Smith, E. De Wit, V.J. Munster, Aerosol and Surface Stability of SARS-CoV-2 as Compared with SARS-CoV-1, *N Engl J Med* 382 (2020) 1564–1567. <https://doi.org/10.1056/NEJMc2004973>.
- [49] Y. Liu, Z. Ning, Y. Chen, M. Guo, Y. Liu, N.K. Gali, L. Sun, Y. Duan, J. Cai, D. Westerdahl, X. Liu, K. Xu, K.-F. Ho, H. Kan, Q. Fu, K. Lan, Aerodynamic analysis of SARS-CoV-2 in two Wuhan hospitals., *Nature* 582 (2020) 557–560. <https://doi.org/10.1038/s41586-020-2271-3>.
- [50] P. Di Carlo, P. Chiacchiarretta, B. Sinjari, E. Aruffo, L. Stuppia, V. De Laurenzi, P. Di Tomo, L. Pelusi, F. Potenza, A. Veronese, J. Vecchiet, K. Falasca, C. Ucciferri, Air and surface measurements of SARS-CoV-2 inside a bus during normal operation, *PLOS ONE* 15 (2020) e0235943. <https://doi.org/10.1371/journal.pone.0235943>.
- [51] T. Moreno, R.M. Pintó, A. Bosch, N. Moreno, A. Alastuey, M.C. Minguillón, E. Anfruns-Estrada, S. Guix, C. Fuentes, G. Buonanno, L. Stabile, L. Morawska, X. Querol, Tracing surface and airborne SARS-CoV-2 RNA inside public buses and subway trains, *Environment International* 147 (2021) 106326. <https://doi.org/10.1016/j.envint.2020.106326>.

- [52] J.A. Lednicky, M. Lauzardo, Md.M. Alam, M.A. Elbadry, C.J. Stephenson, J.C. Gibson, J.G. Morris, Isolation of SARS-CoV-2 from the air in a car driven by a COVID patient with mild illness, *International Journal of Infectious Diseases* 108 (2021) 212–216. <https://doi.org/10.1016/j.ijid.2021.04.063>.
- [53] A. Mikszewski, L. Stabile, G. Buonanno, L. Morawska, The airborne contagiousness of respiratory viruses: A comparative analysis and implications for mitigation, *Geoscience Frontiers* (2021) 101285. <https://doi.org/10.1016/j.gsf.2021.101285>.
- [54] A. Mikszewski, L. Stabile, G. Buonanno, L. Morawska, The vaccination threshold for SARS-CoV-2 depends on the indoor setting and room ventilation., *BMC Infect Dis* 21 (2021) 1193. <https://doi.org/10.1186/s12879-021-06884-0>.
- [55] L. Stabile, A. Pacitto, A. Mikszewski, L. Morawska, G. Buonanno, Ventilation procedures to minimize the airborne transmission of viruses in classrooms., *Build Environ* 202 (2021) 108042. <https://doi.org/10.1016/j.buildenv.2021.108042>.
- [56] O.T. Ng, K. Marimuthu, V. Koh, J. Pang, K.Z. Linn, J. Sun, L. De Wang, W.N. Chia, C. Tiu, M. Chan, L.M. Ling, S. Vasoo, M.Y. Abdad, P.Y. Chia, T.H. Lee, R.J. Lin, S.P. Sadarangani, M.I.-C. Chen, Z. Said, L. Kurupatham, R. Pung, L.-F. Wang, A.R. Cook, Y.-S. Leo, V.J. Lee, SARS-CoV-2 seroprevalence and transmission risk factors among high-risk close contacts: a retrospective cohort study, *The Lancet Infectious Diseases* 21 (2021) 333–343. [https://doi.org/10.1016/S1473-3099\(20\)30833-1](https://doi.org/10.1016/S1473-3099(20)30833-1).
- [57] L.D. Knibbs, L. Morawska, S.C. Bell, The risk of airborne influenza transmission in passenger cars, *Epidemiology and Infection* 140 (2012) 474–478. <https://doi.org/10.1017/S0950268811000835>.
- [58] S.L. Miller, W.W. Nazaroff, J.L. Jimenez, A. Boerstra, G. Buonanno, S.J. Dancer, J. Kurnitski, L.C. Marr, L. Morawska, C. Noakes, Transmission of SARS-CoV-2 by inhalation of respiratory aerosol in the Skagit Valley Chorale superspreading event, *Indoor Air* n/a (2020). <https://doi.org/10.1111/ina.12751>.
- [59] G. Buonanno, L. Morawska, L. Stabile, Quantitative assessment of the risk of airborne transmission of SARS-CoV-2 infection: Prospective and retrospective applications, *Environment International* 145 (2020) 106112. <https://doi.org/10.1016/j.envint.2020.106112>.
- [60] A. Mikszewski, L. Stabile, G. Buonanno, L. Morawska, Increased close proximity airborne transmission of the SARS-CoV-2 Delta variant, *Science of The Total Environment* (2021) 151499. <https://doi.org/10.1016/j.scitotenv.2021.151499>.
- [61] G.N. Sze To, C.Y.H. Chao, Review and comparison between the Wells–Riley and dose-response approaches to risk assessment of infectious respiratory diseases, *Indoor Air* 20 (2010) 2–16. <https://doi.org/10.1111/j.1600-0668.2009.00621.x>.
- [62] Z. Zhang, J. Capecehatro, K. Maki, On the utility of a well-mixed model for predicting disease transmission on an urban bus, *AIP Advances* 11 (2021) 085229. <https://doi.org/10.1063/5.0061219>.
- [63] C.J. Noakes, P.A. Sleigh, Mathematical models for assessing the role of airflow on the risk of airborne infection in hospital wards., *J R Soc Interface* 6 Suppl 6 (2009) S791–800. <https://doi.org/10.1098/rsif.2009.0305.focus>.
- [64] P.S.J. Lakey, Y. Won, D. Shaw, F.F. Østerstrøm, J. Mattila, E. Reidy, B. Bottorff, C. Rosales, C. Wang, L. Ampollini, S. Zhou, A. Novoselac, T.F. Kahan, P.F. DeCarlo, J.P.D. Abbatt, P.S. Stevens, D.K. Farmer, N. Carslaw, D. Rim, M. Shiraiwa, Spatial and temporal scales of variability for indoor air constituents, *Communications Chemistry* 4 (2021) 110. <https://doi.org/10.1038/s42004-021-00548-5>.

- [65] V. Mathai, A. Das, J.A. Bailey, K. Breuer, Airflows inside passenger cars and implications for airborne disease transmission, *Sci. Adv.* 7 (2021) eabe0166. <https://doi.org/10.1126/sciadv.abe0166>.
- [66] N. Hudda, S.P. Eckel, L.D. Knibbs, C. Sioutas, R.J. Delfino, S.A. Fruin, Linking In-Vehicle Ultrafine Particle Exposures to On-Road Concentrations., *Atmos Environ* (1994) 59 (2012) 578–586. <https://doi.org/10.1016/j.atmosenv.2012.05.021>.
- [67] R.W. Lewis, P. Nithiarasu, K.N. Seetharamu, *Fundamentals of the finite element method for heat and fluid flow*, Wiley, Hoboken, NJ, 2004.
- [68] M. Scungio, F. Arpino, G. Cortellessa, G. Buonanno, Detached eddy simulation of turbulent flow in isolated street canyons of different aspect ratios, *Atmospheric Pollution Research* 6 (2015) 351–364. <https://doi.org/10.5094/APR.2015.039>.
- [69] A.M. Dolatabadi, E. Lakzian, M. Heydari, A. Khan, A modified model of the suction technique of wetness reducing in wet steam flow considering power-saving, *Energy* 238 (2022) 121685. <https://doi.org/10.1016/j.energy.2021.121685>.
- [70] D. Hoseinzade, E. Lakzian, A. Hashemian, A blackbox optimization of volumetric heating rate for reducing the wetness of the steam flow through turbine blades, *Energy* 220 (2021) 119751. <https://doi.org/10.1016/j.energy.2020.119751>.
- [71] S. Yazdani, E. Lakzian, Numerical simulation and passive control of condensing flow through turbine blade by NVD Method Using Eulerian–Lagrangian Model, *Computers & Mathematics with Applications* 80 (2020) 140–160. <https://doi.org/10.1016/j.camwa.2020.03.007>.
- [72] F. Foroozesh, A.B. Khoshnevis, E. Lakzian, Improvement of the wet steam ejector performance in a refrigeration cycle via changing the ejector geometry by a novel EEC (Entropy generation, Entrainment ratio, and Coefficient of performance) method, *International Journal of Refrigeration* 110 (2020) 248–261. <https://doi.org/10.1016/j.ijrefrig.2019.11.006>.
- [73] R. Hosseini, E. Lakzian, Optimization volumetric heating in condensing steam flow by a novel method, *J Therm Anal Calorim* 140 (2020) 2421–2433. <https://doi.org/10.1007/s10973-019-09001-1>.
- [74] G. Buonanno, L. Stabile, L. Morawska, Estimation of airborne viral emission: Quanta emission rate of SARS-CoV-2 for infection risk assessment, *Environment International* 141 (2020) 105794. <https://doi.org/10.1016/j.envint.2020.105794>.
- [75] J.H. Yang, S. Kato, H. Nagano, Measurement of airflow of air-conditioning in a car with PIV, *J Vis* 12 (2009) 119–130. <https://doi.org/10.1007/BF03181954>.
- [76] Y. Ozeki, J.-H. Yang, H. Nagano, S. Kato, E. Nomura, M. Inoue, S. Kobayashi, Ventilation Characteristics of Modeled Compact Car Part 1 Airflow Velocity Measurement with PIV, *SAE Int. J. Passeng. Cars – Mech. Syst.* 1 (2008) 631–639. <https://doi.org/10.4271/2008-01-0732>.
- [77] European Commission. Joint Research Centre. Institute for Energy and Transport., *Driving and parking patterns of European car drivers: a mobility survey.*, Publications Office, LU, 2012. <https://data.europa.eu/doi/10.2790/7028> (accessed July 12, 2023).
- [78] F.R. Menter, M. Kuntz, R. Langtry, Ten years of industrial experience with the SST turbulence model, *Turbulence, Heat and Mass Transfer* 4 (2003) 625–632.
- [79] B. Pirouz, D. Mazzeo, S.A. Palermo, S.N. Naghib, M. Turco, P. Piro, CFD Investigation of Vehicle’s Ventilation Systems and Analysis of ACH in Typical Airplanes, Cars, and Buses, *Sustainability* 13 (2021) 6799. <https://doi.org/10.3390/su13126799>.
- [80] S. Ullrich, R. Buder, N. Boughanmi, C. Friebe, C. Wagner, Numerical Study of the Airflow Distribution in a Passenger Car Cabin Validated with PIV, in: A. Dillmann, G. Heller, E. Krämer, C. Wagner, C. Tropea, S. Jakirlić (Eds.), *New Results in Numerical*

- and Experimental Fluid Mechanics XII, Springer International Publishing, Cham, 2020: pp. 457–467. https://doi.org/10.1007/978-3-030-25253-3_44.
- [81] B.H.W. Te Lindert, E.J.W. Van Someren, Chapter 21 - Skin temperature, sleep, and vigilance, in: A.A. Romanovsky (Ed.), *Handbook of Clinical Neurology*, Elsevier, 2018: pp. 353–365. <https://doi.org/10.1016/B978-0-444-63912-7.00021-7>.
- [82] M. Abkarian, S. Mendez, N. Xue, F. Yang, H.A. Stone, Speech can produce jet-like transport relevant to asymptomatic spreading of virus, *Proc Natl Acad Sci USA* 117 (2020) 25237–25245. <https://doi.org/10.1073/pnas.2012156117>.
- [83] T.-B. Chang, J.-J. Sheu, J.-W. Huang, Y.-S. Lin, C.-C. Chang, Development of a CFD model for simulating vehicle cabin indoor air quality, *Transportation Research Part D: Transport and Environment* 62 (2018) 433–440. <https://doi.org/10.1016/j.trd.2018.03.018>.
- [84] E. Teyssou, H. Delagrèverie, B. Visseaux, S. Lambert-Niclot, S. Brichler, V. Ferre, S. Marot, A. Jary, E. Todesco, A. Schnuriger, E. Ghidaoui, B. Abdi, S. Akhavan, N. Houhou-Fidouh, C. Charpentier, L. Morand-Joubert, D. Boutolleau, D. Descamps, V. Calvez, A.G. Marcelin, C. Soulie, The Delta SARS-CoV-2 variant has a higher viral load than the Beta and the historical variants in nasopharyngeal samples from newly diagnosed COVID-19 patients, *Journal of Infection* 83 (2021) e1–e3. <https://doi.org/10.1016/j.jinf.2021.08.027>.
- [85] T. Watanabe, T.A. Bartrand, M.H. Weir, T. Omura, C.N. Haas, Development of a dose-response model for SARS coronavirus., *Risk Anal* 30 (2010) 1129–1138. <https://doi.org/10.1111/j.1539-6924.2010.01427.x>.
- [86] P. Gale, Thermodynamic equilibrium dose-response models for MERS-CoV infection reveal a potential protective role of human lung mucus but not for SARS-CoV-2, *Microb Risk Anal* 16 (2020) 100140–100140. <https://doi.org/10.1016/j.mran.2020.100140>.
- [87] P. Gale, Using thermodynamic equilibrium models to predict the effect of antiviral agents on infectivity: Theoretical application to SARS-CoV-2 and other viruses., *Microbial Risk Analysis* (2021) 100198. <https://doi.org/10.1016/j.mran.2021.100198>.
- [88] E. Vicenzi, F. Canducci, D. Pinna, N. Mancini, S. Carletti, A. Lazzarin, C. Bordignon, G. Poli, M. Clementi, Coronaviridae and SARS-associated coronavirus strain HSR1, *Emerg Infect Dis* 10 (2004) 413–418. <https://doi.org/10.3201/eid1003.030683>.
- [89] X. Zhang, J. Wang, Dose-response Relation Deduced for Coronaviruses From Coronavirus Disease 2019, Severe Acute Respiratory Syndrome, and Middle East Respiratory Syndrome: Meta-analysis Results and its Application for Infection Risk Assessment of Aerosol Transmission., *Clin Infect Dis* 73 (2021) e241–e245. <https://doi.org/10.1093/cid/ciaa1675>.
- [90] Hawks Seth A., Prussin Aaron J., Kuchinsky Sarah C., Pan Jin, Marr Linsey C., Duggal Nisha K., Lednický John A., Infectious SARS-CoV-2 Is Emitted in Aerosol Particles, *mBio* 12 (n.d.) e02527-21. <https://doi.org/10.1128/mBio.02527-21>.
- [91] A. Henriques, N. Mounet, L. Aleixo, P. Elson, J. Devine, G. Azzopardi, M. Andreini, M. Rognlien, N. Tarocco, J. Tang, Modelling airborne transmission of SARS-CoV-2 using CARA: Risk assessment for enclosed spaces, *medRxiv* (2021) 2021.10.14.21264988. <https://doi.org/10.1101/2021.10.14.21264988>.
- [92] W. Yang, L.C. Marr, Dynamics of Airborne Influenza A Viruses Indoors and Dependence on Humidity, *PLOS ONE* 6 (2011) e21481. <https://doi.org/10.1371/journal.pone.0021481>.
- [93] S.E. Chatoutsidou, M. Lazaridis, Assessment of the impact of particulate dry deposition on soiling of indoor cultural heritage objects found in churches and

- museums/libraries, *Journal of Cultural Heritage* 39 (2019) 221–228. <https://doi.org/10.1016/j.culher.2019.02.017>.
- [94] Adams, William C., Measurement of Breathing Rate and Volume in Routinely Performed Daily Activities. Final Report., Human Performance Laboratory, Physical Education Department, University of California, Davis, 1993.
- [95] International Commission on Radiological Protection, Human respiratory tract model for radiological protection. A report of a Task Group of the International Commission on Radiological Protection., 1994.
- [96] L.T. Brandal, E. MacDonald, L. Veneti, T. Ravlo, H. Lange, U. Naseer, S. Feruglio, K. Bragstad, O. Hungnes, L.E. Ødeskaug, F. Hagen, K.E. Hanch-Hansen, A. Lind, S.V. Watle, A.M. Taxt, M. Johansen, L. Vold, P. Aavitsland, K. Nygård, E.H. Madslie, Outbreak caused by the SARS-CoV-2 Omicron variant in Norway, November to December 2021, *Eurosurveillance* 26 (2021) 2101147.
- [97] A. Goyal, D.B. Reeves, E.F. Cardozo-Ojeda, J.T. Schiffer, B.T. Mayer, Viral load and contact heterogeneity predict SARS-CoV-2 transmission and super-spreading events., *Elife* 10 (2021). <https://doi.org/10.7554/eLife.63537>.
- [98] P. Tupper, H. Boury, M. Yerlanov, C. Colijn, Event-specific interventions to minimize COVID-19 transmission, *Proc Natl Acad Sci USA* 117 (2020) 32038. <https://doi.org/10.1073/pnas.2019324117>.
- [99] A. Sciacchitano, F. Arpino, G. Cortellessa, Benchmark PIV database for the validation of CFD simulations in a transitional cavity flow, *International Journal of Heat and Fluid Flow* 90 (2021) 108831. <https://doi.org/10.1016/j.ijheatfluidflow.2021.108831>.
- [100] H.K. Versteeg, W. Malalasekera, An introduction to computational fluid dynamics: the finite volume method, 2nd ed, Pearson Education Ltd, Harlow, England ; New York, 2007.
- [101] D.C. Wilcox, Turbulence modeling for CFD, 3rd ed, DCW Industries, La C nada, Calif, 2006.
- [102] D.C. Wilcox, Formulation of the k-w Turbulence Model Revisited, *AIAA Journal* 46 (2008) 2823–2838. <https://doi.org/10.2514/1.36541>.
- [103] B.E. Launder, D.B. Spalding, The numerical computation of turbulent flows, *Computer Methods in Applied Mechanics and Engineering* 3 (1974) 269–289. [https://doi.org/10.1016/0045-7825\(74\)90029-2](https://doi.org/10.1016/0045-7825(74)90029-2).
- [104] T.-H. Shih, W.W. Liou, A. Shabbir, Z. Yang, J. Zhu, A new k- ϵ eddy viscosity model for high reynolds number turbulent flows, *Computers & Fluids* 24 (1995) 227–238. [https://doi.org/10.1016/0045-7930\(94\)00032-T](https://doi.org/10.1016/0045-7930(94)00032-T).
- [105] V. Yakhot, S.A. Orszag, S. Thangam, T.B. Gatski, C.G. Speziale, Development of turbulence models for shear flows by a double expansion technique, *Physics of Fluids A: Fluid Dynamics* 4 (1992) 1510–1520. <https://doi.org/10.1063/1.858424>.
- [106] Z. Tong, Y. Li, D. Westerdahl, G. Adamkiewicz, J.D. Spengler, Exploring the effects of ventilation practices in mitigating in-vehicle exposure to traffic-related air pollutants in China, *Environment International* 127 (2019) 773–784. <https://doi.org/10.1016/j.envint.2019.03.023>.
- [107] H. Alsaad, C. Voelker, Could the ductless personalized ventilation be an alternative to the regular ducted personalized ventilation?, *Indoor Air* 31 (2021) 99–111. <https://doi.org/10.1111/ina.12720>.
- [108] J. Pantelic, K.W. Tham, D. Licina, Effectiveness of a personalized ventilation system in reducing personal exposure against directly released simulated cough droplets, *Indoor Air* 25 (2015) 683–693. <https://doi.org/10.1111/ina.12187>.

- [109] A.C. D'Alicandro, A. Mauro, Effects of operating room layout and ventilation system on ultrafine particle transport and deposition, *Atmospheric Environment* 270 (2022) 118901. <https://doi.org/10.1016/j.atmosenv.2021.118901>.
- [110] M. Mirzaie, E. Lakzian, A. Khan, M.E. Warkiani, O. Mahian, G. Ahmadi, COVID-19 spread in a classroom equipped with partition – A CFD approach, *Journal of Hazardous Materials* 420 (2021) 126587. <https://doi.org/10.1016/j.jhazmat.2021.126587>.
- [111] A. Foster, M. Kinzel, Estimating COVID-19 exposure in a classroom setting: A comparison between mathematical and numerical models, *Physics of Fluids* 33 (2021) 021904. <https://doi.org/10.1063/5.0040755>.
- [112] Q. He, J. Niu, N. Gao, T. Zhu, J. Wu, CFD study of exhaled droplet transmission between occupants under different ventilation strategies in a typical office room, *Building and Environment* 46 (2011) 397–408. <https://doi.org/10.1016/j.buildenv.2010.08.003>.
- [113] H. Arjmandi, R. Amini, F. khani, M. Fallahpour, Minimizing the respiratory pathogen transmission: Numerical study and multi-objective optimization of ventilation systems in a classroom, *Thermal Science and Engineering Progress* 28 (2022) 101052. <https://doi.org/10.1016/j.tsep.2021.101052>.
- [114] J. Pantelic, K.W. Tham, Adequacy of air change rate as the sole indicator of an air distribution system's effectiveness to mitigate airborne infectious disease transmission caused by a cough release in the room with overhead mixing ventilation: A case study, *HVAC&R Research* 19 (2013) 947–961. <https://doi.org/10.1080/10789669.2013.842447>.
- [115] S. Ferrari, T. Blázquez, R. Cardelli, G. Puglisi, R. Suárez, L. Mazzarella, Ventilation strategies to reduce airborne transmission of viruses in classrooms: A systematic review of scientific literature, *Building and Environment* 222 (2022) 109366. <https://doi.org/10.1016/j.buildenv.2022.109366>.
- [116] S.R. Narayanan, S. Yang, Airborne transmission of virus-laden aerosols inside a music classroom: Effects of portable purifiers and aerosol injection rates, *Physics of Fluids* 33 (2021) 033307. <https://doi.org/10.1063/5.0042474>.
- [117] Y. Kang, Y. Wang, K. Zhong, Effects of supply air temperature and inlet location on particle dispersion in displacement ventilation rooms, *Particuology* 9 (2011) 619–625. <https://doi.org/10.1016/j.partic.2010.05.018>.
- [118] Z. Liu, R. Li, Y. Wu, R. Ju, N. Gao, Numerical study on the effect of diner divider on the airborne transmission of diseases in canteens, *Energy and Buildings* 248 (2021) 111171. <https://doi.org/10.1016/j.enbuild.2021.111171>.
- [119] C. Zhuang, G. Yang, T. Long, D. Hu, Numerical comparison of removal and deposition for fully-distributed particles in central- and split-type air-conditioning rooms, *Building and Environment* 112 (2017) 17–28. <https://doi.org/10.1016/j.buildenv.2016.11.027>.
- [120] A. Jurelionis, L. Gagyte, T. Prasauskas, D. Čiužas, E. Krugly, L. Šeduikytė, D. Martuzevičius, The impact of the air distribution method in ventilated rooms on the aerosol particle dispersion and removal: The experimental approach, *Energy and Buildings* 86 (2015) 305–313. <https://doi.org/10.1016/j.enbuild.2014.10.014>.
- [121] E. Ding, D. Zhang, P.M. Bluyssen, Ventilation regimes of school classrooms against airborne transmission of infectious respiratory droplets: A review, *Building and Environment* 207 (2022) 108484. <https://doi.org/10.1016/j.buildenv.2021.108484>.

- [122] J.H. Ferziger, M. Perić, *Computational methods for fluid dynamics*, 3rd, rev. ed ed., Springer, Berlin ; New York, 2002.
- [123] ISO, ISO/IEC Guide 98-3:2008. *Uncertainty of measurement - part 3: guide to the expression of uncertainty in measurement (GUM: 1995)*, (2008).
- [124] M. Raffel, C.E. Willert, F. Scarano, C.J. Kähler, S.T. Wereley, J. Kompenhans, *Particle Image Velocimetry: A Practical Guide*, Springer International Publishing, Cham, 2018. <https://doi.org/10.1007/978-3-319-68852-7>.
- [125] J.B. Joshi, K. Nandakumar, A.W. Patwardhan, A.K. Nayak, V. Pareek, M. Gumulya, C. Wu, N. Minocha, E. Pal, M. Kumar, V. Bhusare, S. Tiwari, D. Lote, C. Mali, A. Kulkarni, S. Tamhankar, *Computational fluid dynamics*, in: *Advances of Computational Fluid Dynamics in Nuclear Reactor Design and Safety Assessment*, Elsevier, 2019: pp. 21–238. <https://doi.org/10.1016/B978-0-08-102337-2.00002-X>.
- [126] L. Morawska, J. Allen, W. Bahnfleth, P.M. Bluyssen, A. Boerstra, G. Buonanno, J. Cao, S.J. Dancer, A. Floto, F. Franchimon, T. Greenhalgh, C. Haworth, J. Hogeling, C. Isaxon, J.L. Jimenez, J. Kurnitski, Y. Li, M. Loomans, G. Marks, L.C. Marr, L. Mazzarella, A.K. Melikov, S. Miller, D.K. Milton, W. Nazaroff, P.V. Nielsen, C. Noakes, J. Peccia, K. Prather, X. Querol, C. Sekhar, O. Seppänen, S.-I. Tanabe, J.W. Tang, R. Tellier, K.W. Tham, P. Wargocki, A. Wierzbicka, M. Yao, *A paradigm shift to combat indoor respiratory infection*, *Science* 372 (2021) 689–691. <https://doi.org/10.1126/science.abg2025>.
- [127] L. Morawska, G. Buonanno, A. Mikszewski, L. Stabile, *The physics of respiratory particle generation, fate in the air, and inhalation*, *Nature Reviews Physics* 4 (2022) 723–734. <https://doi.org/10.1038/s42254-022-00506-7>.
- [128] J. Jimenez, L. Marr, K. Randall, T.E. Ewing, Z. Tufekci, T. Greenhalgh, D.K. Milton, R. Tellier, J. Tang, Y. Li, L. Morawska, J. Mesiano-Crookston, D. Fisman, O. Hegarty, S. Dancer, P.M. Bluyssen, G. Buonanno, M. Loomans, W. Bahnfleth, M. Yao, C. Sekhar, P. Wargocki, A.K. Melikov, K. Prather, *What Were the Historical Reasons for the Resistance to Recognizing Airborne Transmission during the COVID-19 Pandemic?*, *SSRN* (2021).
- [129] N. Haug, L. Geyrhofer, A. Londei, E. Dervic, A. Desvars-Larrive, V. Loreto, B. Pinior, S. Thurner, P. Klimek, *Ranking the effectiveness of worldwide COVID-19 government interventions*, *Nature Human Behaviour* 4 (2020) 1303–1312. <https://doi.org/10.1038/s41562-020-01009-0>.
- [130] E. Raffetti, G. Di Baldassarre, *Do the Benefits of School Closure Outweigh Its Costs?*, *Int J Environ Res Public Health* 19 (2022). <https://doi.org/10.3390/ijerph19052500>.
- [131] G. Buonanno, L. Ricolfi, L. Morawska, L. Stabile, *Increasing ventilation reduces SARS-CoV-2 airborne transmission in schools: A retrospective cohort study in Italy's Marche region*, *Frontiers in Public Health* 10 (2022). <https://www.frontiersin.org/articles/10.3389/fpubh.2022.1087087>.
- [132] ASHRAE, *Standard 62.1 - Ventilation for Acceptable Indoor Air Quality*, (2013).
- [133] European Committee for Standardisation, *UNI EN 16798-1 - Energy performance of buildings - Ventilation for buildings. Indoor environmental input parameters for design and assessment of energy performance of buildings addressing indoor air quality, thermal environment, lighting and acoustics. Module M1-6.*, (2019).
- [134] C. Xu, L. Liu, *Personalized ventilation: One possible solution for airborne infection control in highly occupied space?*, *Indoor and Built Environment* 27 (2018) 873–876. <https://doi.org/10.1177/1420326X18777383>.

- [135] V.C.-C. Cheng, D.C. Lung, S.-C. Wong, A.K.-W. Au, Q. Wang, H. Chen, L. Xin, A.W.-H. Chu, J.D. Ip, W.-M. Chan, H.-W. Tsoi, H. Tse, K.H.-L. Ng, M.Y.-W. Kwan, S.-K. Chuang, K.K.-W. To, Y. Li, K.-Y. Yuen, Outbreak investigation of airborne transmission of Omicron (B.1.1.529) - SARS-CoV-2 variant of concern in a restaurant: Implication for enhancement of indoor air dilution, *Journal of Hazardous Materials* 430 (2022) 128504. <https://doi.org/10.1016/j.jhazmat.2022.128504>.
- [136] C.M. Orton, H.E. Symons, B. Moseley, J. Archer, N.A. Watson, K.E.J. Philip, S. Sheikh, B. Saccente-Kennedy, D. Costello, W.J. Browne, J.D. Calder, B.R. Bzdek, J.H. Hull, J.P. Reid, P.L. Shah, A comparison of respiratory particle emission rates at rest and while speaking or exercising, *Communications Medicine* 2 (2022) 44. <https://doi.org/10.1038/s43856-022-00103-w>.
- [137] W. Liu, L. Liu, C. Xu, L. Fu, Y. Wang, P.V. Nielsen, C. Zhang, Exploring the potentials of personalized ventilation in mitigating airborne infection risk for two closely ranged occupants with different risk assessment models, *Energy and Buildings* 253 (2021) 111531. <https://doi.org/10.1016/j.enbuild.2021.111531>.
- [138] A.K. Melikov, COVID-19: Reduction of airborne transmission needs paradigm shift in ventilation., *Build Environ* 186 (2020) 107336. <https://doi.org/10.1016/j.buildenv.2020.107336>.
- [139] A.K. Melikov, Personalized ventilation., *Indoor Air* 14 Suppl 7 (2004) 157–167. <https://doi.org/10.1111/j.1600-0668.2004.00284.x>.
- [140] A.K. Melikov, M.A. Skwarczynski, J. Kaczmarczyk, J. Zabecky, Use of personalized ventilation for improving health, comfort, and performance at high room temperature and humidity., *Indoor Air* 23 (2013) 250–263. <https://doi.org/10.1111/ina.12012>.
- [141] J. Pantelic, G.N. Sze-To, K.W. Tham, C.Y.H. Chao, Y.C.M. Khoo, Personalized ventilation as a control measure for airborne transmissible disease spread, *Journal of The Royal Society Interface* 6 (2009) S715–S726. <https://doi.org/10.1098/rsif.2009.0311.focus>.
- [142] C. Xu, X. Wei, L. Liu, L. Su, W. Liu, Y. Wang, P.V. Nielsen, Effects of personalized ventilation interventions on airborne infection risk and transmission between occupants, *Building and Environment* 180 (2020) 107008. <https://doi.org/10.1016/j.buildenv.2020.107008>.
- [143] J. Xu, C. Wang, S.C. Fu, C.Y.H. Chao, The effect of head orientation and personalized ventilation on bioaerosol deposition from a cough, *Indoor Air* 32 (2022) e12973. <https://doi.org/10.1111/ina.12973>.
- [144] J. Yang, S. Sekhar, K.W.D. Cheong, B. Raphael, Performance evaluation of a novel personalized ventilation-personalized exhaust system for airborne infection control, *Indoor Air* 25 (2015) 176–187. <https://doi.org/10.1111/ina.12127>.
- [145] H. Ma, H. Shen, T. Shui, Q. Li, L. Zhou, Experimental Study on Ultrafine Particle Removal Performance of Portable Air Cleaners with Different Filters in an Office Room, *Int J Environ Res Public Health* 13 (2016) 102. <https://doi.org/10.3390/ijerph13010102>.
- [146] A. Pacitto, F. Amato, T. Moreno, M. Pandolfi, A. Fonseca, M. Mazaheri, L. Stabile, G. Buonanno, X. Querol, Effect of ventilation strategies and air purifiers on the children's exposure to airborne particles and gaseous pollutants in school gyms, *Science of The Total Environment* 712 (2020) 135673. <https://doi.org/10.1016/j.scitotenv.2019.135673>.
- [147] M.O.P. Alvarenga, J.M.M. Dias, B.J.L.A. Lima, A.S.L. Gomes, G.Q.M. Monteiro, The implementation of portable air-cleaning technologies in healthcare settings - a

- scoping review., *J Hosp Infect* 132 (2022) 93–103. <https://doi.org/10.1016/j.jhin.2022.12.004>.
- [148] J.E. Castellini, C.A. Faulkner, W. Zuo, D.M. Lorenzetti, M.D. Sohn, Assessing the use of portable air cleaners for reducing exposure to airborne diseases in a conference room with thermal stratification, *Building and Environment* 207 (2022) 108441. <https://doi.org/10.1016/j.buildenv.2021.108441>.
- [149] M.S. Zuraimi, G.J. Nilsson, R.J. Magee, Removing indoor particles using portable air cleaners: Implications for residential infection transmission, *Building and Environment* 46 (2011) 2512–2519. <https://doi.org/10.1016/j.buildenv.2011.06.008>.
- [150] M. Rodríguez, M.L. Palop, S. Seseña, A. Rodríguez, Are the Portable Air Cleaners (PAC) really effective to terminate airborne SARS-CoV-2?, *Science of The Total Environment* 785 (2021) 147300. <https://doi.org/10.1016/j.scitotenv.2021.147300>.
- [151] G. Song, Z. Ai, Z. Liu, G. Zhang, A systematic literature review on smart and personalized ventilation using CO₂ concentration monitoring and control, *Energy Reports* 8 (2022) 7523–7536. <https://doi.org/10.1016/j.egy.2022.05.243>.
- [152] M. Dalewski, A.K. Melikov, M. Vesely, Performance of ductless personalized ventilation in conjunction with displacement ventilation: Physical environment and human response, *Building and Environment* 81 (2014) 354–364. <https://doi.org/10.1016/j.buildenv.2014.07.011>.
- [153] R. Gao, H. Li, H. Zhang, C. Wang, A. Li, W. Du, B. Deng, Research on a Personalized Targeted Air Supply Device Based on Body Movement Capture., *Indoor Air* (2020).
- [154] M. Fan, Z. Fu, J. Wang, Z. Wang, H. Suo, X. Kong, H. Li, A review of different ventilation modes on thermal comfort, air quality and virus spread control., *Build Environ* 212 (2022) 108831. <https://doi.org/10.1016/j.buildenv.2022.108831>.
- [155] J. Yan, Q. Zeng, Y. Liang, L. He, Z. Li, Modeling and Implementation of Electroactive Smart Air-Conditioning Vent Register for Personalized HVAC Systems, *IEEE Access* 5 (2017) 1649–1657. <https://doi.org/10.1109/ACCESS.2017.2664580>.
- [156] H.E. Khalifa, M.I. Janos, J.F. Dannenhoffer III, Experimental investigation of reduced-mixing personal ventilation jets, *Building and Environment* 44 (2009) 1551–1558. <https://doi.org/10.1016/j.buildenv.2008.11.006>.
- [157] A.K. Melikov, R. Cermak, M. Majer, Personalized ventilation: evaluation of different air terminal devices, *Energy and Buildings* 34 (2002) 829–836. [https://doi.org/10.1016/S0378-7788\(02\)00102-0](https://doi.org/10.1016/S0378-7788(02)00102-0).
- [158] Z.T. Ai, K. Hashimoto, A.K. Melikov, Airborne transmission between room occupants during short-term events: Measurement and evaluation, *Indoor Air* 29 (2019) 563–576. <https://doi.org/10.1111/ina.12557>.
- [159] B. Yang, P. Liu, Y. Liu, D. Jin, F. Wang, Assessment of Thermal Comfort and Air Quality of Room Conditions by Impinging Jet Ventilation Integrated with Ductless Personalized Ventilation, *Sustainability* 14 (2022). <https://doi.org/10.3390/su141912526>.
- [160] W. Oh, R. Ooka, H. Kikumoto, S. Lee, Numerical investigation of the transmission route of infectious particles produced by human, *CLIMA* (2022). <https://doi.org/10.34641/clima.2022.411>.
- [161] G. Buonanno, G. Giovinco, L. Morawska, L. Stabile, Tracheobronchial and alveolar dose of submicrometer particles for different population age groups in Italy, *Atmospheric Environment* 45 (2011) 6216–6224. <https://doi.org/10.1016/j.atmosenv.2011.07.066>.
- [162] European Communities, How Europeans spend their time, (2004).

- [163] P. Wargocki, D. Wyon, The Effects of Moderately Raised Classroom Temperatures and Classroom Ventilation Rate on the Performance of Schoolwork by Children (RP-1257), *HVAC&R Res.* 13 (2007) 193–220. <https://doi.org/10.1080/10789669.2007.10390951>.
- [164] O. Hänninen, A.B. Knol, M. Jantunen, T.-A. Lim, A. Conrad, M. Rappolder, P. Carrer, A.-C. Fanetti, R. Kim, J. Buekers, R. Torfs, I. Iavarone, T. Classen, C. Hornberg, O.C.L. Mekel, the EBoDE Working Group., Environmental Burden of Disease in Europe: Assessing Nine Risk Factors in Six Countries, *Environmental Health Perspectives* 122 (2014) 439–446. <https://doi.org/10.1289/ehp.1206154>.
- [165] S.-J. Lee, J.-H. Yoon, Temperature field measurement of heated ventilation flow in a vehicle interior, *International Journal of Vehicle Design* Vol. 19 (1998) pp 228–243.
- [166] V.P. Adhikari, A. Nassar, Q.H. Nagpurwala, Numerical Studies on the Effect of Cooling Vent Setting and Solar Radiation on Air Flow and Temperature Distribution in a Passenger Car, *Numerical Studies on the Effect of Cooling* (2009) 2009–28–0048. <https://doi.org/10.4271/2009-28-0048>.
- [167] J.P. Lee, H.L. Kim, S.J. Lee, Large-scale PIV measurements of ventilation flow inside the passenger compartment of a real car, *J Vis* 14 (2011) 321–329. <https://doi.org/10.1007/s12650-011-0095-9>.
- [168] M. Konstantinov, W. Lautenschlager, A. Shishkin, C. Wagner, Numerical Simulation of the Air Flow and Thermal Comfort in Aircraft Cabins, in: A. Dillmann, G. Heller, E. Krämer, H.-P. Kreplin, W. Nitsche, U. Rist (Eds.), *New Results in Numerical and Experimental Fluid Mechanics IX*, Springer International Publishing, Cham, 2014: pp. 293–301. https://doi.org/10.1007/978-3-319-03158-3_30.
- [169] F.J. Huera-Huarte, X. Cort, E. Aramburu, X. Vizcaino, L. Casto, DPIV Measurements of the HVAC Aerodynamics Inside a Passenger Car, *SAE Technical Paper* (2014) 2014-36–0214. <https://doi.org/10.4271/2014-36-0214>.
- [170] H.A. Elmaghraby, Y.W. Chiang, A.A. Aliabadi, Ventilation strategies and air quality management in passenger aircraft cabins: A review of experimental approaches and numerical simulations, *Science and Technology for the Built Environment* 24 (2018) 160–175. <https://doi.org/10.1080/23744731.2017.1387463>.
- [171] J. Sip, F. Lizal, J. Pokorný, J. Elcner, J. Jedelsky, M. Jicha, Automotive cabin vent: Comparison of RANS and LES approaches with analytical-empirical equations and their validation with experiments using Hot-Wire Anemometry, *Building and Environment* 233 (2023) 110072. <https://doi.org/10.1016/j.buildenv.2023.110072>.
- [172] M. Fojtlín, M. Planka, J. Fišer, J. Pokorný, M. Jicha, Airflow Measurement of the Car HVAC Unit Using Hot-wire Anemometry, *EPJ Web of Conferences* 114 (2016) 02023. <https://doi.org/10.1051/epjconf/201611402023>.
- [173] F. Lizal, O. Pech, J. Jedelsky, J. Tuhovcak, M. Jicha, The automotive ventilation test case: Investigation of the velocity field downstream of a benchmark vent using smoke visualization and hot-wire anemometry, *Proceedings of the Institution of Mechanical Engineers, Part D: Journal of Automobile Engineering* 233 (2019) 2146–2160. <https://doi.org/10.1177/0954407018776137>.
- [174] F. Arpino, V. Fericola, A. Frattolillo, L. Rosso, A CFD Study on a Calibration System for Contact Temperature Probes, *Int J Thermophys* 30 (2009) 306–315. <https://doi.org/10.1007/s10765-008-0451-8>.
- [175] B.L. Smith, The difference between traditional experiments and CFD validation benchmark experiments, *Nuclear Engineering and Design* 312 (2017) 42–47. <https://doi.org/10.1016/j.nucengdes.2016.10.007>.

- [176] T. Ležovič, F. Lízal, J. Jedelský, M. Jícha, HVAC automotive vents evaluation and their performance, *HVAC&R Research* 19 (2013) 1073–1082. <https://doi.org/10.1080/10789669.2013.824498>.
- [177] A. Piovano, L. Loreface, N. Paola, L. Miretti, E. Ribaldone, Automated CFD multi-objective optimization for a passenger vehicle panel duct, (2014).
- [178] J.-H. Yoon, S.-J. Lee, Velocity field measurements of ventilation flow in a vehicle interior, (2003).
- [179] A. Mueller, A. Landolt, T.K. Rösger, Probe capture for quantitative flow visualization in large scale wind tunnels, in: 28th Aerodynamic Measurement Technology, Ground Testing, and Flight Testing Conference, American Institute of Aeronautics and Astronautics, New Orleans, Louisiana, 2012. <https://doi.org/10.2514/6.2012-3317>.
- [180] A. Müller, Real-Time 3D Flow Visualization Technique with Large Scale Capability, ETH Zurich, 2017. <https://doi.org/10.3929/ETHZ-B-000228428>.
- [181] J. Bartl, A. Müller, A. Landolt, F. Mühle, M. Vatn, L. Oggiano, L. Sætran, Validation of the real-time-response ProCap measurement system for full field wake scans behind a yawed model-scale wind turbine, *J. Phys.: Conf. Ser.* 1104 (2018) 012018. <https://doi.org/10.1088/1742-6596/1104/1/012018>.
- [182] Vectroflow GmbH, iProbe Datasheet, (n.d.). https://procap.tech/wp-content/uploads/2023/02/2022-11-30_iProbe_Datasheet_EN.pdf.
- [183] Streamwise, ProCap Compact - User manual, 2021.
- [184] J. Westerweel, Fundamentals of digital particle image velocimetry, *Meas. Sci. Technol.* 8 (1997) 1379–1392. <https://doi.org/10.1088/0957-0233/8/12/002>.
- [185] H.W. Coleman, W.G. Steele, Experimentation, Validation, and Uncertainty Analysis for Engineers, John Wiley & Sons, Inc., Hoboken, NJ, USA, 2009. <https://doi.org/10.1002/9780470485682>.
- [186] J. Nogueira, A. Lecuona, P.A. Rodríguez, J.A. Alfaro, A. Acosta, Limits on the resolution of correlation PIV iterative methods. Practical implementation and design of weighting functions, *Exp Fluids* 39 (2005) 314–321. <https://doi.org/10.1007/s00348-005-1017-1>.
- [187] A. Sciacchitano, B. Wieneke, PIV uncertainty propagation, *Meas. Sci. Technol.* 27 (2016) 084006. <https://doi.org/10.1088/0957-0233/27/8/084006>.
- [188] D.R. Neal, A. Sciacchitano, B.L. Smith, F. Scarano, Collaborative framework for PIV uncertainty quantification: the experimental database, *Meas. Sci. Technol.* 26 (2015) 074003. <https://doi.org/10.1088/0957-0233/26/7/074003>.
- [189] C.D. Argyropoulos, N.C. Markatos, Recent advances on the numerical modelling of turbulent flows, *Applied Mathematical Modelling* 39 (2015) 693–732. <https://doi.org/10.1016/j.apm.2014.07.001>.
- [190] A. Sciacchitano, Uncertainty quantification in particle image velocimetry, *Meas. Sci. Technol.* 30 (2019) 092001. <https://doi.org/10.1088/1361-6501/ab1db8>.
- [191] J.M. Wallace, Quadrant Analysis in Turbulence Research: History and Evolution, *Annu. Rev. Fluid Mech.* 48 (2016) 131–158. <https://doi.org/10.1146/annurev-fluid-122414-034550>.
- [192] R. You, C. Lin, D. Wei, Q. Chen, Evaluating the commercial airliner cabin environment with different air distribution systems, *Indoor Air* 29 (2019) 840–853. <https://doi.org/10.1111/ina.12578>.
- [193] R. You, J. Chen, Z. Shi, W. Liu, C.-H. Lin, D. Wei, Q. Chen, Experimental and numerical study of airflow distribution in an aircraft cabin mock-up with a gasper on,

- Journal of Building Performance Simulation 9 (2016) 555–566. <https://doi.org/10.1080/19401493.2015.1126762>.
- [194] W. Liu, J. Wen, C.-H. Lin, J. Liu, Z. Long, Q. Chen, Evaluation of various categories of turbulence models for predicting air distribution in an airliner cabin, *Building and Environment* 65 (2013) 118–131. <https://doi.org/10.1016/j.buildenv.2013.03.018>.
- [195] C. Yang, X. Zhang, Z. Yao, X. Cao, J. Liu, F. He, Numerical study of the instantaneous flow fields by large eddy simulation and stability analysis in a single aisle cabin model, *Building and Environment* 96 (2016) 1–11. <https://doi.org/10.1016/j.buildenv.2015.10.022>.
- [196] W. Liu, S. Mazumdar, Z. Zhang, S.B. Poussou, J. Liu, C.-H. Lin, Q. Chen, State-of-the-art methods for studying air distributions in commercial airliner cabins, *Building and Environment* 47 (2012) 5–12. <https://doi.org/10.1016/j.buildenv.2011.07.005>.
- [197] C. Wu, N.A. Ahmed, A novel mode of air supply for aircraft cabin ventilation, *Building and Environment* 56 (2012) 47–56. <https://doi.org/10.1016/j.buildenv.2012.02.025>.
- [198] J. Fišer, M. Jícha, Impact of air distribution system on quality of ventilation in small aircraft cabin, *Building and Environment* 69 (2013) 171–182. <https://doi.org/10.1016/j.buildenv.2013.08.007>.
- [199] Y. Yan, X. Li, Y. Shang, J. Tu, Evaluation of airborne disease infection risks in an airliner cabin using the Lagrangian-based Wells-Riley approach, *Building and Environment* 121 (2017) 79–92. <https://doi.org/10.1016/j.buildenv.2017.05.013>.
- [200] R. You, J. Chen, C.-H. Lin, D. Wei, Q. Chen, Investigating the impact of gaspers on cabin air quality in commercial airliners with a hybrid turbulence model, *Building and Environment* 111 (2017) 110–122. <https://doi.org/10.1016/j.buildenv.2016.10.018>.
- [201] R. You, Y. Zhang, X. Zhao, C.-H. Lin, D. Wei, J. Liu, Q. Chen, An innovative personalized displacement ventilation system for airliner cabins, *Building and Environment* 137 (2018) 41–50. <https://doi.org/10.1016/j.buildenv.2018.03.057>.
- [202] J.-H. Thysen, T. Van Hooff, B. Blocken, G.J.F. Van Heijst, CFD simulations of two opposing plane wall jets in a generic empty airplane cabin: Comparison of RANS and LES, *Building and Environment* 205 (2021) 108174. <https://doi.org/10.1016/j.buildenv.2021.108174>.
- [203] Q. Cao, M. Liu, X. Li, C.-H. Lin, D. Wei, S. Ji, T. (Tim) Zhang, Q. Chen, Influencing factors in the simulation of airflow and particle transportation in aircraft cabins by CFD, *Building and Environment* 207 (2022) 108413. <https://doi.org/10.1016/j.buildenv.2021.108413>.
- [204] V. Bianco, O. Manca, S. Nardini, M. Roma, Numerical investigation of transient thermal and fluidynamic fields in an executive aircraft cabin, *Applied Thermal Engineering* 29 (2009) 3418–3425. <https://doi.org/10.1016/j.applthermaleng.2009.05.020>.
- [205] P. Zítek, T. Vyhlídal, G. Simeunović, L. Nováková, J. Čížek, Novel personalized and humidified air supply for airliner passengers, *Building and Environment* 45 (2010) 2345–2353. <https://doi.org/10.1016/j.buildenv.2010.04.005>.
- [206] R.R. Rajendran, F.E. Țurcanu, R.Md. Tawfiqur, H. Askarpour, Computational fluid dynamic analysis of corona virus patients breathing in an airplane, *Physics of Fluids* 35 (2023) 035129. <https://doi.org/10.1063/5.0139733>.
- [207] K. Talaat, M. Abuhegazy, O.A. Mahfoze, O. Anderoglu, S.V. Poroseva, Simulation of aerosol transmission on a Boeing 737 airplane with intervention measures for

- COVID-19 mitigation, *Physics of Fluids* 33 (2021) 033312. <https://doi.org/10.1063/5.0044720>.
- [208] M. Liu, J. Li, J. Liu, M.A. Hassan, Turbulence characterization of instantaneous airflow above passengers with different air distribution systems in a commercial airliner cabin, *Physics of Fluids* 35 (2023) 085118. <https://doi.org/10.1063/5.0159621>.
- [209] N. Li, L. Yang, X. Li, X. Li, J. Tu, S.C.P. Cheung, Multi-objective optimization for designing of high-speed train cabin ventilation system using particle swarm optimization and multi-fidelity Kriging, *Building and Environment* 155 (2019) 161–174. <https://doi.org/10.1016/j.buildenv.2019.03.021>.
- [210] M. Visone, M. Lanzetta, M. Lappa, C. Lanzaro, L. Polizio, Three-dimensional simulation of clouds of multi-disperse evaporating saliva droplets in a train cabin, *Physics of Fluids* 33 (2021) 083318. <https://doi.org/10.1063/5.0059649>.
- [211] C. Peña-Monferrer, S. Antao, R. Manson-Sawko, Numerical investigation of droplets in a cross-ventilated space with sitting passengers under asymptomatic virus transmission conditions, *Physics of Fluids* 33 (2021) 123314. <https://doi.org/10.1063/5.0070625>.
- [212] F. Li, E.S. Lee, B. Zhou, J. Liu, Y. Zhu, Effects of the window openings on the micro-environmental condition in a school bus, *Atmospheric Environment* 167 (2017) 434–443. <https://doi.org/10.1016/j.atmosenv.2017.08.053>.
- [213] S. Zhu, J. Srebric, J.D. Spengler, P. Demokritou, An advanced numerical model for the assessment of airborne transmission of influenza in bus microenvironments, *Building and Environment* 47 (2012) 67–75. <https://doi.org/10.1016/j.buildenv.2011.05.003>.
- [214] S. Zhu, P. Demokritou, J. Spengler, Experimental and numerical investigation of micro-environmental conditions in public transportation buses, *Building and Environment* 45 (2010) 2077–2088. <https://doi.org/10.1016/j.buildenv.2010.03.004>.
- [215] Q. Luo, C. Ou, J. Hang, Z. Luo, H. Yang, X. Yang, X. Zhang, Y. Li, X. Fan, Role of pathogen-laden expiratory droplet dispersion and natural ventilation explaining a COVID-19 outbreak in a coach bus, *Building and Environment* 220 (2022) 109160. <https://doi.org/10.1016/j.buildenv.2022.109160>.
- [216] Z. Zhang, T. Han, K.H. Yoo, J. Capecehatro, A.L. Boehman, K. Maki, Disease transmission through expiratory aerosols on an urban bus, *Physics of Fluids* 33 (2021) 015116. <https://doi.org/10.1063/5.0037452>.
- [217] Y. Yang, Y. Wang, L. Tian, C. Su, Z. Chen, Y. Huang, Effects of purifiers on the airborne transmission of droplets inside a bus, *Physics of Fluids* 34 (2022) 017108. <https://doi.org/10.1063/5.0081230>.
- [218] Y. Yang, Y. Wang, C. Su, X. Yuan, X. Liu, Z. Chen, A rapid method for prediction of airborne disease infection risks in an intercity bus, *Physics of Fluids* 34 (2022) 083323. <https://doi.org/10.1063/5.0107895>.
- [219] C.C. Ooi, A. Suardi, Z.L. Ou Yang, G. Xu, C.K.I. Tan, D. Daniel, H. Li, Z. Ge, F.Y. Leong, K. Marimuthu, O.T. Ng, S.B. Lim, P. Lim, W.S. Mak, W.C.D. Cheong, X.J. Loh, C.W. Kang, K.H. Lim, Risk assessment of airborne COVID-19 exposure in social settings, *Physics of Fluids* 33 (2021) 087118. <https://doi.org/10.1063/5.0055547>.
- [220] C.-J. Yang, T.-C. Yang, P.-T. Chen, K.D. Huang, An Innovative Design of Regional Air Conditioning to Increase Automobile Cabin Energy Efficiency, *Energies* 12 (2019) 2352. <https://doi.org/10.3390/en12122352>.
- [221] S. Khatoun, M.-H. Kim, Thermal Comfort in the Passenger Compartment Using a 3-D Numerical Analysis and Comparison with Fanger's Comfort Models, *Energies* 13 (2020) 690. <https://doi.org/10.3390/en13030690>.

- [222] H. Zhang, L. Dai, G. Xu, Y. Li, W. Chen, W.-Q. Tao, Studies of air-flow and temperature fields inside a passenger compartment for improving thermal comfort and saving energy. Part I: Test/numerical model and validation, *Applied Thermal Engineering* 29 (2009) 2022–2027. <https://doi.org/10.1016/j.applthermaleng.2008.10.005>.
- [223] H. Zhang, L. Dai, G. Xu, Y. Li, W. Chen, W. Tao, Studies of air-flow and temperature fields inside a passenger compartment for improving thermal comfort and saving energy. Part II: Simulation results and discussion, *Applied Thermal Engineering* 29 (2009) 2028–2036. <https://doi.org/10.1016/j.applthermaleng.2008.10.006>.
- [224] T. Dehne, P. Lange, A. Volkmann, D. Schmeling, M. Konstantinov, J. Bosbach, Vertical ventilation concepts for future passenger cars, *Building and Environment* 129 (2018) 142–153. <https://doi.org/10.1016/j.buildenv.2017.11.024>.
- [225] M. Djeddou, A. Mehel, G. Fokoua, A. Tanière, P. Chevrier, On the application of statistical turbulence models to the simulation of airflow inside a car cabin, *Physics of Fluids* 35 (2023) 025106. <https://doi.org/10.1063/5.0132677>.
- [226] V. Mathai, A. Das, K. Breuer, Aerosol transmission in passenger car cabins: Effects of ventilation configuration and driving speed, *Physics of Fluids* 34 (2022) 021904. <https://doi.org/10.1063/5.0079555>.
- [227] N. Sen, K.K. Singh, Spread of virus laden aerosols inside a moving sports utility vehicle with open windows: A numerical study, *Physics of Fluids* 33 (2021) 095117. <https://doi.org/10.1063/5.0061753>.
- [228] P. Dancă, A. Jamin, I. Nastase, B. Janssens, W. Bosschaerts, C. Coşoiu, Experimental and numerical study of the flow dynamics and thermal behavior inside a car cabin: Innovative air diffusers and human body plumes interactions, *Energy Reports* 8 (2022) 992–1002. <https://doi.org/10.1016/j.egy.2022.07.133>.
- [229] P.A. Danca, I. Nastase, F. Bode, The influence of different air flows introduced on the thermal comfort of car passengers during the cooling period – Numerical Study, *IOP Conf. Ser.: Earth Environ. Sci.* 664 (2021) 012112. <https://doi.org/10.1088/1755-1315/664/1/012112>.
- [230] M. Djeddou, A. Mehel, G. Fokoua, A. Tanière, P. Chevrier, A Diffusion-Inertia Model for the simulation of particulate pollutants dynamics inside a car cabin, *Journal of Aerosol Science* 175 (2024) 106279. <https://doi.org/10.1016/j.jaerosci.2023.106279>.
- [231] Y. Pan, W. Huang, H.K. Dai, Y. Bian, K.-F. Ho, C. Chen, Evaluation of intervention measures in reducing the driver's exposure to respiratory particles in a taxi with infected passengers, *Science of The Total Environment* 902 (2023) 166099. <https://doi.org/10.1016/j.scitotenv.2023.166099>.
- [232] P. Bandi, N.P. Manelil, M.P. Maiya, S. Tiwari, T. Arunvel, CFD driven prediction of mean radiant temperature inside an automobile cabin using machine learning, *Thermal Science and Engineering Progress* 37 (2023) 101619. <https://doi.org/10.1016/j.tsep.2022.101619>.
- [233] ANSI/ASHRAE Standard 55-2020: Thermal Environmental Conditions for Human Occupancy, (2020).
- [234] I. Golasi, F. Salata, E. de Lieto Vollaro, M. Coppi, A. de Lieto Vollaro, Thermal Perception in the Mediterranean Area: Comparing the Mediterranean Outdoor Comfort Index (MOCI) to Other Outdoor Thermal Comfort Indices, *Energies* 9 (2016) 550. <https://doi.org/10.3390/en9070550>.

- [235] A. Alahmer, A. Mayyas, A.A. Mayyas, M.A. Omar, D. Shan, Vehicular thermal comfort models; a comprehensive review, *Applied Thermal Engineering* 31 (2011) 995–1002. <https://doi.org/10.1016/j.applthermaleng.2010.12.004>.
- [236] P. Danca, A. Vartires, A. Dogeanu, An Overview of Current Methods for Thermal Comfort Assessment in Vehicle Cabin, *Energy Procedia* 85 (2016) 162–169. <https://doi.org/10.1016/j.egypro.2015.12.322>.
- [237] P. Danca, I. Nastase, F. Bode, C. Croitoru, A. Dogeanu, A. Meslem, Evaluation of the thermal comfort for its occupants inside a vehicle during summer, *IOP Conf. Ser.: Mater. Sci. Eng.* 595 (2019) 012027. <https://doi.org/10.1088/1757-899X/595/1/012027>.
- [238] I. Nastase, P. Danca, F. Bode, C. Croitoru, L. Fechete, M. Sandu, C.I. Coşoiu, A regard on the thermal comfort theories from the standpoint of Electric Vehicle design — Review and perspectives, *Energy Reports* 8 (2022) 10501–10517. <https://doi.org/10.1016/j.egypr.2022.08.186>.
- [239] ISO, ISO/TS 14505-1:2007. Ergonomics of the thermal environment — Evaluation of thermal environments in vehicles — Part 1: Principles and methods for assessment of thermal stress, (2007).
- [240] F. Tartarini, S. Schiavon, pythermalcomfort: A Python package for thermal comfort research, *SoftwareX* 12 (2020) 100578. <https://doi.org/10.1016/j.softx.2020.100578>.
- [241] D. Khovalyg, O.B. Kazanci, H. Halvorsen, I. Gundlach, W.P. Bahnfleth, J. Toftum, B.W. Olesen, Critical review of standards for indoor thermal environment and air quality, *Energy and Buildings* 213 (2020) 109819. <https://doi.org/10.1016/j.enbuild.2020.109819>.
- [242] P.J. Roache, QUANTIFICATION OF UNCERTAINTY IN COMPUTATIONAL FLUID DYNAMICS, *Annu. Rev. Fluid Mech.* 29 (1997) 123–160. <https://doi.org/10.1146/annurev.fluid.29.1.123>.
- [243] F. Nicoud, F. Ducros, Subgrid-Scale Stress Modelling Based on the Square of the Velocity Gradient Tensor, *Flow, Turbulence and Combustion* 62 (1999) 183–200. <https://doi.org/10.1023/A:1009995426001>.
- [244] W.-W. Kim, S. Menon, A new dynamic one-equation subgrid-scale model for large eddy simulations, in: 33rd Aerospace Sciences Meeting and Exhibit, American Institute of Aeronautics and Astronautics, Reno, NV, U.S.A., 1995. <https://doi.org/10.2514/6.1995-356>.
- [245] I.B. Celik, Z.N. Cehreli, I. Yavuz, Index of Resolution Quality for Large Eddy Simulations, *Journal of Fluids Engineering* 127 (2005) 949–958. <https://doi.org/10.1115/1.1990201>.
- [246] S.B. Pope, *Turbulent Flows*, 1st ed., Cambridge University Press, 2000. <https://doi.org/10.1017/CBO9780511840531>.
- [247] R. Poletto, T. Craft, A. Revell, A New Divergence Free Synthetic Eddy Method for the Reproduction of Inlet Flow Conditions for LES, *Flow Turbulence Combust* 91 (2013) 519–539. <https://doi.org/10.1007/s10494-013-9488-2>.
- [248] M. Shur, M. Strelets, A. Travin, A. Probst, S. Probst, D. Schwamborn, S. Deck, A. Skillen, J. Holgate, A. Revell, Improved Embedded Approaches, in: C. Mockett, W. Haase, D. Schwamborn (Eds.), *Go4Hybrid: Grey Area Mitigation for Hybrid RANS-LES Methods*, Springer International Publishing, Cham, 2018: pp. 51–87. https://doi.org/10.1007/978-3-319-52995-0_3.

- [249] K. Gładyszewska-Fiedoruk, T.J. Teleszewski, Modeling of Humidity in Passenger Cars Equipped with Mechanical Ventilation, *Energies* 13 (2020) 2987. <https://doi.org/10.3390/en13112987>.
- [250] TERNA, SNAM, Documento di Descrizione degli Scenari 2022, (n.d.). https://download.terna.it/terna/Documento_Descrizione_Scenari_2022_8da74044f6ee28d.pdf.
- [251] IRENA, Green hydrogen for industry: A guide to policy making, International Renewable Energy Agency, Abu Dhabi, 2022.
- [252] IRENA, Green hydrogen supply: A guide to policy making, International Renewable Energy Agency, Abu Dhabi, 2021.
- [253] IRENA, Green Hydrogen: A guide to policy making, International Renewable Energy Agency, Abu Dhabi, 2020.
- [254] IRENA, Making the breakthrough: Green hydrogen policies and technology costs, International Renewable Energy Agency, 2021. https://www.irena.org/-/media/Files/IRENA/Agency/Publication/2020/Nov/IRENA_Green_Hydrogen_breakthrough_2021.pdf?la=en&hash=40FA5B8AD7AB1666EECBDE30EF458C45EE5A0AA6.
- [255] K. Park, J. Koo, Optimal design of the distributed H₂ production system with cost and safety considerations, *International Journal of Hydrogen Energy* 45 (2020) 34316–34325. <https://doi.org/10.1016/j.ijhydene.2020.01.165>.
- [256] J.M. Lee, S. Lee, D.H. Kye, H.J. Park, W. Park, J. Shin, K. Park, Environ-economic analysis of high-temperature steam electrolysis for decentralized hydrogen production, *Energy Conversion and Management* 266 (2022) 115856. <https://doi.org/10.1016/j.enconman.2022.115856>.
- [257] C. Jarosch, P. Jahnke, J. Giehl, J. Himmel, Modelling Decentralized Hydrogen Systems: Lessons Learned and Challenges from German Regions, *Energies* 15 (2022) 1322. <https://doi.org/10.3390/en15041322>.
- [258] S. Prince-Richard, M. Whale, N. Djilali, A techno-economic analysis of decentralized electrolytic hydrogen production for fuel cell vehicles, *International Journal of Hydrogen Energy* 30 (2005) 1159–1179. <https://doi.org/10.1016/j.ijhydene.2005.04.055>.
- [259] E.M. Barhoumi, P.C. Okonkwo, I. Ben Belgacem, M. Zghaibeh, I. Tlili, Optimal sizing of photovoltaic systems based green hydrogen refueling stations case study Oman, *International Journal of Hydrogen Energy* 47 (2022) 31964–31973. <https://doi.org/10.1016/j.ijhydene.2022.07.140>.
- [260] M. Gökçek, C. Kale, Techno-economical evaluation of a hydrogen refuelling station powered by Wind-PV hybrid power system: A case study for İzmir-Çeşme, *International Journal of Hydrogen Energy* 43 (2018) 10615–10625. <https://doi.org/10.1016/j.ijhydene.2018.01.082>.
- [261] M.S. Okundamiya, Size optimization of a hybrid photovoltaic/fuel cell grid connected power system including hydrogen storage, *International Journal of Hydrogen Energy* 46 (2021) 30539–30546. <https://doi.org/10.1016/j.ijhydene.2020.11.185>.
- [262] D. Caravantes, J. Carbajal, C. Celis, D. Marcelo-Aldana, Estimation of hydrogen production potential from renewable resources in northern Peru, *International Journal of Hydrogen Energy* (2023) S0360319923039046. <https://doi.org/10.1016/j.ijhydene.2023.07.350>.
- [263] S. Di Micco, F. Romano, E. Jannelli, A. Perna, M. Minutillo, Techno-economic analysis of a multi-energy system for the co-production of green hydrogen, renewable

- electricity and heat, *International Journal of Hydrogen Energy* (2023) S0360319923020992. <https://doi.org/10.1016/j.ijhydene.2023.04.269>.
- [264] J. Zhou, Y. Wu, Z. Zhong, C. Xu, Y. Ke, J. Gao, Modeling and configuration optimization of the natural gas-wind-photovoltaic-hydrogen integrated energy system: A novel deviation satisfaction strategy, *Energy Conversion and Management* 243 (2021) 114340. <https://doi.org/10.1016/j.enconman.2021.114340>.
- [265] M. Zare Oskouei, H. Mehrjerdi, Optimal allocation of power-to-hydrogen units in regional power grids for green hydrogen trading: Opportunities and barriers, *Journal of Cleaner Production* 358 (2022) 131937. <https://doi.org/10.1016/j.jclepro.2022.131937>.
- [266] R. Bhandari, R.R. Shah, Hydrogen as energy carrier: Techno-economic assessment of decentralized hydrogen production in Germany, *Renewable Energy* 177 (2021) 915–931. <https://doi.org/10.1016/j.renene.2021.05.149>.
- [267] M. Cavana, A. Mazza, G. Chicco, P. Leone, Electrical and gas networks coupling through hydrogen blending under increasing distributed photovoltaic generation, *Applied Energy* 290 (2021) 116764. <https://doi.org/10.1016/j.apenergy.2021.116764>.
- [268] L. Cheli, G. Guzzo, D. Adolfo, C. Carcasci, Steady-state analysis of a natural gas distribution network with hydrogen injection to absorb excess renewable electricity, *International Journal of Hydrogen Energy* 46 (2021) 25562–25577. <https://doi.org/10.1016/j.ijhydene.2021.05.100>.
- [269] https://www.snam.it/en/energy_transition/hydrogen/snam_and_hydrogen/, (n.d.).
- [270] Ministero della Transizione Ecologica, Aggiornamento al decreto del Ministro dello sviluppo economico 18 maggio 2018, recante: «Regola tecnica sulle caratteristiche chimico fisiche e sulla presenza di altri componenti nel gas combustibile», 2022.
- [271] M. Dell'Isola, G. Ficco, L. Moretti, J. Jaworski, P. Kułaga, E. Kukulka–Zajac, Impact of Hydrogen Injection on Natural Gas Measurement, *Energies* 14 (2021) 8461. <https://doi.org/10.3390/en14248461>.
- [272] Trina Solar Vertex Backsheet Module TSM-DE21 Datasheet (Version Number: TSM_EN_2021_A), (n.d.). https://static.trinasolar.com/sites/default/files/DT-M-0012_A_Datasheet_Vertex_DE21_EN_2021_A_web.pdf.
- [273] H.Z. Al Garni, A. Awasthi, M.A.M. Ramli, Optimal design and analysis of grid-connected photovoltaic under different tracking systems using HOMER, *Energy Conversion and Management* 155 (2018) 42–57. <https://doi.org/10.1016/j.enconman.2017.10.090>.
- [274] P. Pal, V. Mukherjee, Off-grid solar photovoltaic/hydrogen fuel cell system for renewable energy generation: An investigation based on techno-economic feasibility assessment for the application of end-user load demand in North-East India, *Renewable and Sustainable Energy Reviews* 149 (2021) 111421. <https://doi.org/10.1016/j.rser.2021.111421>.
- [275] Agora Verkehrswende, Agora Energiewende, Frontier Economics, *The Future Cost of Electricity-Based Synthetic Fuels*, 2018.
- [276] C. Xu, Y. Ke, Y. Li, H. Chu, Y. Wu, Data-driven configuration optimization of an off-grid wind/PV/hydrogen system based on modified NSGA-II and CRITIC-TOPSIS, *Energy Conversion and Management* 215 (2020) 112892. <https://doi.org/10.1016/j.enconman.2020.112892>.

- [277] D. Bessarabov, H. Wang, H. Li, N. Zhao, eds., *PEM Electrolysis for Hydrogen Production: Principles and Applications*, 0 ed., CRC Press, 2016. <https://doi.org/10.1201/b19096>.
- [278] B. Bensmann, R. Hanke-Rauschenbach, I.K. Peña Arias, K. Sundmacher, Energetic evaluation of high pressure PEM electrolyzer systems for intermediate storage of renewable energies, *Electrochimica Acta* 110 (2013) 570–580. <https://doi.org/10.1016/j.electacta.2013.05.102>.
- [279] A. Mehmeti, A. Angelis-Dimakis, G. Arampatzis, S. McPhail, S. Ulgiati, Life Cycle Assessment and Water Footprint of Hydrogen Production Methods: From Conventional to Emerging Technologies, *Environments* 5 (2018) 24. <https://doi.org/10.3390/environments5020024>.
- [280] A. Christensen, Assessment of Hydrogen Production Costs from Electrolysis: United States and Europe, International Council on Clean Transportation, 2020.
- [281] F. Fazelpour, N. Soltani, M.A. Rosen, Economic analysis of standalone hybrid energy systems for application in Tehran, Iran, *International Journal of Hydrogen Energy* 41 (2016) 7732–7743. <https://doi.org/10.1016/j.ijhydene.2016.01.113>.
- [282] S. Salisu, M.W. Mustafa, L. Olatomiwa, O.O. Mohammed, Assessment of technical and economic feasibility for a hybrid PV-wind-diesel-battery energy system in a remote community of north central Nigeria, *Alexandria Engineering Journal* 58 (2019) 1103–1118. <https://doi.org/10.1016/j.aej.2019.09.013>.
- [283] P. Fragiaco, M. Genovese, Technical-economic analysis of a hydrogen production facility for power-to-gas and hydrogen mobility under different renewable sources in Southern Italy, *Energy Conversion and Management* 223 (2020) 113332. <https://doi.org/10.1016/j.enconman.2020.113332>.
- [284] Z. Liu, Y. Chen, R. Zhuo, H. Jia, Energy storage capacity optimization for autonomy microgrid considering CHP and EV scheduling, *Applied Energy* 210 (2018) 1113–1125. <https://doi.org/10.1016/j.apenergy.2017.07.002>.
- [285] S. Diaf, G. Notton, M. Belhamel, M. Haddadi, A. Louche, Design and techno-economical optimization for hybrid PV/wind system under various meteorological conditions, *Applied Energy* 85 (2008) 968–987. <https://doi.org/10.1016/j.apenergy.2008.02.012>.
- [286] A. Kaabeche, M. Belhamel, R. Ibtouen, Sizing optimization of grid-independent hybrid photovoltaic/wind power generation system, *Energy* 36 (2011) 1214–1222. <https://doi.org/10.1016/j.energy.2010.11.024>.
- [287] H. Belmili, M. Haddadi, S. Bacha, M.F. Almi, B. Bendib, Sizing stand-alone photovoltaic–wind hybrid system: Techno-economic analysis and optimization, *Renewable and Sustainable Energy Reviews* 30 (2014) 821–832. <https://doi.org/10.1016/j.rser.2013.11.011>.
- [288] M. Smaoui, A. Abdelkafi, L. Krichen, Optimal sizing of stand-alone photovoltaic/wind/hydrogen hybrid system supplying a desalination unit, *Solar Energy* 120 (2015) 263–276. <https://doi.org/10.1016/j.solener.2015.07.032>.
- [289] M. Šúri, T.A. Huld, E.D. Dunlop, PV-GIS: a web-based solar radiation database for the calculation of PV potential in Europe, *International Journal of Sustainable Energy* 24 (2005) 55–67. <https://doi.org/10.1080/14786450512331329556>.
- [290] M. Šúri, T.A. Huld, E.D. Dunlop, H.A. Ossenbrink, Potential of solar electricity generation in the European Union member states and candidate countries, *Solar Energy* 81 (2007) 1295–1305. <https://doi.org/10.1016/j.solener.2006.12.007>.
- [291] M. Suri, T. Huld, T. Cebecauer, E.D. Dunlop, Geographic Aspects of Photovoltaics in Europe: Contribution of the PVGIS Website, *IEEE J. Sel. Top. Appl. Earth*

- Observations Remote Sensing 1 (2008) 34–41.
<https://doi.org/10.1109/JSTARS.2008.2001431>.
- [292] T. Huld, M. Šúri, E.D. Dunlop, Geographical variation of the conversion efficiency of crystalline silicon photovoltaic modules in Europe, *Prog. Photovolt: Res. Appl.* 16 (2008) 595–607. <https://doi.org/10.1002/pip.846>.
- [293] T. Huld, R. Müller, A. Gambardella, A new solar radiation database for estimating PV performance in Europe and Africa, *Solar Energy* 86 (2012) 1803–1815. <https://doi.org/10.1016/j.solener.2012.03.006>.
- [294] D.Z. Djurdjevic, Perspectives and assessments of solar PV power engineering in the Republic of Serbia, *Renewable and Sustainable Energy Reviews* 15 (2011) 2431–2446. <https://doi.org/10.1016/j.rser.2011.02.025>.
- [295] J. Hofierka, J. Kaňuk, Assessment of photovoltaic potential in urban areas using open-source solar radiation tools, *Renewable Energy* 34 (2009) 2206–2214. <https://doi.org/10.1016/j.renene.2009.02.021>.
- [296] M. Hossain, S. Mekhilef, L. Olatomiwa, Performance evaluation of a stand-alone PV-wind-diesel-battery hybrid system feasible for a large resort center in South China Sea, Malaysia, *Sustainable Cities and Society* 28 (2017) 358–366. <https://doi.org/10.1016/j.scs.2016.10.008>.
- [297] Z. Abdin, W. Mérida, Hybrid energy systems for off-grid power supply and hydrogen production based on renewable energy: A techno-economic analysis, *Energy Conversion and Management* 196 (2019) 1068–1079. <https://doi.org/10.1016/j.enconman.2019.06.068>.
- [298] S. Bhakta, V. Mukherjee, Performance indices evaluation and techno economic analysis of photovoltaic power plant for the application of isolated India's island, *Sustainable Energy Technologies and Assessments* 20 (2017) 9–24. <https://doi.org/10.1016/j.seta.2017.02.002>.
- [299] C. Li, X. Ge, Y. Zheng, C. Xu, Y. Ren, C. Song, C. Yang, Techno-economic feasibility study of autonomous hybrid wind/PV/battery power system for a household in Urumqi, China, *Energy* 55 (2013) 263–272. <https://doi.org/10.1016/j.energy.2013.03.084>.
- [300] D. Jang, K. Kim, K.-H. Kim, S. Kang, Techno-economic analysis and Monte Carlo simulation for green hydrogen production using offshore wind power plant, *Energy Conversion and Management* 263 (2022) 115695. <https://doi.org/10.1016/j.enconman.2022.115695>.
- [301] I.P. Panapakidis, D.N. Sarafianos, M.C. Alexiadis, Comparative analysis of different grid-independent hybrid power generation systems for a residential load, *Renewable and Sustainable Energy Reviews* 16 (2012) 551–563. <https://doi.org/10.1016/j.rser.2011.08.021>.
- [302] P. Marocco, D. Ferrero, M. Gandiglio, M.M. Ortiz, K. Sundseth, A. Lanzini, M. Santarelli, A study of the techno-economic feasibility of H₂-based energy storage systems in remote areas, *Energy Conversion and Management* 211 (2020) 112768. <https://doi.org/10.1016/j.enconman.2020.112768>.
- [303] T.M.I. Mahlia, P.L. Chan, Life cycle cost analysis of fuel cell based cogeneration system for residential application in Malaysia, *Renewable and Sustainable Energy Reviews* 15 (2011) 416–426. <https://doi.org/10.1016/j.rser.2010.07.041>.
- [304] M. Pellegrini, A. Guzzini, C. Saccani, A Preliminary Assessment of the Potential of Low Percentage Green Hydrogen Blending in the Italian Natural Gas Network, *Energies* 13 (2020) 5570. <https://doi.org/10.3390/en13215570>.

- [305] C. Saccani, M. Pellegrini, A. Guzzini, Analysis of the Existing Barriers for the Market Development of Power to Hydrogen (P2H) in Italy, *Energies* 13 (2020) 4835. <https://doi.org/10.3390/en13184835>.
- [306] G. Glenk, S. Reichelstein, Economics of converting renewable power to hydrogen, *Nat Energy* 4 (2019) 216–222. <https://doi.org/10.1038/s41560-019-0326-1>.
- [307] J. Tu, G.H. Yeoh, C. Liu, *Computational fluid dynamics: a practical approach*, Third edition, Butterworth-Heinemann, Oxford ; Cambridge, MA, 2018.
- [308] Joel Guerrero, *Introduction to Computational Fluid Dynamics: Governing Equations, Turbulence Modeling Introduction and Finite Volume Discretization Basics.*, (2021).
- [309] Y.A. Çengel, M.A. Boles, M. Kanoğlu, *Thermodynamics: an engineering approach*, Ninth edition, McGraw-Hill Education, New York, NY, 2019.
- [310] C.J. Greenshields, H.G. Weller, *Notes on computational fluid dynamics: general principles*, CFD Direct Limited, Reading, UK, 2022.
- [311] S.J. Hulshoff, *CFD II Part 2: Computation and Modelling of Turbulence*, (2105).
- [312] André Bakker, *Applied computational fluid dynamics. Lecture 10 - Turbulence models*, (2008). <http://www.bakker.org>.
- [313] Y.A. Çengel, J.M. Cimbala, G. Cozzo, C. Santoro, *Meccanica dei fluidi*, 3. ed, McGraw-Hill Education, Milano, 2015.
- [314] S.V. Patankar, *Numerical heat transfer and fluid flow*, CRC Press, Boca Raton, 2009.
- [315] S.V. Patankar, D.B. Spalding, A calculation procedure for heat, mass and momentum transfer in three-dimensional parabolic flows, *International Journal of Heat and Mass Transfer* 15 (1972) 1787–1806. [https://doi.org/10.1016/0017-9310\(72\)90054-3](https://doi.org/10.1016/0017-9310(72)90054-3).
- [316] R.I. Issa, Solution of the implicitly discretised fluid flow equations by operator-splitting, *Journal of Computational Physics* 62 (1986) 40–65. [https://doi.org/10.1016/0021-9991\(86\)90099-9](https://doi.org/10.1016/0021-9991(86)90099-9).

ACKNOWLEDGEMENTS

With my days as a doctoral student coming to an end, I would like to acknowledge all the people who supported me in this journey and contributed, directly and indirectly, to the realization of my PhD thesis.

First and foremost, I wish to express my deepest gratitude to my supervisors, Prof. Fausto Arpino and Prof. Gino Cortellessa, for the invaluable support and guidance I have received throughout my PhD journey. Thank you for making me passionate about fluid dynamics, for being my mentors and not simply supervisors, for all your ideas, suggestions and much more. I owe you a lot both academically and personally. I would like to extend my sincere thanks to Prof. Giorgio Ficco: with his quick wit, he always manages to elicit a smile. Thanks to all of you for making me feel part of a family.

I express my gratitude to Prof. Andrea Sciacchitano, who hosted me for six months at Delft University of Technology, for his friendly behaviour and his scientific support during my Dutch experience. I had great time there and I always felt welcome.

I am also thankful to all my colleagues in Cassino, with a special mention to Michele, with whom I shared my experience in Delft, and who contributed to the realization of part of the research presented in this booklet.

Many thanks also to the friends I met in Delft (Andrea, Giorgio, Tullio and Martina) for making my days in the Netherlands even more enjoyable.

A special thanks to my childhood friend Simone, for all the great moments spent together. Your contagious laughter always cheers me up.

I couldn't forget to thank my wonderful and noisy family: my parents, Angela and Guido, and my siblings, Gloria and Gabriele. Thank you for your unconditional support, for your constant presence, for all the countless moments that I will always bring with me. What I am today, I owe it to you. Thanks to my grandparents and my uncles, in particular to my grandpa Raffaele, whom I grew up with and who unfortunately left us several years ago. I believe you would have been proud.

Finally, Sara, the love of my life, thank you! We met just over 9 years ago, and from that moment, my life changed forever. Thank you for your unconditional love, for being my light in dark times, for always encouraging and supporting me in my decisions. With you by my side, everything is possible. My achievements are also yours.

Giorgio Grossi
Cassino, January 03, 2024

LIST OF PUBLICATIONS

JOURNAL ARTICLES

Arpino F., Cortellessa G., Grossi G. and Nagano H. (2022). A Eulerian-Lagrangian approach for the non-isothermal and transient CFD analysis of the aerosol airborne dispersion in a car cabin. *Building and Environment*, 209, 108648.

Arpino F., Grossi G., Cortellessa G., Mikszewski A., Morawska L., Buonanno G. and Stabile L. (2022). Risk of SARS-CoV-2 in a car cabin assessed through 3D CFD simulations. *Indoor air*, 32(3), e13012.

Cortellessa G., Canale C., Stabile L., Grossi G., Buonanno G. and Arpino F. (2023). Effectiveness of a portable personal air cleaner in reducing the airborne transmission of respiratory pathogens. *Building and Environment*, 235, 110222.

Arpino F., Cortellessa G., D'Alicandro A. C., Grossi G., Massarotti N. and Mauro A. (2023). CFD analysis of the air supply rate influence on the aerosol dispersion in a university lecture room. *Building and Environment*, 235, 110257.

Arpino F., Canale C., Cortellessa G., Dell'Isola M., Ficco G., Grossi G. and Moretti L. (2024). Green hydrogen for energy storage and natural gas system decarbonization: An Italian case study. *International Journal of Hydrogen Energy*, 49, 586-600.

Grossi G., Arpino F., Bertone M., Cortellessa G. and Sciacchitano A. (2024). On the effectiveness of Reynolds-averaged and subgrid scale models in predicting flows inside car cabins. Accepted to *Physics of Fluids* (DOI: 10.1063/5.0180823).

Bertone M., Arpino F., Cortellessa G., Grossi G. and Sciacchitano A. (2024). Experimental characterisation of ventilation flow in a real car cabin: a benchmark case (submitted for publication).

CONFERENCE PROCEEDINGS

Grossi G., Arpino F., Buonanno G., Cortellessa G., Moretti L., Nagano H. and Stabile L. (2022). A Eulerian-Lagrangian approach for the CFD analysis of airborne disease transmission in a car cabin. *Journal of Physics: Conference Series* (Vol. 2177, No. 1, p. 012015). IOP Publishing.

Moretti L., Arpino F., Cortellessa G., Dell'Isola M., Ficco G., Grossi G., Zuena F., Di Palma M. and Vanoli L. (2022). Analytical and numerical modelling of biomass

gasification in downdraft gasifiers. *Journal of Physics: Conference Series* (Vol. 2177, No. 1, p. 012028). IOP Publishing.

Grossi G., Arpino F., Buonanno G., Cortellessa G., Mikszewski A., Morawska L. and Stabile L. (2022). SARS-CoV-2 risk assessment for a 30-minute car journey. *Proceedings of the 17th International Conference on Indoor Air Quality and Climate, INDOOR AIR 2022*. International Society of Indoor Air Quality and Climate (ISIAQ).

Arpino F., Fallone C., Bertone M., Canale C., Cortellessa G., Dell'Isola M., Grossi G., Ficco G. and Moretti L. (2022). Green hydrogen for RES energy storage and natural gas system decarbonization: a case study in central-southern Italy. *Atti del XXII Congresso Nazionale CIRIAF*.

Arpino F., Dell'Isola M., Fallone C., Ficco G., Grossi G., Grimaldi M., Lisi S., Mignacca B. and Moretti L. (2022). Design and development of a technology park for the exploitation of green hydrogen in an abandoned industrial area in Central Italy. *Proceedings of FORGAZ 2022 Scientific and Technical Conference "Techniques and technologies for gas industry"*.

Grossi G., Arpino F., Bertone M., Canale C., Canale L., Cortellessa G., Dell'Isola M., Ficco G. and Moretti L. (2022). Natural gas system decarbonization by green hydrogen injection: a distributed approach. *IOP Conference Series: Earth and Environmental Science* (Vol. 1106, No. 1, p. 012004). IOP Publishing.

Grossi G., Sciacchitano A., Arpino F., Bertone M., Canale C., Cortellessa G. and Moretti L. (2022). CFD numerical simulations of a real car cabin: design, potential and limitations of numerical analysis. *Proceedings of the 39th UIT International Heat Transfer Conference*.

Bertone M., Sciacchitano A., Arpino F., Canale C., Cortellessa G., Grossi G. and Moretti L. (2023). Experimental Characterization of the Airflow within a Car Cabin. *Journal of Physics: Conference Series* (Vol. 2509, No. 1, p. 012024). IOP Publishing.

Grossi G., Arpino F., Canale C., Cortellessa G., Dell'Isola M., Del Plato L., Fallone C. and Ficco G. (2023). I possibili impieghi dell'idrogeno verde nell'industria pesante e il ruolo chiave delle hydrogen valleys. *Atti del XXIII Congresso Nazionale CIRIAF*.

Grossi G., Arpino F., Canale C., Cortellessa G., Ficco G. and Lombardi T. (2023). CFD design of a novel device for temperature profile measurement in Waste-to-Energy plants. *Proceedings of the 40th UIT International Heat Transfer Conference*.

Canale C., Arpino F., Cortellessa G., Ficco G., Grossi G., Huovinen M. and Karvinen A. (2023). A 3D numerical model for the performance analysis of a differential pressure flow meter in transient conditions for liquid fuels. *Proceedings of the 40th UIT International Heat Transfer Conference*.